



UPPSALA
UNIVERSITET

*Digital Comprehensive Summaries of Uppsala Dissertations
from the Faculty of Science and Technology 2249*

Functional and Modular $As=C$ and $P=C$ Group Motifs

DANIEL MORALES SALAZAR



ACTA
UNIVERSITATIS
UPSALIENSIS
UPPSALA
2023

ISSN 1651-6214
ISBN 978-91-513-1740-3
URN urn:nbn:se:uu:diva-498018

Dissertation presented at Uppsala University to be publicly examined in Beurlingrummet, Ångströmlaboratoriet, Lägerhyddsvägen 1, Uppsala, Friday, 28 April 2023 at 15:00 for the degree of Doctor of Philosophy. The examination will be conducted in English. Faculty examiner: Professor Jose Goicoechea (Veronica Siedle Professor of Chemistry and Veronica Siedle Chair in Inorganic Chemistry at Indiana University Bloomington).

Abstract

Morales Salazar, D. 2023. Functional and Modular As=C and P=C Group Motifs. *Digital Comprehensive Summaries of Uppsala Dissertations from the Faculty of Science and Technology* 2249. 259 pp. Uppsala: Acta Universitatis Upsaliensis. ISBN 978-91-513-1740-3.

This work focuses on the design, synthesis, characterization, and application projections of low-coordinated heavy pnictogen-containing (described by the generic letter E, hence E=C) phosphalkenes (P=C) and arsaalkenes (As=C), with emphasis on the E=C group motifs. The work aims to understand their functional and modular character, reactivity, and potential applications by stabilizing, isolating, and characterizing these species in low-coordination environments. The thesis defines a set of elementary principles that allowed the author to better understand the materials from the perspective of "functional materials", with a subset of the compounds categorized as "smart materials" after exploring and elucidating their fascinating responses in a series of experiments using electrochemical and spectroscopic techniques. The thesis successfully explains the role of the As=C and P=C units and their innate role as "directors" of the molecular electronic structure of the compounds based on their relevant actions and interactions, which led to their naming as "group motifs". By focusing on fluorene-based and DBU-based phosphalkene systems, the research projects extend these two families of compounds. It characterizes their responses to different functional groups, environmental conditions, and constraints as settings. The work illustrates the ability of hydrogen bonding to regulate or stabilize the reactivity of the P=C sites, showing the synthesis of hydrogen-bonded adducts that are more stabilized while maintaining the intrinsic compound identity with the P=C moieties. In addition, a fascinating copper(I)-phosphalkene complex exhibiting photoluminescence and ambipolar properties is studied. The excited state lifetimes of the compound were measured to be in the nanosecond range, which is of interest for applications. Overall, this work represents a comprehensive study of the chemistry of heavy p-block elements and their potential as materials. This work sheds light on their modularity, reactivity, and potential use as "functional materials" and "smart materials" for a variety of future applications ranging from organic electronics and catalysis to artificial intelligence

Keywords: materials, physical chemistry, arsaalkenes, phosphalkenes, DBU, fluorene, photochemistry, arsenic, phosphorus, carbon, hydrogen, sulfur, gold, copper, organic materials, organic electronics, molecular electronics, polymers, transition metal complexes, molecular materials, small molecule, hydrogen bonding, electrochemistry, cyclic voltammetry, chronoamperometry, electropolymerization, artificial intelligence, potentiodynamic, modularity, functionality, XPS, DFT, π -conjugation effects, 2D-NMR, disilenes, siliconoids, group motifs, functional group, emergence, reactivity, reactive systems, organometallic complexes, π -delocalization, low-coordinate, main group chemistry, heavy p-block elements, pnictogens, copper(I) complex, gold(I) complex, photosensitizer, XRD, spectroelectrochemistry, electrochromism, smart materials, synthesis, phosphalkene ligands, imine ligands, hysteresis-like criteria, representative settings, optimal criteria, transient covalence, interactive image, conformer, isomer, ligand scrambling, nanomaterials, stimuli-responsive, optical properties, ligand design, molecular design, X-ray crystallography, emission, self-assembly, As=C, Si=Si, P=C, multiple bond, equilibrium, heteroalkenes, alkenes, reversibility, Raman, ATR-FTIR, ERDA

Daniel Morales Salazar, Department of Chemistry - Ångström, Synthetic Molecular Chemistry, 523, Uppsala University, SE-751 20 Uppsala, Sweden.

© Daniel Morales Salazar 2023

ISSN 1651-6214

ISBN 978-91-513-1740-3

URN urn:nbn:se:uu:diva-498018 (<http://urn.kb.se/resolve?urn=urn:nbn:se:uu:diva-498018>)

*To my beloved Emilia, Ines, Patricia, Sophia, Melissa, Mateo, family, and
friends, with love and gratitude.*

Published and Unpublished Work

This section provides a comprehensive list of published and unpublished materials, organized by chapter number (Ch.) in the dissertation. If several entries correspond to the same chapter, they are distinguished by alphabetical subscripts.

1. **(a)** Morales Salazar, D. Unpublished (Thesis Introduction), 2023.
2. **(a)** Morales Salazar, D., Mijangos, E., Pullen, S., Gao, M. & Orthaber, A. Functional small-molecules & polymers containing P=C and As=C bonds as hybrid π -conjugated materials. *Chem. Commun.* 53, 1120–1123, 2017.
(b) Morales Salazar, D. & Orthaber, A. Modular and smart materials containing P=C and As=C group motifs. Manuscript in Preparation (Unpublished), 2023.
3. **(a)** Green, J. P., Morales Salazar, D., Gupta, A. K. & Orthaber, A. Golden Age of Fluorenylidene Phosphaalkenes–Synthesis, Structures, and Optical Properties of Heteroaromatic Derivatives and Their Gold Complexes. *J. Org. Chem.* 85, 14619–14626, 2020.
4. **(a)** Morales Salazar, D. & Orthaber, A. NMR, theoretical, and relational studies and projections for atypical π -conjugated materials based on heavy main group motifs (Si=Si, P=C, As=C, unsaturated siliconoid). Manuscript in Preparation (Unpublished), 2023.
5. **(a)** Morales Salazar, D., Gupta, A. K. & Orthaber, A. Reactivity studies of an imine-functionalised phosphalkene; unusual electrostatic and supramolecular stabilisation of a $\sigma^2\lambda^3$ -phosphorus motif via hydrogen bonding. *Dalton Trans.* 47, 10404–10409, 2018.
(b) Morales Salazar, D. & Orthaber A. Examination of the interplay between hydrogen bonding and P=C-containing networks using NMR, DOSY-NMR, ATR-FTIR. Manuscript in Preparation (Unpublished), 2023.

6. (a) Clausing, S. T., Morales Salazar, D., Orthaber, A. Preparation, photo- and electrochemical studies of a homoleptic imine-phosphaalkene Cu(I) complex. *Inorganica Chimica Acta* 513, 119958 2020.

No reprints were made.

Contents

Ch. 1. Introduction.....	11
1.1. Group 15. Heavy p-block elements. Molecular inorganic chemistry, Organic chemistry.....	14
1.1.1. “Atypical” inorganic precursors and forms of phosphorus and arsenic (pnictogens and group 15 elements).....	14
1.1.2. Multiple bonding of heavier p-block elements in low coordinate environments, including P=C, As=C compounds. Elementary equivalence relations between relevant inorganic and organic systems. Links to higher abstractions, such as modular and emergent phenomena.....	14
1.1.3. Breaking the “double bond rule” with thermodynamic and kinetic approaches. The importance of neutral and inclusive language in science.....	17
1.1.4. Advantages and potential of unusual bonding situations with Group 15 compounds in π -conjugated environments. E=C as functional groups and group motifs. Conceptual construct or scheme integration.....	20
1.1.5. Summary of primary techniques.....	24
1.1.6. Conclusions.....	27
Ch. 2. Functional and modular small molecules and polymers with P=C and As=C group motifs on fluorene.....	28
2.1. Introduction: Organic and main group approaches to fluorene and thiophene derivatives for conjugated polymers.....	28
2.2. Synthesis and Characterization: P=C and As=C Small Molecules.....	33
2.3. NMR and XRD characteristics of dibromo and dithienyl phosphalkenes and arsaalkenes.....	35
2.4. Analysis of phosphalkene and arsaalkene compounds via UV-Vis-NIR, DFT, TD-DFT. Extended π -conjugation and intrinsic roles of P=C and As=C.....	38
2.5. Electrochemistry of dibromo and dithienyl phosphalkene and arsaalkene small molecules.....	42
2.6. Electropolymerization and characterization of P=C and As=C polymers.....	43

2.7. Functionality and modularity of P=C (<i>poly-6</i>) and As=C (<i>poly-7</i>) polymers. Unique features and electrochromism.	52
2.7.1 Electropolymerization process and mechanisms. Potentiodynamic responses of <i>poly-6</i> and <i>poly-7</i> . Development of the hysteresis-like criteria, optimal criteria, and representative settings for electropolymerization of As=C and P=C polymers. Action exhibitions from <i>poly-7</i> during/after polymer growth.	52
2.7.2. Spectroelectrochemistry. Chronoamperometry. Electrochromism results.	79
2.7.3. TD-DFT cationic Systems. Experimental UV-Vis-NIR spectroelectrochemical. Conducting polymer coupling to minor redox polymer form. Conclusions on experimental evidence. Relations to previous sections. Example of application.	80
2.7.4. Outlook for P=C and As=C polymer systems.	84
2.8. Additional characterization and analysis of P=C and As=C π -conjugated polymers. EDX, ERDA, Raman, and XPS spectroscopy.	85
2.8.1. EDX spectroscopy of monomers and polymers. Confirmation of polymer atomic composition via elemental analysis.	85
2.8.2. ERDA spectroscopy. Confirmation of low oxygen content on the polymeric surface.	87
2.8.3. Raman Spectroscopy of <i>poly-6</i> . Analysis of enhanced Raman resonance signals due to optical gap-to-laser matching and typically low fluorescence of the E=C group motifs. Characterization of nanostructure and order through signature Raman features.	89
2.8.4. XPS Spectroscopy. Confirmation of P=C and As=C group motifs in monomers and polymers. Not oxidized or defects but redox polymer states.	95
2.9. Post-functionalization of <i>poly-6</i> with Au(I) ions.	100
2.9.1. Preparation procedures for the synthesis of 8 and <i>poly-8</i>	100
2.9.2. Spectroscopy, DFT, TD-DFT characteristics of 8 and <i>poly-8</i> . Significant effects on the optical properties of the P=C materials upon gold incorporation.	101
2.10. Optical, microscopic, morphological, crystallographic, and electronic properties of the studied systems.	104
2.10.1. Scanning Electron Microscopy of polymers.	104
2.10.2. DFT calculations - monomer to tetramer - stabilization of frontier orbitals and higher number of frontier states. Experimental optical gaps.	106
2.10.3. X-Ray diffraction analysis: relevant features, π - π interactions in the solid state.	107
2.11. Summary and conclusions.	108
Ch. 3. New exotic P=C molecules for π -conjugated organic materials.	109
3.1. Motivations towards fluorene-derivatized P=C compound.	110

3.2. Synthesis of materials. Stille coupling. Unique fluorene-substituted molecules via P=C induced asymmetric side accessibility.	116
3.2.1. Synthetic procedures and schemes. Spectroscopic findings.	116
3.2.2. Utilization of gold atoms in molecular Au(I) complexes.	
Synthesis of 16 , 19 , 21	120
3.3. NMR Spectroscopy features.....	121
3.4. Single-crystal X-ray diffraction (XRD) study.....	125
3.5. Computational chemistry (DFT) study.....	128
3.6. Summary, conclusions, and outlook.....	131
Ch. 4. Functionalization, reactivity, and interaction of Arsaalkenes, Disilenes, Phosphines, Phosphaalkenes, Siliconoids.	132
4.1. Introduction and scientific motivations.	132
4.2. Synthesis and NMR characterization. Salient features of phosphaalkene, arsaalkene, disilene, materials (steric hindrance, magnetic/structural inequivalences, π -conjugation effects) with potential applications. Comparison with phosphine-disilene compound with limited features. Evidence of dynamic equilibrium between phosphaalkene/phosphindole-siliconoid species.	139
4.3. Computational characterization of phosphaalkene-disilene-containing material, phosphaalkene-siliconoid, phosphine-disilene. Analysis of orbital densities and energies, optical gaps, and π -delocalization using DFT and TD-DFT.	152
4.4. Summary and conclusions.....	156
Ch. 5. Phosphaalkene-functionalized DBUs with hydrogen-bonded extensions: stabilization of E=C (P=C) via HB interactions.....	160
5.1. Introduction to relevant topics.....	161
5.1.1. Literature review on reactivity of E=C bonds with small molecules highlights their irreversible reactivity (decomposition) as the norm.	161
5.1.2. Chemistry and applications of the DBU superbase.	163
5.1.3 Chemistry of strong acids and superacids. Water and water/halide clusters. Hydrogen bonding interactions.....	163
5.2. Synthesis and characterization of DBU-phosphaalkene (36), hydrogen-bonded HCl adducts (37), and water-containing dimer (38)..	165
5.2.1. Synthesis and high reactivity of DBU-PA (36) due to structural frustration (π -conjugation + bicyclic torsional strain + sterically-encumbering Mes* substituents).	166
5.2.2. DFT analysis of the neutral DBU-PA system (36) explains its high atmospheric sensitivity.	170
5.2.3. Synthesis of 37 via the reaction between 36 and HCl in anhydrous and inert media.....	171

5.2.4. Formation and crystal structure of 38 . A water-based hydrogen-bonded dimeric network containing phosphalkenes.....	172
5.2.5. Confirmation of the HB nature of 37 and 38 and the existence of H ₂ O and H ₂ O/Cl clusters. Unanimous dimeric nature of 38 confirmed by DOSY-NMR spectroscopy.....	172
5.2.6. Analysis of the elementary electronic structure of 37 and 38-monomer . QTAIM analysis of 38	181
5.2.7. FTIR/ATR spectroscopic and computational chemistry study of HB in solution mixtures of 37 and 38	183
5.3. Reaction with superacids: Hydrogen bonding formation over P=C decomposition after reacting with HOTf (39) and HPF ₆ (40).	186
5.4. Reactivity study 37 (38), 39 , 36 via ³¹ P NMR spectroscopy. Potential for a new “type of stabilization” construct for low-coordinated compounds and heavy p-block elements.....	188
5.5. Synthesis and characterization of Pd(II) complex (41) and organic DBU-HCl (42) species.	189
5.6. Miscellaneous: Unpublished work and future avenues.	191
5.7. Conclusions.	193
Ch. 6. Photophysical and electrochemical properties of an emissive Cu(I) complex with DBU and Phosphalkene ligands.	194
6.1. Literature background. Introduction to low-coordinated P=C ligand-based copper(I) complexes.....	194
6.2. Copper(I) complexes with bis(diimine) ligands. Characterization of 46 by photophysical, electrochemical, NMR, and DFT/TD-DFT.....	195
6.3. Conclusions and outlook.	209
Ch. 7. Summary and conclusions.....	211
Svensk sammanfattning	213
Acknowledgments.....	216
References.....	219

Ch. 1. Introduction.

This thesis has seven chapters (Ch. 1-7). The general researcher can gain perspectives from reading individual Chapters or sections of choice.

Ch. 1 presents a brief introduction to the thesis work from general and specialized short perspectives dealing with the materials science and p-block element perspectives. We focus on phosphalkene ($P=C$) and arsaalkene ($As=C$) group motifs, their relations to $C=C$ groups, and their stabilization via sterically encumbering and protecting groups. We discuss their introduction as π -conjugated fragments into organic scaffolds. Some emphasis is placed on constructing a rational argument highlighting certain equivalences or relations between various 2D material combinations and the $P=C$ or $As=C$ introduction into organic scaffolds.

Ch. 2 deals with our published and unpublished studies on $P=C$ and $As=C$ in thienyl-substituted fluorene-based small molecular and polymeric systems, with the demonstration of their utility as novel optoelectronic organic materials. The materials exhibit stable electrochromism in their polymer state. We present arguments that motivate the use of electropolymerization as a robust process. For example, as a process to cherish and understand the natural potential of polymeric forms based on different criteria, and hence their ability to be used programmatically for problem-solving within various realms. Oppositely, we argue that in most chemical polymerization processes, polymeric forms are filtered through sequences of harsh treatments that generate the loss of modularity and complexity, leading to materials that become enclaves of a particularized function, which blurs the line of natural functionality. While characterizing the grown polymers in electrochemical cells filled with transparent electrolyte liquid solutions, some signatures of emergent phenomena, such as structurally organized segmentation and memory-like occurrences, are exhibited as electrochemical events, for example, characterized by discrete and organized changes in current or potential as the polymers are cycled. Functionalization of small molecules and phosphorus polymers with $Au(I)$ is achieved, in contrast to unobserved $Au(I)$ -arsenic reactions for the small molecules and polymers. A detailed characterization of the materials is provided.

Ch. 3 presents our published studies into $P=C$ group motifs through the design, synthesis, and characterization of novel small molecules, expanding upon the unusual and challenging family of $P=C$ -containing fluorene-based π -conjugated materials. The materials present discrete variations of their

optoelectronic properties as characterized through NMR, XRD, UV-Vis-NIR, and DFT, providing access to tailored structural motifs with specific optical, electronic, and structural features such as increased intermolecular packing based on the extension of the π -backbone, decreased optical gaps as well as HOMO-LUMO gaps. Some unexpected and exciting results regarding output variety from synthetic protocols, λ_{onset} , and observed solid-state features concerning π -conjugation extension effects are found. Coordination by Au(I) significantly affects the optoelectronic and structural features of the compounds, which empowers their use based on relations to relevant topics in organic electronics or molecular electronics, where the organic element-to-gold element interface dictates the central properties of several types of electronic objects.

Ch. 4 parades our unpublished studies on the preparation, theoretical investigation (DFT), and NMR characterization of compounds comprising combinations of “atypical” group 14 (Si=Si, Si₆ siliconoid) and “atypical” group 15 (P=C, As=C) fragments simultaneously. The two-separated research areas, both concerned with the design of organic materials featuring multiply bonded heavy group 14 or 15 group motifs in low-coordinated states, produce a confluent path for the synthesis and partial characterization of new materials. Our efforts realize an initial direction for creating one of the most sophisticated families of organic materials, simultaneously incorporating two “atypical” group motifs onto one organic molecule. Our presentation of the materials and motivations behind the study is done from the perspective of future applications. That is, where the complexity of the compounds (while simultaneously incorporating several salient features such as well-separated frequencies as well as kinetic stability that give them with the necessary typicality) could be cherished in future areas such as novel systems design, organic electronics, molecular electronics, or quantum material electronics.

Ch 5. introduces our published and unpublished studies with the organic base DBU. Derivatives containing P=C motifs are synthesized. Their engagement in non-covalent interactions (NCIs) of the hydrogen bonding type (HB) is qualitatively studied. Stability experiments in solution NMR elucidate the role of HB and supramolecular chemistry in stabilizing the P=C group motifs among the set of obtained products relative to the starting material, providing a new type of stability approach, or “conceptual construct” towards the stabilization of E=C groups via peripheral HB using savior atoms. As organic crystals, the solid-state features of the parent species and products are studied with an emphasis on HB and NCIs. Interesting observations related to sudden physical or spectroscopic property changes of the materials relative to their immediate previous state, sometimes in a fully reversible fashion after some sequence of operations, which adds some functional character to them. We relate some of the occurrences to the concomitant overlap of an isomorphic relation between variable-based or parameter-based equivalences in some descriptor range, as conditions are varied, which among others, cascade in the generation of highly viscous solutions that did not solidify during solvent

evaporation or generation of HB H₂O clusters via hydrophobic effects (as measured spectroscopically). The most inspiring observation from the materials relates to the exhibition of a hydrogen-bonded H₂O-based network, which corresponds to the challenging task of finding complex supramolecular material examples in which equivalent hydrogen-bonded structures up to isomorphism can be generated and observed, both in the solid state and in solutions.

Before concluding remarks in Ch. 7, Ch. 6 finalizes the thesis work with our comprehensive study of a Cu(I) complex with the homoleptic and bidentate phosphalkene parent ligand from the previous chapter as an electrochemically rich and emissive compound with interesting photophysical properties such as emission in various environments and detectable emission lifetimes of 9 ns. A DFT set of two naturally acquired isomeric forms during *in silico* optimizations successfully helps us rationalize experimental observations. The DFT set is characterized by the minimal energy differences between the two structures, coupled with their representativity as energy minima points on the PES and as proactively inductive tetrahedral and tetragonal structure types relative to the two metastable structure types typically observed for photoexcited Cu(I) complexes. Observations for distinct kinds of emission populations are established. One of the populations possesses markedly intensified emission intensities as the temperature decreases and the excitation energies increase. The disappearance of the typical metal-to-ligand transfer events is coupled with the concomitant appearance of mixed events with ligand character at higher energies and the intensification of events at lower points (> 700 nm). We assign the latter to the potentiation of other events or emissive processes at low temperatures and in correspondence to some structural transformation, representing the isomeric forms, with its identity based on the differing photophysical features. Characterization of the unitary Cu(I)-P=C complex via cyclic voltammetry is realized through its *in-situ* preparation in the electrochemical cell, which confirms the premises on structural lability due to ligand exchange, which potentiates the establishment of equilibrium phenomena where a structurally isomeric major and minor form becomes available during the experimental lifetimes.

1.1. Group 15. Heavy p-block elements. Molecular inorganic chemistry, Organic chemistry. Inorganic chemistry.

1.1.1. “Atypical” inorganic precursors and forms of phosphorus and arsenic (pnictogens and group 15 elements).

Our Ph.D. created organic compounds containing inorganic phosphorus (P) and arsenic (As) atoms in unusual or “atypical” bonding situations and environments. P and As possess a ground-state valence electron configuration of $3s^23p^3$ and $4s^24p^3$, which relates to the electrons and shells involved in bond formation. In their elemental forms, phosphorus is considered a non-metal, whereas arsenic is regarded as a metalloid. However, material descriptors are based on the assignment of a material form to a labeled category (or “class”), such as insulators (non-metallic), semiconductors (semimetal), or metals (metallic or metalloids). More interesting elemental forms exist, for example, “atypical” allotrope forms. Then phosphorus and arsenic can become representatives of the metals, semiconductors, or insulators, depending on the freedom we permit during preparation. Black phosphorus is the thermodynamically stable form of P at standard temperature and pressure (STP). It is a direct semiconductor (band gap energy = 0.3-2 eV).¹ Arsenic is a metalloid and a semimetal in its most abundant grey allotrope form (band gap energy = 0 eV). As with phosphorus, arsenic also possesses a black arsenic crystalline allotrope. Both black arsenic (band gap energy = 0.31 eV)² and black phosphorus are equivalent semiconductors from the group number perspective; also, both belong to the 2D single-element layered materials category. In this category, materials possess features, parameters, functions, and properties (i.e., equivalences or relations) shared with graphene and silicene (silicon 2D analog of graphene).

1.1.2. Multiple bonding of heavier p-block elements in low coordinate environments, including P=C, As=C compounds. Elementary equivalence relations between relevant inorganic and organic systems. Links to higher abstractions, such as modular and emergent phenomena.

The central topic of this thesis surrounds the design, study, and introduction of new molecular, oligomeric, polymeric, and transition metal-containing systems that present multiple bonding between heavy group 15 elements (E: P=C, As=C) and carbon-based organic compounds, with a small part dedicated to their mutual use in connection to heavy group 14 elements as disilenes and unsaturated siliconoids (E: Si=Si, Si₆).

Compounds and atoms in compounds can be described through a plethora of descriptors, out of which the $\lambda^n\sigma^n$ descriptor refers to an individual atom's valence (λ), and coordination number (σ).³ Low-coordinate compounds with pnictogens in trivalent states and two-coordinated modes are represented by the descriptor $\lambda^3\sigma^2$, where λ corresponds to their valence state and σ corresponds to their coordination number.

Regarding the specified types of bonding situations under scrutiny, we focus on acyclic, localized, and neutral phosphorus-carbon (3p-2p) π and arsenic-carbon double bonds (4p-2p) π or bonding situations. Phosphaalkenes of this type were first described in a publication dating back to 1976.⁴ Homologous arsaalkenes were first synthesized in 1977.⁵ The frontier electronic structure or reactivity of P=C groups resembles the one for C=C groups in a few cases (see below); however, some significant differences exist between the two unsaturated groups such as the preference of the P=C to coordinate through the lone pair while C=C does so through π -coordination. The equivalences or relations between the two (see below) have led to the creation of the 'phosphorus, a carbon copy' as an interesting "conceptual construct", which refers to the fruitful space of outcomes one may realize when regarding phosphaalkenes and alkenes as mutually related functional groups or motifs.

Due to the boundedness of the n_p on the phosphorus atom and localization on a more diffused electron orbital shell, the charge density on n_p decreases as the distance from the nuclei increases. As a result, for example, and comparatively, the imine nitrogen (n_p, e^-) corresponds to the HOMO orbital, which is not the case in small P=C fragments where the HOMO orbitals localize on the P=C π -orbital. This reactivity order can be partially explained by the larger and smaller s-orbital contributions ("high s-character") to the electron lone pair and p(π) orbital, respectively. However, in π -conjugated systems without the P=C group motifs, the HOMO tends to be localized on the conjugated system or electron-donating groups. Therefore, in the presence of electron-donating functional groups such as thiophene, anionic groups, or disilenes, the P=C becomes a strong or stronger π -acceptor, which is one of the crucial tenants of the work of this thesis in which stabilized E=C compounds are presented. The electronegativity of phosphorus is lower than that of nitrogen. The σ -electronegativity and first ionization potential of phosphorus are close to those of carbon.⁶ The isoelectronic relation between P=C and C=C and the similarity in electronegativities and first ionization potential leads to their equivalent reactivity (of both P=C and C=C) in many synthetic protocols (e.g., Wittig, Diels-Alder reactions). Therefore, the relation from P=C groups to C=C groups is essential for developing materials. Moreover, we could argue that P=C and As=C possess more functionality and a richer potential to generate a variety of systems than homologous C=C in relevant areas where doubly-bonded carbons are ubiquitous. What can we learn from the inorganic systems we introduced above now that we know the relations of the organic materials to the P=C, As=C, Si=Si group motifs, and more (and vice versa)?

For example, while graphene and silicene are metallic in these 2D single-element allotrope forms, their interconversion to semiconductor forms can be achieved by chemical treatments (such as using oxygen adatoms) or pressure (dislocations). Interconversion of black arsenic and black phosphorus semiconductors to metallic forms can be achieved via pressure, doping, or ion implantation (dislocations). We can abstract relationships to the small molecules. For example, an organic polymer containing As=C group motifs and interacting heterogeneously but fluidly with an environment composed of ions could correspond to a representation from which equivalences can be abstracted to a stack of black arsenic and graphene or carbon nanotubes. More sophisticated relations can be developed with some technology by induction of states and transitions. The transitions can be converted into processes, and the states represent the operation system, among other approaches. In the following paragraphs, we trace two elementary relations between the inorganic and organic materials we study in this subsection, which help us abstract concrete information from equivalent concepts, making their relationship more substantial:

(i) The presence of π -conjugated bonding connections in both categories of materials; 3p-type orbitals generate π -conjugation links in black phosphorus; 3p-type orbitals generate π -conjugation connections in Mes*-P=C(fluorene). Via energy transfer, a stack of black phosphorus and graphene can “excite” some π -group in Mes*-P=C(fluorene) reversibly, where the excited state or product has some direct relation to an arbitrary goal (i.e., application functionality). By induction or construction, the conditions correspond to an equivalence between the two types of materials, which corresponds to some abstract link (or relation) between (two) π -conjugation connections.

(ii) The existence of π -type orbitals in their frontier **bands** or frontier **orbitals**. The black phosphorus and graphene valence band top and conduction band bottom are characterized by p_z bonding and antibonding orbitals, which form π -type or π^* -type bonding or antibonding orbitals. The P=C HOMO and LUMO orbitals are characterized by bonding and antibonding p_z orbitals, which form π -type or π^* -type bonding or antibonding orbitals equivalently.

Now, from (i), (ii), group number, and atomic identity, we could establish some orbital and stoichiometric criteria based on available sets of appropriate C=C, As=C, Si=Si, P=C, protecting groups, and synthetic methods to design (or predict, in the future) specific organic products. The products retain various similarities to inorganic stacks incorporating black phosphorus or black arsenic combined with silicon and graphene from the properties generated via equivalence relations (e.g., reflexivity, symmetry, transitivity, preorder, and more).

Elementary relations or equivalences between these two types of materials helped us exemplify the suitability of the comparison. Below, we informally extend it via logical relations, expanding concepts such as “functionality” towards more advanced notions such as “emergent phenomena”, “modularity”,

and “behavior” (Section 2.7 has a formal introduction), which helps us span the entirety of our goals, from a holistic basis.

For example, organic materials with inorganic motifs are excellent sources of advanced functionality due to their tunability via types of available states in a discrete manner, as well as flexibility and, thus, processability. Materials with advanced functionalities can exhibit modular, enhanced, and emergent phenomena or performance. The enhanced phenomena correspond to a higher abstraction, represented by the more advanced primitive forms underlying their exhibited functionality. Evolutionarily, an arbitrary set of primitives that generate a higher abstraction can correspond to one type of emergent phenomena, which we can reference through relations to concepts such as behavior. Representable and representative functionality can emerge from unconventional approaches. Our goal to create small molecules or polymers with “atypical” bonding situations ($P=C$, $As=C$, $Si=Si$, and more) has transformed into the realization that higher abstraction or higher complexity may be generated from their interactions, from which novel primitive forms presenting more advanced state responses, can be constructed. Thus, we see their “atypical”, “exotic”, and “reactive” character as a source of crucial features, vital complexity, and, therefore, an indispensable source. At a sufficiently elevated level of abstraction, order, and interconnectivity, advanced primitive forms, such as small molecular systems, complexes, or polymers with unique features, can be developed or advertised as “smart materials”. By stabilizing specific types of compounds, as exemplified through their isolation and characterization, we have established a degree of regularity and typicality from which functional and modular transformations can be inferred or abstracted. Based on relations and hierarchies, this approach forms the foundation of our work throughout all chapters, including the study of small molecules, hydrogen-bonded supramolecular complexes, transition-metal complexes, and “smart polymers”. We can now realize the importance of understanding organoarsenic and organophosphorus compounds and materials, particularly those in unusual bonding situations. As we will see, heavy p-block elements can powerfully extend the π backbone, giving us access to compounds with unique features, enhanced functionality, and modularity.

1.1.3. Breaking the “double bond rule” with thermodynamic and kinetic approaches. The importance of neutral and inclusive language in science.

The preparation of main group compounds with p-block elements characterized by (p-p) π multiple bonds between them or other elements was previously thought to be a secluded area only for the light elements of the 2nd row. That is, C, N, and O engaged in multiple bonding and created stable (2p-2p) π compounds that were separable and kinetically stable under atmospheric or

pseudo-inert (“mild”) conditions. The absence of these types of compounds was evident for elements in rows 3 to 6. Through frozen matrices, some researchers achieved the transient formation of some compounds such as methylidyne-phosphine ($\text{HC}\equiv\text{P}$) and methylene-phosphine ($\text{H}_2\text{C}=\text{PH}$); however, the compounds decomposed readily at low temperatures lower than +150 K ($< -123\text{ }^\circ\text{C}$), yielding insoluble polymers. This observation outcome became known as the double bond rule.⁷

The double bond rule specified the reluctance of elements with a principal quantum number > 2 to form stable (p-p) π bonds. However, the double bond rule was broken by the incorporation of thermodynamic or kinetic stabilization approaches, such as via incorporation into rings (e.g., phosphinines), π -delocalization via π -conjugation (e.g., acetylenic-phosphaalkenes), incorporation into cyanine-like structures or the stabilization via NHCs (e.g., phosphamethine cyanine, phosphenium or phosphinidine compounds). Incorporating the pnictogen into cyclic structures enhances the thermodynamic stability of the compounds. The delocalization of charge density along the edges of path-connected charge density regions comprising $[\text{C-As-C}]_{\text{unsaturated}}$ explains the phenomenon well; this stability can occur, for example, through π -conjugation (orbital effect) or π -delocalization (electron effect). The same effect increases acyclic compounds' stability, where the multiple heavy bonds conjugate to neighboring π orbitals. A second approach involves using salts, through which the generation of positive charges on phosphorus compounds generates a phosphacyanine dye, until recently, an academically new type of phosphorus compound. In this case, however, there is no localization of the $\text{P}=\text{C}$ double bond.

The favored approach for stabilizing heavy p-block elements and incorporating them into acyclic or localized units containing $\text{E}=\text{C}$ bonds (E: P, As) uses sterically encumbering or “bulky” protecting groups. We made use of 2,4,6-tri(*tert*-butyl)phenyl (Mes*), which is also known as supermesityl and pronounced: “Mes star”. We also used 2,4,6-tri(iso-propyl)phenyl (Tip), which is pronounced: “Tip”. The repulsive forces typical of steric moieties keep small and large reactive molecules away from the functional $\text{E}=\text{C}$ or $\text{E}=\text{E}$ groups, preventing their decomposition or irreversible reactivity. Protecting groups are characterized by essential contributions other than steric protection, despite the biased labels some researchers assign to them, such as irrelevant or annoying. Protecting groups can contribute to the expressed reactivity and functionality of the molecular system.

Regarding reactivity, the large electron density of Mes* (*tert*-butyl groups: strong σ -donor) can be reflected in the Mes*-based orbital contributions close to the bonding and antibonding orbitals near the FMOs (vide infra, e.g., Ch. 4, 6 vs. Ch. 2, 3, and more). The increased contribution (e.g., extended π -conjugated systems in Ch. 2 vs. reactive starting material in Ch. 5 or products in Ch. 4) can also affect the reactivity of intermediates, as in the case of arsaalkene or phosphaalkene single-bonded precursor intermediates, for which

a CH-activation path through cyclization of the pnictogen via a *tert*-butyl group can become a competitive path in some conditions, such as elevated temperature or excess radiation, forming phosphindole and arsindole.⁸ It has been suggested that this is the major contributor to difficulties synthesizing Mes*-protected arsaalkenes. In terms of functionality, the presence of non-polar *tert*-butyl groups, and an aromatic phenyl ring, which stabilize and decrease the reactivity of the multiple heavy bonds as their primary function, can give rise to secondary functionality.

The formation of relevant and observable NCI effects, such as the increased contribution of weak hydrogen bonds from CH₃ hydrogen bond donors and aromatic proton groups, was observed via NMR. The formation of weak hydrogen bonds in a liquid solution can also be epitomized in long-range effects in liquid solution and the solid state, such as viscosity changes and related clusters (Ch. 5) or supramolecular complex formation occurrences and spectroscopic observations. In addition, the crystal structure of the same compounds exhibited the presence of separated polar-nonpolar regions, wherein the existence of NCIs was evident as these separated regions were present in a membrane-reminiscent fashion that, in a sense, confirmed the role of hydrophobic-hydrophilic effects. The observables correspond to contributions of NCIs that dictated the character of the observations in the long-range or large-scale characterization of the compounds, given the dramatic energy and time-scale differences between the experimental techniques (i.e., XRD, NMR), directly confirming or evidencing clear signatures of the phenomenon.

Definitive experimental evidence then begs the question of whether their categorization as ‘weak’ or ‘secondary’ hydrogen bonds accurately portrays their aggregated role and nature. Thus, the classification of chemical compounds, reactivity, and observations, by use of adjectives or language that can be used to profile materials or others erroneously can be a problem in science and in general (for example, in the argument above: ‘annoyance’, ‘irrelevance’, ‘weakness’). First, it leads to the biasing of observation toward the desired outcome while minimizing or demonizing a concept or observation and its representative adjoints (e.g., the importance of NCIs) via semantics. It also obfuscates the importance of secondary factors, which may be of research interest or value. However, it is easy to see how the instantiation of some realization or potentiality as “bad” is far worse than the overly exciting type of “good” connotation some researchers may assign to a concept, observation, or idealization, without going into the extremes of exaggeration under unprovable attribution to a concept or observation. It can be problematic because such instances create boundaries and imaginary preconceptions on the achievable types of research outcomes by creating and perpetuating “beliefs” coupled with the instantiating of the boundary based on a single observation or the relative bias of the presented work. Furthermore, the presence of preconceived boundaries and imaginary preconceptions (i.e., not thoroughly accurate, generalizable, provable, or disprovable) isolates research into

increasingly specialized areas, where the potential of creative approaches is hampered if the approach overlaps or coincides with some of these artificial boundaries.

We have used general and inclusive language while minimizing instances of certain adjectives. In the relevant section of Ch. 2, we use certain adjectives to describe compound realizations and phenomena that are interconnected to "modular behavior" and "emergent phenomena" and thus phenomena that accurately placed the compounds in the category of "smart materials". We analyzed our results with Mes* as representative and relevant substituents. At the same time, our work has focused on phosphalkenes and arsaalkenes bearing Mes* substituents, and our findings can be of general interest and extrapolated to other systems or applications by considering the potential that protecting groups offer functionally. Our observations are relevant as we and others are increasingly unmasking or thinking about this issue.

1.1.4. Advantages and potential of unusual bonding situations with Group 15 compounds in π -conjugated environments. E=C as functional groups and group motifs. Conceptual construct or scheme integration.

Using organophosphorus and organoarsenic groups in π -conjugated backbones presents a unique strategy for tailoring materials with beneficial structural, optical, electronic, and electrochemical properties. During or following action, our materials should generate a higher (or lower, where appropriate), characterizable, or ascribable **distinguishability** relative to the C=C ones (or others), and hence which may be of consequence in the generation of advanced functionality, modularity, or emergent phenomena. The emergent phenomena can be presented from a collective or selective set of action-derived or response-derived representations resulting from some stimuli-responsive criteria or forms. Extrinsic characteristics such as localizability, delocalizability, or decoupling from external or backbone group actions or responses can be constructed, and the induction of an E=C frame or perspective (i.e., framed spaces) may become a realization (e.g., for using towards modularity, decreased biases, and more). Under special conditions, these framed spaces may be protected spaces from which abstractions and access to secondary or "hidden" functionality become suitable and available (e.g., Section 2.7.1.5 results and definitions of modularity, emergence, and more).

While attempting to characterize some material in our case, actions or responses should be reversible, whereas, for the use of the compounds as materials in electronics, their use is contingent on some criterion of stability of the E=C group. Hence the importance of compound identity or E=C group motif integrity, in general, and why our focus on characterizing the nature and effects of E (P, As) incorporation, particularly in terms of the E=C bonding

existence. Some exceptions to this rule may be in catalysis, where the main goal is a product, and in industrial scenarios, where there is less interest in how the product was catalytically achieved. However scientific and academic curiosity-driven approaches certainly lead to the discovery of novel mechanisms, the design of powerful molecular compounds or synthons, and the elucidation of unknown paths. For future applications that cherish or exploit effects at the atomic or molecular level, it is crucial to maintain the structural properties (descriptors) of the compound, such as its covalent bonding environment, throughout the process (i.e., preserving its equivalent identity). Any significant or irreversible changes to the local structures or sites (e.g., E=C) may compromise the overall scheme through loss of functionality or distortion of the responses (e.g., information flows). On the other hand, yet homologically, the reactive and sensitive nature of the E=C group motifs can be coupled in critical systems, where the modification of the E=C signifies some structural deviation, for which the E=C follows its desired function by changing its structure either reversibly or irreversibly, depending on the goal of the designer or engineer. Thus, they can serve as critical indicators precisely because of their nature and sensitivity to certain environmental changes. Therefore, the decomposition of E=C groups in these applications during testing can be a "positive sign" because it means that these units will perform their critical function within the system during real-world scenarios, responding reactively to specific environmental cues and delivering a message indicating that some desired or undesired component in the system has been modified ("externally") or has undergone an anomalous variation ("internally"), thus justifying and highlighting their importance as group motifs in a particular (but not limited to) application. That is, this is a typical example where the system or set, or group, follows the definition of E=C structures (more precisely E=C-containing structures) as group motifs. An E=C structure (and others such as E=E) can be considered a functional group, but not all functional groups are group motifs. However, suppose that the E=C moiety acts as a "leader" or "director" (and other distinguishing characteristics and properties that will be realized throughout the thesis) of the entire molecule or system to which it is bonded. In this case, this statement seems accurate because the E=C structure can describe the properties or actions of the larger entity in a more general way (in different settings) that follows the definitions of groups and motifs. By comparison, a C=C containing molecule or C=C site (or even the case where we consider a C=C to be a group motif while the E=C is considered part of the larger structure, e.g. as a module) cannot meet the criteria of an E=C (or E=C group motif) because it does not contain the elements necessary for E=C reactivity and cannot follow the (bi)nary properties of an E=C.

Most functional or modular reactivity can be ascribed to density configurations, resulting in energy levels or partitions attained while the material interacts with various perturbations or stimuli. The compounds in this study were used to investigate the effects of doping and other forms of "biasing

stimulus”, such as salts, voltage, applied fields, delocalization, or localization. Doping can generate both local and global effects, which may be potentiated or enhanced by the intrinsic presence of heavy phosphorus or arsenic atoms in these materials, which interestingly are used in specific amounts to dope inorganic or hybrid materials in other fields. Both phosphorus and arsenic can be categorized as electron donors relative to group 14 elements (C, Si). New phenomena relating to incorporating functional groups or group motifs into organic frameworks should be envisioned from the perspectives of increased reactivity, reversibility, and differential characteristics over some variables. We hope that introducing P=C, As=C (and others, Si=Si) in materials will coherently accentuate some features for some target criteria. By experience, researchers have learned that these compounds are more sensitive than all-carbon or typical analogs (C, H, N, S, O), which we believe also grants more exciting and complicated responses once they are stabilized in their prepared form. Thus, observations should relate to sequences of reversible or irreversible responses based on a series of imparted changes in the relevant environments in connection with a goal. This analogy applies equally to tertiary and pentavalent P and As, which display pyramidalization of their environments, which, however, may cause π -conjugation inhibition or avoidance. The exemplified short sequence below can be generated through some arbitrary application system (see Ch. 5). The conditions below, coupled with some stimuli, can, as a technological scheme, generate the forms and spectrum responses specified and acquired, from which we may abstract relations, features, or functions toward a goal realization.



Scheme 1.1.4.1. Arbitrary short loop sequence process starting from $\{0\}$ and returning to $\{0\}$, which implies reversibility of the process, with a series of steps in the middle, characterized by physical changes (right arrow direction) and as actions that generated spectrum responses (left arrow directed). In the example, we abstracted from our observations during the study with some family of P=C compounds that formed hydrogen-bonded (HB) adducts with functional character, explored in Ch. 5. We assigned the HB adduct descriptor to some instances where HB was evidenced. In contrast, in this example, the HB motif descriptor refers to the presence of HB evidence coupled to equivalences or relations to P=C group motifs (e.g., via supra-molecular interaction or ^{31}P NMR spectral shift observations of some product or upon HB exchanges as observed via X-ray diffraction and NMR spectroscopy).

In extended π -conjugated systems, the HOMO orbital may delocalize along the path that provides the largest π -extension or the one that stabilizes the electronic structure more upon electron addition or removal or applied feed (i.e., bias) depending on the number of π -electrons, the number of rings, and others.

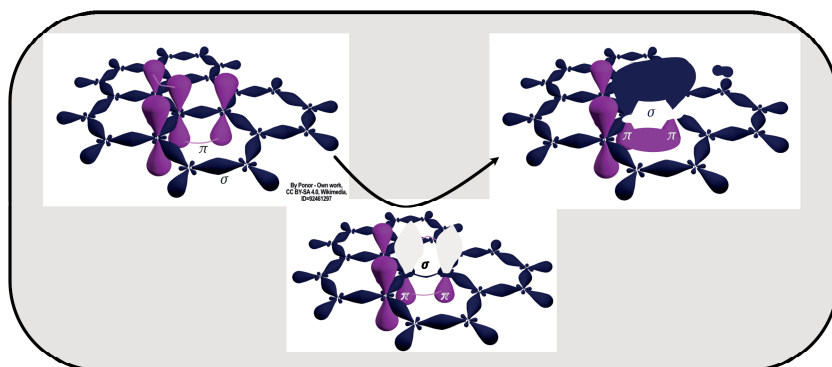


Fig. 1.1.4.1. Schematization of $\{(\pi, \sigma)_{\text{hybridized orbitals}}\} \rightarrow \{[\pi - \sigma, \pi + \pi]_{\text{linear combination}}\} \rightarrow \{(\pi, \pi, \sigma, \sigma)_{\text{extended } \pi\text{-conjugation}}\}$. In the left Fig., the p_z orbitals corresponding to MOs (p_x and p_y omitted for clarity) are present without distinguishing their orbital phase differences. Molecular orbitals of the same or different phases result in density overlap or absence of overlap, along with low or high-energy σ -type ground connections—see acknowledgment in Fig. inset.

In this subsection, we explore how combining two or more conceptual constructs or frameworks concurrently or parallelly can be used to realize an amplified or novel response in materials.

For example, the combination or realization of compounds that simultaneously cherish aromaticity and quinoid character, or redox polymer and conducting polymer states, can be used to create systems with modular character or that introduce the functioning capacity of the $\text{P}=\text{C}$ or $\text{As}=\text{C}$ group motifs. These naturally rendered directors of the electronic structures of the compounds can take advantage of their augmented (or extended) and flexible (or dynamic) structure as well as local interactions in stabilizing highly delocalized states in the material, in which the $\text{As}=\text{C}$ or $\text{P}=\text{C}$ maintain their identity while generating modular and functional behavior to the materials via these exchanges (see Ch. 2).

In the same way, we can combine hydrogen bonding with the stabilization of phosphalkenes. We can imagine an abstraction in which long-range and NCIs are favored by self-complementarity (i.e., cohesive supramolecular synthons) and by which the $\text{P}=\text{C}$ group motifs are stabilized and protected, while at the same time, NCIs between hydrogen-bonded structures and $\text{P}=\text{C}$ groups are emphasized in some settings. For example, the simultaneous use of hydrogen bonding and $\text{P}=\text{C}$ groups can enhance their intrinsic properties, creating a more dynamic structure and material (e.g., "deformable" and modular) that is typically flexible and adaptable and which may even exhibit interactivity between phosphorus atoms and hydrogen-bonded networks in some settings, such as in the solid state (see Ch. 5).

1.1.5. Summary of primary techniques.

This subsection summarizes a few of the prominent experimental techniques we used during the Ph.D. study cycle to characterize molecules, compounds, and materials. Other methods, either more specialized or less frequently used, are presented immediately before the results.

Nuclear magnetic resonance (NMR) spectroscopy is a powerful analytical technique used to study the structure and properties of molecular materials. It is based on the principle that atomic nuclei absorb and emit electromagnetic radiation at specific frequencies when placed in a strong magnetic field. A second coil detects the emitted radiation, which typically corresponds to a precise resonance frequency that depends on the external magnetic field and the chemical state and environment of the sample. In NMR spectroscopy, a sample is placed in a magnetic field and exposed to a radio frequency (RF) pulse or an oscillating magnetic field. This radiation causes the excited nuclei to absorb the energy, align with the magnetic field, and be perturbed and resonate or emit energy (or radiation) during/after the RF pulse (depending on the static magnetic field and the nuclei of interest). ^{31}P NMR spectroscopy is a specialized technique used to study the properties of ^{31}P nuclei. The ^{31}P NMR spectroscopy technique is routinely used because ^{31}P has an isotopic abundance of 100 %, a high gyromagnetic ratio, and a nuclear spin of $\frac{1}{2}$, which allows NMR spectra to be obtained and interpreted. The resulting ^{31}P NMR spectrum is a plot of the absorption or emission of the nuclei as a function of frequency (Hz), which depends on the strength of the external magnetic field or chemical shift (ppm), which depends on the choice of a reference compound. The spectrum contains information about the chemical environment and bonding situation of the phosphorus atoms in the material. ^{31}P NMR spectroscopy is widely used in chemistry, biochemistry, and medicine to study the structure and function of phosphorus-containing molecules, such as nucleic acids, phospholipids, phosphines, and phosphalkenes ($\text{P}=\text{C}$). The so-called nuclear spin-spin couplings or J-couplings are mediated by chemical bonds or non-bonded interactions arising from local interactions between the corresponding nuclei and local electrons, thus providing crucial information about the local electronic and molecular structure and the bonding situation of the investigated nuclei and constitutive structural motifs. NMR spectroscopy was a crucial technique throughout our Ph.D. studies and corresponding chapters (see Ch. 2-6), allowing us to detect essential structural motifs such as phosphalkenes ($\text{P}=\text{C}$), differentiated proton populations corresponding to asymmetric fluorene sides or Mes* populations, and the presence of non-covalent interactions (NCIs) based on chemical shift changes in different settings. By providing detailed information about the chemical environment and bonding situation of the nuclei under investigation, NMR spectroscopy enabled us to confidently identify and analyze these critical structural features.

UV-Vis-NIR absorption and IR spectroscopy are types of spectroscopy that use ultraviolet (UV), visible (Vis), near-infrared (NIR), and infrared (IR) light to study the structure and properties of materials. These techniques are based on the principle that when a material absorbs light, it transitions or can be excited to a different electronic or vibrational state. These transitions or excitations can be detected and measured, providing information about the structure and properties of the material. In UV-Vis-NIR or IR spectroscopy, a sample is illuminated with light of different wavelengths. The resulting energy changes in the material or compound are measured using a spectrometer. The resulting UV-Vis-NIR (or FTIR) spectrum plots the light absorption of the sample as a function of wavelength (or wavenumber). UV-Vis-NIR spectroscopy detects electronic transitions in the visible region of the electromagnetic spectrum, whereas IR spectroscopy detects vibrational mode excitations in the IR region. For π -conjugated materials (or transition metal complexes), the spectrum is typically dominated by electronic changes or shifts between π -bonding (or d-orbitals) and antibonding orbitals in the case of UV-Vis-NIR spectroscopy, while in IR spectroscopy, different vibrational modes are detected depending on factors such as symmetry, degree of unsaturation, and molecular size. UV-Vis-NIR and IR spectroscopy are widely used in many fields, including chemistry, biology, materials science, and environmental science, to study the structural and energetic properties of materials and molecules. UV-Vis-NIR spectroscopy and IR spectroscopy helped us characterize our materials and the nature of their response to light. For example, the former technique helped us identify HOMO-LUMO or optical gaps and extinction coefficients, while the latter was crucial for identifying hydrogen bonding interactions and accurately characterizing a network.

Emission or fluorescence spectroscopy is a complementary technique to absorption spectroscopy. It measures the emission of light from a sample after it has been excited by absorbing light at a specific wavelength (i.e., the excitation wavelength). This technique is based on the principle that molecules can emit light at a particular wavelength when they relax from an excited state to a lower energy state. The emitted light typically has a wavelength higher than the excitation wavelength due to various energy losses during the structural relaxation processes that follow the excited state generation. Depending on the region of the spectrum, other factors (e.g., excited state lifetimes), and some knowledge of the molecular structure of the material or compound under study, statements can be made about the nature of the emission or transitions (e.g., fluorescence vs. phosphorescence, MLCT vs. LLCT) and the material based on molecular orbital considerations, providing valuable information about the electronic structure and properties of the sample. This technique was instrumental in identifying the emissive nature and inferring the structural dynamics in solution samples of a copper(I) phosphalkene complex, as we will see in Ch. 6.

Potentiodynamic techniques in electrochemistry are methods used to study the electrochemical behavior of compounds, molecules, and materials. These techniques involve applying a controlled potential or voltage, called the feed, bias, or stimulus (i.e., the “biasing stimulus”), to a molecule and measuring the resulting current or charge. The biasing stimulus controls and manipulates the material's electrochemical properties and responses (i.e., feedback), which can provide insight into its functional character, chemical structure, and reactivity. In potentiodynamic techniques, the applied bias is often used to drive the sample toward a specific electrochemical state, allowing for a detailed analysis of its behavior and properties. One of the most used potentiodynamic techniques is cyclic voltammetry (CV), in which the applied potential is cycled between two potential values while the resulting current is measured. In CV, a sample is placed in an electrochemical cell, and a potential is applied. The potential gradually changes between two values as it is linearly varied, resulting in the typical triangular waveform and cyclic current responses. As the potential changes, the electrochemical reactions and structural interactions of the sample at the surface of the electrode, or at the electrode itself in the case of functional electrodes (see Ch. 2), are triggered, causing a current to flow through the cell. This current is measured and recorded as a function of the applied potential, resulting in a CV curve, graph, or cycle that can provide valuable information about the electrochemical response of the material, including redox behavior, structure, mechanisms, behavior, and more. Cyclic voltammetry is an invaluable tool for studying the electrochemical properties of molecules and compounds and developing new materials and technologies, as we will see in Ch. 2, 5, and 6.

X-ray photoelectron spectroscopy (XPS) is a powerful analytical technique for studying the chemical composition and electronic structure of a wide range of materials. When a material is irradiated, perturbed, or stimulated with a beam of X-rays, electrons are emitted from the material's surface. These electrons have a specific energy that is characteristic of the chemical elements, chemical environment, and bonding states present in the material. The resulting photoejected electrons are collected and measured using a spectrometer. The resulting XPS spectrum shows the number of photoelectrons as a function of their energy, expressed as the binding energy (BE). The spectrum provides information about the chemical composition and electronic structure of the material. XPS is widely used in materials science, chemistry, and other fields to study the surface structure or network of materials, including semiconductors, polymers, and molecules. High-resolution XPS was essential in characterizing the arsaalkene ($\text{As}=\text{C}$) nature of our synthesized polymers in Chapter 2, allowing us to report the first example of a polymer and π -conjugated material containing arsenic-carbon double bonds. This discovery was significant because these types of double bonds are highly reactive and are mostly confined to small molecules. The ability to incorporate them into a more extensive π -conjugated material has potential implications for the design of new

materials with unique electronic and optical properties and the development of so-called "smart materials," as we show in Ch. 2.

1.1.6. Conclusions.

We have explored the potential of low-coordinated, multiply-bonded P=C and As=C group motifs in π -conjugated organic or molecular inorganic systems, which, by exploiting the unique atomic properties of P or As and their various forms, and based on some relations to their functionalizable nanostructure-based "low-dimensional" material homologs, allow us to obtain enhanced or augmented responses in these types of more complex organic systems. Approaches such as tailored mixing (e.g., P/Si, P/S, As/Si or As/S; push-pull systems), inclusion (e.g., doping, host-guest chemistry), correlation (e.g., $^{31}\text{P}/^{29}\text{Si}/^1\text{H}/^{13}\text{C}$; orbital-based donor-acceptor electron transfer), extension (e.g., π -conjugation or delocalization; transition metal complexation), frustrated character (e.g., Ch. 5 \rightarrow torsional strain coupled to π -delocalization), and reactive-based approaches (Ch. 2 \rightarrow As=C polymers) are crucial to realize the full potential of these systems.

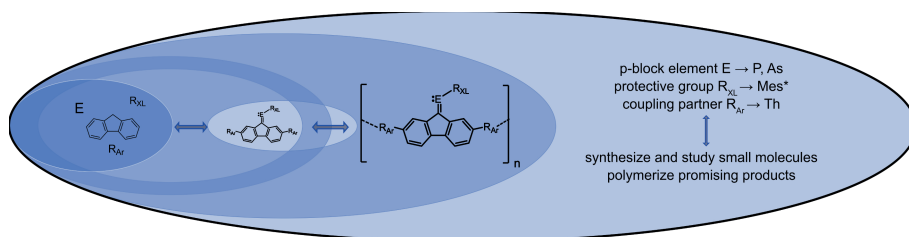
One of the unique features of low-coordinated multiply-bonded heavy group 15 systems is the orthogonalization of the protecting group due to the reluctance of the pnictogens to planarize in the same way as nitrogen-bonded molecules. This property, coupled with the non-bonding properties of the lone pair of electrons, induces increased anisotropy in these systems. For As=C and P=C, π and π^* type molecular orbitals can become representative and representable directors of frontier energy levels in subtly more unconventional or "atypical" ways than the prescribed reduced energy gap. By maintaining non-planarity, enhanced anisotropy, and embedding the P=C and As=C motifs within the appropriate π -conjugated core and π -extended system in some stacked configuration, we can achieve functional (and modular) behavior characteristic of their inorganic counterparts (see references in respective sections). This strategy can augment the functionality and modularity of the E=C-containing materials compared to the all-organic lighter homologs.

Researchers can exploit the general properties of anisotropy and conductivity and derived transport or responses to obtain functional and robust materials with advanced functionality, such as increased output intensity with a reduced pattern size, increased output intensity or sensitivity due to pnictogen incorporation, increased processability with metal electrodes (e.g., Cu, Au, and more) due to pnictogen lone pair electrons, and emergent or modular phenomena due to the E=C group motif incorporation. Using compactified architectures and precisely utilizing these functionalized material combinations, we can access different, attributable, and observable values associated with a given problem or solution, which is the primitive and fundamental basis of computation and problem-solving.

Ch. 2. Functional and modular small molecules and polymers with P=C and As=C group motifs on fluorene.

2.1. Introduction: Organic and main group approaches to fluorene and thiophene derivatives for conjugated polymers.

This chapter studies our work on phosphalkene-containing and arsaalkene-containing small molecules and polymers based on fluorene and thiophene backbones. The chapter is extensive; relevant information is introduced in the respective (sub)sections. In this section, we summarize our scientific approach to this chapter, the heavy p-block element incorporation into π -conjugated polymers, including P=C polymers, as well as the general organic polymer theme, comments, and issues on electropolymerization and π -conjugated polymers, displaying relevant building units (e.g., polythiophene and polyfluorene).



Scheme 2.1.1. Phosphalkene (P=C) and arsaalkene (As=C) chemistry connection to π -conjugated polymers. Derivatization follows the incorporation of the Mes*As or Mes*P fragments onto the 9H-fluorene core with coupling partners. Other approaches we did not study here could correspond to variation of the protecting group from Mes* to another. Then, polymer synthesis via electropolymerization, or oxidative chemical polymerization (FeCl_3), is performed. Synthetic protocols compatible with P=C, As=C groups should focus on work-up conditions that can be straight-forwardly executed under inert (i.e., anhydrous and deoxygenated under argon) conditions without the use of strong oxidizing, reducing, or secondary agents. In this work, the p-block elements are P & As, the protecting group is 2,4,6-tri-*tert*-butylbenzene (Mes*), the coupling partner is thiophene, and the polymerization method is electropolymerization (with a minor emphasis on oxidative chemical polymerization, which is noted when presented). The resulting polymeric materials were characterized in detail.

The basic building block we used as a template for executing main group transformations via the introduction of pnictidene moieties consists of the all-carbon 9H-fluorene core (Scheme 2.1.1). The fluorene backbone is a vital organic material due to its high thermodynamic stability and multiple-site reactivity (2,7-bromo-substituted sites and weakly acidic protons on the 9-H site).⁹ As a flexible template for further functionalization, the fluorene core has attracted the attention of the main group (MG) and heavy p-block element communities. MG chemistry researchers use diverse approaches toward modification of the fluorene core, in two directions. **(i)** The exchange of the methylene carbon bridge with a heavy p-block element, cherishing the formation of stable heteroatom derivatives (phosphole, arsole,¹⁰ silole polymers, and more).¹¹ **(ii)** The second tactic incorporates main group fragments to fluorene, our approach to small molecules and conjugated polymers, as shown in Scheme 2.1.1. The primary building blocks relevant to our studies with conducting polymers are polyfluorene,¹² polythiophene, polyaniline, and polyphenylene-vinylene derivatives. Compared to conducting polymers and the overall theme of π -conjugated polymers, the number of organic polymers incorporating heavy pnictogen elements in π -conjugated environments is minimal and exceptionally minimal when considering those in unusual bonding situations (e.g., low-coordination).¹³ After successful electropolymerization of phosphole-containing compounds, researchers presented some of the first examples of π -conjugated heavy pnictogen-containing organic polymers. Pnictogen atoms in heterocyclic rings, such as phospholes, phosphinines, or arsoles, as well as acyclic species (vinyl-substituted phosphine or arsine, phosphalkene polymers, and more) have become increasingly studied due to their atmospheric stability or optical properties (See Fig. 2.1.1).¹⁴

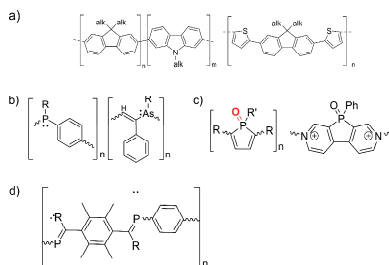
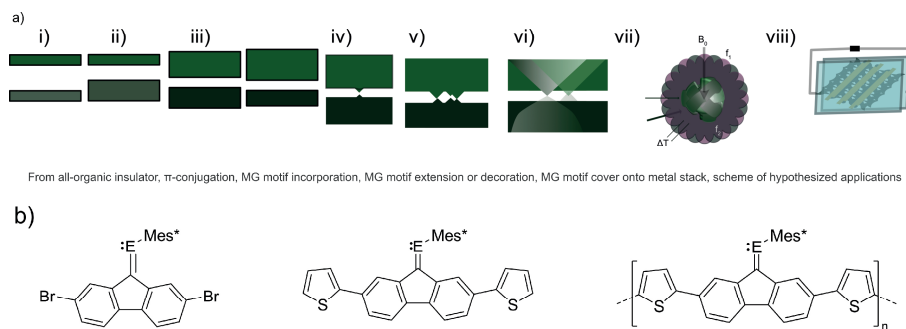


Fig. 2.1.1. a) Polyfluorene-based materials. b) Tricoordinate phosphine and arsine polymers with conjugated electron lone pairs have been synthesized. Pyramidalization of the heavy group 15 element leads to diminished π -conjugation. c) Phosphole-based materials are among the most studied π -conjugated organophosphorus materials. The pyramidalization of the lone pair may inhibit effective π -conjugation with the pnictogen. On the other hand, and as a similar note, the pyramidal electron lone pair generates negative hyperconjugation with the butadiene fragment, which extends “conjugation” (in the sense of being “negative”) or instantiates delocalization based on antibonding orbitals, and which stabilizes the molecular structures involved. d) Poly(p-phenylenephosphaalkene) derivatives are among the very few examples of P=C polymers. These polymers are emissive, which is rare for P=C systems. The bulky [C₆Me₄] linker leads to conformational nonplanarity, which inhibits or reduces extensive π -conjugation.

Our work in this chapter consisted of synthesizing and characterizing novel compounds (small molecules and polymers) based on highly coplanar thiophene-functionalized fluorene derivatives with P=C and As=C group motifs as intrinsic units. Post-functionalization with Au(I)Cl demonstrated their ability to sense and bind gold, a relevant electrode metal in applications. Creating novel conjugated materials by introducing heavy p-block element units in unusual bonding situations is helpful because these elements direct the system's electronic structure by their sizable contribution to the frontier molecular orbitals (FMOs). Naturally, the above outcome events on orbital contribution upon pnictogen incorporation apply not only to the as-prepared unperturbed compounds but also to the occurrences in which the compounds are exposed to a relevant electric, thermal, or magnetic bias or stimulus. Compared to the same all-carbon systems without modification, unusual bonding effects or interactions may amplify the response of compounds under a field to achieve a goal more precisely. This amplification is crucial in unexplored areas like molecular electronics, organic electronics, and organic quantum materials, where the functionalities must exhibit noticeable gains due to the relations between their constituents. The dimensionality or magnitude of an observable, per area unit or time unit, may be limited by density or other homologous factors (e.g., energy contributions) or by the difficulty of synthetically accessing the effect-homologous organic systems at the examined or applied energies in comparison or contrast to the unusually-bonded pnictogen-containing systems. Some simple examples confirming our argument about the advantages offered by π -conjugated materials incorporating heavy p-block elements in unusual

bonding situations in comparison to all-organic materials correspond to the technical utilization of some observables (i.e., for some **function**, **goal**, or **application**) such as: *i*) hyperfine splitting (main group radicals) constants, *ii*) nuclear-spin dipolar coupling frequencies at ^{31}P ^{29}Si interfaces, *iii*) photon transmission and detection (or dispersion relations) via asymmetrically induced high polarizability E=C-containing materials, *iv*) non-trivial changes in the electrical conductance or detected currents upon applied potentials. Concerning a **function**, **goal**, or **application**, some of these and other observables may be realized, enhanced, or tailored by the appropriate incorporation of heavier p-block elements into the π -conjugated environments of organic compounds, as argued before.



Scheme 2.1.2. a) **i) to vi)** Elementary and schematized energy diagram representations summarizing minimal anticipated effects expected after the introduction of π -conjugation (ignoring second order and modulative effects). Typical heteroatom incorporation and relative changes in the frontier levels, incorporation of MG heavy motifs adds effects, later potentiated by the addition of more effects (e.g., unsaturation as in E=C, asymmetry, metal incorporation, and more), then stacking with metal or semiconductor under bias, which leads to transmission paths (colored shades are a compactified dimensional representation of the added effects). **vii)** Top-view arbitrary scheme exemplifying a hypothetical application that uses nuclear spin coupling (e.g., ^{31}P , ^1H , ^{13}C), correlation under different biases, and rotating frames. **viii)** Schematic of a photonic-electronic object comprising asymmetric MG compounds (light grey) deposited over gold strips (orange), deposited over a second material (light-blue surface), connected to external elements (top black square). b) Structural formulas and selected interesting features of compounds studied here: ^{31}P nuclear spin available, functional electron pair (E = P, As), polarizable MG motifs, asymmetrically locked local conformations through protecting groups.

The chemistries and understanding of conducting polymers, conjugated polymers, organic polymers, synthetic polymers, π -conjugated polymers, redox polymers, and other variations illustrative of unsaturated organic polymers have increasingly been under study and in development during the last five decades. Industry and academic researchers use conducting polymers in opto-electronic applications as elements with roles and indirect (or direct) functions in packaging, electrical insulation, photoresist elements, and more. Other

sophisticated applications include organic-field-effect transistors (see Ch. 3 for intro to small molecule applications). All applications cherish molecular materials' processability and discreteness (size and energy level-wise). In the case of polymeric materials (relative to small molecules or oligomers), the resulting system (i.e., the polymer, in its presented or prepared form and as applied) corresponds to or is linked as a variety of hybrids (which we refer to as "polymeric forms" in various instances, where it is contextually appropriate). In terms of the final process product or application product (i.e., compound after purification or as used in the application), the materials science or applied chemistry of " π -conjugated polymers" typically deals with the synthesis of polymers in their monodisperse and soluble forms, whereas similar "conducting polymer" (CP) materials are realized in a polydisperse and insoluble state. Conducting polymers are widely used in various applications (e.g., insulating surfaces, semiconducting surfaces, conducting surfaces, electrode coatings, and more). Redox polymers may be considered a subset with some intersections with the former two families of materials; while being soluble and containing π -conjugated fragments in many cases (which relates them to " π -conjugated polymers"), their "redox" character is cherished by depositing on electrode surfaces as with "conducting polymers". The cases where π -conjugated groups are connected to (in some sense) non-conjugated polymer points or linkers are unusual cases of redox polymers because the observed optoelectronic and electrochemical properties may resemble those of the monomers. It is difficult to make strict distinctions between the several denominations, as the introduction of some tailored perturbation or constraint steers the properties of the materials towards the exhibition of functionality from another material family. This chapter will show this is the case, with the mutual observation of redox polymer and conducting polymer states.

A comprehensive review of all conjugated and conductive polymer literature would go beyond the scope of this thesis (and it would be unwise for one's sanity). Thus, only selected families relevant to the studied materials are included. Our work arises from initial work in our group with *acetylenic phosphalkenes*.¹⁵ We did not evaluate these compounds in polymerization reactions, but they are small molecule derivative representations of widely studied polyacetylenes.¹⁶ Polythiophenes are among the most studied, influential, and so-far suitable organic polymers, at the same level as polypyrroles and polyfluorenes. Our research efforts relevant to this chapter focused on conducting polymers, specifically conjugated polymers synthesized through electropolymerization, which have been widely studied.¹⁷ Several relations may also be traced to π -conjugated polymer materials and organic semiconductors (e.g., π -conjugated small molecules), the former of which, in our case, was advanced to the polydiverse polymer preparative stage due to the absence of suitable polymerization processes compatible with $P=C$ and $As=C$ groups.

Although thousands of reference works or publications exist, essential topics, such as electropolymerization mechanisms and appropriate definitions for

charge transport models based on polaron and bipolaron quasiparticles, are dealt with high intensity and fervor. However, we noted that studies that attempted to point out the diversity and complexity of conducting polymers, and thus the impossibility of generalizing phenomena, should have been more considered regarding the number of citations or views.

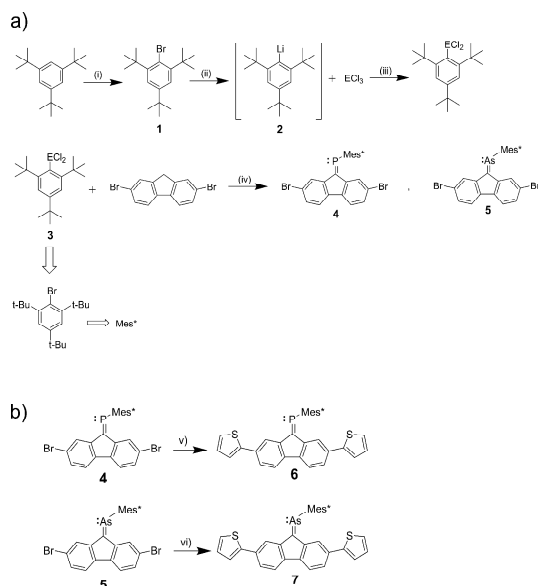
Conducting polymers are systems beyond the several-atom ensemble and exhibit complex physical and chemical phenomena that may express a multivariate, dynamic, modular, or nonlinear nature; therefore, many observations are not generalizable, and extended schemes accounting for all relevant statements should be envisioned. Conditions for performing experiments should be introduced and be widely adopted concerning optimal criteria (e.g., arbitrary polymerization convergence) and representative settings of electropolymerization (including during polymer growth and study) per polymer unit, class, family, species, or type.

Also, there being hundreds of thousands of publications about relevant phenomena we discuss in this chapter, we apologize for the accidental neglect of pertinent work in our referenced materials or for any presentation of our results that may conflict with the reader, for example, if the results are not perceived to be innovative or be interpreted in the same light. Our developments were assessed to be novel from our extensive literature research observations and in relation to the experimentally observed properties, polymer scaffolds, and from the perspective of E=C bonding. Therefore, we kindly want to reflect and emphasize that the novelty aspects lie in the structural novelty of the introduced main group motifs into the polymer backbones, primarily because of the high reactivity and rarity of E=C motifs relative to their saturated or tricoordinate cousins or lighter analogs, as well as their novel or observed properties. For example, this work represents the first example of a polymer with arsenic-carbon (As=C) double bonds, as we confirmed by appropriate and relevant methods.

2.2. Synthesis and Characterization: P=C and As=C Small Molecules.

The synthesis of the dithienyl-substituted products starts with preparing the protecting group of choice. We use the supermesityl 1,3,5-tri-*tert*-butyl-benzene substituent, also known as Mes*. Due to the optimal synthesis of the brominated species, coupled with the kinetic stability Mes* provides to the underlying sensitive [P=C, As=C] groups, it has been historically favored by low coordinate pnictogen researchers (Scheme 2.2.1). Due to the sensitivity and toxicity of these materials, proper risk assessments must be done under some supervision framework before handling. This stage is crucial since most intermediate species are sensitive; therefore, it is a limiting stage in the

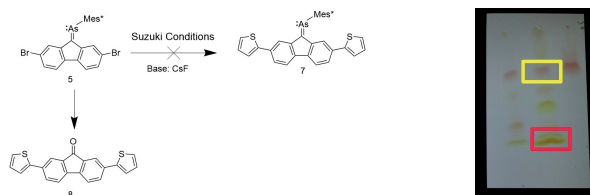
synthesis processes. For the dichloro-substituted pnictogen compound **3** (Scheme 2.2.1 a)), the larger arsenic atoms increase intramolecular reactivity towards CH activation and cyclization with an ortho *tert*-butyl group from the Mes* protecting group through dehydrochlorination. Thus, the product must always be maintained at a low temperature.



Scheme 2.2.1. a) Optimized conditions for the synthesis of dibromophosphaalkene and dibromoarsaalkene materials (**4**, **5**); i) Br₂, triethylphosphite, ii) *n*-BuLi, iii) PCl₃, or AsCl₃ (low T), iv) *n*-BuLi; DBU. b) Optimized conditions for the synthesis of dithienyl-phosphaalkene and dithienyl-arsaalkene (**6**, **7**) materials. E = P, As; v) 2-(Tributylstannyl)thiophene, vi) THF, MW (30 min), 140 °C.

Inspired by previous work on phosphaaalkenes¹⁵ in our unit and work on a *tert*-butyl substituted arsaalkene,¹⁸ we designed and optimized our protocols towards the multigram syntheses of **4** and **5**, allowing us to explore the reactivity of these materials with several substrates, ultimately focusing on the reactions with thiophene, another well-known organic electronics building block.¹⁹ The main difficulties occurred while finding the correct stoichiometry and reaction times for all synthetic and processing steps before E=C double bond formation. Once the P=C and As=C double bonds have been formed, the resulting materials are indefinitely stable in the solid state under standard atmospheric conditions. Suzuki conditions potentiated some decomposition pathways towards the ketone **8** via a base-assisted oxidative mechanism of the fluorenylidene-pnictidene core (Scheme 2.2.2). Mechanisms for the decomposition of other types of fluorenes with alkyl substituents have been described; however, based on our search, this has not been the case with aryl substituents, which points to the sensitivity of As=C and P=C groups.²⁰ The

syntheses of the dithienyl derivatives were done using the Stille coupling reaction. The optimized average yields of 40-60 % for **6** and **7** are quite positive, considering the syntheses involved elevated temperatures (140 °C) under MW radiation, and a potential for phosphalkene and arsaalkene coordination to the Pd catalyst via the lone pair of electrons acting as competing coordination pathways.



Scheme 2.2.2. a) Decomposition pathway during syntheses of **6** and **7**. The ketone product was characteristic due to its retention on column chromatography, red color, and indicative differences based on ^1H NMR and ^{13}C NMR resonances. Right: Chromatographic characteristics of purification procedure; eluent, pentane/DCM (80:20); red rectangle: product **7**; yellow rectangle: ketone impurity. Other products are unidentified impurities.

As a side note, arsaalkene ($\text{As}=\text{C}$) compounds are rare compared to phosphalkenes ($\text{P}=\text{C}$) and dramatically more so compared to alkenes ($\text{C}=\text{C}$) and tricoordinate or pentacoordinate congeners. A SciFinder search returned the following number of references: 41 references \rightarrow “arsaalkene”, 812 references \rightarrow “phosphalkene”, 1404 references \rightarrow “organoarsenic”, 1663 references \rightarrow “phosphole”, 109655 references \rightarrow “phosphine”, and 402326 references \rightarrow “alkene”.

2.3. NMR and XRD characteristics of dibromo and dithienyl phosphalkenes and arsaalkenes.

The ^1H NMR of compounds (**4-7**) possessed one highly shielded proton resonance on the fluorene core, which was caused by the enforced asymmetry imposed on the Mes^* substituent by doubly bonded phosphorus and arsenic atoms. The asymmetry occurs for “normally polarized” or “inversely polarized” $\text{P}=\text{C}$ or $\text{As}=\text{C}$ environments with a stable double bond configuration.²¹ After thiophene incorporation, deshielded shifts of 1.1 ppm occurred for the $\text{P}=\text{C}$ carbon of **6** (100 MHz, 167.7 ppm vs. externally referenced TMS) and 1.4 ppm for the $\text{As}=\text{C}$ carbon of **7** (100 MHz, 182.0 ppm vs. externally referenced TMS). The ^{31}P NMR of **4** exhibited a resonance at 273.7 ppm, whereas **6** was surprisingly shielded to 264.9 ppm; this region is typical for $\text{P}=\text{C}$ in

delocalized π -conjugated environments. At first sight, this suggested some π -conjugation as the π -system was extended or some increased susceptibility factor of the ^{31}P nuclei. The typical ^1H NMR of As=C (**7**, **5**) and P=C (**4**, **6**) compounds are shown in Fig. 2.3.1. The ^1H NMR spectra exhibited a chemical shift difference of > 2.0 ppm between the most shielded and most deshielded aromatic protons of the fluorene core (**5**; 2.78 ppm). In comparison, the parent 9H-fluorene (0.5 ppm) and the 9H-fluoren-9-one (0.3 ppm) molecules exhibited much narrower NMR resonance differences in similar conditions,²² which confirmed our hypotheses on the double bond-induced asymmetry. The characteristic ^{13}C NMR of arsaalkene **7** and **5** showed a deshielded chemical resonance at 182.02 ppm compared to the signals at 143.00 ppm for the parent fluorene molecule. Overall, these features indicated a carbon environment in π -conjugation. The 17 and 25 aromatic signals in the ^{13}C NMR spectra of **5** and **7** confirmed the purity and structures for both As=C compounds. Single crystals of compounds **4-6** were grown from DCM/acetonitrile layered solutions under inert conditions. The structures were consistent with E=C bond lengths (BL) of 1.693(5), 1.677(5), and 1.807(3) Å for **4**, **6**, and **5**, respectively. Coplanarity between E=C and fluorene core was confirmed by the slight deviation of 0.061(1) (**4**), 0.063(1) (**5**), and - 0.007(2) (**6**) above the least-squares plane of the fluorene core. The overall results supported our idea on the effect of planarity in concomitance to extended π -conjugation via thiophene rings, which was strengthened by the ~ 10 % lower deviation from planarity and ~ 1 % BL reduction of **6** vs. **4** after thiophene introduction.

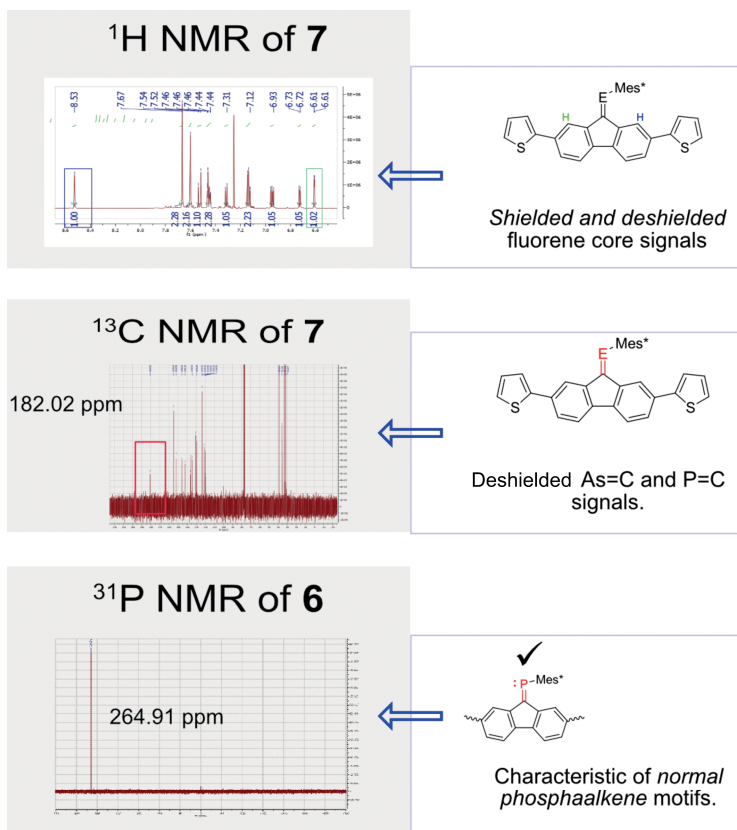


Fig. 2.3.1. Characteristic or relevant NMR signatures or features of phosphaaalkenes and arsaalkenes as observed or exemplified via ^1H NMR of 7, ^{13}C NMR of 7, and ^{31}P NMR of 6.

NMR theoretical studies have studied the effects of variables on the observed ^{13}C and ^{31}P NMR resonances. The study confirmed the interplay between electron density distributions and orbital mixing.²³ Delocalization has a high paramagnetic shielding term contribution to the eigenvalues (i.e., resonances). Here, intermediate $\text{P}=\text{C}$ ^{31}P chemical shifts at approximately +260 ppm may be analyzed from an electron density perspective. The effects on the $\text{P}=\text{C}$ ^{13}C NMR resonances also depend on electronegativity and the degree of orbital mixing with adjacent units (i.e., P atoms). Increasing electron density differences (assuming the carbon becomes more positive than the compared case and the reference compound) and decreasing excitation energies can lead to larger ^{13}C NMR chemical shifts, explaining the higher ^{13}C NMR chemical shifts of $\text{P}=\text{C}$ and $\text{As}=\text{C}$ compared to homologous saturated systems (e.g., **6** = 167.7 ppm vs. $\text{Fl}[\text{H}][\text{O}=\text{PPh}_2] = 50.68$ ppm vs. $\text{Fl}[\text{H}][\text{PPh}_2] = 46.19$ ppm).²⁴ As seen in the previous example, the electronegativity impact on the observed chemical shifts seemed minimal since the phosphine oxide is even more shielded than the $\text{P}=\text{C}$ systems and barely deshielded than the phosphine, the

latter illustrating the electron-withdrawing effects on the chemical shift also. We analyzed bond-distance-dependent $^XJ_{C-P}(X: 1, 3; \text{compound label})$, (Fl: fluorene) coupling constants in a similar compound, which relate to the effects caused by the shorter bond lengths of P=C (and thus π -bonding, more indirectly, given that the coupling constants are empirically known to be affected by σ -bond effects) systems. For **4** vs. Fl[(P=O)(OCH₂CF₃)₂][H] **II**, the $^XJ_{C-P}(X: 1, 3; \textbf{4}) = 45, 24$ Hz versus $^XJ_{C-P}(X: 1, 3; \textbf{II}) = 138, 7$ Hz varied differently.²⁵ The $^3J_{C-P}$ in **4**, **6** vs. **II** pointed at a larger degree of orbital overlap in the former two due to the induced planarity caused by the Mes* and the shorter E=C double bond.²³

2.4. Analysis of phosphalkene and arsaalkene compounds via UV-Vis-NIR, DFT, TD-DFT. Extended π -conjugation and intrinsic roles of P=C and As=C.

We studied the electronic transitions of **4** to **7** via UV-Vis-NIR absorption spectroscopy in DCM. The dibromo-substituted derivatives presented the lowest energy absorption bands at 371 and 398 nm for **4** and **5**. The 27 nm red-shifted absorption **5** can be ascribed to the distinct effect caused by the As=C bonding situation. The molecular electronic structure of compound **5** was more effectively perturbed by As atoms, resulting in a reduced optical energy gap due to E=C orbital mixing and enhanced π conjugation. This effect was further enhanced by the LUMO-stabilizing properties of the heavier pnictogen As (**5**) compared to P (**4**). Introducing the thiophene rings resulted in red-shifted low-energy absorption bands because of the increased degree of π -conjugation/delocalization across fluorene, E=C units, and potentially some Mes* density. The possibility of localizing discrete charges via charge transfer events in excited states is an advantage gained from using two p-block element functional groups (e.g., intramolecular charge transfer from sulfur-containing π orbitals \rightarrow phosphorus-containing π^* orbitals or sulfur-containing π orbitals \rightarrow arsenic-containing π^* orbitals) in the π -framework. Additional features in the spectrum of **6** (shoulder: 399 nm, br: 485 nm) and **7** (band: 409 nm, br: 530 nm) were evident, the latter with a low-lying onset at ~ 596 nm (Fig. 2.4.1).

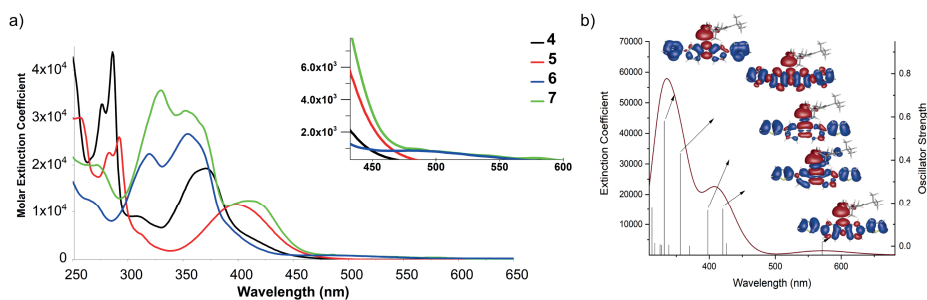


Fig. 2.4.1. a) UV-Vis-NIR absorption spectroscopy of phosphalkenes (**4**, **6**) and arsaalkenes (**5**, **7**). The absorption features and extinction coefficients of **7** are λ_{max} (ϵ) = 330 nm ($3.6 \times 10^4 \text{ M}^{-1}\text{cm}^{-1}$), 351 nm ($3.2 \times 10^4 \text{ M}^{-1}\text{cm}^{-1}$), 409 nm ($1.2 \times 10^4 \text{ M}^{-1}\text{cm}^{-1}$), 530 ($1.3 \times 10^3 \text{ M}^{-1}\text{cm}^{-1}$). The absorption features and extinction coefficients of **6** are λ_{max} (ϵ) = 320 nm ($2.2 \times 10^4 \text{ M}^{-1}\text{cm}^{-1}$), 353 nm ($2.7 \times 10^4 \text{ M}^{-1}\text{cm}^{-1}$), 399 nm (shoulder, $5.3 \times 10^3 \text{ M}^{-1}\text{cm}^{-1}$), 485 nm ($0.9 \times 10^3 \text{ M}^{-1}\text{cm}^{-1}$). The introduction of an As=C in an extended π -framework was unprecedented when published. b) Quantum chemical calculations via density functional theory (DFT) for ground states and TD-DFT for excited states (Gaussian 09; B3LYP-D3/6-311G**). Electron density difference maps (EDDM) of **7**, representing electron density distribution due to electronic excitations; blue: electron depleting (donor); red: electron increase (acceptor). Electronic depletion (blue) was observed for π -orbitals, corresponding to donor states. Oppositely, electronic increase (red) was assigned to π^* orbitals. Some observations follow. (i) Through-space density difference contributions (357 nm, fulvene center). (ii) The significant contribution of the As=C π^* orbitals to most key transitions. (i) The transition at ~ 320 nm contains a significant degree of charge transfer character from thiophene to the fulvenoid-As=C center. (i) The strange symmetry of the transitions at ~ 425 nm, with twisted depleting donor density swirling around the As=C bond and through the fulvene ring center (p-derived σ -type and regular π -symmetry donating sites and π^* acceptor sites).

The extinction coefficient differences presented an interesting dichotomy, $\epsilon_{\text{P=C } \mathbf{4}} > \epsilon_{\text{As=C } \mathbf{5}}$, whereas $\epsilon_{\text{P=C } \mathbf{6}} < \epsilon_{\text{As=C } \mathbf{7}}$, which interestingly was reflected for polymers, Au-functionalized cases, and doped polymers. This observation may seem trivial, but it is interesting because better π -exchange and π -density due to orbital overlap and smaller E=C distances suggested that P=C should display higher absorptivity in the π -extended systems. However, other effects (e.g., dipole moment differences, π -conjugation factors, “ π -electronegativity”, and more) become dominant upon incorporating thiophene groups in As=C **7**. Based on the higher absorptivity and the previous factors, the incorporation of arsenic has a crucial role in directing the observed response of **7** during the measurement. The study evaluated three functionals (B3LYP, PBE1PBE, CAM-B3LYP) for various molecules and types of calculations. The B3LYP functional was our choice. B3LYP most closely approximated the studied models' observed energies and structural parameters (while CAM-B3LYP performed the worst) vs. experimental data. DFT results are described in the present tense for the rest of the thesis work.

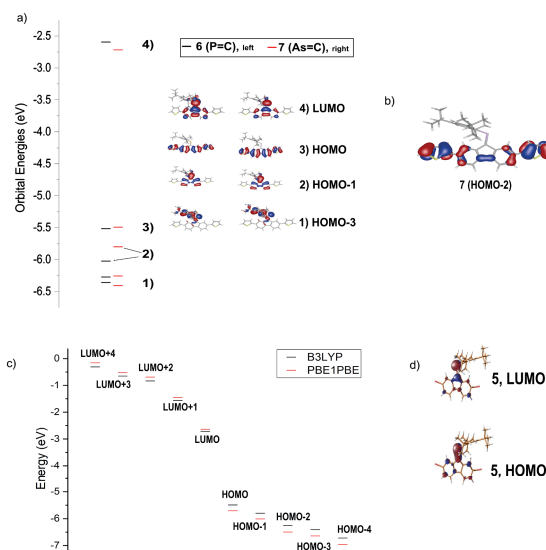


Fig. 2.4.2. a) Frontier orbital densities and energies, **6** (left) and **7** (right). b) **7**, HOMO-2 density corresponds to an orbital density of π -symmetry. The frontier orbital distributions were similar for **6** and **7**. The HOMO and HOMO-2 correspond to delocalized π -orbitals across the Fl-Th fragments. The LUMO corresponds to π^* orbitals with a significant contribution from the E=C bonds. Interestingly, the HOMO-1 is destabilized in the As=C system in comparison to **6**, nicely agreeing with the experimental observations about increased reactivity of **7**. The HOMO-3 orbital densities exhibit contributions from the pnictogen electron lone pair for **6** and **7**. c) Orbital energy frontier densities of **7** (LUMO to LUMO+4; HOMO to HOMO-4) using PBE1PBE (red levels) and B3LYP (black levels). The comparable results give reasonable confidence in these calculations. d) HOMO and LUMO orbital densities of **5** fundamentally differ from those of the π -extended **7**.

The delocalization of the π -electron system across the thiophene-fluorene backbone characterizes the HOMO levels of **6** and **7**, which leads to close HOMO levels for both compounds. The lower LUMO level of As=C vs. P=C and C=C congeners entails a larger or higher π -accepting character to the former and heaviest species.

Compound	C-*Mes-E (Exp.)	C=E (Exp.)	C-E-C angle (Exp.)	HOMO-LUMO gap
	Å	Å	°	eV
4	1.912 (1.837)	1.731 (1.694)	106.8 (104.0)	3.41
6	1.916 (1.844)	1.730 (1.678)	107.8 (108.4)	2.88
5	2.003 (1.970)	1.826 (1.807)	105.4 (102.6)	3.12
7	2.010	1.825	106.8	2.81

Table 2.1. Relevant DFT parameters of optimized ground states (experimental values in parenthesis). The values agreed well with the experimental information and helped us validate the utilization of the respective functional (B3LYP/6-311G(d,p)).

We did not approach the problem from the perspective of cross-conjugation or cross-conjugation across $E=C$ (e.g., from Fl to Mes* through the $E=C$ group) units. Nevertheless, Tip and Mes* protecting groups, gold, copper, and other substituents across the $E=C$ can become relevant based on our excited state (EDDM), ground state (frontier orbital density), and experimental observations. Our group and others have made exciting advances in the field by decorating $P=C$ with acetylenic substituents to stabilize gold nanoparticles, a novel tailored utilization of cross-conjugation.²⁶ Due to the orthogonalization of Mes*, there is potential to induce cross-conjugation via Mes* and Fl sites or through extension or decoration of P (or As) lone pair of $P=C$ (or $As=C$) group motifs. The absence of extended cross-conjugation due to Mes*-orthogonalized protecting groups leads to asymmetric localization of $P=C$ or $As=C$, which relates to the exciting optoelectronic properties of these materials. The absence of coplanarity in the cross-conjugation communicating two sites has been described under a framework of switching potential and tunneling across a barrier to provide the basis for the basic design of logical gates in spiro-coupled thiophene sites connectors of the π - σ - π mixed-valence type, for example.²⁷ In terms of frontier orbital density and functional group (FG) energy contributions, the [(thiophene)₁-(($E=C$)₄-fluorene)₃-(thiophene)₂] “tetramer” forms the functional basis of the presented materials in our current approach (the subscript indicates the number of functional fragments in distinct chemical environments, in this case where there are two thiophene groups due to Mes*-induced changes in their surroundings). By treating the protecting group as FG, we obtain [(thiophene)₂-((Mes*)₅-(($E=C$)₄-fluorene)₃-(thiophene)₁], which after pnictogen-gold complexation yields [(ClAu)₆-((Mes*)₅-((($E=C$)₄-fluorene)₃-(thiophene)₂)-(thiophene)₁]. The last system cherishes six functional groups or subsystems (i.e., modules), two of which are “immersed” (Fl and $E=C$), one of which is slightly more polar (AuCl), two of which are electron-rich soft sites (Th_(Site 1), Th_(Site 2)), and one which is nonpolar and keen on London dispersion types of interactions (Mes*_{tert-butyl}). The quantum mechanical effect of introducing an $[Ar_{(\pi)}-P=C]$ or $[Ar_{(\pi)}-As=C]$ scaffold across a sizeable molecular system is difficult to visualize. Hence, it is difficult to predict the effects of transmission or transport across $P=C$ or $As=C$ units compared to the all-carbon path. Initial states (e.g., groups other than thiophene rings or *tert-butyl* substituents on Mes*) can increase linear transmission coefficient values or conductance. It is not easy to generalize whether the presence of cross-conjugation across a linear system is beneficial, especially in real-world applications, where the dynamics of the systems are considered both in fluids and solids. Cross-conjugation is pertinent, even where cross-conjugation is seen as deleterious to the transmission coefficients, in areas where precise charge transmission (modulation) is needed, such as for single-molecule transistors or hyper-resistive molecular insulators. Utilization of cross-conjugation provides a motivating avenue for low coordinate group 15 materials since the lone pair of electrons on P or As are attracted to gold or

other metals (Ch. 3, 5, 6). More complex architectures that contain multiple transmission pathways for information transport at the single-molecule level can benefit from the possibility of accessing gold-bounded P=C or As=C molecular paths or access through a hydrogen-bonded (HB) network between two gates (e.g., Ch. 5). In Ch. 4, we can see how the utilization of highly donating Si=Si groups leads to relevant frontier density contributions of the protecting groups (Tip and Mes*). Ch. 4 and Ch. 5 show that geometric frustration is relevant in frontier orbital densities from Mes*.

2.5. Electrochemistry of dibromo and dithienyl phosphalkene and arsaalkene small molecules.

High stability and development of synthetic procedures helped us study the systems further. We minimized the ubiquitous effects of O₂ and H₂O contamination by performing electrochemical studies (cyclic voltammetry: CV) under inert conditions (Schlenk or glovebox). We used DCM as a solvent due to its lower hydrophilicity and good solubilizing properties, although some experiments were performed in acetonitrile (ACN = MeCN). We used tetrabutylammonium hexafluorophosphate as the electrolyte of choice, which is non-oxidizing, non-nucleophilic, non-coordinating, and displays no appreciable chemical reactivity with the compounds.

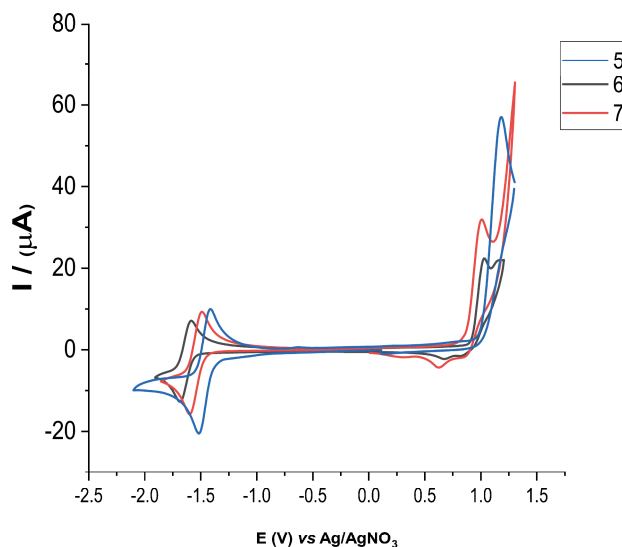


Fig. 2.5.1 CVs of **6**, **7**, and **5** at 100 mV/s (SR: 0.1 V/s). Solvent: DCM. Fc/Fc⁺ E_{ox} (~ + 37 to + 40 mV vs. 10 Mm in MeCN Ag/AgNO₃).

The basic electrochemical properties of compounds **4-7** were studied using CV (Fig. 2.5.1, **4** not shown). The electrochemical investigations were

performed in a 3-electrode cell comprising the working electrode (WE), reference electrode, and counterelectrode, which were tightly separated by glass frits to avoid leaking that could affect the chemistry or electrochemistry of the compounds or experiments. A rich electrochemical response was observed for all compounds, characterized by one reversible reduction event and one irreversible oxidation (although **6** and **7** seemed to possess two oxidation events, the second peak occurred too close to the switching potential, yet there is a clear irreversible event based on the forward and reverse cycle currents). The reduction potential of **5** is less negative than that of **6** and **7**, which means that the species is easier to reduce, which can be explained in terms of the higher electron-donating ability of the thiophene groups. $E_{\text{red1/2}} = -1.47$ V (**5**), -1.54 V (**7**), -1.63 V (**6**). The $E_{\text{ox, peak}} = +1.00$ V (**7**), $+1.03$ V (**6**), $+1.18$ V (**5**) (vs. Ag/AgNO₃ ref.). The electron affinity of **7** was calculated at the DFT level after geometrical optimization of anion and neutral systems; the obtained value (-174.14 kJ/mol) is negative, which was experimentally corroborated by the stability of the anionic species formed upon electrochemical reduction. The lower reduction potential of **5** is attractive because bromide substituents can effectively function as σ -electron donors, despite their large electronegativity. Thiophene rings are electron donors (ED) due to the presence of an electron-rich C-S-C sulfur atom (although slightly stabilized by aromaticity). Thus, we can conclude that the electron-accepting character in all studied systems is produced after incorporating As=C and P=C in general, which is further explained by the electrochemical and chemical stability of the reduced species. Therefore, E=C moieties behave as strong electron-withdrawing (EWD) units that lead to an increased electron-accepting ability in comparison to unadorned fluorene homologs.

2.6. Electropolymerization and characterization of P=C and As=C polymers.

Electropolymerization or electrochemical polymerization was a versatile technique that allowed us to cherish the structural and optoelectronic properties of the presented materials vibrantly. This process allowed us to synthesize uniform, functional films of phosphalkenes (*poly-6*) and arsaalkenes (*poly-7*) with tunable properties. Electropolymerization is a widely used polymerization technique with several advantages over other methods.²⁸ High reproducibility, controlled film thickness, polymer films of high surface densities, and the absence of harsh chemical reagents or workup procedures are attractive aspects of this method.^{29,30,20}

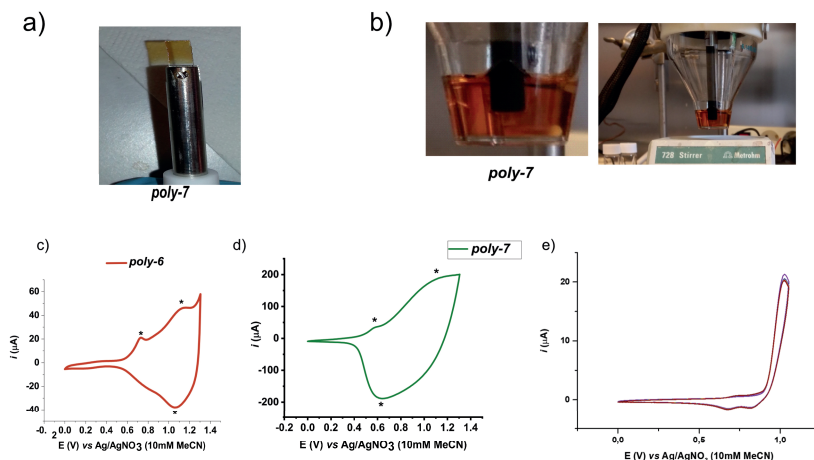


Fig. 2.6.1. a) Arbitrary picture of *poly-7* (As=C) outside the glovebox. b) Arbitrary picture of electrolyte solution containing monomer (i.e., **7**) during the synthesis of *poly-7* (not visible) on a GC electrode inside the glovebox. c) CV *poly-7* and d) CV *poly-6* under similar experimental conditions in transparent (monomer-free) electrolyte fluid mixtures (on FTO electrode). Anodic (E_{pa}) and cathodic (E_{pc}) peak potentials (“cathodic” ~ anodic cycle reverse sweep) for these representative experiments were found to be, $E_{pa1} = +0.73$ (*poly-6*), $+0.57$ (*poly-7*); $E_{pa2} = +1.20$ (*poly-6*), $+1.07$ (*poly-7*); $E_{pc} = +1.06$ [(*poly-6*)⁺], $+0.64$ [(*poly-7*)⁺] vs. Ag/AgNO₃ (10 Mm MeCN). At identical conditions in terms of monomer and liquid electrolyte concentrations (per moles), constant volume (cm³), and given the enormous size of the electrodes relative to the size of the monomers in solution, we assigned the larger currents of *poly-7* to increase of the polymerization efficiency of *poly-7* processes via increases of redox capacity, which we present quantitatively in Section 2.7. The role of low-coordinated arsenic As=C and P=C polymers are studied in Sections 2.7.3 and 2.10. e) Attempts to polymerize **4**. After 30 scans, there is no increase in current. Polymerization of dibromo monomers does not occur oxidatively but reductively (e.g., Ni(0) catalysis).³¹ Therefore, no polymerization was found for **4** and **5**, as seen by the absence of current increase and visual inspection of the films (more details in the main text).

For **6** and **7**, electropolymerization of monomeric units was achieved in fluid electrolyte solutions of DCM (or MeCN). Polymer synthesis occurred at the working electrode (WE) surface through potentiodynamic cycling between a selected anodic potential (i.e., $E_{ox-polymerization} > E_{ox-monomers}$) and the zero potential point at a defined scan rate (SR; typically, 0.1 V/s), and a selected number of cycles (NC), as summarized in the parenthesis (~ 0 V to + 1.2-1.3 V vs. Ag/AgNO₃ 10 mM in MeCN; SR: 100 mV/s; NC: 3-100). These standard conditions or representative settings yielded robust polymer films (Fig. 2.6.1). We could polymerize the dithienyl compounds **6** and **7** only. The bulky nature of Mes* coupled to the induced asymmetry localized over one bromo side and hindered any polymerization process at the cationic or dicationic intermediate stages of monomeric states. We confirmed this idea in control experiments, where polymerization of dibromo precursors (**4**, **5**) measured by CV showed

no polymerization. The absence of polymerization for dibromo precursors **4** and **5** was initially acquired as solid proof that the polymerizations occurred externally through the α -positions of the thiophene rings (see below). Interestingly, the two cathodic signals (reverse sweep, anodic cycle) are similar in current level and waveform, yet their potentials were significantly separated, along with the presence of a single anodic event. These events were assigned to a dimeric species from the coupling of two radical monocations, which diffused or did not attach to the electrode surface. Polymers were prepared on various surfaces, including glass substrates (FTO), amorphous glassy carbon electrodes (GC), and platinum (Pt).¹⁷ In the field of phosphorus polymer synthesis via P=C precursor activation and polymerization, it is well-known that Mes*-substituted P=C compounds do not undergo polymerizations through the carbon-phosphorus double bond due to the kinetic protection effect, which is indirect but relevant evidence to our arguments and results with the presented scaffolds.³²

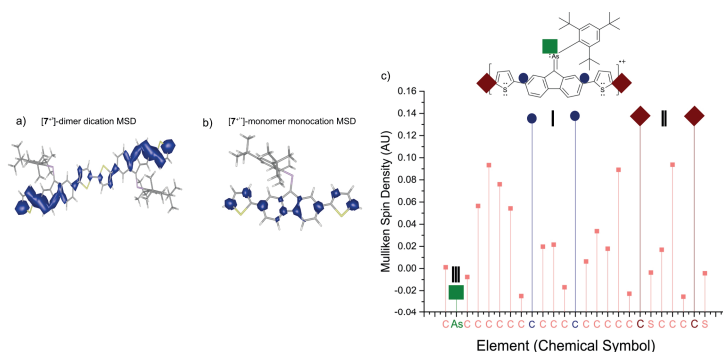


Fig. 2.6.2. a) Mulliken electron spin density (MSD) for dicationic (singlet) and b) cationic (doublet) model species of **7**, which is representative of reactive sites during polymerization processes involving radical or cationic species. c) MSD was located on the external α -positions on the thiophene rings (**II**) and the 2,7-fluorenylidene external carbon atoms, which are unlikely places to lead polymerization processes since they involve C-C bond breaking (**I**). Most importantly, no MSD was found to be localized on the As=C fragments (**III**). Therefore, as postulated, no irreversibly covalent reactivity can be expected to occur via E=C group motifs (more details in the main text).

Due to the potentially sensitive nature of the studied polymers, *potentiodynamic* (i.e., CV) conditions during polymer growth (monomer-containing) and electrochemical or structural analysis (both monomer-containing and monomer-free) presented an optimal balance. The potentiodynamic approach, by cycling, decreased the time the growing polymer chains remained in anodic (oxidized) or conducting states during the growth process. Our research goal motivated us to reduce the amount of time the P=C and As=C groups spent in an anodic state, which decreased the risk of decomposition of the functional forms of interest. As a result, byproduct reactions with trace amounts of

undesired scavengers (O_2 , H_2O , excess H^+) were also reduced compared to constantly applied stimuli in the potentiostatic process or heating effects caused by electric current in galvanic conditions. Additionally, the approach provided time for relaxation (diffusion) and exchange processes (solvent, electrolyte) to occur and for resulting polymer chains to structurally “evolve” **(1)** during the reverse cathodic scan and **(2)** anodic scan before the oxidation of the structurally most principal polymer chains (i.e., “the polymer”) re-occurred. Furthermore, by switching the applied anodic potential within an optimal window ($E_{\text{study}} \sim E_{\text{switch}} \sim E_{\text{polymerization}} \sim E_{\text{ox, monomer}}$), the polymer growth occurred through external thiophene α -carbon units, as widely accepted (albeit β -carbon units have also been shown to be involved in polymerization processes, these positions correspond to minor reaction paths which are expected to become even less preferential for *poly-6* and *poly-7* due to steric hindrance on one of the two positions due to the Mes*-induced asymmetry).¹⁷ Interestingly, reversible color changes from light-yellow-green to dark-blue-black (electrochromism) were evident as the polymers were produced (i.e., during “polymer growth”). Thin-film processes of excellent quality and polymers with various structural and optical properties were obtained based on their visible differences at different scanning rates and further characterization (vide infra) while their electrochemical responses remained controlled and ordered. This statement applies to polymer growth stages and partially to their study in monomer-free solutions.

Due to the multiple goals of our research, some problems have not been studied in detail thus far. For example, films grown at slower SR were denser and darker (dark green) in their “undoped” state (+ 0 V vs. Ag/AgNO₃). Mass transport limitations may be less pervasive at slower SR for some periods. At low SR, the $E_{\text{polymerization}}$ (+ 1.2 to + 1.3 V region) of polymer formation was continuously applied longer than during the faster SR processes, while the polymer was charged and discharged cyclically. However, this made it hard to analyze films spectroscopically or electrochemically because of the significant charge accumulation at slow scan rates, especially for *poly-7*. The timeframe (potential) of polymer formation occurs while anodically cycling above the minimal potential of polymer oxidation that generates a polymer surface-bounded oxidized oligomer with enough energy, from which proton elimination leads the oligomer to polymer surface introduction. During fast SR (e.g., > 1 to 5 V/s), due to mass transport accumulation differences, monomers and smaller oligomers are expected to become increasingly present and thus bound to the growing polymer at the electrode surface, limiting some properties of the polymerization growth process, for some polymers. The opposite may also be true. At some arbitrary optimal criteria or using some representative settings, non-potentiodynamic methods may be favored during polymer growth or polymer study, as opposed to potentiodynamic methods.

We think that based on the optimal criteria that links, obtaining the optically densest polymer (*poly-7*) that can be successfully characterized

(“optimal criteria O_I ”), an optimal timespan between switching potential changes using potentiodynamic methods, is favorable over the equivalent non-potentiodynamic polymerization method. In this scenario, potentiodynamic methods such as CV can lower the number of voids or defects coupled to sudden loss of polymer functions. For some polymers, CV supports the creation and expansion of orderly and correlated domains in the polymer films (e.g., links, loops, folds, and more) as the polymer growth emerges, which is coupled to applicable criteria, such as effective π -conjugation, and more. Interestingly, for more typical monomer precursors such as pyrrole or thiophene, potentiodynamic techniques have, in some cases, shown to be disadvantageous because the polymerization growth processes are interrupted while switching potentials. We assert that no generalization can be made as to which single methodology or set of conditions works better during the design of experiments (DOE during growth or study) where variables are not appropriately introduced, interchanged, or varied. For example, one must consider (i) purpose, (ii) type of monomer, (iii) desired functional sequence, and more. This assertion is due to the wide microscopic variations among similar or dissimilar materials, and wide variations of resulting electrochemical observables, based on slight variations of the initial experimental conditions.³³

Our qualitative principle explains how electropolymerization via potentiodynamic cycling was used within a set known as the “optimal criteria” coupled with the “representative settings” set. The qualitative principle may relate to areas other than chemistry (see below and following sections), despite its seeming simplicity or seeming triviality once fully understood or appreciated. The optimal criteria point (O_{II}) has been set to correspond to the successful polymer growth up to a *point* where potentiodynamic cycling does not generate an appreciable increase or decrease of the polymer current (e.g., a “thick polymer” is grown, albeit thickness is not the only function parameter or descriptor through which, this *point* can be realized). As said, this boundary point can be set as “optimal criteria O_{II} ”, where the two optimal criteria, thus far, share equivalences and appropriate correspondences based on some overlap of experimental objectives and representative settings. This *point* is illustrative of a polymeric form or overall polymer volume. Typically, it is related to “thick polymer” films, or their maximally doped state given that, for such a polymer $I \sim (E_{\text{switch}} > E_{\text{polymer}})$, then, $E_{\text{switch}} \sim$ maximally doped state at its maximal thickness $\sim I$, where \sim is some correspondence, well-defined relation, or equivalence. Throughout the chapter, we allude to a mechanism that illustrates the current optimal criteria (i.e., O_{II}) and from which relevant and useful abstractions (in the sense of the existence of other such optimal criteria \sim mechanism \sim abstraction) and relation to the observations from a first-principles perspective, can be acquired. The boundary conditions within the concept of “optimal settings” were actual experimental events during our studies. They correspond to sets of standard settings we optimized for successful

characterization or understanding of the processes (which, in some sense, became “**representative settings**”).

Given the establishment of two *boundary conditions* for well-defined optimal criteria statements (i.e., objective settings), one can easily see how any well-defined experiment which overlaps or is contained within some boundary condition can be set to be a “virtual” or inner boundary. From this set, abstractions can be generated (e.g., optimal criteria O_{III} , where the three optimal criteria share equivalences, and correspondences, as before). In some cases, the overlap at some inner or arbitrary point, which is *appropriate*, may allow access to more complex abstractions or correspond to points from which a more extensive set of observations may apply. For example, the maximally doped state optimal setting O_{II} overlaps, or it contains within its boundary points some elements (i.e., equivalences, correspondences, relations) from the densest polymeric forms that can be characterized, with optimal setting O_I , through the maximal color expression of the electrochromic polymers at the maximum potential point. This relation means that it is appropriate to utilize some experiments where the optimal criteria may have been either of the two, to make some abstractions of the other. This process is designed while keeping some “**crucial representative settings**” (e.g., SR, electrolyte, molar concentrations, electrodes, type of polymer or monomer, and more) in equivalence, on top of the boundary condition overlaps (the optimal criteria), and therefore following the scientific method approach.

Informally, (i) $\{O_I, O_{II}, O_{III}\} \sim I$, for some equivalences, these optimal criteria are contained within a set which freely allows to abstract, so long as we do not “abandon” (i.e., arbitrarily break the set boundaries) $\{(I)\}$. (ii) $\{[O_I \supset O_{II} \supset O_{III}], [O_{II} \supset O_I \supset O_{III}]\}$, which means that by inclusion, we can (in some sense) abstract **for** O_{III} , **from** O_{II} or O_I . (iii) $\{O_I \cup O_{II} \cup O_{III}\} \sim [O_I | O_{II} | O_{III}] \sim [N] \sim \{(I)\}$; where $|$ signifies “or”, and $\{(I)\}$ some open or “free-like”, conditions in the setting of electropolymerization for I , for some optimal criteria abstraction ($[N]$), where we do not “abandon” I , for example. Arbitrarily more complex boundary conditions can be set, and under those considerations, this principle may only hold for the representative set of overlapping conditions established above. This way, we have coupled the qualitative principle in a way from which we could abstract functional relations and information from a sequence of experiments, using our optimal criteria, representative settings, and “hysteresis-like criteria” (see below) approach, which is what we demonstrate in the following sections.

In the following paragraphs, we introduce and define a “smart material” in a way based upon which an affirmative occurrence automatically implies that the material has demonstrated functionality, modularity, and emergent phenomena. To induce or be able to generate modularity, a process rendered as the source through which such a potentially inductive or deductive behavior is created or observed must itself conform to that realization. Having done that successfully, we would have connected electropolymerization to modularity,

emergent phenomena, and “smart materials”. We can define “modular phenomena”, “modularity”, and “modular” aspects (phenomena) arising from a complex system in relation to some ideal or optimal characteristic operating form, sometimes hierarchical, as actions or responses whose individual parts or modules (e.g., group motifs, functional groups) could not yield some phenomena or observation, individually. In a modular system, modulation may refer to adjustments in one or more of the “modules” of the system to change its behavior or properties without fundamentally changing its overall structure, which allows it to be flexible, adaptable, and in some cases, robust to incoming actions. For example, for training in deep learning (CS paradigm), problem solutions using analog computing (using electrochromic materials), modulation has very recently³⁴ been conditionally related to optimization abstractions illustrated by state transitions, which are, in some sense, opposite to those meant initially to store information (i.e., ‘non-volatility’). This assertion corresponds to some of our arguments and observations below regarding *i1*) electropolymerization versus chemical polymerization as processes (see next section) and *i2*) electropolymerization products as potential sources of abstract and valuable relations. On the other hand, modularity in ecological contexts has been defined from the perspective of support towards resilience to environmental or ecological pressures or tensions.³⁵ Modularity has been intrinsically related to emergent phenomena and reactive systems, particularly in physical and computer sciences.³⁶ Emergence refers to system characteristics, behaviors, phenomena, or properties that differ and cannot be traced or predicted from the individual system parts’ (or modules; e.g., functional groups, group motifs, non-covalent and covalent types of interactions, and more) characteristics, behaviors, properties, or phenomena.³⁷ Reactive systems generally refer to artificial systems (e.g., computer architectures)³⁸ that appropriately and timely respond to environmental changes or pressures and that adapt their “behavior” in response to the changes, which makes them suitable for many research and applied areas; the realization of highly contextual, modular, and reactive systems at the single material level can bring exciting developments in various fields such as materials science, computer science, artificial intelligence, and artificial life. The adjective “chaotic” has been used to describe a type of time evolution resulting from a dynamical system; more precisely, moments or motions whose time evolution (cycles) appear very complex.³⁹ During the study of cellular automata, nonlinear dynamical or chaotic behavior has been mentioned;⁴⁰ this is relevant because properties and behavior traced to polymer growth or study, as we will explore, may be related to or connected to cellular automata systems in the future.⁴¹ Adaptive systems have been defined as systems that adapt and live “on the edge of chaos”, able to adapt and self-organize. Highly sophisticated reactive systems like the olfactory or visual cortex have been modeled as low-dimensional global chaotic attractors with multiple wings.⁴² It can be seen that complex systems, while evolving (implying short-term or sudden changes in stability in “short-lived”

species), maintain “long-term stability” (see Section 2.7.1.5) and undergo cycles characterized by “chaos” (as defined above). This relationship between reactive and adaptive systems is underpinned by chaos, modularity, and emergence, which provide a rich framework for understanding how complex systems work.

We postulate the following criteria **(1)**, as definitional or prerequired, for a material to be categorized as a “smart material”. **(1)** A *reactive system* that combines some inner and modulated response, which is coupled **(1)** with the exhibition of some “hidden” complexities based on indirect or deductible evidence (i.e., emergence), **(1)** exhibits signatures of chaos (which coupled to the following requirement implies the existence of self-organization), and which **(1)** reacts to some environmental actions with some response that corresponds to some negative feedback or controlled process and derivable mechanism (therefore, an *adaptive system*), underpins the criteria of **(1)** a “smart material”. This definition inherently embeds the criterion of **(1)** “emergence”, modularity, and “adaptive systems” simply by comparison with another material **(H)** that irreversibly fragments or loses function upon some arbitrary and *appropriately* equivalent application of biasing stimulus (therefore, not modular, or adaptive) or **(H)** which possesses trivial response functions. In some sense, **(H)** does not evolve or transform (therefore, not emergent or reactive), while the set of exogenous or extrinsic conditions is maintained in closed form or while the introduction of a slight variation that does not correspond to arbitrary immersions (not *appropriate*) to the set of initial conditions (optimal criteria), is applied. We define and utilize these premises to categorize *poly-7* as a “smart material” and a material exhibiting emergent phenomena or “behavior” as a response to biasing stimulus characterized through current-to-voltage and cycle examinations. That is, based upon the hysteresis-like criteria (Scheme 2.7.1.5.1 to 2.7.1.5.3) we use, the responses from *poly-7* were characterized as functional and representative of instances of modular phenomena, in some cases, coupled to instantiations of emergent phenomena, and importantly overall, the system met the criteria of signatures of chaos, negative feedback or inner actions and the existence of hidden complexities based on deductible or derivable observations.

This conclusion was reached by realizing the concepts of appropriate boundary conditions, optimal criteria, and representative settings, coupled with the hysteresis-like criteria phenomena as “action exhibitions”. These concepts have been individually applied or defined in a plethora of contexts, which, however, in our case, we believe to be novel in some respects, as we present it here. Establishing appropriate boundaries implies that accurate result abstractions using the approach presented here could suggest strong outputs or firm conclusions when the appropriate connectivity of optimal criteria in boundary condition overlapping has been implemented.

We extend our optimal criteria set by introducing some optimal criteria O_{III}, which we identified and coupled as the absence of observability of irreversible

polymer function loss through the “polymer growth” process. One can see that this boundary or optimal criteria occurrence is met automatically by the previous ones, e.g., based on the current relation response to an arbitrary point set which increases or levels through the cycling and maintains a specified current response at a defined potential point or region. These boundaries in monomer-containing mixtures become expandible to “studies” in monomer-free settings by establishing similar correspondences, such as polymer identity, presence of a most principally distinguished representative, polymer redox potential peak (e.g., $E_{ox1, pol, monomer-containing, final\ cycle} \sim E_{ox1, pol, monomer\ free, initial\ cycle}$), as well as by the maintenance of crucial representative settings in both conditions. However, it is easy to see that we are partially limited or restricted in the type of information we can abstract from polymeric outputs based on coupling or association of experiments in monomer-containing and monomer-free mixtures, which is a crucial distinction in applications. Complex systems (vs. simple systems with one FG, like simple polythiophenes or polypyrroles) like *poly-6* and *poly-7*, whose state representations or “evolution” are also highly dependent on initial conditions, can be prescribed an elevated level of functionality and modularity if we can show order, organization, exchange or decoupling, and character while not influencing the optimal criteria set and crucial representative settings set. While maintaining the set of crucial representative settings, appropriately generated and coupled optimal criteria, and hysteresis-like criteria, we do not influence or coerce the electropolymerized system to an output. Concerning *poly-6* and *poly-7*, the only assumption we made and thus controlled was related to their potential atmospheric reactivity, which we limited, by working in atmospheres with < 0.1 ppm of H_2O and O_2 and under inert Ar gas.

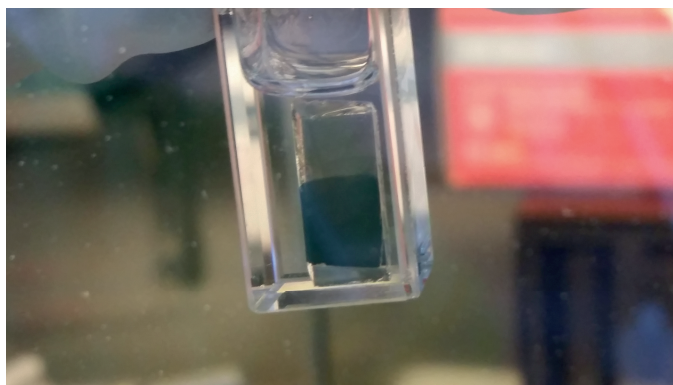


Fig. 2.6.3. Picture of arsaalkene *poly-7* (on FTO) a few hours after disconnection from the electrical circuit (i.e., without any applied bias) in a doped state. The observed stability of the doped polymers may derive from slow structural rearrangement/relaxation processes under inert conditions, stability of (bi)polaron states, (redox polymer \leftrightarrow conducting polymer) exchange, aromatization of the polymer backbone in the doped state, presence of counteranions and hence electroneutrality.

2.7. Functionality and modularity of P=C (*poly-6*) and As=C (*poly-7*) polymers. Unique features and electrochromism.

2.7.1 Electropolymerization process and mechanisms.

Potentiodynamic responses of *poly-6* and *poly-7*. Development of the hysteresis-like criteria, optimal criteria, and representative settings for electropolymerization of As=C and P=C polymers. Action exhibitions from *poly-7* during/after polymer growth.

2.7.1.1. Summary and motivations for electropolymerization.

In the first part of this section, we reviewed electropolymerization mechanisms and studied hysteresis phenomena.⁴³ We define the “hysteresis-like criteria” construct, which from our perspective, is generalizable for electropolymerization studies as a process for some or all relevant polymers under study. The potential realizations from constructing diverse types of hysteresis-like criteria, where the current crossing points between cycles or cycle points become qualitatively or quantitatively valid, are relevant. In future applications, for example, concerning some event, observation, or state, these realizations can be abstracted or transformed from or into appropriate relations through equivalences or correspondences. Instead of the stricter (and technical also, within its context) double self-crossing of a signal as a loop (loop 1: voltammogram, loop 2: self-crossing), considered by some researchers to be the behavior corresponding to a hysteresis, we realized that from a voltammographic perspective, the electrochemical response (loop 1) corresponds to a hysteresis, which by inclusion and identity (i.e., occurrences inside the voltammogram, and for the polymer, which is bounded to the electrode surface), specifies the hysteresis-like criteria, in some physical and logical sense based on current and potential evaluations relative to cycles during electrochemical responses.

The study of technical hystereses can be challenging due to the noise and chaotic responses that often follow self-crossing events. On the other hand, certain intersections or events indicate phenomena of high importance for some compounds or species. Notably, these crossings or events are not always required or predetermined elements of the voltammogram, allowing abstractions to be made (vide infra). In some cases, non-trivial voltammographic responses have been classified as hysteretic without strictly distinguishing the presence of “self-crossing” events, further supporting our approach.⁴⁴

In what follows, we establish the existence and value of the hysteresis-like-criteria events we found. We also introduce, develop, and utilize the concepts of “hysteresis-like criteria”, “optimal criteria”, and “representative settings” in the context of electropolymerization as a process and potentiodynamic

method for the growth and study of the suitable polymers, here focusing on *poly-6* and particularly, *poly-7*, which is more distinguished.

In other words, we do not “claim” novelty (e.g., hysteresis has been used in AI as a principal component) in the individual parts of the construct or approach. However, as expressed here specifically or contextually, we believe (to the best of our knowledge) that it could bring some novelty or relational aspects of potential.

2.7.1.2. Relations to conducting polymers, low coordinate arsaalkenes & phosphaalkenes, artificial intelligence, modularity, smart materials.

The study of materials containing arsaalkenes ($\text{As}=\text{C}$) and phosphaalkenes ($\text{P}=\text{C}$), due to their precise nature and classification as “soft”, “sensitive”, and “reactive”, naturally connects to broader fields such as artificial intelligence, computer science, and philosophy. The study of these materials (and the materials themselves) share commonalities with reactive systems, modularity, logic, conditioning interpretability, non-univalence, framed rationality, and microlocal interactions.

The vast natural existence of diverse forms, differential forms, and other structures beyond the human brain offers some potential for the successful design and development of AI systems. Introducing contextual and connective interpretations and algorithmic strategies from chemical phenomena is as essential as theoretical physics for lifting phenomena for practical applications.

Due to societal biases, the human brain is an inappropriate basis for the design of advanced AI systems. Other approaches include using alternative materials (e.g., polymers or compounds containing phosphaalkenes, arsaalkenes, or other heavy p-block elements in unusual bonding situations) and processes (e.g., electropolymerization as a method) also provide appropriate and contextual approaches for abstracting useful information and designing AI systems.

The “reactive”, “atypical”, “exotic”, and augmented nature of phosphaalkenes and arsaalkenes in conducting polymer or other types of studies arises from their unique chemical properties such as the unusual bonding situation, multiredox and multivalent state attainability, non-bonding lone pair of electrons available to sense or interact, and the “director” role of the electronic structure of the materials (as we have previously argued).

Furthermore, we present the added functionality and emergent phenomena of *poly-7* through five sets of linked experiments, demonstrating their relevance to “smart materials” and providing representative, representable, and relevant abstractions. In this context, we analyze the results using a modularity approach, highlighting the importance of these materials in the study of emergent phenomena. The EU funded this part of our work to design “smart inorganic polymers” (SIPs COST network), which makes our approach relevant.

The atmospherically sensitive nature of the $\text{As}=\text{C}$ and $\text{P}=\text{C}$ group motifs naturally lends itself to be of use in the approach since working under “mild”

conditions is inherently necessary, which we now realize as a vital asset, if not a top quality of functional approaches and materials for in-house AI modelling and development, rather than a disadvantage. We believe that such a tailored, strategic, and considerate (i.e., “intensional”) approach to polymers and materials gives “the materials” room to naturally exhibit the intrinsic or natural functionality or properties they hold and comprise, from which sustainable and robust functional solutions can be constructed for future applications. While some may consider our approach unconventional, we believe it is essential to explore our work's potential research abstractions thoroughly. We connect the chemistry of this new family of conducting polymers and all conducting polymers exhibiting relevant criteria with the statements and arguments we present and where those statements are valid, which is our scientific motive.

2.7.1.3. Overview electropolymerization mechanism.

The mechanism of electropolymerization consists of sequences of steps, some of which overlap or exchange order positions with one another in limited cases. For example, in the autocatalytic mechanism, monomers are chained onto the growing polymer, in addition to oligomers. The competition between processes is equivalent to a competition between mechanisms, which depend on several global, local, microlocal, and effective representations of concurrent processes. A successful electropolymerization mechanism must meet some minimal standard criteria of polymerization convergence, corresponding to at least one polymer chain of two or more monomer units covering (and becoming) the electrode surface. However, as exemplified in nature, more exciting polymers correspond to polymers with many more covalently bonded fragments and the addition of nanostructure or other functionality via non-covalent interactions, as presented here. Individually, it is an overlapping, dynamic, competitive, concurrent, recurrent sequence of synthesis of generational and new products (both in the polymeric chains and electrode surface).^{17,45}

2.7.1.4. Conceptual introduction of “hysteresis-like criteria” and “action exhibitions” from polymeric forms, and their relation to “optimal criteria” and “representative settings” for electropolymerization.

The presence of hysteresis effects as a representation of memory effects is associated with structural changes with slow relaxation rates and complex dynamics in neuronal ensembles.⁴⁶ Hysteretic phenomena have been explained based on timings and potentials in which the polymers were maintained in the neutral state.¹⁷ This observation is an example of different types of hysteresis in which dynamic cycling produces local structural changes when the time parameters for the resting state are modified. At the same time, some diffusion and dissipation processes and some other local equilibria are maintained in other unchanged or relaxed states. Therefore, in general, structural states are

bounded or tensioned and become observable in the subsequent cycles as representations of some convergent structural set point, which by nature, becomes a relevant point that can have essential relations because it has the same electrical current and potential value (i.e., it represents an intersection, and therefore, a “hysteresis-like criteria” instance).

A crucial hysteresis occurs in the first cycle of monomer-containing solutions. This hysteresis is the first form of structural integrity or memory-like events. Furthermore, the hysteresis effect in the first cycle of monomer-free electrolyte solutions correlates with a structural response due to a significant variation in the environmental state at the surface interface relative to deeper layers, which triggers diffusion events. It is the most crucial direct set of observations relative to later cycles. It acts as a “ripple effect”, where the polymer response is fundamentally and categorically linked to the response/reaction in subsequent cycles. More abstractly, it corresponds to the fastest exchange rate the polymer is exposed to during applied stimuli (cycles). For more functional or adaptive polymer forms, it may be represented by the formation of a tower-like structure (based on our observations; however, we do not explore this further as it is beyond the scope of this thesis), from which further structural variations emerge during cycling. The few subsequent cycles are equally critical, as they define the structural response or advertise the structural integrity of the polymeric species.

Any hysteresis-like criteria event, whether identified or not, may relate to a trigger of structural events, some of which may be partially obscured from our view, depending on their structure relative to our observation window. This type of observation alone corresponds to the exhibition of modularity and emergence because it implies the presence of “modules” and “hidden complexities”. We confirmed this phenomenon (see below) after observing the corresponding responses in an expanded electrochemical window (EW), which allowed us to confirm the phenomenon indirectly. The observation helped us to question the previous labeling of the polymer as “unstable” after an experimental response. We linked the reaction to structural changes over time (e.g., structural “evolution”), an action exhibition (e.g., anthropomorphizable as some fail-safe or stop), or chain re-equilibration.

Highly tensioned small molecules (previously conditioned or treated, with considerable negative potentials in the presence of a base) have been shown to exhibit hysteresis criteria in their responses; that is, hysteresis only was expressed after a significant bias was applied to the molecular structure by a preceding polarization with negative potentials of - 1.5 V, SR of 5 V/s, in the presence of secondary agents (“under special experimental conditions” as the author interestingly observed: this type of special conditions will become relevant later during polymer experiments).⁴⁷ In other reports, “anomalous” and hysteretic effects in conducting polymers were related to structural rearrangement processes.⁴⁸ This observation is relevant in our case for several reasons. Due to structural modulation, As=C, and P=C group motifs (and relevant

sites) localized frames that acted as a redox polymer (instead of conducting polymers), and that served as charge micro-reservoirs or modulators, as observed by non-trivial electrical current increments in unsupported environments (i.e., monomer-free environments).

Memory effects, in general, have been postulated from nonequilibrium perspectives.⁴⁹ Mechanistic views are complemented by accounting for dynamic processes (relaxation rates, transport through paths,⁴³ percolations⁵⁰). Hysteresis criteria (see Section 3.1 for memristor applications and references) have been postulated as a general property effect exhibited by conducting polymers. We agree with the postulation that hysteresis, as a property effect, is a general feature of these materials. For a vast space of representative settings, this feature becomes expressible (i.e., monomer type, polymer type, molarities, solvent type, electrolyte type, polymer growth, study input type, number of cycles (NC), scan rates (SR), start potential, end potential, temperature, pressure, stirring rate, gas matrix, counterelectrode, reference electrode, reference electrode profiles, illumination conditions and more). Meanwhile, we try to classify them as a variety of types of responses or **hysteresis-like criteria** during growth (monomer-containing electrolyte solution) or during polymer study (monomer-free electrolyte solution), whose responsiveness we denominate as **action exhibitions**. That is, action responses that may signify a function, such as a memory function or a signaling pathway, that transcend as observations, represented primitively by structural changes, in some sense, relative to the initially unperturbed functional state representation, or relative to the exhibited or inhibited function or signal.

As shown below by the qualitative presentation of relations and relation equivalences between sets of experiments and observations, the categorization of this phenomenon became realizable. Therefore, types of hysteresis-like criteria became useful in both stages, polymer growth, and polymer study.

In our view, following polymer growth in an environment containing chemically inert salts and monomer species as support and electric potential as the main driving force, memory effects transcend from the accumulation of complexity parameters. These can exploit the stimuli-responsive nature of the materials, for which relevant phenomena may be observed in the form of “action exhibitions”. Thus, electropolymerization can generate highly functional and modular species, as opposed to the regularized or chemically filtered monodisperse polymers from chemical polymerizations after isolation and whose complexity parameters have been “filtered” through sequential processes of chemically harsh conditions such as exposure to many solvents and water-based washing processes under heat and environmental conditions.

2.7.1.5. Comparison of chemical polymerization vs. electropolymerization methods. Polymer characterization (*poly-6* and *poly-7*) via potentiodynamic methods. Experimental demonstrations of functional, modular, and emergent phenomena from *poly-7*.

The utilization of representative settings during electropolymerization leads to the emergence of order and organization, and this is naturally intrinsic to the conducting polymer setting, where quasiparticle transport generation through doping involves polymer growth and degrees of localization. Even in cases where polymerization efficiency is *limited* for some goal under some specific considerations, one could argue that there are an infinite number of arbitrary goals for which the limited efficiency may become expressible and functional, and therein lies some potential of the approach.

When considering electropolymerization or chemical polymerization processes as a source, one realizes the processes exhibit programmatic characteristics as the understanding of the polymer is gained. From a feasibility of systems engineering and application programmability (complexity perspective), chemical polymerization processes are less feasible than electropolymerization. Thus, electropolymerization and the polymers are sources of abstractions during growth and their study. We argue that organic polymers obtained via chemical polymerization and, as *used in the application*, have often been filtered off some of their valuable attributes or realizable and utilizable complexity (i.e., those particular polymer distributions that were filtered). Chemical polymerization in solutions involves increased degrees of freedom, chemically active secondary agents, the absence of phase boundaries, and the presence of convection. All the mentioned qualities lead to an enormous size of the state space representations (or other parameter space) as the chemical polymerizations proceed (in some helpful manner, not accessible in functionality during or after the chemical polymerization process). The large and diverse initial crude polymer set relative to the final monodisperse polymer form presented after isolation (where structure representations of complexity, such as roots, branches, folds, and towers, have been filtered) blurs the lines of *natural functionality* intrinsic to the polymers in their final presentation, which in practical terms, become an enclave of a particularized function in a device application.

In contrast, electropolymerization is more practical today when representative settings and optimal criteria of polymerization are anticipated, for example, through the action exhibition of structural properties or property effects or forms. The optimal criteria, representative settings, and other presented concepts can be used to establish relations and equivalences from the following types of considerations, among others: current and potential relations and factors ~ structural effects ~ current or potential increases or decreases ~ polymer growth or function loss ~ structural and electrochemical reversibility ~ order characterization ~ electrochemical window dependent responses ~

memory effects via hysteresis or hysteresis-like criteria \sim applied voltage, feed, or stimuli \sim reactive or delayed response (e.g., electrochromism) \sim generative evolution. As an analogy, a chemical polymerization system mimics the early universe forms and the universal evolution processes, as better as an electropolymerization system mimics the early biologic forms and biological evolution processes.

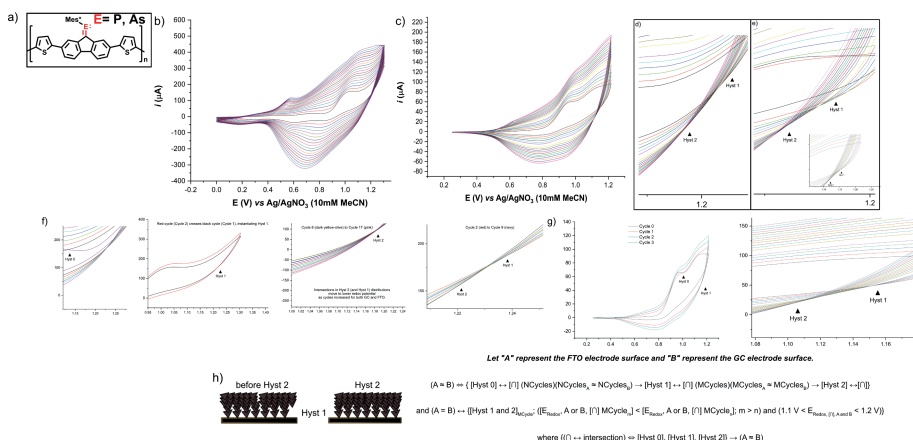
In summary, we introduced motivating factors for the utilization of electropolymerization systems **(I0)** where the resulting products are used **(I1)** or as a process in terms of the resulting relations of equivalences via abstractions derived from polymeric form expressions or experimental observations from the perspective of **optimal criteria** (i.e., tightly related to boundaries), **hysteresis-like criteria** (exhibited in the voltammogram and potentially spectroscopic responses), **representative settings** (experimental conditions, variables, parameters) of electropolymerization for polymers in the study. The **(I1)** factor is believed to be relevant in this thesis based on results, discussions, and directly or indirectly by many others.

The complete structural characterization of polymer films from a categorical perspective based on experimental modifications and observations of the resulting systems is a challenging problem to tackle experimentally due to the plethora of variables involved. Access to potentially arbitrary types of hysteresis criteria derivations towards types of observations (deductive) that become structures, modular sequences, and forms can be envisioned in some future, where the approach exists under some framework of studies.

With suitable As=C and P=C polymers, this became a fascinating aspect of the electropolymerization processes. The illustrations (schemes) in these sections are accompanied by five characteristic and crucial experiments with *poly-7* that support our thesis chapter.

We conducted two electropolymerization experiments using two different electrode surfaces (GC and FTO) under identical conditions. Both experiments exhibited critical points (Hyst 0, Hyst 1, Hyst 2), corresponding intersection distributions, and overlapping regions where the materials showed coordinated responses and decoupled their dependence from the electrode surfaces. Thus, we observed remarkably similar hysteresis-like criteria and related phenomena in the FTO and GC electrode surfaces. Initially, the events were characterized by the occurrence of critical points in the forward sweep (Hyst 0) at around + 1.0 V in both experiments, as seen in the first graphs from the left in f) and g) below, followed by two distributions of intersections (Hyst 1 and Hyst 2) between + 1.15 to around + 1.25 V, as seen in Scheme 2.7.1.5.1, which possessed several equivalences such that the redox potentials of the intersections of the following cycles were less positive compared to the previous ones (see Scheme 2. 7.1.5.1 below), branching or potential gaps between Hyst 1 and 2 (see the inset/zoomed-in graph in e) and the fourth graph from the left in f)), and the absence of intersections following a crucial point where the Hyst 2 distribution ended (see, for example, the third graph from the left

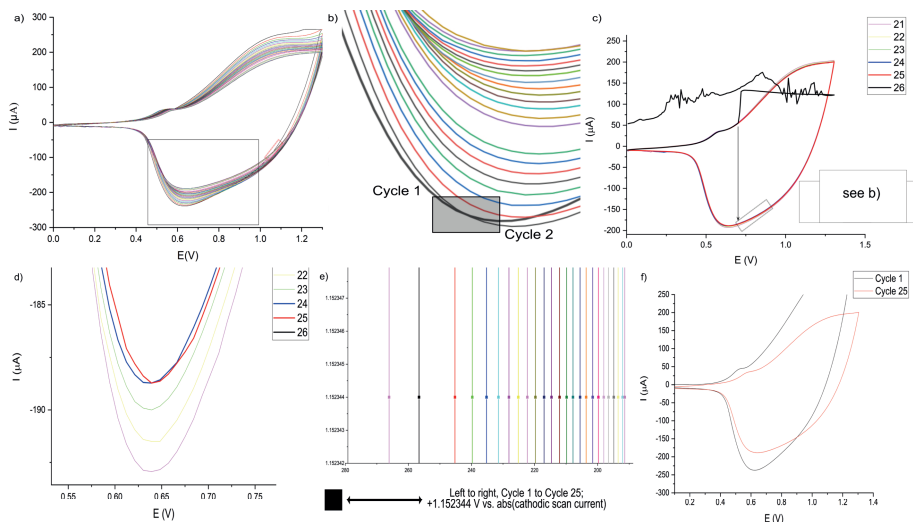
in f) and the second in g)). This observation confirms the equivalence of the polymer growth mechanism in the two surfaces under identical conditions and the existence of a substrate-independent quasi-exact transformation type of sequence during polymer growth, which we express as a simple logical equation in the scheme below. The voltammographic responses are observed throughout the application of the optimal criteria concept (and representative settings and hysteresis-like criteria concepts). They are primarily reflected by the consistency of the experimental variables and parameters (“crucial representative settings”) used in both experiments, including monomer identity (purity), NC = 20, electrolyte concentration, solvent = DCM, reference and counterelectrode, the gas atmosphere under Ar, same electrochemical cell and potentiostat, SR = 100 mV/s, start potential = + 0 V, end potential = + 1.2 to + 1.3 V, and more).



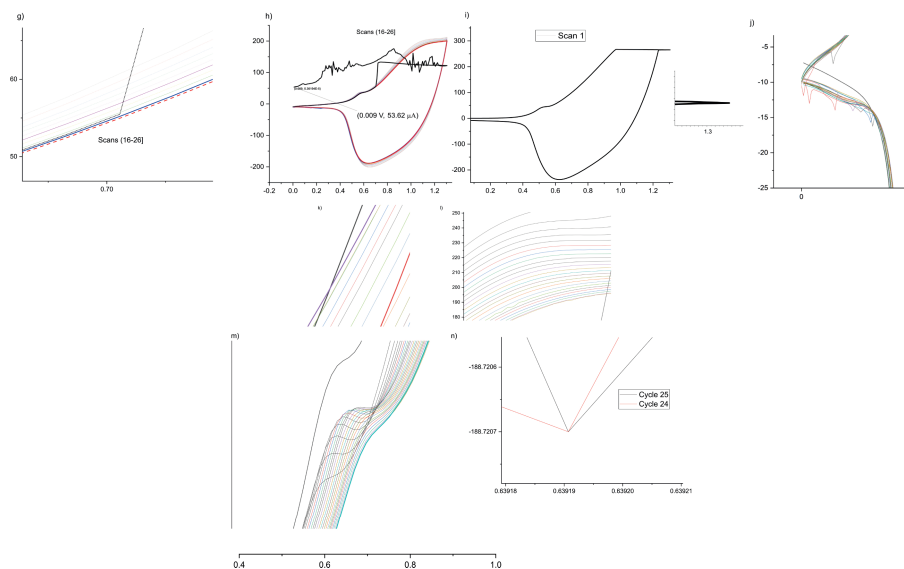
Scheme 2.7.1.5.1. (Unpublished). a) Molecular formula of *poly-6* and *poly-7*. b) Electropolymerization of **7** on FTO to give *poly-7*. SR: 100 mV/s (NC = 20). c) Electropolymerization of **7** on glassy carbon (GC) to give *poly-7*; SR: 100 mV/s (NC = 20). d) Inset FTO exp. Apart from the occurrence of the critical point Hyst 0 (see below), note that there are two major distributions of crossings (Hyst 1, Hyst 2). As the potential was cycled, the intersection of the following cycle had a less positive redox potential than the previous one, which was a trend also observed in the GC experiments (see e) below). f) Graph insets of the FTO experiment in a). The left experiment shows the initial intersection event, corresponding to cycle 1 (black curve), crossing cycle 0 (purple curve) and instantiating Hyst 0, which is equivalent to that observed in the GC experiments (see g) left), relative to the total number of cycles in the experiment and the experimental cycle number in which the observation occurred (scan or cycle 2). The second graph from the left shows the first intersection occurrence, which instantiates Cycle 1 and Hyst 1. Other cycles are omitted for clarity. The third graph from the left shows the region corresponding to Hyst 2 crossings (see text inset), which is about 20 to 30 mV less positive redox potential. No other crossings occur after this point, confirming that the observations correspond to a valid occurrence of hysteresis-like criteria and not to a random or arbitrary selection. This behavior also indicates that the polymerization process and mechanism are ordered. The fourth plot from the left shows a unique perspective of earlier cycles (Cycle 1 to Cycle 8) relative to the third plot from the left, confirming that earlier crossing events occur at more positive potentials. g) Graph insets of the GC experiment in b). The left plot shows Hyst 0 and Hyst 1 events. Other cycles are omitted for clarity. The right plot shows similar phenomena, with Hyst 2 events reaching a less positive threshold than the previous crossings and distribution (i.e., Hyst 1). h) Pictorial representation of the transition or transformation that leads to three hysteresis-like criteria events during polymer growth on two different surfaces. Such discrete responses and discrete response transformations suggested the existence of relevant isostructural motifs and equivalent structural motif transformations. The existence of "special points" of increased structural dimensionality, e.g., a structural manifestation from 1D to 2D (3D) physical space (e.g., chaining or linking), may be causative (i.e., left → right transformation or transition). Based on the abovementioned observations and analysis, the bottom equation states that the FTO and GC electrodes are equivalent in both experiments.

After the successful processes of polymerization growth, coupled with their equivalences in the form of hysteresis-like criteria and identical observations using two different electrode surfaces, we abstracted an initial assignment to a type of optimal criteria for our study case based on the observability of polymer color change and larger current levels. Thus, we chose FTO electrodes, *poly-7*, and p-doping conditions while considering the exhibition of electrochromism as a goal. In the same way, we abstracted representative settings of the electropolymerization process and for *poly-7*. In Scheme 2.7.1.5.2 (2 pages) below, we introduce the second critical study (third experiment) with *poly-7*, performed in a monomer-free solution and under quasi-equivalent conditions to those abstracted above, with no additional biasing or secondary reagents in the mixture.

The electropolymerization experiment was characterized by intrinsic order and modularity in the responses, which suggested *poly-7* cherished the addition of nanostructure on the polymeric structure. At the point of maximal positive current, there was only one intersection (see l) above), indicating fluidity. The fluidity was congruent with those state representations of higher doping (p-doping) at high positive electrode potential, where (when) the structure possessed the largest quasiparticle character and where (when) it was maximally colored (dark blue or black color). The stable response over the initial set of cycles at the maximal electron current (-) on the reverse sweep signified structural recuperation from doping and integral response from doped *poly-7*, experiencing sequential and cyclic undoping without any oligomer surface layer of support. Interestingly, Cycle 1 showed two minima on the forward and two on the reverse sweep. During the forward sweep, the inflection point at $\sim +0.97$ V was highly pointed (see i) above), and outstandingly, this point was presented as an isopotential with the last, “typical hysteresis” event in Cycle 26, in some sense, establishing a correspondence between Cycle 1 and 26 and closing the overall process. That is, the inflection point onset in Cycle 1 and the last memory-like event (see h) and i), inflection points) in Cycle 26 occurred at the same potential, which in our view, by being in some sense predictable or traceable not only to Cycle 25 but also to Cycle 1, proved that the event was illustrative of some form of expressivity (“quasi-chaotic”, evolution, transformation, or action exhibition) instead of an “unstable response”.



Scheme 2.7.1.5.2. (Unpublished). Response from *poly-7* (FTO) sample in transparent (monomer-free) electrolyte-containing fluid solution; 0.1 M *n*-Bu₄NPF₆; electrode: FTO glass; SR: 0.1 Vs⁻¹; glovebox: < 0.1 ppm H₂O, O₂; 26 scans. a) Voltammogram showed good stability over time; red-dashed rectangle: hysteresis-like criteria event; dark rectangle: inset of interest. b) Hysteresis-like criteria; Cycle 2 crossed Cycle 1 in the most reducing part of the voltammogram out of all cycles. Cycle 2 has a more negative current than Cycle 1, which instantiated some structural integrity confirmation signal (which we have now confirmed by the subsequent order). c) A second hysteresis-like criteria occurrence in Cycle 25 (also shown in d)), before the differential signal in Cycle 26. The sudden current increase in Cycle 26 occurred at a potential close to that (+ 0.6 to + 0.7 V ~ 100 mV) at which the hysteresis-like criteria event was evidenced in Cycle 25. This behavior observation may be anthropomorphized as some “warning”. The **most principally distinguished representative** of the polymer shifted anodically by ~ 60 mV, which is a small amount for 26 cycles, indicating structurally robust polymeric forms evolved as the system cycled. This shift indicates a polymer species that became slightly harder to dope, which an accumulation of irrecoverable segment transformations could have caused. However, as seen below in the next experiment, the charge may have been “exchanged” or “transferred” somewhere from or onto polymer motifs structurally not involved in transactions at positive potentials, which was also supported by the graph in f), where form (structure, based on the shape of the graph) and “discharging capacity” were not lost dramatically (based on our EW view). e) Graph of constant potential response from *poly-7* at ~ +1.15 V vs. magnitude of the cathodic scan currents, from Cycle 1 (left) to Cycle 25 (right), which validates our view that the entire process was well-directed, given the gradual decrements in current loss over time. f) Comparison between Cycle 1 and Cycle 25, evidencing ~ 20 % discharge capacity loss only after Cycle 25.



Scheme 2.7.1.5.2. (Continued). X-axis: E (V), Y-axis: I (μA). g) Cycle 26 followed a *generational path* (i.e., trace relation to previous cycles). It suddenly turned upward. h) Cycle 25 (red) and Cycle 26 responses. Cycle 26 should be read from bottom-left (CCW) to top left, which is 0 V. Transient circuit “failure”, “error”, and “response” (vertical path, followed by dramatic horizontal path) were transient and rectified. Reverse sweep exhibited structure and typical memory-like hysteresis-criteria (i.e., “self-crossing”: 19 occurrences from +1.23 to +0.97 V, +126.48 μA). i) Cycle 1 (inset: zoomed-in uppermost right potential region) exhibited an intense inflection. Crucially, Cycle 1 exhibited the inflection point at +0.97 V (+267.06 μA), which demonstrated some equivalence or correspondence between Cycle 1 and Cycle 26 through two inflection point occurrences at an isopotential point, in an abstract sense, proving the events were not related to arbitrary failure or stochastic processes. j) Similar triangular-like basin occurrences corresponding to current discontinuities are only observed in this voltammogram region. k) Cycle 24 (purple), Cycle 2 (black) only intersection (return sweep: +1.06 V), which established a relation between one critical inner event and one critical event prior to Cycle 26, as seen in q) below. Cycle 3 (red curve) indirectly showed that the crossing was not trivial per se, concerning the crossing between 25 and 24. l) *poly-7* responsiveness at the maximally doped stages. No intersections (crossings) were evidenced, except on the bottom (Cycle 25 crossed Cycle 24), instantiating the only hysteresis-like criteria event in this region. m) Evolution of *poly-7* polymeric forms representations at $E_{\text{ox}1}$. The first $E_{\text{ox}1, \text{peak}}$ in our view, corresponds to the most principally distinguished representative (i.e., structures or states) of the polymer, which tends to be related to the “HOMO orbital” (some investigators consider the onset of this event to correspond to the HOMO level equivalence in the polymeric picture). The important aspect is to notice the exquisite nature of the evolution of the events; cycle 1 (black curve, top left) and Cycle 26 (cyan curve, bottom right) spanned the entire process. n) Crucial “singular” point occurrence at (+0.639 V, -188.7 μA) between Cycle 25 (black) and Cycle 24 (red), which was shown in d) above, here zoomed (see comment in the text), which, when coupled with the observation provided in l), gives credence to our argument that the quasi-chaotic response in Cycle 26 followed these coupled events as a singular occurrence.

Optimizing or maximizing the ion transport coupling to charge transfer and solvent under the specific set of optimal conditions we use can provide the spatiotemporal environment necessary to minimize trapped loops. The Interestingly, the inflection points of the highly pointed event in Cycle 1 did not self-intersect on the reverse sweep (see i), inset), which was in some sense a different manner of expression from *poly-7* in Cycle 1 relative to other polymers (see hysteresis review section and references above). We postulate that the occurrence had some relation to growth conditions to study condition relations (i.e., $E_{\text{switch, growth}} = +1.2 \text{ V}$ vs. $E_{\text{switch, study}} = (\text{electrolyte-only environment} + \text{monomer support})$, vs. $E_{\text{switch, "unfamiliar" environment}} = (\text{electrolyte-only environment})$). Given that the monomer-free and monomer-containing conditions relate to characteristically distinct environments for *poly-7*, the otherwise identical experimental conditions represent an appropriate change in representative settings. The new set of conditions maximizes the polymer's volume based on the general understanding or consensus while maximizing the polymer "charging" (or discharging, based on hole/electron or analogous external circuit element position interpretation) while staying within the growth and EW windows, generates a p-doped species, and creates color expression (i.e., dark color vs. light in the undoped state), all which match conditions ascribed to the previously described boundary conditions and optimal criteria during the introduction of the concept. The resulting events associated with studying the material under the prescribed conditions are integral to our boundary condition and optimal criteria scheme. They have significant implications for the material's structural properties, behavioral response, and quasiparticle density. We argue that changing the electrolyte solution to a monomer-free one (while maintaining the same equivalent conditions) results in a slight environmental change relative to the fully grown polymer in monomer-containing situations, which, however, does not represent an arbitrary inclusion and would not break boundaries cyclically due to charge conservation. Furthermore, subsequent observations of the integrity of the polymer and the critical redox potentials over cycles confirm its recurrence. One can argue that specific changes such as solvent, counterion type or concentration, electrodes, argon atmosphere to earth atmosphere, SR, large overoxidation (e.g., beyond EW or window of study based on polymer response), current injection, etc., are "overwhelming" or significant and not isogenous in the sense that these produce an instantiation of some *instigation* with potentially undesired effects via large perturbations relative to growth or optimal study conditions. Based on our approach, these types of changes (i.e., changes in "crucial representative settings") were considered "inappropriate" as they cause significant changes in the material's natural response (e.g., based on polymer growth conditions) and may even break their functional and modular action exhibitions; this can significantly obscure their natural or innate potential and complicate the development of well-coupled or connected abstractions from their behavior. For example, sampling far outside the EW window, introducing an excess

of oxygen or water, or applying a constant voltage or external current for a long time can produce chemically reactive byproducts of reactions between *poly-7* and environmental components, as well as structural deviations, which we avoided by using optimal criteria and representative settings while not varying crucial representative settings during the coupling of different experiments that allowed us to generate connections and make abstractions. The presentation of an overpotential or, more importantly, the absence of monomer support in our monomer-free conditions can be considered an environmental event (i.e., an “unfamiliar” environment). In terms of the polymers under study, the analysis of such potential regions is naturally associated with unusual feedback or responses (see n-doping experiments below). In some cases, the effects of an action exhibition can be inferred but not directly observed (e.g., non-trivial current increases in the experiments above and below). The environmental events specific to our case here now correspond to the maximally doped state of *poly-7*, the maximally increased volume of *poly-7* as cycled or through all cycles (phase space), and corresponds to the optically densest state (i.e., monomer-free state \sim charge conservation principle \sim Cycle 1 generation).

The response (see i) above) of the polymer then indicated some transient event that did not produce critical “trauma” (e.g., structural change, characterized by a memory instantiation via self-crossing hysteresis, or irreversible change in current response as a failure mode, or other runaway processes) on the polymer. As seen by the non-self-intersecting sharp curve, the response indicated some exhibition of adaptive responsiveness or elastic behavior (stretching). In dynamical systems, assuming that the self-intersecting event is coupled to memory-like event instantiation, a closely spaced non-self-intersecting event otherwise implies the absence of some instantiation or type of instance. This absence could (counterintuitively) relate the polymer to some attractor basin. This assertion can be shown to be accurate by the fact that **(i)** Cycle 2 crossed Cycle 1 at + 1.26 V, **(ii)** presented two such inflection points, indicating some equilibrium transitions became apparent, **(iii)** was the only cycle to cross Cycle 1 in this region, corresponding to some path instantiation in Cycle 1 \leftrightarrow Cycle 2 (by being the very next sequence cycle, obviously), from which the familiar fold/unfold process proceeded for the rest of the cycles in the same region close to + 1.3 V. It is important to note that we confirmed the behavior on the positive current of Cycle 1 to be intrinsic to the polymer or material by comparing it with equivalent films and much thicker films for which responses exhibited similar phenomena or distorted current responses, respectively, confirming that the current detection of our experimental setup did not limit the behavior. Intersections, as seen in magnified (zoomed-in) voltammogram plots, generated ordered polytopes (we know that any minimally bounded small set of magnified graphs can generate a polytopic type of view); however, in this voltammogram region, we refer to an

ordered or organized “dense set” or graph (which need not be the case in random cycles), indicative of high structural order.

The polymer (*poly-7*) was characterized by fluidity (in the sense of the smooth nature of its responses as seen in b), l), and m), for example), and generational order as seen in m), where cycle-to-cycle historical evolution path order fluctuated predictably over time (i.e., orderly, well-organized, smooth response), with the existence of some set of attractor-like points that the system fluctuated or evolved towards while maintaining the stability of its most distinguished representative (see Scheme 2.7.1.5.2 captions).

The 1st hysteresis-like criteria type of occurrence was at the intersection between Cycle 2 and Cycle 1 at + 0.6 V, as seen in b), which demarcated the following. *(i)* Cycle 2 was the only cycle with larger negative currents than Cycle 1, which is a rare occurrence in typical monomer-free experiments based on our literature research since the polymer is known to lose capacity over increasing cycles as the structure of the polymer breaks or decomposes (and based on charge conservation, since there is no monomer support). This observation is relevant (see b) above) because the larger current in Cycle 2 occurred for the entirety of the reverse cathodic sweep (see b) on the plateau region). *(ii)* Cycle 2 was the only one that crossed Cycle 1 after the global negative current minimum point. The intersection occurred after the response represented by the change in the direction of the current plateau to more positive values (i.e., the inflection point). Neither of these two events (especially *(i)* above) is trivial, as they did not occur for any other cycles in the corresponding region of the voltammogram. They suggest an ordering and alignment (or unfolding) process occurred, which is associated with higher current observations in Cycle 2 relative to Cycle 1 (and for the entirety or span of Cycle 2 vs. Cycle 1, which is crucial and robust proof in support of our thesis) and subsequent hysteresis-like criteria as a relevant intersection. We denominate the current increment sources “hidden currents” and confirmed the idea in the experiment below (in the experiment above, referring to current or charge events not observable in Cycle 1 and underlying forms that became accessible for Cycle 2, for a while longer than that expected if the sources of the response were systematic or random errors or purely kinetically derived responses). The polymer self-organization was significant, and the higher negative current magnitude and hysteresis-like criteria observation in Cycle 2 was critical in an abstract sense to establish the integrity of the polymer structure and to allow unavailable (available) structures and thus corresponding currents to flow (“free” or “saved” currents from the perspective in Cycle 1). We additionally consider Cycle 1 to be critical because, in an abstract sense, it sets the “tower of structural relations” from which the remaining cycles branch in some sort (not shown; initially in an arc-like manner from the perspective of the tower generated by Cycle 1), a pattern that can provide information about the exchange process following the maximally doped state of the polymer and the representative switch potential. We conclude that the crossing of Cycle 2

with 1 was an action exhibition from *poly-7*, which by (and coupled with) the direct relation to the maximum current and reducing potential intersection point (hysteresis-like criteria) observations relative to the rest of the cycles, constitutes evidence of the polymer's structural integrity, both actions which we categorize as “primitive” (this attribute to *poly-7* is strengthened with the analyses from other observations presented below).

These types of nascent families of “smart polymers” and “smart materials” are typically envisioned as single active polymer units mounted on a “bare” substrate and an electrolyte fluid medium under monomer-free conditions. In cyclic experiments, we believe that the most primitive types of hysteresis-like criteria (i.e., the earliest occurrences) are related to the instigations and the applied bias (i.e., feed, voltage, stimuli, stress, or tension). It is important to note that this notion of control or manipulation and subsequent response can be problematic for reasons of bias. Structural changes in polymer chain segments “characterize” the instigations. Some correspond to action exhibitions. Others must correspond to action inhibitions (e.g., non-inferential, non-derivable, and non-expressive actions that do not lead to observable responses and are difficult to define and not explored after this mention), and more. It is crucial to understand that some of these action exhibitions or expressive actions may not be immediately realized in our EW or experimental windows but may also occur (e.g., “inner actions”, exchange of distinguished representatives such as the most principally distinguished representatives, and more). Additional or corresponding responses correspond to quantitative or qualitative I/V characteristics represented by a current or voltage change in the following cycle (e.g., higher current of Cycle 2 than Cycle 1). Each current/voltage relation depends on the path of the feed or applied bias trajectory (i.e., applied potential, sweep direction) and the feedback path and waveform (polymer responses). Thus, *poly-7* and conducting polymers generate some “finite” isomorphic or homomorphic responses for configurations of the same (or similar) representation or value of some parameter product state spaces (e.g., parameter values at the prescribed or quantified moment, or each current/potential point, number of intersections in a specific region across all cycles or process, the peak potential of distinguished representatives, and more). In addition, the same (or similar) representations, which may have some assigned value through a valuation process, are observed in the current/voltage relation across different cycles. These “finite” responses may be realized or materialize while “locally moving frames” finalize their trajectories and interactions, and the excited or non-interacting states diffuse and dissipate as the actions generated propagate in space. The moment of these actions (by the process or from the polymer evolution) from a starting generation or action response to an end generative response and coinciding effect perspective must not transcend instantaneous or equivalent to the time of the applied potential for any or another cycle. For many exhibited responses, the same points (or region or events) at a subsequent Cycle may have covered residual states from

previous cycles, whose curves relative to the Cycle curve or past cycles carried some values (e.g., relations, equivalences). In addition, we consider points that led to or linked to the intersections we used in our analysis (“hysteresis-like criteria” events) based on their importance or distinguishability relative to the response of the polymer in similar conditions. Under special *considerations* (optimal criteria, representative settings, relative “freedom” or low imposition of control) such as the ones we provided for *poly-6* and *poly-7* during these experiments, the polymers can evolve a generational or organized response to the settings, as we can see in the historically ordered trajectory of the current responses of some cycles (see l) and m) above), while keeping an appropriate level of flexibility as seen by the characteristics of the described events (see below also), which allows us to consider the observed intersections as valid and representative of related phenomena. We did not arbitrarily choose intersections or coerce the system to the observed output. At the same time, we ascribed observations a value through an anthropomorphization process (which serves to make the occurrences relatable or the overall scheme potentially applicable as a process, as we argue), which, as derived from first-principle-based processes and observations under scientific principles, makes the approach rigorous.

Several intersections or different phenomena (see below) were observed close to the positive potential switching points, corresponding to structural paths at higher or lower tension, through which (doping \leftrightarrow undoping) yielded a response from *poly-7*. This paragraph will analyze the anodic potential switching point observations, whereas the zero potential switching point region is explored below. At the anodic scan switching potential (+ 1.3 V), the trace of the scans accumulated or bunched together (see a) and b) at $\sim + 1.3$ V regions), indicating a turbulent or rapid return to the undoped state. This accumulation is not extraordinary given that the polymer chains go from a more fluid state due to high quasiparticle density at higher doping (lower effective masses) to a state in which a gradient of exchanges introduces electrons and counteranions over time, while the structure is increasingly undoped (as it goes from positive to zero potential). However, it is interesting to note that several intersections can be observed following the switch, which was not an occurrence in the forward path as shown in l) above. Even with intersections through these turbulent points after switching potential (from + 1.3 V to $\sim + 1.0$ V in the + 1.3 V \rightarrow 0 V reverse sweeps), causal effects on the global state (e.g., local extremum points or their derivatives) or the polymers (I/V responses) were more difficult to predict or understand. Thus, we later refer to these observations and intersections with their seeming effect or relation to global and long-term effects or changes, which we observe and can ascertain from the system's high stability (*poly-7*). This intersection behavior contrasts the hysteresis-like criteria intersection events we considered in regions further from switching potential points, which were not only distinguished (i.e., unique and thus not picked arbitrarily) but were related closer or linked to

more immediate or short-term effects. About these different events close to the switching potentials (i.e., bunched curves, turbulent or rapid change, and intersected curves) and their assigned effect relations ("long-term" stability), we could argue that it is also in these gradient paths of higher density (e.g., p-doped states following the anodic sweep switching potential) and which are recurrent over cycles where (when) the complexity of the paths and intersections, implicitly or inertially underlies the structural forms (and responsiveness) exhibited by *poly-7*, and which become types of generational traits (e.g., the redox potential of the most principally distinguished representatives as well as other features) coupled to higher-order events secondary to the evolving responses (e.g., topologies) with the natural evolution of the applied bias (feed) and response (feedback). It is important to note that generational changes (as we investigate or cycle the material through the process) become generational not from recurrence exclusively but from recurrence over structural changes (which itself leads to "generations" or "inherited traits"). In conclusion, intersections close to maximum potential and current points can be linked to "long-term" changes.

The point of highest fluidity of the polymer is when *poly-7* is maximally doped, expressive and colorful (~ dark blue), as seen in l) above. In this region, there were no intersections except for Cycle 25, which crosses Cycle 24 (see Scheme 2.7.1.5.2, l), bottom of the curve), as mentioned above. Additionally, at the bottom of the return sweep (see d) and n)), an event (~ + 0.65 V) corresponding to the only intersection or hysteresis-like criteria type of event in the region (except for Cycle 1 and Cycle 2) was consistent with the previous observation of Cycle 25 crossing Cycle 24 in the same cycle, as was just mentioned at the beginning of this paragraph.

We attribute a direct relationship between these two hysteresis-like criteria events in Cycle 25 ↔ Cycle 24 to the quasi-chaotic event in Cycle 26, mainly because of the isopotential of the crossing in Cycle 25 (~ + 0.65 V) and the inflection point (~ 50 mV; see g)) leading the quasi-chaotic behavior in Cycle 26 (see vertical discontinuity in c)), and because it was the cycle immediately following the two different Cycle 25 ↔ Cycle 24 critical crossings (see d) and n) vs. b), g), and h)), the two factors together demonstrating that the argument does not correspond to an arbitrary relational choice or a stochastic event.

Although not exactly where the polymer becomes neutral, a relative lack of fluidity has been suggested at the lowest negative current of the cathodic sweep (reverse sweep, p-doping) versus the highest positive current of the anodic sweep (forward sweep, p-doping). These two regions illustrate the polymer transformations of doping/ undoping (expanding/contracting). As a doped basin with maximum electron current, some maximum tension with respect to the previous thread images, such as state structures or residues ("polymeric forms" and given by Cycle 25 crossing Cycle 24 in the fluid area) on both the doped and undoped, generated some internal action ("inner action") that is critically related through some paths, as observed in Cycle 26.

The "inner action" is critical because it reveals the boundary conditions or limits of the polymer. This assertion is evidenced by the subsequent generation of chaotic events in Cycle 26 and supported by other arguments previously explored. The presence of two critical crossings between Cycle 25 and Cycle 24, followed by quasi-chaotic behavior in Cycle 26, is particularly significant in our later arguments that declare *poly-7* a "smart material" because, in this way, the polymer exhibits negative feedback (self-organization) in a stronger sense than the typical one (given that the last occurrence of "memory-like" hysteresis events in Cycle 26 was related to Cycle 1), that shows the significant degree of self-organization that the polymer exhibited until the last memory event while maintaining its modular and functional character (given the polymer was very expressive/dark at that point) before the experiment was halted.

Initially, we characterized the events in Cycle 26 as action exhibitions that showed instability in *poly-7*. The cycle was described by sequential vertical and horizontal transitions with no potential or current changes, followed by a series of 19 self-crossing events (memory-like hysteresis events) on the reverse sweep before the end of the experiment. Overall, Cycle 26 represented a counterclockwise (CCW) response from *poly-7*, which was in the opposite direction of standard CV. The response or action exhibition from *poly-7* in Cycle 26 is depicted in c), g), and h) above. We could have labeled Cycle 26 as "unstable" from our frame of reference, but this approach is biased. Rather, from an *intensional* perspective, *poly-7* completed Cycle 26 with a greater dopant concentration (positive current value at + 0 V) and ~ 80 % of remaining current/charge based on cathodic current magnitude. Both state representation descriptions and parameters could be related to a more sophisticated response from the polymer. We strongly validated this by demonstrating the hysteresis-like criteria and relation between Cycle 1 and Cycle 26 at isopotential points, indicating some form of equivalence. Moreover, as shown in j) above, current discontinuity signals with triangular or V-shaped structures relative to the cycle potential were reproducibly exhibited across various cycle numbers (e.g., Cycles 21, 22, 24), all confined within the same potential window region. We have not developed an advanced explanation for these observations beyond their recurrence, suggesting that either (i) some variety or adaptive metastable or stable states are generated as local minima (e.g., charge basins) or (ii) structural interconversion related to mass transport or mobility constraints occur as the polymers close. When clustered, as shown in m), some of the wells are reminiscent of neural network burst responses (see figures in reference)⁵² of a primitive form.

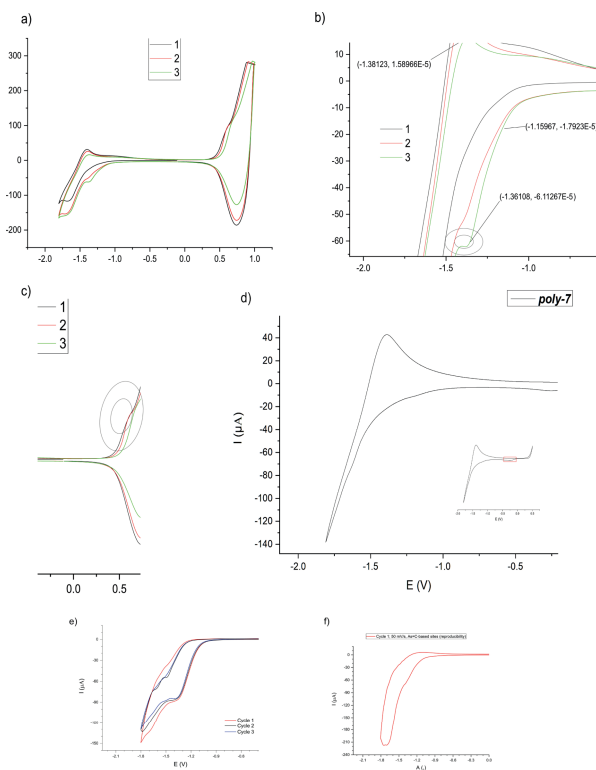
By experimental evidence (see Scheme 2.7.1.5.2), we have shown that events, as well as potentially "recurrent (or convergent) effects", can underlie either "long-term stability" or the presumed "short-term effects" characterized by "instability" or transformations (e.g., via some evolution, extensive exchange, and more). "Concurrent events" are those attributed to parallel events

that could occur by *(a)* assuming the use of many interconnected systems of *poly-7* in a concerted manner or *(b)* the rapid execution of the process (thus considering 2-cycle effects as “parallel”); however, the notion of short-term “sequential events” seems to precisely fit our setting better, without making any assumptions. For instance, *i)* hysteresis-like criteria events \leftrightarrow “short-term effects” were observed in Cycle 24 \leftrightarrow Cycle 25 \rightarrow Cycle 26 (as we just argued), or Cycle 1 \rightarrow Cycle 2 (as argued before). More examples can be found in the experiments below. Recurrent or convergent effects are those attributed to sequential or decoupled events that converged or recurred after many cycles. For example, *poly-7* exhibited high organization near the distinguished $E_{\text{peak, anodic}}$ representative, as well as $E_{\text{max I, anodic}}$ & $E_{\text{max I, cathodic}}$ regions, based on the responses in Cycle 1 $\rightarrow \rightarrow \rightarrow$ Cycle 26 and Cycle 1 $\rightarrow \rightarrow \rightarrow$ Cycle 25, respectively. These cases were coupled with many hysteresis-like criteria occurrences in the reverse sweep near the positive potential switch point. Thus, hysteresis-like criteria \leftrightarrow “long-term” effect relationships were observed via recurrence, as well as via the presence of a “long-term” recurrent connection between Cycle 1 \rightarrow Cycle 26, epitomized by the + 0.97 V isopotential point occurrence (i.e., matching the inflection point of the sharp curve in Cycle 1 and the last memory-like hysteresis event in Cycle 26). In summary, we identified critical hysteresis-like criteria points and correlated them to track both long-term stability and short-term effects from specific sequences of events, potentially cascading into a “singular” type of event.

In addition to the consequences of extremum points in the graphs, as described in some detail, their derivatives are also essential (e.g., E_{ox} onset \sim HOMO molecular orbital \sim valence band level polymer).

In general, as we could observe, an accumulation of intersections can precede either a leveling (“long-term” effects) or drastic structural changes as responses (“short-term” effects), such as that observed from *poly-7* in Cycle 26, which can be considered as something expressive inferred from the vibrant relationships we encountered for the polymer response both in the short-term (Cycle 24 \leftrightarrow 25 \rightarrow Cycle 26) and long-term (Cycle 1 \leftrightarrow Cycle 26) via the hysteresis-like criteria process.

The last set of distinguished experiments representative of the functional and modular character of *poly-7* is shown below in Scheme 2.7.1.5.3 (Experiments 4: a) to c); Experiment 5: d)), where we measured monomer-free electrochemical responses throughout the EW while keeping other parameters equivalent. This experiment lent credence to our argument that previous instances that had characterized the response during Cycle 26 as “unstable” were biased, because *poly-7* instead exhibited a sophisticated response in this space, where charge was atypically exchanged as the polymer was repeatedly n-doped and p-doped.



Scheme 2.7.1.5.3. (Unpublished). a) *poly-7* (FTO) film, full EW potentiodynamic response ($[-0.25 \text{ V} \rightarrow -1.8 \text{ V} \rightarrow +1.0 \text{ V} \rightarrow -0.25 \text{ V}]_3$), monomer-free fluids, 3 cycles (**Experiment 4**). b) Reductive scan region; note the appearance of the distinguished representative feature at -1.36 V (green curve, gray ring). c) b) Oxidative scan region; see the disappearance of the distinguished feature (green curve shoulder disappearance, gray ring). The signals indicated that *poly-7* presented action exhibitions, which we explain as a transformation between a “redox polymer” state representation (“minor polymeric form”) during the initial reductive cycling and a “conducting polymer” state representation during the oxidative cycling (“major polymeric form”). More details are given in the main text. d) One cycle (i.e., Cycle 1) experiment (**Experiment 5**) starting from a p-doped oxidative potential (an insignificant amount of O_2 was present in the Cycle, which we show in the inset and relate it directly to the later response as an instigation); graphs demonstrated pointed features like that from before (Scheme 2.7.1.5.2. i)). In the n-doped state, the representative settings we used were equivalent to those mentioned above (except for the starting position and NC). The nice shape of the curve on the anodic sweep (positive current) and the larger current magnitude relative to Cycle 1 above confirmed the reversibility of $\text{As}=\text{C}$. e) Experiment with *poly-7* (SR: 50 mV/s) for 3 Cycles in a limited EW window. Interestingly, the signals showed great robustness, and the current magnitude only changed slightly from -145 to $-133 \mu\text{A}$ over 3 cycles, which is interesting, in conjunction with the emergent occurrence in Cycle 2 (see return sweep, Cycle 2). We cannot easily explain the observation but attribute these events to charges or sources made available via folding/unfolding processes. f) Experiment using another sample of *poly-7* (SR: 50 mV/s) in a confined EW and reduced SR (50 mV/s), successfully showing the $\text{As}=\text{C}$ -based signals with a massive charge level of $-220 \mu\text{A}$.

In Scheme 2.7.1.5.3 a), b), and c), charge redistribution occurred via an exchange between polymeric forms, as evidenced by the current increase in the reduction current on the reductive side, from time-limited decreases in the reduction current on the oxidative side. However, some of the current may have been partially acquired from hidden (latent) states. These occurrences were present for oxidation levels on the reductive side and oxidation levels on the oxidative side that had maintained a similar current. They also contained reduction levels on the reductive and oxidative sides with similar potential levels of their currents. Very critically, the maximum current level or magnitude on the positive side of the anodic (p-doping) cycles also increased from Cycle 1 to Cycle 3 (compare positive Y-axis values for Cycle 3 vs. Cycle 2 and Cycle 1), which may indicate some equilibrium or stability in a closed (safe) manner. At the same time, an exchange of correspondence (\sim the equivalent current level magnitude between them) appeared to have generated a concomitant change characterized by the movement of the energy gap level and most principally distinguished representatives. By “redox polymer” state representation, we refer to the clear presence of As=C group motifs (and corresponding sites) based on their characteristic response and represented by a potential close to that of the monomer **7** here with current levels of polymers and obviously from a polymer sample, which we denote as indicative of a type of localization on the As=C groups and coupled sites. Specific to Scheme 2.7.1.5.3 a) to c), the charges have been made available through exchange processes. For many reasons (see below), this is the most unique and sophisticated response we have observed (due to its subtle complexity) among the action exhibitions of *poly-7*.

(1) The action showed some closed form (cyclical and internal) associated with the maintenance of charge and structure. That is, expressed function decoupling occurred, due to the two polymeric forms, while preserving unchanged critical external and internal current or voltage positions unchanged (local and global limits), which evaluated to:

(1a) modular characteristics.

(1b) high stability by minimizing losses through an internal trade-off between its redox polymer and conducting polymer nature (“negative feedback”), as seen from the increased reduction currents despite constant chemical reversibility (irreversibility) in the return sweep,

(1c) increased isolation of As=C group motifs and associated sites, with electron charge localization on the corresponding polymeric sites.

(2) The polymers were involved in a modular inhibitory mechanism (“modular negative feedback”):

- (2a) during cycling, when the negative charge magnitude of the anodic polymeric form was lower than that of the cathodic polymeric form, then,
- (2b) the reductive side (followed by the oxidative side) became more positive for both redox potentials of *crucial representatives* (i.e., the redox potential onsets in both sides),
- (2c) this event was simultaneous (in the sense that the two following events followed from a triggering event when the reduction current maxima exchanged value), accompanied (in each case) by the appearance of the most principally distinguished redox representative on the reductive side (i.e., As=C-containing sites and frames that were lifted “from the shadows” on one side only) and the disappearance of the most principally distinguished representative on the oxidative side.
- (3) The polymers exhibited positive feedback as well as expressivity forms, such as electrochromic phenomena, as the potential was increased (more abstractly, the response is consistent with “positive feedback” based on the expected increase in quasiparticle density or conductivity as the potential is increased, which in turn leads to a higher color intensity of the material).
- (4) The arsaalkene-based ***poly-7*** was confirmed to be a redox polymer and a conducting polymer by electrochemical experiments, computational results, and spectroscopic results. These methods also supported the emergent phenomena and modularity of the polymer as previously defined in the chapter based on principles from the literature.

A polymer system with modular behavior expresses these sequential, coupled, and decoupled processes. More precisely, functionally decoupled, distinctive structures perform specific tasks toward some perpendicular goals (tasks; functions), which then become similar goals (tasks; functions), while some crucial characteristics and properties of the polymers remain unchanged.

This combination of features corresponds to *global structural stability*. For example, unchanged $\{E [- + I_{\text{red max}}], E + [I_{\text{ox max}}]\}$, where the blue color indicates the very slight change in the positive current maximum in the reductive side (homomorphism) at an isopotential point, while a fundamentally unchanged positive current maximum at an isopotential point in the oxidative side (isomorphism), characterized ***poly-7*** in Experiment 4 (Scheme 2.7.1.5.3 a) through c), as discussed).

The results obtained in our experiments clearly and consistently demonstrate (also categorically) the existence of hidden structures that play a modular role in the system. We observed non-trivial current-based or potential-based features in all four quadrants of the voltammograms, all observed in

experiments with transparent liquid solutions with no monomer support on the [electrode, polymer] surface. These features demonstrated the masking of the p-doped oxidation potential (in an isogenic manner with the revealing of the distinguished representative on the n-doped reduction potential) and non-trivial increases in the electric current/charge maximum magnitude for the p-doped states during the anodic cycle, as previously noted and shown in Scheme 2.7.1.5.3 a), which corresponds to quadrant 1 of the voltammogram. In Scheme 2.7.1.5.2 b), the increased reduction potential and current in cycle 2 compared to cycle 1 in monomer-free liquid solutions were unexpected (quadrant 4). The reversibly increased oxidation current in the n-doped region is seen in Scheme 2.7.1.5.3. d) (quadrant 2), a result we attribute to structural recovery from oxygen instigation (see Scheme 2.7.1.5.3 d), inset, red rectangle, indicating an “insignificant” amount of O₂ in the sample), which was evidenced on the forward sweep with the pointed and sharp peak feature.

Finally, the revelation of the most principally distinguished representative (Scheme 2.7.1.5.3. a) and b)) of the n-doped reduction potential coupled with the non-trivial increases in the reduction current for > 1 cycle (quadrant 3), a completion in terms of the overall current/potential responses of *poly-7*. These observations suggest that the polymers were structurally robust and more stable than our narrow EW criteria originally predicted for electrochromic observations. We attribute the observations to modular shapes or structures in *poly-7* that operated in a hidden or shadowed manner, manifesting as hidden current sources.

All the polymer observations were obtained while keeping most variables and parameters constant and all crucial variables and parameters constant while opening observational paths (through the “EW window”).

First, in a slightly more oxidizing “empty” space, where electrochromism was exploited. Second, in reducing spaces representative of the polymeric forms and within boundaries. The second revealed the crucial role of the As=C group motifs as distinguishable representatives with intrinsic functionality and augmented modular actions (As=C) expressed as action exhibitions or vital observations.

Internally, *poly-7* is in correspondence and equivalence with both polymeric forms and the present global polymer state in one of its abstract states, otherwise present in some virtual, inactive, or hidden form during the electrochromic and p-doping cycling processes.

The experiments with *poly-7* presented here demonstrate the importance of considering structural complexity through representative settings and optimal criteria. Our approach, which emphasizes the importance of “appropriateness” for introducing changes and is tightly coupled to boundary conditions, provides valuable and usable information that can be applied in practical contexts. The concepts of optimal criteria, representative settings, and hysteresis-like criteria, which are crucial to our analysis, will increasingly be recognized (if not already, given the wide interdisciplinary range of relevant applications of

"smart materials" and "behavior") as essential tools for understanding complex systems. We are excited about the potential applications of our approach, although humbled by the complexity of the systems and the application challenges that "smart materials" present. We hope that this work will inspire further research and contribute to a better understanding of complex systems. We have also presented our conceptualization and definition of "smart materials" as materials that meet specific criteria, and we hope that our presentation has been logically coherent and without logical flaws. By introducing concepts such as modularity, "reactive systems", emergence, and "adaptive systems" (negative feedback ~ self-organization) to a chemistry and materials chemistry (and general) audience, we believe we have highlighted their importance and will inspire further research and contribute to a better understanding of complex systems. We hope these concepts will help better define the criteria for "smart materials" or their successful exemplification when presented, particularly in the areas of organic (main group) and molecular inorganic chemistry, and will aid in their design and development.

From a primitive computational perspective, the observations were not trivial. That is, even if one creates a computer or processor type (simultaneously functional and modular) or a story (program), the structural and functional frameworks (e.g., stacks, modules) underlying it must follow delicate and vital balances in order for complex processes (e.g., process management, concurrency) to operate error-free.⁵³

This computational perspective from different angles (perspectives) then puts the stress (tension) on the system *poly-7* and its response to the applied bias or feed, which we can interpret in some primitive computational form. Internally, some of these angles (perspectives) and stresses were manifested as follows.

(I) Mutually exclusive:

While the increase in chemical reversibility was not instantiated (and not previously generated relative to the previous Cycle), the cathodic current magnitude increased drastically on the reduction side; or (and); while the chemical reversibility/current magnitude remained almost constant on the oxidation Cycle_(n-1), cathodic current magnitude increased on the reduction Cycle_(n).

(II) Diametrically opposite, which we believe to be stronger than *simply opposite*, in a sequentially "coupled-like" and sequentially "safe-like"⁵⁴ sense (see reference point on "safety"):

At the point of intersection of the negative current magnitudes (in reductive and oxidative positions), or the point of intersection, the most principally distinguished representatives globally, anodic (+/positive) and cathodic (-/negative) current potential points ($E_{1, \text{peak, red}}$ vs. $E_{1, \text{peak, ox}}$), were exchanged in terms of "visibility" (e.g., abstraction layer), while at the same time "hiding" the opposite, most principally distinguished representative (i.e., the appearance and disappearance of the shoulder on diametrically opposite

sides). Thus, the diametrically opposite process occurred sequentially but equivalently (Cycle 3 → Appearance distinguished representative on the reductive side for As=C group motif states and relevant sites → [Reduction potential current magnitude]_{Cycle 3} ≈ [Oxidation potential current magnitude]_{Cycle 2} → Disappearance distinguished representative on the oxidative side for conducting polymer states → [Oxidation potential current magnitude]_{Cycle 3} < [Reduction potential current magnitude]_{Cycle 3}, demonstrating the highly modular nature of the polymer. The presence of "emergent phenomena" can only explain such a non-trivial observation, which we believe can ultimately be used to categorically declare *poly-7* a "smart material". Based on all the evidence, the overall general analysis comes to the same conclusion.

(III) Parallel:

Potential and current "savings" relative to "cycle images" (i.e., some crucial characteristics, including potential and current features or points, remained unchanged through individual cycles, implying that they can be "saved" or used "to save"). Also, potential and current differences, relative to current changes, in cycles and decoupled from secondary functions. For example, (i) potential position vs. slightly limited current relations (~ "isogenies") in the positive current of the reduction side; (i) "isomorphisms" in the positive current level vs. potential points relation, on the oxidation side). Therefore, (i) the potential position remained constant, while the current (+) decreased only slightly on the reduction side; (ii) constant current (+) levels at the constant potential on the oxidation side.

The observed increases in current in response to potential cycling, where the corresponding reactive behavior of a trivial system would have been a decrease in current, suggests the existence of inner negative feedback mechanisms and responses in the polymer system. This self-organizing mechanism helps prevent the polymer from deviating from its set point in the presence of incoming actions and at least provides evidence for negative feedback. These instances demonstrate the potential "programmatic nature" and "behavioral" properties of the polymer system in response to an independent external cycle generated by *poly-7*.

We hope this abstraction is accurate and, in some sense, non-trivial to some transformable functions for some types of logical operations, here expressed semantically as they occurred primitively. That is, as changes of a) positive electric currents, b) negative electric currents, c) electric current magnitudes, d) positive electric potential positions, e) negative electric potential positions, some of which express relations decoupled from each other. Informally, as morphisms from a set or categorical point of view.

From a chemical and physical point of view, these were also non-trivial observations. For example, sequential charge transfer exchanges (e.g., controlled charge increments on the reductive side; controlled charge decrements

on the oxidative side) were not necessary events, given the high chemical irreversibility of the return sweep on the reductive side, coupled with the maintenance of a structural current maximum point in the positive current of the anodic scan, and others. The non-triviality was further supported by decoupling the processes from some characteristic features (i.e., current levels as just mentioned and unchanged potentials for others), demonstrating the modular nature of the polymers. For being “sensitive”, the As=C (and P=C) group motifs exhibited remarkable kinetic and thermodynamic stability as a result of performing all the experiments according to the concept of representative settings and optimal criteria, from which abstractions were generated that did not necessarily have to be recurring themes throughout our experimental sequences.

Modular characteristics (**1a**) can be seen, by distinguishing features (shoulder appearance; forward cathodic sweep; green curve, Cycle 3) exchange (shoulder disappearance; forward anodic sweep; green curve, Cycle 3), furthered in non-triviality by the fact that there was not only an exchange of distinguishing features but also a decoupled reversal of one of them (the shoulder disappearance, in the opposite direction relative to the initial charge exchange). We can compare different cycles simply by setting identities of the same initial states and abstracting from different timings in series or parallel correspondences. The non-triviality was further supported below by spectro-electrochemical observations of major polymeric form interconversions when *poly-7* (or *poly-6*) was anodically cycled, where the representative As=C (or P=C) group motif and related sites did not participate in the events. Lastly, DFT revealed much more orbital delocalization for ground and excited states in the fluorene-thienyl backbone, with no interaction from As=C, while maintaining virtual orbital support in a localized and disconnected fashion at the same plotted isosurface value.

In summary, as *poly-7* was cycled, a charge (and structure exchange) was established between the n-doped and p-doped states, representing an equilibrium type of exchange between some polymeric forms that can be better described as state representations equivalent to redox polymer and conducting polymer.

Overall, from both an internal perspective (the polymer) and external perspective (the observer), the observed responses were highly illustrative of emergent phenomena, all of which were shown to be appropriately coupled to optimal criteria, representative settings, and hysteresis-like criteria from which relevant sequences of responses or expressive interactions were found as action exhibitions. These were representative of *poly-7*, their stimuli-responsive nature, principally linked in a modular manner to the presence of the distinguished As=C group motifs, possessing high visibility and representability through σ - and π -interconnected low coordination, coherent NCIs, as well as other nuclear and electronic characteristics (features) of augmented nature.

2.7.2. Spectroelectrochemistry. Chronoamperometry. Electrochromism results.

The polymer films exhibited vivid color changes with applied potential. Electrochromic materials change optical properties in response to applied electric input differences. This behavior has been observed in phosphorus materials, such as phospholes.⁵⁵ There is an immense interest in developing electrochromic responses with dual, triad-like, or more identifiable functions, ascribing multifunctional (e.g., modular) character to the identity of a single compound. With advanced technology, electronic devices will become more present. Intelligent screens, windows, filters, glass, metals, and electrodes can be used for transmission or functional processes.

Applications of As=C and P=C as group motifs, consider them from contextual functional development of electronics and computing-related fields as we showed previously, where expressiveness, and “atypical” nature are supported in protected environments, or form the basis for new paradigmatic modifications to operating systems or logical systems using the augmented character of heavier atoms such as phosphorus (P) and arsenic (As). A sustainable approach is also crucial (ref. discusses phosphorus scarcity).⁵⁶ The relevant chemistry of electrochromism is based on two domains: inorganic (WO₃) and organic materials.⁵⁷ The second domain uses organic or organic hybrid systems, among which conjugated molecules or compounds are central and used in electronic screens. The electropolymerization of thiophene or fluorene with widely-used organic functional groups or substituents (e.g., 9-O, alkyl, and more) has been described.⁵⁸ The existence of polymer chains, characterized as the polymer species, was found through spectroelectrochemical experiments via the presence of isosbestic points at ~ 509 nm (*poly-6*) and ~ 496 nm (*poly-7*) as the potential was cycled. This result indicated that a “single” polymer species was interconverted between “two” primary polymeric forms, characterized as the neutral and oxidized states (doped or undoped and insulating or conducting). A secondary signature of single polymer species interconversion was the smooth and reversible transformation of the λ_{max} on the optical spectrum as the potential was cycled. During the oxidative cycle, the λ_{max} was blue-shifted, which related to the higher excitation energy of an increasingly oxidized polymer. Interestingly, a higher-energy transition (reminiscent of monomeric signals), corresponding to one of the π - π^* transitions, was maintained from the neutral to the maximally doped state, as seen in the 350-400 nm region. This signal represents a contribution of redox polymer form states to the configuration of the polymers, where the As=C or P=C preserved double bonding character as confirmed by the signals (and a plethora of methods) but are localized and orthogonal to orbitals involved in the electrochromic response, regarding the observable electrochemical window. The signal confirmed the abovementioned experimental observations obtained during electrochemical experiments. Introducing electrons or holes in the

polymers may induce aromatic or quinoid stabilization by rendering the As=C sites (e.g., fulvenoid frame) redox polymers through charge localization, while maintaining the double bond character specified by the response similar to the monomers. The spectroelectrochemical experiments in pure and transparent electrolyte fluid solutions confirmed the electrochromic properties of the polymers (see Fig. 2.7.3.1). Further studies using chronoamperometry coupled with optical spectroscopy demonstrated the stability of *poly-7*. A stable signal with no loss of optical response was maintained for 10 cycles and > 7 minutes of cycling, at which point the experiment was stopped. The stability of the doped species was confirmed as previously mentioned (Fig. 2.6.3). Most doped systems 1) bleach rapidly due to diffusion of the counterions in solution, which recombine the neutral and oxidized states, or 2) produce a nonuniform optical density distribution via voltage switching⁵⁹. For the polymers here, the optically dense states spanned the entire polymer surface.

The homogeneous nature of the thin films, which looked slightly semicrystalline yet slightly flexible, as observed during the peeling and mechanical manipulation of thick films with tweezers in the glovebox, was a compelling reason for future investigations. Relevant studies were presented previously (e.g., Raman, e-chem), and more are presented in later sections (e.g., SEM, XPS). Measurements and estimations typical of electrochromic materials were done with a *poly-7* sample using representative settings. A contrast ratio of 58 % was found at 600 nm. Standard samples yielded redox charge densities of $\sim 1.8 \text{ mC} \times \text{cm}^{-2}$, volumetric charges of $\sim 90000 \text{ mC} \times \text{cm}^{-3}$, and volumetric capacitances of $\sim 75000 \text{ mF} \times \text{cm}^{-3}$ from films with a known number of scans (NC) and estimated thickness from SEM measures. These values are within the same order of magnitude as other organic electrochromic materials.⁶⁰

2.7.3. TD-DFT cationic Systems. Experimental UV-Vis-NIR spectroelectrochemical. Conducting polymer coupling to minor redox polymer form. Conclusions on experimental evidence. Relations to previous sections. Example of application.

The spectroelectrochemistry and modeled cationic systems pointed at resonant modes of polaronic (cationic) and bipolaronic (dicationic) nature. As previously discussed, they confirmed the nature of the “redox polymer” states based on the UV-Vis-NIR spectral response at lower wavelengths, coupled to the appearance of absorption bands at ~ 600 and > 1100 nm corresponding to the “typical” conducting polymer response, as the polymers were doped (complementary to the purely electrochemical results, which supported the idea). We calculated the absorption profiles of full-atom, Mes*-containing, monocationic (charge: +1; total spin S: 1/2) oligo-6 and oligo-7 up to the tetramer units, and dicationic systems (charge: +2; total spin S: 0, 1) up to the dimers.

These calculations helped us elucidate the effect of charge localization on the system's absorption, asymmetry, and spin density (described before). Charge transport in conducting polymers is explained by invoking the formation of discrete quasiparticles known as polarons (monocations) and bipolarons (dications) as characterized by their optical signatures via absorption spectroscopy or other spectroscopic techniques. A polaron or bipolaron can be described as a localized or nonlocalized electron (hole) response within a continuum of atoms; the quasiparticle can also be considered a phonon-dressed unpaired electron cloud. Their resonant regions lie within the NIR-IR regions for conducting polymers. As bound quasiparticles, they exhibit discrete features, such as resonant frequency and periodicity during measurements, charge density, and discretized energy levels, which relate to the optical event outcomes from spectroelectrochemistry. We should understand that the concepts of polaron, bipolaron (more generally, solitons)⁶¹, have a vast stretch. They are essential in quasiparticle models explaining: **(1)** charge transport of conjugated polymer species especially conducting polymers; **(2)** condensed matter physics, and theoretical physics (e.g., it is believed that long-range polaron-polaron or bipolaron-bipolaron interactions follow a Bose-Einstein condensate behavior, which has been hypothesized).⁶² A relation between bipolarons and superconductivity (high-temperature superconductivity of some copper-containing compounds⁶³) was found. Therefore, understanding the role of polaron and bipolaron in terms of charged states while considering the inclusion of P=C or As=C group motifs is a relevant problem now that we have introduced this family of materials.⁶⁴ We studied systems with varying degrees and orders of charged species relative to other chains. We obtained a mixture of two distributions (minor: redox polymer, major: conducting polymer) on the spectroelectrochemical spectra, which possessed characteristic extremum points of high importance, such as the monomer resemblance, which confirmed the redox polymer distribution and the isosbestic point and (multi)polaronic bands which correspond to the conducting polymer distribution, the latter epitomized by the expressive electrochromic response. We observed one clear isosbestic point from the single transformation limit representative of polymer distribution exchange between two transitions of “the polymer” (doped polymer \leftrightarrow undoped polymer), illustrative of one major species (i.e., the drawn polymer structure).

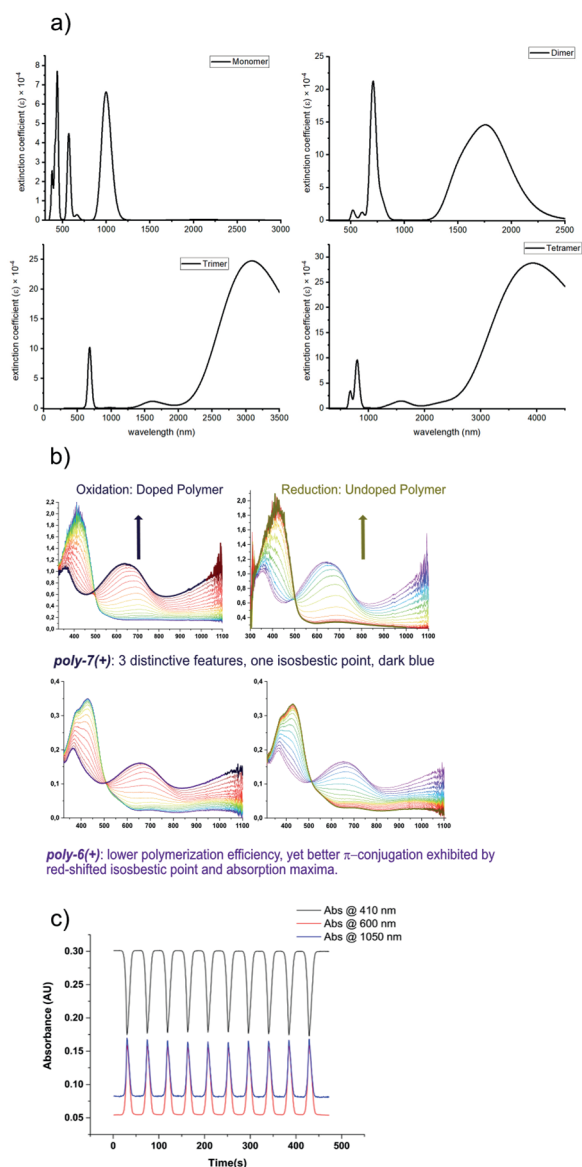


Fig. 2.7.3.1. a) Calculated absorption transitions for *poly-7* oligomeric cations. b) Spectroelectrochemistry of *poly-6* and *poly-7* was performed using representative settings above. Hence spectra were measured while cycling between 0 V \leftrightarrow + 1.3 V at an SR of 0.1 Vs⁻¹. The left and right arrows indicate UV-Vis-NIR transition spectra changes as oxidation and reduction were applied. c) Chronoamperometry of *poly-7* demonstrated robust electrochromic reversibility at various absorption wavelengths for ~ 8 minutes, using representative settings.

In the complexity of the bulk, some segments may locally hold a charge of + m. In contrast, others may comprise a charge of + n, where n > m. Also, some segments may “non-locally” hold a charge that can only be described as a

partial charge because the boundaries of the chain segments are (co)bordered by different statistical particles with different soliton character (e.g., neutral redox polymer, polaron, bipolaron), where the ground and excited states may be non-trivial. For all these relevant cases, results from the spectroelectrochemical analysis may parallel summations or products, and they could also be close to the theoretical responses based on many different TD-DFT models. We found qualitative agreements between cationic and dicationic states, indistinguishable from the experimental results based on different models using different basis sets. In this case, as can be seen by the absorbances of the tetramer models, the relative size visible bands in green and NIR regions agreed well with the spectroelectrochemical results, which, however, were limited by the wavelength cutoff. The monomeric and dimeric systems agreed well qualitatively regarding the high energy absorption bands. The transitions, characterized by bands below 400 nm in the visible region, were kept between the two states of the polymeric system. While they matched the monomeric and dimeric models as mentioned, this does not imply the presence of 1-to-2-unit segments. The observation only indicates that 1-2 repeating units are sufficient to describe the most prominent electronic transitions, which relate to the redox polymer abstraction by the link between monomer and polymer responses in redox polymer systems (i.e., redox polymer response \sim monomer response). In conclusion, we must remember that the TD-DFT data validated the redox polymer explanation when linked to the spectroelectrochemical results, given the non-innocent redox and augmented roles of As=C and P=C group motifs as initially observed electrochemically and later on XPS. Continuing with the low wavelength observations below 400 nm, the spectroelectrochemical data of *poly-6* or *poly-7* coupled to the TD-DFT results above indicated that various excitations characterize the polymer forms as combinations of polaronic, bipolaronic, or others arising from redox polymer localization or propagated character between “ground” (electrons in the undoped polymer) and “excited” (electrons in the doped polymer, in quasiparticle-derived states) state forms more typical of conducting polymers, nicely validating the results and conclusions from electrochemistry experiments above. Crucially, we potentially and indirectly observed some complex or “hidden” sequence path representations, as were alluded to in the mechanism, via some event connectivity from which the corresponding electrical charge completion or complement (i.e., charge not accounted, following the charge exchange process, between two polymeric states), is in correspondence to some of the irreversible currents from structure representations that avoided the quasi-irreversible breaking-down path (i.e., the path which would have led to oxidation and reduction potential redox event current decrements over increasing cycles for “representative experiments” 3 and 4 above). This consideration more descriptively corresponds to partial charge transfer events between the “redox polymer state” and “conducting polymer state”, which in some abstract sense is related to the n-doped and p-doped states, respectively.

We understand that identifying a projection for which the amount of irreversible current is minimized, coupled with the aforementioned optimal criteria projection, corresponds to the interesting case of equivalence differences between two sets of optimal criteria projections. This occurrence could correspond to a solution path or completion to any arbitrary optimization problem in various areas, including but not limited to network optimization, machine learning or AI, circuit design, finance, and more. The reason is that the modulated complexity variations or differences in the behavior expressed by the material in the cycles can correspond to the general themes or abstractions that characterize the material across different conditions (e.g., experiments 1-5). We are also inclined to find “slight changes” in representative settings while maintaining the optimal criteria or to dynamically generate one that generatively leads to a modulated path (either from growth differences after a variation or minor changes in monomer-free study conditions) that balances the current exchange process (e.g., in “experiment 4” in the previous section) directly (right-to-left), or via chemically reversible observable states (left-to-right), in order to evaluate the modular or hidden complexity of the polymer and reflect it to some previously unknown factor in the application of choice, among other approaches. Meanwhile, observing how polymeric form structures change generationally over time, either with the same optimal criteria (while continuously imposing a “slight change” in the dynamic optimal setting case) or with a differentiated and overlapping one, allows one to make strong connections. Naturally, some low-bound or high-bound equivalence conditions or constraint sets can be realized concerning some instances using the non-potentiodynamic methods, corresponding to some interactive or faster occurrence than that achievable in the potentiodynamic case, which can be used to study phenomena (e.g., an arbitrary process carried out in a batch process vs. an interactive session, a “faster process”, and more).

The last paragraph was illustrative of some arbitrary approaches that justify or “shed some light”, in some sense, regarding the utility of the concepts and arguments we introduced above for cherishing the electropolymerization process and phosphorus-containing or arsenic-containing polymers in unusual bonding situations, such as reactive, atypical, sophisticated, and expressive *poly-7*.

2.7.4. Outlook for P=C and As=C polymer systems.

Future studies with *poly-6* or *poly-7* could focus on characterizing more profound photophysical properties of the doped polymers. Encapsulating the films under strictly inert conditions or measuring other properties, such as electrical conductivity, can be fascinating. Variation of the optimal criteria, representative settings, hysteresis-like criteria concept, and using electropolymerization in solving or finding options for solutions to problems could be an exciting area of future work (i.e., finding applications for the concept).

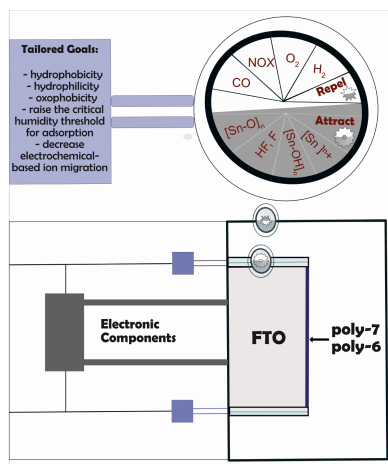


Fig. 2.7.3.1. A schematic diagram illustrating a general device-like configuration for the stability of *poly-6* and *poly-7*, applicable to other atmospherically sensitive polymers, is shown. The lower figure shows a simple setup with an external covering that must repel water and oxygen at the air-device interface (double-star). The inner object consists of a sample of polymer deposited on FTO, with secondary protective layers at the FTO-device lateral interface (cogwheel) that minimize FTO ion leaching toward the polymer by attracting the species while preventing water, oxygen, or other external contaminants from entering. The two blue-gray square elements on the left drive the electronics of the secondary protective layers that act as purifiers/stabilizers/attractors. The top left schematic lists the possible goals or functions such a process must accomplish (e.g., increase the low limit at which moisture enters the system). The top right wheel shows various chemicals that can be targeted to minimize exposure of the sensitive polymers compared to the double-star or cogwheel from the diagram below. Finally, one wonders whether the tailored control of quasiparticle states in conducting polymers can be used to realize emergent quantum mechanical phenomena on the large or long-time scale or range, where coupled electrochromic materials in their quasiparticle doped states generate quantum mechanical coherence (i.e., entanglement).

2.8. Additional characterization and analysis of P=C and As=C π -conjugated polymers. EDX, ERDA, Raman, and XPS spectroscopy.

2.8.1. EDX spectroscopy of monomers and polymers.

Confirmation of polymer atomic composition via elemental analysis.

The presence of arsenic and phosphorus in all polymer samples was corroborated by energy dispersive x-ray spectroscopy (EDX) analysis. Samples of *poly-6*, *poly-7*, monomers **5** and **7** as powders, and bare FTO films, confirmed

their compositions. The monomers and bare films were used as control experiments to confirm the technique's suitability and validate the results obtained for *poly-6* and *poly-7*. All samples were measured fresh; after preparation, they were thoroughly cleaned with pure DCM and acetonitrile, dried, and then transferred under argon to a cleanroom facility. Sample preparation consisted of stabilization of the samples in a carbon conductive tape and sputtering with Au or Pd ions to increase conductivity and avoid localized charging, reducing thermal damage or decomposition of the samples.

The elemental composition of the samples in EDX corresponds to the characteristic X-ray emission energy profile of the atoms in the samples. The concentration of P/S and As/S atoms in *poly-6* and *poly-7* occurred at an approximate 1:2 ratio, with the relative differences caused by overlapping signals. The results are shown in Fig. 2.8.1.1. Additionally, the presence of arsenic and bromine in samples of **5**, as well as of the respective characteristic atoms in the other control experiments, confirmed the suitability of EDX as an elemental analysis tool from which qualitative and relatively accurate quantitative results were obtained. Some relevant observations related to quantitative stoichiometries of arsenic, sulfur, and phosphorus in the polymer samples confirm their atomic composition in an elemental analysis fashion.

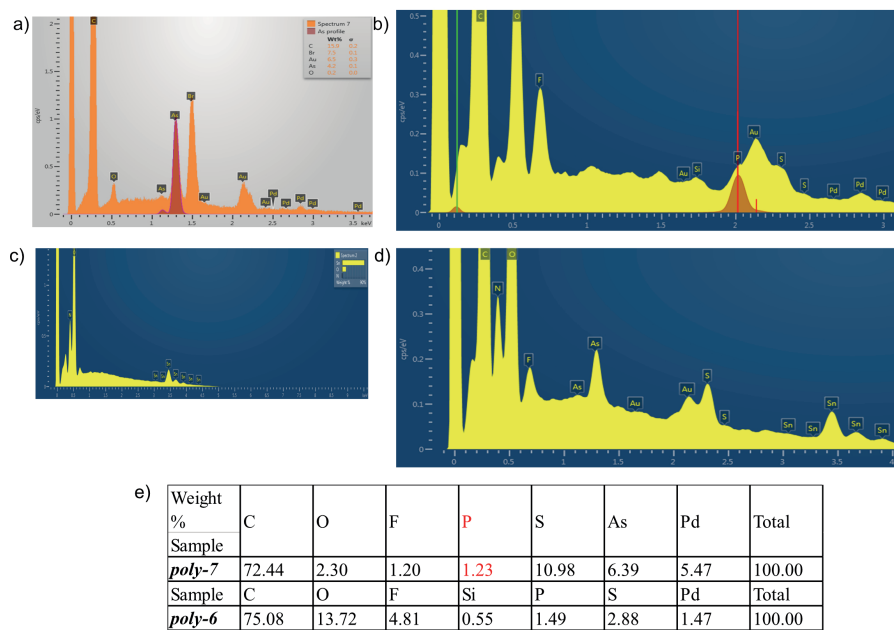


Fig. 2.8.1.1. Characteristic EDX spectra of **5**, *poly-6*, *poly-7*,

The presence of oxygen, silicon, fluorine, and tin in *poly-6* and *poly-7* is caused by the FTO glass substrate; part of the fluorine concentration, as well as the presence of phosphorus in *poly-7*, are connected to the presence of

remaining electrolyte counterions (i.e., $[\text{PF}_6^-]$) in the polymer films, which is a typical and expected result in conducting polymer synthesis. The oxygen content in monomer samples, for example, for a powder sample of **5** as seen in a) above, occurred at a normalized atomic concentration of only 0.2 %, which is exceedingly low and at the limit of detection of the detection system.

2.8.2. ERDA spectroscopy. Confirmation of low oxygen content on the polymeric surface.

Elastic recoil detection analysis (ERDA) with heavy 36 MeV ^{127}I projectile ions was used to characterize samples because of its ability to accurately detect lighter elements as a function of sample depth, via atom recoil and time of flight differences of different detection channels, after calibration with a known sample. We found that little to no oxygen content was present in a sample of *poly-6*, thereby confirming the stability of the polymers, with little to no ketone or other oxygen species formed on the surface of the materials. Since the surfaces of the polymer samples are the most sensitive areas for oxygen contamination, the bulk can be assumed to be pure, up to the limit given by FTO oxygen ion leaching. Logically, only the surfaces of the samples are relevant in our experiments, as shown schematically in Fig. 2.8.2.1. So, the 65° tilt angle versus the detector, which enhances recoil collection, also introduces non-trivial kinematic contributions over time and side reactions with the substrate. This limitation results from the lower density of organic materials compared to bulk metallic samples. Other reasons are related to the high sensitivity of organic samples compared to most inorganic materials.

In short, due to the above factors and the high beam energies, only after a finite amount of time and a discrete amount of incoming iodine flux has hit the sample (relative to an arbitrary t_1 and a thickness d) do the detected atoms correspond to recoils from the iodine \leftrightarrow sample interaction process. Recoiled atoms or detected sample species in subsequent measurements correspond to a later flux, described by a time t_2 , and contain more significant amounts of recoiled atoms from the FTO substrate and side reactions with the FTO. The FTO contains oxygen atoms; therefore, oxygen over the period $\Delta(t_2 - t_1)$ affected the resulting measurements. As a result, only the initial time frame of the measurements (t_0 to t_1) was found to be accurate.

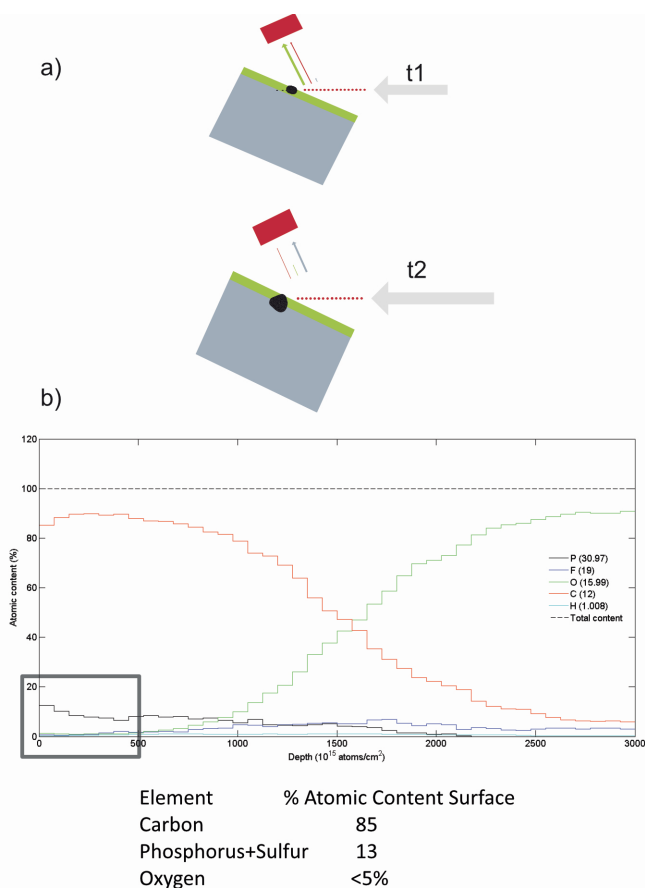


Fig. 2.8.2.1. (Unpublished). a) Pictorial representation of experimental measurement process at two times t_1 and t_2 ($t_2 > t_1$) within the same experiment. The measurement until t_1 is accurate in connection with the authentic sample composition and corresponds to the sample's surface. In contrast, the measurement until t_2 (later) is not representative and contains a contribution of surface, experiment-induced defects or impurities, or substrate atoms. Red dots: incoming iodine beams, grey rectangle: FTO substrate, green rectangle: poly-6 sample, red rectangle: detector, green vector: recoil atoms from the sample, red vector: scattered iodine atoms, grey vector: FTO substrate recoil atoms and experiment induced impurities. b) Calibrated atomic composition for ERDA measurements and depth profiling analyses of poly-6 sample. The relevant region corresponded to the sample surface early, where the gray rectangle is located. Notably, the % atomic content on the sample surface, < 5 % (shown in the table), established oxygen contents of around 3-5 % for polymer samples. Due to uncertainty, the percentage does not add up to 100 %; thus, oxygen content at 5 % is an upper bound.

After energy calibration with known samples as standards and depth profiling calculations, we calculated the oxygen concentrations of a *poly-6* sample to be ~ 3-5 %, which is exceptionally low (upper bounds, based on uncertainty)

yet far from the detection limit given by ERDA (0.1 to 1 %). This result provided direct evidence of the stability and purity of the polymer films.

2.8.3. Raman Spectroscopy of *poly-6*. Analysis of enhanced Raman resonance signals due to optical gap-to-laser matching and typically low fluorescence of the E=C group motifs. Characterization of nanostructure and order through signature Raman features.

It is well-known that Raman scattering occurs relative to coordinated molecular or atomic motions, for example, upon excitation of a sample with a laser source of an arbitrary wavelength at a given power. This event is followed by energy exchange with the sample, simultaneous energy emission, and energy dispersion. The energy difference between the absorbed and emitted states is primarily observed as events in the vibrational and rotational regions. These correspond to Raman modes that induce changes in the polarizability of the molecular or polymeric ensemble.⁶⁵ Raman spectroscopy is used in studying π -conjugated and conducting polymers, as it can provide information on the microstructure and macrostructure of the studied samples. For example, Raman spectroscopy has routinely been used to study polythiophene and polyfluorene polymers and fluorene-thiophene copolymers; information on the morphological, electronic, and bonding characteristics of the samples has been extracted.⁶⁶ Raman spectroscopy has been categorized as a tool or a probe for gauging the degree of π -delocalization (or conjugation) in conjugated materials.⁶⁷

Raman spectroscopy experiments of thin films of *poly-6* and **6** were performed (FTO substrate). Due to the spectrum's complexity for **6**, we will focus only on our measurements of *poly-6*, representing the presented polymers. The polymers were excited with laser excitation sources of two wavelengths (i.e., 633 and 785 nm). A 633 nm wavelength of excitation was chosen after initial probing. Low power ($4\ \mu\text{W} \approx 1.3 \times 10^{13}$ photons/s) inputs were used for the 633 nm measurements to avoid damaging the film. An enhanced response characterized the obtained spectrum for *poly-6*, as shown in Fig. 2.8.3.1 a). The corresponding peak assignments are shown in b). The enhancement relates to a fortuitous “on-resonance” or “Resonance Raman” condition of the experiments, which we had not predicted. The enhanced Raman resonances are related to processes caused by electronic excitation bands in the 633 nm wavelength region with respect to the scattered particles and energies, further explored below.

A study on the Resonance Raman (from now on “RR”) response of 9H-fluorene radical cations found that a 625 nm incoming pulse induced RR enhancement.⁶⁸ This is relevant since the polymers here are partially doped even in the neutral state, as discussed before (trapped charged states and $[\text{PF}_6]^-$

counteranions). The RR enhancement of the signals in a) and b) can be easily deduced based on their high Raman intensity, resolution, and sharpness. RR is a well-known phenomenon, and various examples can be found.⁶⁹ We validated our supposition by comparison with the measured optical gap of *poly-6*, which occurs at 647 nm (1.92 eV), for a sample of similar characteristics. Lastly, as can be seen in Fig. 2.8.3.1 c), we confirmed the RR enhancement argument by showing the absence of a similar, multiple-sharp line, enhanced response, when exciting *poly-6* at 785 nm, for which the energy of the laser pulses is not high enough to induce RR enhancement. In agreement with our Raman study of **6** (characterized by over 25 signals, a high fluorescent background, and low count numbers for some modes), the complexity of the Raman spectrum for the obtained cationic radical fluorene system was high. The issue concerns the number of regular harmonic and combination bands crowding the small molecule spectra.

For *poly-6*, a “stable” and “simple” Raman response was acquired. The presence of some envelope and broad bands may link to polymer modes with no enhancement or quasiparticle modes. As the 633 nm laser field resonated with an electronic excitation, we measured RRs with contribution effects from electronically excited states to the resulting signals. The electronic excitation has a valence, conduction band, and “intraband gap” contribution. Thus, it contains contributions of a) neutral and b) charged state transitions. The long duration of the experiment led to a more considerable proportion of contributions from b) compared to a). Electronic excitations are extremely fast (fs to ps), over the thickness of uniform and homogeneous *poly-6*, a symmetrized, ordered, and thus averaged distribution of polymer states and hence charged state contributions, are well-behaved, which relates to the number of signals. A highly symmetrized or averaged distribution of monomer **6** does not cherish from self-organization or polymeric form order propagation; hence the spectrum is more complex than for *poly-6* and regular fluorene small molecules, which can be advantageous in applications where many transitions are desired. The advantage results from sums of two different symmetry populations vs. symmetrical fluorene, which we know are caused by Mes*-induced asymmetry. The complexity of the small molecule was caused by asymmetry and the high number of polarized and polarizable bonding situations such as [C=C], [P=C], [C_(Ar)-S_(Ar)-C_(Ar)]. As said previously, the 647 nm (1.92 eV) optical onset of standard *poly-6* was 0.04 eV (3.86 kJ × mol⁻¹; 0.92 kcal × mol⁻¹) below from the incoming radiation source, therefore **highly** in resonance. In QM operator-driven derivations of RR effects (non-linear), an equation directly relates the mass of atoms involved in RR to the frequency of RR.⁶⁵ Thus, in P=C and As=C modes, RR signals at higher wavenumbers and higher intensity were expected (> ~ 800-1200 cm⁻¹), which explains signals at ~ 2021 cm⁻¹, a higher energy Raman region involving unsaturated bonding situations, such as X=X, X=R (X: heteroatom, carbon, R: heteroatom, carbon). The non-linear RR relation opposes the empirical relation ascribed to normal Raman

modes, where vibrational resonances of heavier atoms typically have lower wavenumbers.

In a polymeric sample containing mixed sp^2 (unsaturated) and sp^3 (saturated) interactions, laser Raman sources preferentially excite modes from sp^2 states.⁷⁰ It was proposed that sharper signals characterize highly organized structures, such as those containing semicrystalline segments or domains and some organized glassy states, compared to more amorphous states.⁷¹

Due to the significant computational effort required to calculate Raman eigenvalues for large model systems, especially with large *tert*-butyl groups and heavy atoms (P, As, S), our DFT support is limited. We have focused on finding literature support for the argumentation.⁶⁶ The computational Raman spectroscopy models we used included static or dynamic Raman calculations of the monomeric and dimeric **6** and **7** units in their fully converged geometries as calculated by DFT (B3LYP//6-311g**); 633 nm excitation wavelength for dynamic Raman). The calculated dynamic Raman spectra of **6** and **6-dimer** were compared. The main observations follow.

a) The absence of 800-1200 cm^{-1} signals, which typically comprise a large $[E=C]$ character in small molecules, in this case, $P=C$, supporting the RR enhancements in our experiments for bonding modes involving heavier atoms since we observed enhancement for these signals in our experimental spectra for *poly-6*,

b) The disappearance of $> 3000\text{ cm}^{-1}$ signals from monomer (**6**) to dimer (**6-dimer**). The $> 3000\text{ cm}^{-1}$ signals correspond to CH_3 *tert*-butyl group stretches and external thiophene C-H proton stretches. Therefore, we confirmed the suitability of Raman spectroscopy for sp^2 modes and that the simplification of the spectra was due to mode coupling involving non-external modes, in addition to any non-linear order parameter expressions and quasiparticle binding expressions as opposed to the crowded or obfuscated spectra of the monomers.

c) The calculated spectra displayed no Raman activity in the 1800-2500 cm^{-1} ‘silent region’, disagreeing with our experimentally obtained spectra. Assuming model or DFT model failures, then it gives credence to RR enhancement arguments.

The signal at $\sim 1350\text{ cm}^{-1}$ was observed prominently in the calculated **6-dimer** spectrum ($\sim 1320\text{ cm}^{-1}$). Its contributions gave credence to the argument that strong coupling leads to a small number of signals in the resulting spectra and the disappearance of external modes. Argument b) above nicely demonstrated the rapid changes of Raman responses from “single molecules” (remembering a monomer already possesses several fragments) to “larger oligomers” and absence in the polymeric motifs. We wonder if there is any exciting relation between Raman active fragments in *poly-6* (or *poly-7*) and the region between 1800 to 2800 cm^{-1} where no significant Raman vibrations of biological nature can be seen except for triple-bond vibrations, which may be

abstracted or projected towards applications (e.g., contrasting or “stealthy” agents, for imaging or drug delivery).

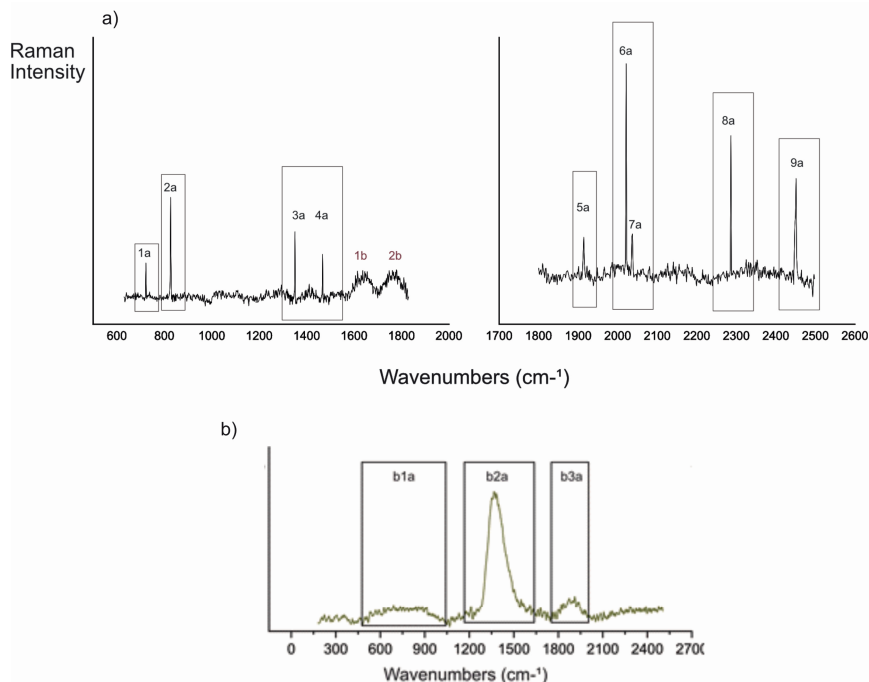


Fig. 2.8.3.1. (Unpublished). a) Raman spectra of the *poly-6* film (FTO substrate, $E_{\text{exc}} = 633$ nm, input power = 4 μW) 600-1800 cm^{-1} . Region 1, Left: carbon-rich organic electronic materials. Region 2, Right: biological, ‘silent region’ of the spectrum; activation of this region also occurs in low-dimensional or layered nanomaterials. b) Raman spectra of *poly-6* film (FTO substrate, $E_{\text{exc}} = 785$ nm, input power = 700 μW) from 200-2500 cm^{-1} . Two to three broad events are relevant, particularly b2a at 1350 cm^{-1} . This spectrum compares well to other polyfluorene Raman spectra samples. Therefore, it indirectly confirmed that the broad signals in the 633 nm related not to enhancement signals but non-enhanced signals and that their enhanced RR nature resulted in highly simplified spectra with sharp lines. Background and baseline noise (FTO and fluorescence) were removed on Origin 19 using first and second derivative zero points after finding 16 anchoring points automatically and manually, and a Savitzky-Golay smoothing process with a polynomial of degree 2 and a 0.05 threshold was used after which visual inspection confirmed the spectra were unchanged.

The measured spectra correspond to nominally neutral samples of *poly-6*, which hold a small degree of doping based on trapped electrolyte units. However, small doping causes significant local and global changes, as is well-known. We conclude that the sharp signals we observed between 800 and 1000 cm^{-1} , which are not prominent in our computational model, correspond to polymeric modes with $E=C$ ($P=C$ experimentally) contributions. Other features of effective conjugation with a substantial degree of π -character were high mode coupling and high order. A few signals with strikingly similar

intensities that resembled doublets may support the picture of the high persistence of specific patterns through regularity via the presence of organic semicrystalline domains on FTO glass substrates.⁷⁰ High-frequency features $> 2000\text{ cm}^{-1}$ in the Raman spectrum of carbon materials have invoked second-order scattering events such as overtones,⁷² and other double-resonance effects. For example, two-phonon coupling, with the material's electronic structure, has been observed in some graphene samples,⁷³ which supports our arguments that the polymers cherished the introduction of nanostructure (see next paragraph). Very sharp peaks with an FWHM of $\sim 3\text{-}5\text{ cm}^{-1}$ were obtained for all nine enhanced peaks. This sharpness is highly unusual in thin films of conjugated or conducting polymers such as polyfluorene, based on our literature search results (algorithm-driven) and observations of Raman spectra in the reviewed papers. Raman resonances in the “biological silent region” of $1800\text{-}2500\text{ cm}^{-1}$ have been difficult to find for fluorene or thiophene polymers. This could be attributed to the high polymer fluorescence of polyfluorene and polythiophene, which hinders their solid-state study via standard (or RR) Raman experiments. Conversely, the highly non-fluorescent or quenching nature of *poly-6* deobfuscated the spectrum, indirectly operationalizing the distinguished P=C group motif as an incredibly powerful Tailored Access Operator {TAO} for the exaltation of RR-enhanced modes while keeping the noise away in otherwise highly turbulent absorbing regions due to the high fluorescence yields of the typical fluorene-based samples. There is great interest in finding materials with Raman resonances in the “biological silent region” region.⁷⁴

While reading about hexagonal crystalline materials such as graphite and graphene, we found that these compounds exhibit resonances in the Raman silent region of the spectrum that correspond to distinct types of non-trivial combinations of phonon-involved interactions. For example, a signal called “2D”,⁷³ which is located close to this region and is involved in a two-phonon-electron-structure interaction, could, in our case, be related to the inductive coupling of several (bi)polaronic modes along a polymer chain or segment, or across polymer chains or segments. A study with single-walled carbon nanotubes found that several of the observed resonances have an FWHM lower bound limit of 3 cm^{-1} , which is precisely the width of the narrowest resonances we observed as a generalized pattern.⁷⁵

From an electronic perspective, the sharp and intense signals (Lorentzian-like) indicate a degree of structural order or extensive π -conjugation in the polymer motifs. In the study of octyl-substituted oligomers and polyfluorenes, for example, more intense and sharper Raman resonances were associated with forming so-called “ β -phases” (semicrystalline or ‘planar’ domains as proposed in the cited reference).⁷⁶

- 1) Increased induced tacticity due to the large size and asymmetry of the Mes* substituent (these aid in stabilizing cationic traps).
- 2) The high cis/trans isomerization barrier for Mes* substituents in (Mes*)-E=C fragments.
- 3) Stabilization via NCIs, and London dispersion forces.
- 4) Other intermolecular effects from the Mes* phenyl rings (see section 3.4 for small molecule crystal view of long-range Mes* phenyl group, stack order). Electrolyte coupling, via appropriately segmented paths, versus isopotential-structural regions may localize essential electrolyte islands that, through the generation of fluidic forms, induct semi-crystalline states in oppositional regions.

Scheme 2.8.3.1. The formation of semicrystalline segments, or “planar paths”, may be related to polymers exhibiting various aggregated effects.⁷⁷

Additionally, **poly-6** exhibited two prominent features in the 1300-1600 cm^{-1} region, which has been used to describe the most relevant Raman modes in polyfluorene (e.g., five signals) and polythiophene derivatives (seven signals)⁷⁸. Only two peaks were observed in this region (1350, 1467 cm^{-1}).

We now consider these Raman spectral observations to arise due to primarily symmetrized and extended modes due to large delocalization (or extensive, long-range localization) based on effective conjugation and polymeric motif order (see Scheme 2.8.3.1).⁷⁹ Consequently, regarding their Raman activity, our data signals at polymeric states with a simplified and organized response, which is sustained by the previous postulates and arguments made from various literature studies and from elementary principles, which we hope were accurately interpreted. The observations here may reveal effective and extensive oscillative paths, which are indicative of

- i) electron-phonon coupling,⁸⁰ which is simultaneously accompanied by,
- ii) photoexcitation processes, following the resonant laser excitation at 633 nm, stabilized by trapped counteranions $[\text{PF}_6]^-$ (not to be confused with “trap states”).

- iii) some signals are related to polaronic states, given the photoinduced and resonant condition of the Raman signals and the electroactive nature of **poly-6**.⁸¹

- iv) more tentatively, the presence of signals in the ‘silent region’ (i.e., 1800 to 2800 cm^{-1}) generally arises from the presence of coupled $[\text{R}'\text{-E}=\text{C}-(\text{C}=\text{C})\text{-R}]$ modes, with significant contributions from the unsaturated E=C coupling modes; some features in the higher energy silent region, may arise from doubly-resonant or overtone-type of interactions, with a quasiparticle-like character like in graphene.

In these materials, well-resolved outputs could arise from manifestations of correlated interactions across a significant distance or energy ranges coupled by contributions from the induced, electronically excited states.⁸²

The P=C and As=C representatives (i.e., **poly-6** and **poly-7**) exhibited distinguishable features in some “stealthy” manner, e.g., by “hiding” their form from the EW in the electrochemistry experiments (see Section 2.7.1.5) and resonating in the “biologically silent region” of the Raman spectrum, illustrating their functional or modular character or characteristics across two different applications from similar abstraction perspectives. That is, in the π -conjugated polymer and conductive polymer population, the “atypical” E=C-containing materials (i.e., “low representativity”) exhibited decoupled or differing responses (i.e., accurately reflected based on first principles and thus “representable” or presenting “high representability”) that contrasted with the “typical” responses of widely used materials (i.e., “high representativity”), such as some of the responses observed via the electrochemical experiments based upon particular sequences of operations (e.g., three-cycle experiment response from **poly-7** in Section 2.7.1.5, and more) and here based on the presence of enhanced signals and resonances in the “biologically silent region” based on the RR enhancements, in both instances acquired via the utilization of representative settings and optimal criteria (i.e., utilizing non-emissive backbones to potentiate Raman resolution, low power or photon flux laser sources, as well as the optical gap to laser source matching resonance condition), which strengthens our concept.

2.8.4. XPS Spectroscopy. Confirmation of P=C and As=C group motifs in monomers and polymers. Not oxidized or defects but redox polymer states.

X-ray photoelectron spectroscopy (XPS) of **4** and **6** (P=C), **5** and **7** (As=C), as well as **poly-6** (P=C) and **poly-7** (As=C), was performed to probe the atomic composition and the different bonding environments present in the samples, which helped us successfully characterize the P=C and As=C units in the presented polymers. The XPS experiments were completed via survey and high-resolution measurements, which detected photoejected electrons from C 1s, Br 3d, P 2p, As 3d, and S 2p orbitals. Our analysis was based on standard procedures used to characterize the XPS response of materials, which considered several factors, caveats, variables, and parameters. In general, we had access to notable structural features and knowledge of the monomers and polymers, coupled with the high quality of our samples, whose relative comparability helped us to create an internal scale that we used to elucidate the bonding situations of interest (i.e., As=C and P=C). Fig. 2.8.4.1 shows high-resolution XPS spectra of C 1s and As 3d.

The carbon, bromine, and sulfur signals exhibited robust responses with no presence of additional peaks from defects. This quality is rare in the XPS of organic materials due to radiative effects, sample overcharging, impurities, “defects”, inelastically scattered electron background, or any other transport or exchange phenomena that interfere with the kinetic energy of the unbounded electron before it reaches the detector.

Notably, the As 3d signals of **5**, **7**, and *poly-7* indicated high robustness for the As=C samples, which was unexpected due to the high monomer reactivity of **7**, for example. The high-resolution P 2p orbital scans were characterized by two additional signals at higher binding energies of *poly-6*. Initially, we had assigned the middle signal to defects, redox processes, or oxidation ([Defect], [Oxidized], [**Redox polymer**] ~ 2 eV > [P=C] and ~ 1 eV > [As=C]) in the same spirit as we did for *poly-7*, which nicely helped us in our analysis, given the absence of phosphorus signals from the electrolyte to triangulate the middle signal in the [As=C] samples. We realized the signal paralleled the redox polymer state well, which signified it linked to “redox processes” (more details and arguments below). The “trapped” electrolyte ([PF₆]⁻ ~ 6 eV > [P=C]) occurred at approximately 136.54 eV. As the only prominent peak for all C 1s experiments, located at the precise position characterizing sp²-bonded carbon even before charge corrections were applied to later samples, low standard deviation before charge corrections or fitting, then C 1s served as an appropriate and ideal reference. For **4**, **6**, and *poly-6*, the binding energy (BE) of the phosphorus (P 2p) photoejected electrons in phosphalkene environments (P=C) was found to be 129.98 ± 0.08 eV ($n = 9$). For **5**, **7**, and *poly-7*, the binding energy (BE) of the arsenic (As 3d) photoejected electrons in arsaalkene environments was found to be 42.29 ± 0.05 eV ($n = 8$).

Phosphorus is more oxophilic than arsenic in some forms (e.g., Ph₃P vs. Ph₃As, phosphole vs. arsole, and more). The increased stability or lower reactivity towards oxygen, among other reasons, has motivated the study of arsenic-containing organic materials in recent years.⁸³ This difference results from orbital overlap and various other contributions. A transition metal contraction (“d-contraction”) effect over arsenic has also been suggested to contribute to the difference.⁸⁴ It is probable that dicoordinate arsaalkenes also exhibit decreased reactivity towards oxygen.

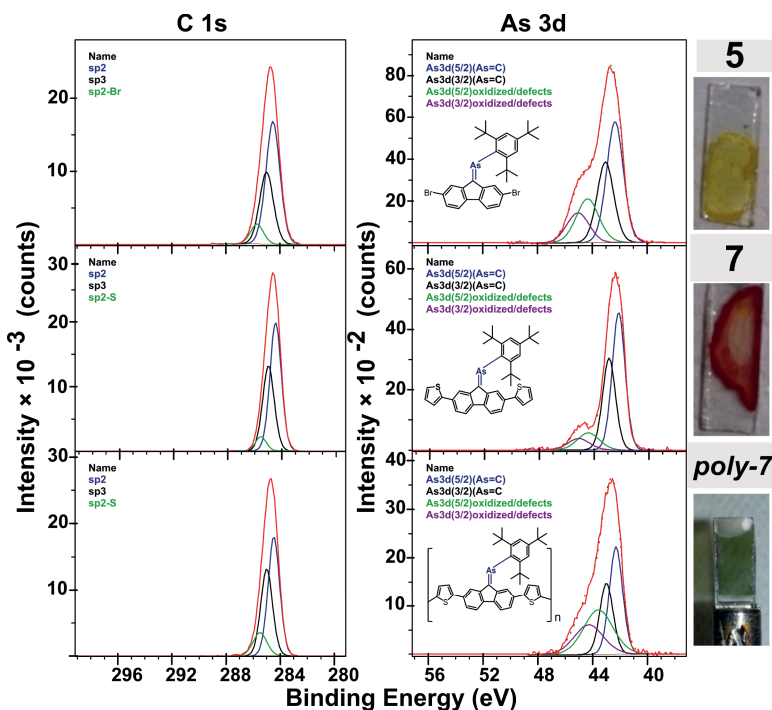


Fig. 2.8.4.1. Representative high-resolution XPS spectra of **5**, **7**, and *poly-7* samples, homogeneously deposited on FTO films in the case of the monomers, samples were drop-casted (DCM) inside the glovebox. Narrow signals were fitted with Lorentzian/Gaussian 70/30 contributions due to slight homogeneous broadening through dispersion. The fitted elements represent the stoichiometry of the compounds and polymers—pictures of monomers **5**, **7**, and polymer *poly-7* thin films.

Control experiments with monomer powder samples yielded extremely broad lines and offset signals, which differed dramatically from the thin films, even after artificial charge correction (Fig 2.8.4.2 a)). Inverse control experiments with older samples of *poly-6* (and *poly-7*) that had been exposed to atmospheric conditions for a longer time showed responses characterized by a more prominent peak for the "defects" or "redox events", corresponding to the middle signal of the P 2p orbital. Fig. 2.8.4.2 shows the representative spectra of the powder and atmospherically exposed samples. The fits were finalized and tested by minimizing residual standard deviations and model stability.

We have better understood the second set of XPS signals for *poly-7* and *poly-6*. Initially, it was technically unfair to refer to the intermediate P 2p events as "defects" or "oxidized" states (in the sense of "P=C decomposition") because of the overwhelming amount of evidence confirming the stability of the polymers and the redox polymer form results we discovered. Previous electrochemical and spectroelectrochemical experiments showed that the samples contained innate As=C and P=C states, some of which we could only assign to redox polymer configurations after transformation. Here, we

attribute the broader middle signal in the "older" (exposed) sample to increased redox polymer contributions based on structural changes after minimal oxygen exposure. This contention is supported by the polymers' high reactivity (or responsiveness), as exemplified previously via electrochromism and modular behavior.

Furthermore, this observation implies that the P=C units remained present in an abstract sense. However, regarding the redox events and restructuring processes accompanying polymer response and transformation, this does not mean that the intermediate signal event does not correspond to an "oxidized" species. Based on the overall evidence, it simply means that the intermediate signal cannot be confidently attributed to the "decomposition" of E=C samples (in this case, P=C) and that it corresponds to the redox polymer type of species we have previously observed.

Overall, we discovered **(1)** the beautiful As=C peaks in the presence of some minimal amount of oxygen in electrochemistry experiment five in Scheme 2.7.1.5.3 c), **(2)** unsupported (in the sense of the monomer-free conditions and other experimental constraints) current increases corresponding to As=C sites as seen in experiment four in Scheme 2. 7.1.5.3 b), **(3)** chronoamperometry events measuring no decomposition of signals directly related to the [As=C] sites for over 8 minutes of cycling, **(4)** a relatively stable [P=C]/[PF₆⁻] signal ratio in both XPS experiments below, all supporting the existence of modulating [E=C] group motifs or sites in conditions characterized as inviable if the polymers were not adaptable and responsive. Notably, **(5)** we did not observe any carbonyl ketone or oxidized carbon sites in the C 1s experiments by XPS (see the SI of the published article).

The E=C-based sites of *poly-6* and *poly-7* recursively modulated their structure while retaining their intrinsic and unique character and responded to oxygen instigations with the adaptations we observed experimentally and analyzed semantically. This event is accompanied by the conducting polymer ↔ redox polymer transformation. The potential access to "hidden currents" as the polymer folds/unfolds is indirectly related to the present analysis. In "decomposition" cases, we would have expected no signals corresponding to As=C or P=C, which was not the case.

The measured high-resolution XPS spectra (left) middle signals of (As 3d) P 2p represented redox polymer configuration contributions in *poly-7* and *poly-6*, where As=C and P=C were more localized in an abstract configuration relative to the conducting polymer/redox polymer initial distribution/equilibrium. The assignment realization is still consistent with what we have referred to in the published literature as XPS signals from "redox events", as we had not studied *poly-7* or *poly-6* in extended detail.

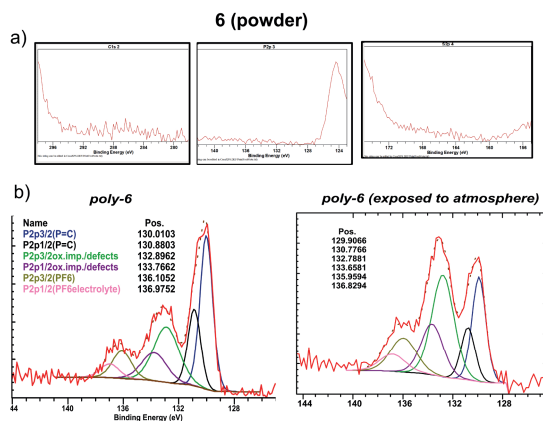


Fig. 2.8.4.2. a) XPS spectra; high-resolution narrow C1s, P2p, S2p orbitals; control experiment of **6** in powder form to validate our approach with thin films; powders or heterogeneous samples are typically not suitable for XPS measurements, as can be seen from the poor result caused by overcharging of the sample, and powder induced anisotropies. b) Inverse control experiment of samples of *poly-6*. The left sample was taken fresh, and the resulting spectrum is representative of P=C states (with the minor form, as well as the electrolyte). The right spectrum corresponds to *poly-6* exposed to the atmosphere for several hours, resulting in an increase in the intensity of the signals at 132.79-133.66 eV, corresponding to an increase in redox polymer states as well as possible secondary redox events (e.g., increased “redox events” such as “defects”). The highest binding energy signals correspond to phosphorus atoms from hexafluorophosphate, the electrolyte we used during the preparation processes, which is expected to remain trapped to maintain electroneutrality.

As=C group motif representation $\{[0] \leftrightarrow [\text{As}^{\delta-}=\text{C}^{\delta+}] \leftrightarrow [\text{As}^{\delta-}-\text{C}^{\delta+}] \leftrightarrow [\text{As}^{\delta+}=\text{C}^{\delta-}] \leftrightarrow [\text{As}^{\delta+}-\text{C}^{\delta-}] \leftrightarrow [0]\} \epsilon \{ \text{As}^{\delta+, -}=\text{C}^{\delta-, +} \leftrightarrow \text{As}^{\delta+, -}-\text{C}^{\delta-, +} \}$, (where ϵ represents some equivalence relation or representation of the minor redox polymer form as the major conducting polymer form was cycled) became isolated or unobservable in some sense. As *poly-7* (or *poly-6*) accepted electrons or holes, the process transformed some parts of the nuclear and electronic structure from "conducting polymer" to "redox polymer" (or vice versa). As the structural transformation progressed, a certain equilibrium was attained, leading to the manifestation of the redox polymer, as observed in the XPS experiment. This transformation occurs due to the higher energy of the incoming bias ("feed") in XPS compared to electrochemical experiments and the naturally higher oxygen levels in the older/exposed samples, coupled with the resulting transformations. However, the As=C group motifs assigned to the "redox polymer" state polymeric forms were not trivially representable by any arbitrary sequence but only by unique sequences of operations, as demonstrated by experiments four and five in the electrochemistry characterization, as shown in Section 2.7.1.5, Scheme 2.7.1.5.3 a) to c) and d), respectively.

These observations may be related to the statement about modularity in graph theory (or network science, that modularity measures in networks or graphs are “unable” to detect some communities based on size alone or that maximizing modularity leads to the appearance of communities in a network), in a way that can be used to design more effective modularity measures. This result may be of interest for further study of the topology and emergence of a polymer system.⁸⁵ In this case, some modularly decoupled and coupled structural associations have emerged within *poly-6* or *poly-7*, while certain parts of interconnectivity and feedback have remained obscured. Such approaches could explain our observations of “hidden sources” and “order” attributed to *poly-7* from more general or technical as well as potentially quantitative perspectives (e.g., see ref. for “network motif” approaches).⁸⁶

Beyond orbital contributions, structural packing, and order, the separated redox polymer fragments become an intricate and fundamental part of the polymeric states as they write/read from/to the conducting polymer sources. At the same time, modularity corresponds to the facilitation of decoupling or parallelization of functions through two “separated” but intrinsically connected states that possess some frames that become hidden over structural stacks.

2.9. Post-functionalization of *poly-6* with Au(I) ions.

2.9.1. Preparation procedures for the synthesis of **8** and *poly-8*.

We attempted the gold post-functionalization of monomers **6** and **7** and polymers *poly-6* and *poly-7* with the gold precursor (tht)-AuCl(I) (tht: tetrahydrothiophene) in homogeneous and heterogeneous processes, respectively. In liquid solution, we rationalized that the gold ion should coordinate linearly with the P or As atom of the monomers. In solid-liquid solutions (i.e., solid polymer surface + gold-ion precursor in solution), we rationalized gold ions could diffuse and be adsorbed through the polymers with retention of the E=C units via chemisorptive processes. The coordination mode of E=C motifs with gold is known to occur via a linear coordinative mode through the lone pair of electrons, which is the preferred bonding situation achieved by Au(I) transition metal complexes; concomitant displacement of the weakly coordinating [tht] ligands would occur, followed by their evaporation.

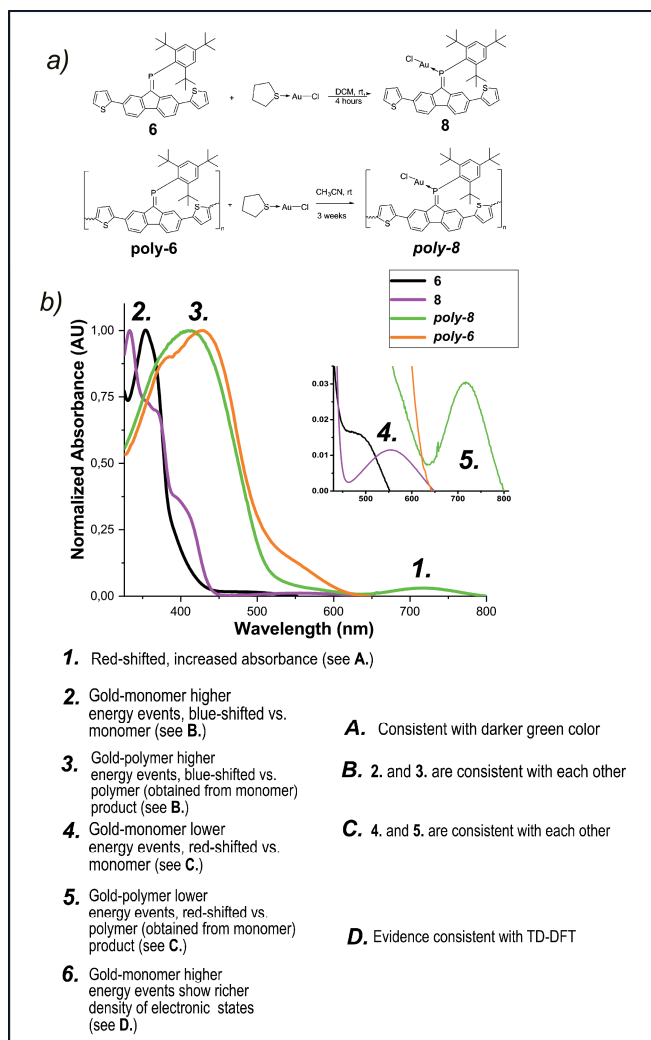
Thus, we set up appropriate reactions between polymer films and AuCl[tht] MeCN-saturated solutions for three weeks in the glovebox. The reaction was hypothesized to occur slowly via diffusion/adsorption.⁸⁷ No observable reactions were evident between the arsaalkenes **5**, **7**, or *poly-7*. MALDI and theoretical results suggested the minimal formation of the arsaalkene monomer product **9** only at a low rate. The lack of As reactivity in the monomers and polymers is surprising given the soft nature of its lone pair of electrons, and

the contraction of the 6s orbitals on Au(I), making them Lewis acid and π -acid species relatively suitable for bonding with As=C moieties.⁸⁸ The unreactive electron lone pairs caused the lack of reactivity (e.g., HOMO-3 density on DFT) or incompatibility of the experimental conditions.

2.9.2. Spectroscopy, DFT, TD-DFT characteristics of **8** and *poly-8*. Significant effects on the optical properties of the P=C materials upon gold incorporation.

In contrast, **6** and *poly-6* reacted smoothly with Au(I) ions. The dark-green product **8** was obtained and fully characterized.

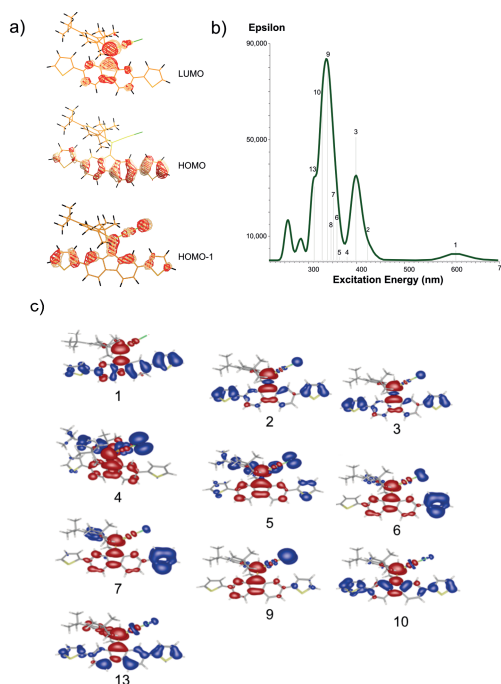
In the case of *poly-6*, successful gold coordination was evident by a substantial color change of the films toward darker green (as opposed to the yellow-light-green of the neutral polymer), yielding *poly-8*. The successful preparation of *poly-8* was confirmed via UV-Vis-NIR spectroscopy and other evidence (Scheme 2.9.2.1). One can consider the resulting polymer species a “metallopolymer”⁸⁹ or metal-containing polymer. These polymeric materials are interesting for several applications, including chemical sensors, catalysis, and memory devices.⁹⁰ It is interesting to note that arsaalkene systems could play a relevant role as sensing materials in chemical sensors, where irreversible reactivity between sensing elements and the analyte is undesirable. Below, a schematic analysis of the UV-Vis-NIR spectra of **6**, **8**, *poly-6*, and *poly-8* summarizes observations and differences, which confirmed the formation of *poly-8*. Notably, the changes of the resulting spectrum for *poly-8* and *poly-6* (light green and orange) occurred equivalently in terms of red shifts and blue shifts in the low-energy and high-energy regions (see inset, and spectra, respectively) concerning **8** and **6** (pink and black traces), providing convincing evidence for the smooth transformation between **6** to **8**, and *poly-6* to *poly-8*.



Scheme. 2.9.2.1. a) Experimental conditions preparation of **8** and *poly-8* with Au(I) ions; b) UV-Vis-NIR of Au(I)-P=C systems **8** and *poly-8*, numbered regions on spectrum correspond to the descriptions on the bottom left and connected to conclusive arguments validating the formation of *poly-8*.

The ^{31}P -NMR spectrum of **8** showed a single resonance at + 180 ppm. This signal was significantly shielded ($\Delta\delta = - 84.9$ ppm) compared to **6** (+ 264.9 ppm). The ^1H NMR of **8** showed the highest frequency resonance at 9.71 ppm, corresponding to only one hydrogen atom, deshielded by over 1.2 ppm compared to **6**. More interestingly, the ^{13}C NMR of **8** presents a richer set of $J_{\text{C-P}}$ (Hz) coupling constants, two resonances of which possessed coupling constants of 70 Hz, thereby validating increased communication across the P=C motif due to coordination with gold, as we previously proposed in the cross-conjugation section. This observation can also be explained by the increased

electronic interactions between the Mes* system and the central P=C core, as demonstrated by the frontier orbital density for the ground states and EDDM transitions (Scheme 2.9.2.2). Several printed excited states have varying contributions from electron density differences arising on or from the Mes* at the printed isosurface values



Scheme 2.9.2.2. a) Frontier orbital densities of Au(I) compound **8**, HOMO-1, HOMO, LUMO densities shown; HOMO-LUMO gap: 2.50 eV. HOMO-1: π -orbitals over the thiophene and fluorene “higher” path extending towards gold as an interaction with $\pi(\text{P})$ -d(Au)-p(Cl) character. HOMO: π -character over the fluorene-thiophene backbone. LUMO: [(fulvene)-P=C] core, with π^* density. b) Calculated UV-Vis-NIR spectrum of **8** (see original paper for methods). c) EDDM for selected transitions (numbers on the spectrum) relevant to the experimental values for **8** and *poly-8*. Blue: electron depleting (donor), red: electron increase (acceptor). Transitions 4-7 possess Mes* character, validating our thesis ideas and hinting at important Mes* roles, expressed majorly after Au(I) coordination.

. For example, an aromatic contribution from the Mes* as a donor is observed for transition 7 in c) below, which takes an interesting asymmetric form that neglects the thiophene fragment on the left side, providing asymmetric functionality [(thiophene)_{Right}⁺(Mes*)_{Left}⁺(Cl)_{Right}). This study is promising because the concept of π -conjugation through the P=C unit as a secondary π -path or σ -path is interesting, as mentioned in the cross-conjugation subsection.

2.10. Optical, microscopic, morphological, crystallographic, and electronic properties of the studied systems.

2.10.1. Scanning Electron Microscopy of polymers.

The materials' morphological and general structural properties were analyzed by scanning electron microscopy (SEM). SEM experiments of **5**, **6**, **7**, and **poly-6** and **poly-7** were performed; representative microscopy images of **poly-7** are shown below (Fig. 2.10.1.1).

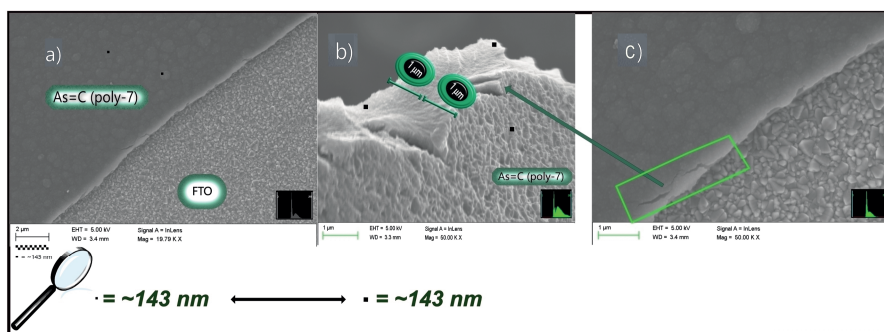


Fig. 2.10.1.1. SEM micrographs of a representative sample of the arsaalkene polymer **poly-7**; small black squares ($\sim 143 \times \sim 143$ nm) scaled through Fig. a) Top-view of the **poly-7**/FTO interface region; note the relatively uniform and homogeneous surface of the polymer, which can be characterized by sets of helical or flower-shaped polymer segment domains (see small globular features on the **poly-7** surface), indicating: i) perpendicular polymer growth from the surface and channel creation for counterion transport and communication; ii) polymer separation, within each structure, as the polymers extend in an orderly fashion through helical⁷⁰ or flower-like arrangements along the growing chain; b) cross-sectional SEM Fig. of **poly-7** that had separated from the FTO substrate due to excessive growth (~ 100 scans), during the growth process; these are characterized by soft, lamellar-like oriented polymer chains that resemble nanomaterial SEM data (e.g., see Fig. 1. in reference).⁹¹ In this case, the patterns were created by ordered interactions. c) View of **poly-7** showing the region where the polymer had detached from the FTO substrate.

As can be seen in Fig. 2.10.1.1, the SEM (**poly-7**) micrograph shows a well-organized and homogeneous polymer film from a cross-section perspective (see b)), with planar, linear surfaces, which indicate a lamellae-like conformation, for those structures directionally parallel with respect to the FTO surface; additionally, there are linear segments down the vertical wall and

connecting different interpolymer domains, as seen in the same micrograph picture. Perpendicular polymer propagation relative to the substrate surface was expected, as we postulated previously from mechanisms; helical polymer growth is the energetically favorable form for polymers based on entropic grounds.⁷⁰ Thus, the SEM patterns agreed well with the mechanism of electropolymerization through external thiophene units. More interesting about these polymers is the cross-section perspective, wherein linearly planar configurations can be observed based on the SEM texture. Furthermore, as shown in a) and c) (top-view), small domains with a globular or perpendicular helical shape become evident. Whether one interprets these as “channels” or “domains” depends on the network configuration for the same motif on the surface relative to its equivalent intersection motif on the polymer/FTO substrate interface. These surface domains were weakly interconnected along some surface segments, as seen more clearly in c). Along the voids, at different depths, these can be expected to form threads/strings that interconnect the polymers, which leads to a singular response, as was seen from the spectroelectrochemistry and cyclic voltammetry in transparent solutions, as well as the picture of the doped polymer under no bias, exhibiting optical activity along and across the entire surface.

It has been shown that perpendicular growth from the substrate surface was not beneficial for device performance (arbitrarily, type A). For example, some bottom-gate OFET device configurations using 9-dialkylated-polyfluorene (alkyl: octyl chains) species as their semiconductor element exhibited poorer responses than those with parallelly-grown compounds. In addition, branched alkyl chains (alkyl: 2-octyldodecyl) are thought to prevent interchain interactions compared to linear chains (arbitrarily, type B). However, it has also been hypothesized that leaving a methylene spacer in alkyl branched chains does not disrupt π - π interactions (arbitrarily, type C).⁹² Interestingly, branched or “extended” conjugated motifs have been reported in the literature and have shown enhanced performances. They have been called “two-dimensional conjugated polymers” (arbitrarily, type D). In the cases we found, the conjugated part of the branched or extended chains was coplanar with the backbone; the E=C branch or extension of the systems presented here is equivalent to those “2D-cases”. On the other hand, in this case, the conjugated benzene ring (Mes*) is perpendicular to the backbone and the E=C branch or extension due to the induced nonplanarity by steric hindrance and the inability of the lone phosphorus pair to form trigonal planar species in dicoordinate systems. Therefore, these systems correspond to cases of “higher dimensionality” (arbitrarily, type E) and are not equivalent to the same systems that were not found to be advantageous when grown perpendicularly from the electrode surface, nor precisely equivalent to those “2D-cases”, highlighting their potential to be helpful in advanced architectures once process development catches up with this type of “exotic” and “atypical” polymers.

2.10.2. DFT calculations - monomer to tetramer - stabilization of frontier orbitals and higher number of frontier states.

Experimental optical gaps.

The oligomeric systems were optimized up to the tetrameric level to gain insights into the orbital densities and energies of the respective systems. The representative structures provided valuable quantitative and qualitative markers for comparison with the monomers, despite the presence of multiple energy minima.

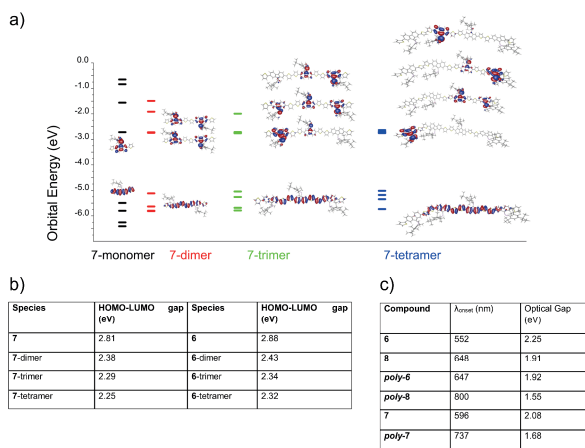


Fig. 2.10.2.1. a) Selected DFT orbital densities and energies of oligomeric model systems are shown for **7** (7-monomer to 7-tetramer). We exemplified the effect of E=C (in this case, As=C) incorporation over the oligomeric compounds, which leads to a decrease between the [(LUMO+n)-(LUMO); n: 1, 2, 3...] energy differences as the oligomer size increases, reaching a band-like regime in the tetrameric case. b) Calculated HOMO-LUMO gaps of computational oligomer model systems **6** and **7**; the calculated energy gaps are smaller for As=C systems due to increased accepting π -character; c) Measured ($\sim \lambda_{\text{onset}}$) optical gaps experimentally according to literature procedure; optical gaps are smaller for bare As=C systems; gold-substituted P=C monomers and polymers (**8** and *poly-8*) exhibit small optical gaps also.

Fig. 2.10.2.1 shows experimental and computational (DFT) information on oligomeric models of **6**, **7**, and polymers (*poly-6*, *poly-7*, *poly-8*). The HOMO-LUMO gaps decrease with increasing oligomer size, indicating increased π -conjugation. In addition, the LUMO orbitals show greater stabilization than the HOMO orbitals, suggesting a more pronounced acceptor character of the molecular motifs via E=C incorporation. In c), the measured optical gaps are shown, illustrating the experimental observations from UV-Vis-NIR spectroscopy for monomeric and polymeric systems. Interestingly, the gold substitution leads to a pronounced effect due to the extension of the π -conjugation over the P=C motif, with electronic transition contributions from AuCl and Mes*. The most highly occupied orbitals delocalize significantly, while the

unoccupied orbitals become more localized, each comprising one to two fulvenoid pnictidene fragments in the tetramer. However, based on the small energy differences in the blue energy levels, it consists of truncated sets of interactions, supporting our conclusions about the redox polymer state as electron accepting becomes preferential.

2.10.3. X-Ray diffraction analysis: relevant features, π - π interactions in the solid state.

Fig. 2.10.3.1 presents the relevant solid-state features of monomeric systems. For all systems, E=C - fluorene coplanarity was found. The unsaturated pnictogen element is therefore incorporated into the relevant frontier density and become an intrinsic part of the molecular electronic structure of the compounds. Increased π - π stacking interactions were observed as going from dibromo substituent (> 4.0 Å) to thienyl substituents (< 3.9), further strengthened in the case of gold-substituted phosphalkene **8** (see Fig. 2.10.3.1 d)).

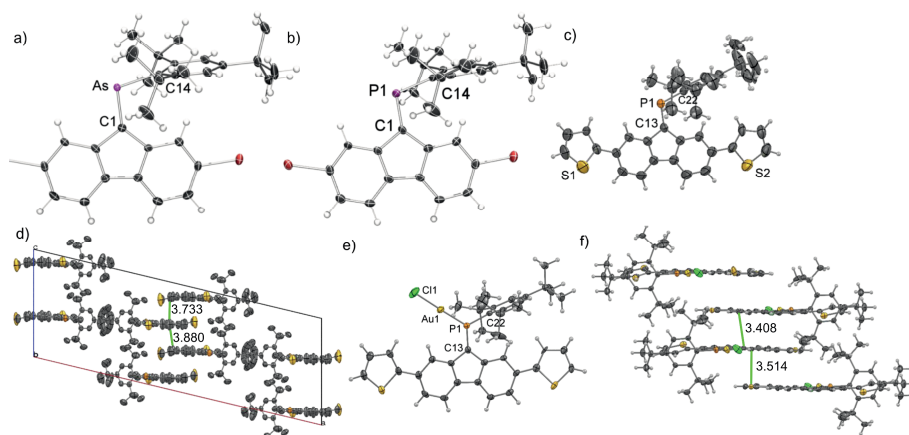


Fig. 2.10.3.1. ORTEP plots of X-ray structures and selected features (BLs [Å]; angles [°]; a) **5**: As1-C1 1.807(3), As1-C14 1.970(3), C1-As1-C14 102.6(1); b) **4**: P1-C1 1.693(5), P1-C14 1.836(5), C1-P1-C14 104.0(2); c) **6**: P1-C13 1.677(5), P1-C22 1.844(4), C13-P1-C14 108.4(2) d) **6**: packing motif along the b axis revealed short intermolecular distances (3.73, 3.88) e) **8**: P1-C13 1.665(5), P1-Au1 2.2144(13), P1-C22 1.810(5), C13-P1-C22 112.8(2); f) **8**: increased intermolecular interactions are exhibited via decreased π - π stacking distances (3.51 and 3.41 Å) in comparison to **6**, demonstrating the valuable role of AuCl in tailoring the solid state properties of the resulting system; generally, all monomers present a coplanar E=C - fluorenylidene backbone, with heteroatoms barely $\sim 0.006^\circ$ (average), above or below the least squares plane of the core.

2.11. Summary and conclusions.

We synthesized and characterized π -conjugated small molecules and polymeric materials containing P=C and As=C group motifs. As a result of the heavy main group motif introduction, the materials exhibited a rich array of exciting properties and phenomena, which we characterized using a variety of spectroscopic and electrochemical methods. We synthesized and characterized phosphalkene and arsaalkene polymers via electropolymerization, which was unprecedented. Interesting properties such as electrochromic phenomena and post-functionalization of the phosphorus derivatives with gold(I) ions were observed. We studied electropolymerization using potentiodynamic methods as a process and the presented As=C materials in extended detail, which helped us realize a potentially valuable scheme based on the concepts of optimal criteria, representative settings, and hysteresis-like criteria for future applications in various fields. Based on the first principles and literature background, we used the presented scheme to demonstrate or prove the functional and modular character and interesting profile exhibited by As=C polymers (i.e., from *poly-7*), which exhibited salient features characteristic of emergent phenomena, positioning *poly-7* (and *poly-6*) as smart materials, based on solid and objective grounds.

Ch. 3. New exotic P=C molecules for π -conjugated organic materials.

In this chapter, we study our work on novel π -conjugated materials containing P=C bonds, focusing on fluorenyl phosphalkenes containing a variety of thienyl-based substituents through their 2,7-substituent positions. We aim at understanding atomic and electronic structure relationships to material properties or functions through synthetic manipulation of compounds containing heavy group 15 elements in low coordinate environments, wherein observation and probing of molecular features via external perturbation is done to characterize and differentiate the unique role of unsaturated heavy pnictogen incorporation in organic scaffolds.

A systematic study reveals the delicate interactive balance that nature establishes when balancing the degree of interaction in liquid and solid states. The manifestation of side pathways in other reaction settings blocks our path to desired product goals, while the opposite occurs in complementary situations that were initially considered equivalent. Our investigation focuses on the effects of the low coordination number and formal trivalency of P=C bonds, which are crucial in driving structural asymmetry. We compare the stability and enhanced properties of “normally polarized P=C” compounds with those of well-known organic materials, especially when incorporated into organic frameworks. We emphasize the importance of our approach for unprecedented access to challenging fluorene compounds and the importance of protecting groups synthetically as they can alter reaction pathways and outcomes due to steric and directional effects while overall maintaining the general P=C group motif role in the compounds as an essential part of the electronic structure and reactivity.

By focusing on conjugated heterocycles and using combinations of heteroatoms, such as phosphorus, sulfur, nitrogen, bromine, and more, we realize the essential effects of each element, functional group, or substituent in synthesized compounds.

3.1. Motivations towards fluorene-derivatized P=C compound.

As previously stated, incorporating low-coordinate heavy p-block element units into π -conjugated frameworks is a multidimensional design strategy for developing new materials. By incorporating P=C group motifs, we can tailor the structure and properties of the resulting materials. In line with cherishing the tunability of organic materials, fluorene, thiophene, pyridine, phosphine, and other conjugated species, have been studied for many applications where their charge transport, structural, photophysical, and electronic properties are helpful.

This section introduces the main application areas for the P=C compounds presented below and references studies using compounds containing functional groups present in the compounds we have prepared, focusing on small molecule and discrete oligomer studies instead of the polymers that were previously the focus in Ch. 2, introducing using organic materials in various device applications.

Applying an electric potential difference across an organic luminescent material layer formed between electrodes is the basis for a practical OLED, which can transform electrical energy into light. See the referenced material for a review of OLEDs from a chemist's perspective.⁹³ Much of the academic literature focuses on polymeric compounds for OLEDs, yet, based on patent literature search results, small molecules appear to be more commercially relevant. From a processing and characterization efficiency perspective, the discrete molecular size of small molecules and oligomers yields cleaner compounds. Fluorene derivatives as oligomers and small molecules have been extensively described.⁹⁴ Phosphine oxides are well-known electron-transport host materials in electroluminescent applications. For example, a phosphine oxide-fluorene hybrid has been reported as an appropriate host material for blue phosphorescent dopants in a blue OLED.⁹⁵ Pyridine-based molecules have been used as ligands towards TM emissive layers in OLED devices.⁹⁶ Similarly, boron and its pyridine complexes⁹⁷ have been used as electron transport material in OLEDs.⁹⁸ In some cases, it has been observed that introducing pyridine imparts thermal and oxidative chemical and electrochemical stability to derived molecules and devices, which should be of interest in cases where pyridine nitrogen lone pairs are further stabilized.

Through the exercise of an electric potential across a semiconducting element of interest, a current is conducted, and a current-potential relationship can be obtained, further characterized at the saturation limit (i.e., observed output at the maximum parameter application) by parameters such as particle carrier mobility, source-drain switching current ratio (on to off current magnitude ratio), gate and drain voltages. Fluorene, thiophene^{99,100}, olefin (C=C), and combinations of these systems with one another,¹⁰¹ and with other

functional groups have been demonstrated and are hypothesized to be used in commercial applications as elements in different types of transistor architectures.

Nonlinear phenomena can arise from various optical and non-photonics particle principles. They can be measured in multiple settings, contingent on the desired applicability of the type of response one aims to engage or acquire. In photonics and optoelectronics, the nonlinear optical phenomena known so far arise as observables that can be derived from a material's response. They correspond to higher-order derivative responses due to oscillative, interactive, resonant coupling or the interference of an incoming field with a material mode, which disperses or propagates. An example of nonlinear optical phenomena of relevance in organic materials occurs via second-order or third-order derivative responses of the energy or polarization function of a molecular material with respect to some variable, such as nuclear coordinates, related to changes in the dipole moment, polarization, polarizability, molecular or atomic polarizability, and hyperpolarizability of a system. More exotic nonlinear behavior resembles plasmas, condensates, or superfluidic states and may involve induced or provoked quasiparticle interactions.¹⁰² Fluorene, thiophene, olefin (i.e., C=C units can be generalized in breadth and depth order of interactions by heavier P=C fragments due to the realizable higher oxidation state or valence of phosphorus), and phosphorus-containing organic compounds have been studied in the direction of NLO materials.¹⁰³ More complex areas include “cavity” experiments (structurally isolated or optically confined systems); remarkably, these exotic ensembles have been prepared using fluorene¹⁰⁴ small molecules and polymers.¹⁰⁵ Other fluorene derivatives¹⁰⁶ have been used in experiments measuring their high-order hyperpolarizability properties in molecules containing pyridine and thienyl centers.¹⁰⁷ This research is essential for developing advanced technologies, including specialized research, equipment, and communications.

The photovoltaic effect exploits the energy and potential mobility of electrons or holes close to the quasi-Fermi level of a material layer in semiconducting-contact interfaces, which form charge-separated states following absorption of UV-Vis-NIR sunlight photons, which under the correct device configuration are collected at the respective cathode/anode, thereby transforming light input to electric output.^{108,109} As with OLEDs, most attention has focused on solution-processed polymer bulk-heterojunction (BHJ) solar cells, so small molecules have received less attention. Apart from isolation ability and reproducibility, small molecules and discrete oligomers offer a range of variables. **(i)** Broad optical absorption, **(ii)** high extinction coefficient in some dyes, **(iii)** the possibility to combine various entities to increase panchromaticity, **(iv)** solubility, as well as **(v)** the possibility to fine-tune the quasi-Fermi level of the complex active material layer to an arbitrary charge collector. Among the compounds we have mentioned thus far, thiophene and benzothiophene derivatives are popular as electron donors (EDs) in the configuration:

ITO/anode/ED/EA/cathode and demonstrate good solar cell efficiencies. For example, a (bithiophene)-(cyclopentadithiophene-bridged-silicon)-containing compound was described in 2012 (See Fig. 3.1.1 below).¹¹⁰ Thiophene-derived electron donors (high band gap or work function) generally act as electron-blocking or hole-transporting layers. In contrast, more recently, fullerene and non-fullerene acceptor derivatives have been used as electron transport or hole-blocking layers.¹⁰⁹ It has been shown that based on regular architectures (non-inverted), a lower HOMO and higher LUMO level in the hole-transport material (and vice versa in the hole-blocking material) can improve the open-circuit potential and performance in general. This “typical” requirement and the relatively lower absorptivity of low-coordinated heavy group 15 E=C-containing materials in the low-energy end of the visible spectrum, coupled with their higher reactivity, have made them difficult to study as active layers either in regular or in inverted architectures (where the typical anode material is used as a cathode) in solar cell devices. However, it is essential to note that these materials have great potential as additives in order to fine-tune the device physics (e.g., tailoring or alignment of energy levels or dipole moments), while novel architectures may also include the use of sensitive or reactive materials as active layers under regular, multilayer, or inverted architectures using different electrodes or under the premise of encapsulation and potentially high transport capability of these materials due to their heavy p-block element incorporation (which may also act as a “self-dopant” under an applied bias), mixed D/A or acceptor character due to relatively higher HOMO and/or low LUMO levels as well as their protecting group-induced asymmetric nature.¹¹¹

Organic materials can be used as substrates, selective layers, or transducer elements (i.e., the sensing elements) to detect a variety of critical analytes (i.e., the compound being sensed or analyzed). Emitted greenhouse gases or toxic molecules, such as NO, NO₂, and CO, can be detected by electronic chemical sensors based on small parameter changes within a transducer’s function arising from a minor change in the substrate’s properties. For example, changes in conductance (conductivity), work function, capacitance, or optical transmission are directly coupled to a reversible interaction between the organic material and the analyte. All device components are made of chemicals (materials), so the distinction between a chemical sensor and a semiconductor-based transistor may sometimes relate to the application context. Most, if not all, chemical sensor devices (e.g., chemiresistors, CHEMFETs, and more) could formally be categorized with transistors or with groups or sets of more primitive electrical circuit elements. Organic semiconductors and organic π -conjugated polymers, including electrochemically active conducting polymers (see Chapter 2), have many applications as active substrates, transducers, or selective layers in sensor devices. This may well be the more mature area of application of these materials.^{112,113} As mentioned previously, the main advantage of organic materials, in terms of their electric and optical properties, relates to the exhibition of discrete energy levels, which may be generally

delocalized, in the limit, towards a band/continuum or a gap. Additionally, their flexible conformance to various processes and shapes makes them valuable. Organic materials and polymers can be tailored toward specific analyte detection. The presence of heteroatoms within the sensing element's scaffold can improve the affinity and specificity of the sensor for an analyte, which is a crucial necessity for a successful sensor configuration. This is due to the distinct atomic and electronic properties that a heteroatom (e.g., p-block element) exhibits based on their polarizability, electronegativity, formal oxidation state, and bonding environment. More fundamental nuclear and electronic properties, such as spin, orbit, field susceptibility, and others, are also critical. These atomic properties allow the doped or main group compound or material to realize a different functional role. The surrounding device elements can always utilize this functional role with enough resolution. In problematic resolution cases, the presence of an analyte can trigger a substantial change in the material response, which can be "directed" by the main group elements (e.g., pnictogens). Thus, pnictogen incorporation is a natural and effective approach since sensors exploit slight changes in the response function of a material. Under identical circumstances, a pnictogen-containing organic material would potentially be more sensitive than the all-carbon counterparts towards detecting a small gaseous analyte (e.g., P, N, or other gases) because of steepening of the wave function response, which leads to increased attraction or repulsion, for example.

The last application we will describe in detail consists of organic memory and organic processing devices (e.g., organic memristors, non-volatile organic memory devices, OFET memories, write once read many \rightarrow 'WORM' devices to simulate backbone functions at the atomic scale, and others to be discovered)^{114,115,116,117}. The several references provide the interested reader with reviews and discussion on advances on the topic from the perspective of organic materials, which can be fruitful to motivate main group chemistry towards the most sophisticated and latest applications.¹¹⁸ This relatively unknown area is now being explored increasingly as a step before the onset of quantum computing and artificial intelligence. Objects comprising molecular systems have exhibited transient or lasting responses under bias, thought to stem from memory states in elementary devices, akin to the behavior seen with functional *poly-7* in the last chapter. For example, a three-state (ON1, ON2, OFF) was achieved by a phosphole-gold complex in a sandwiched configuration with aluminum and ITO glass electrodes.¹¹⁹ Additionally, a spin-coated ruthenium(II)/ITO complex with a low coordinate (phenylazo)-pyridine ligand (Scheme 3.1.1, j), and [PF₆]⁻ counterions, was used in ITO-(RuNCPF)-ITO/Au and ITO-(RuNCPF)/Au_{Np}-ITO/Au (Np: nanoparticles) configurations. Importantly, they demonstrated a stable, write \rightarrow read \rightarrow erase \rightarrow read, hysteresis-containing response system per cycle. Thus, the authors produced an object displaying the hysteresis criteria required for a response to be categorized as one of a memristor element. According to the conclusions, the

redox-active role of the low-coordinated phenylazo unsaturated nitrogen ligands with a mixed- π -donor- π -acceptor electronic nature was crucial in achieving the coordinated response of the material. The electrochemical properties of the complexes in solution exhibited a multi-redox 6-wave response, which directly attests to the excellent structural flexibility (smooth phase transition) and robustness of the material's response at a solid-state interface (electrode interface). This flexibility, coupled with ion mobility, can explain the hysteresis response.¹²⁰ As a strong fluorinated carbonaceous organic hybrid material, strong in the sense that at the applied voltages, the extremely high electric field passing through the solid material containing indistinguishable counterions averages the velocity of the response of the dipole components towards a bent state, towards an oscillation limit given by a flexible structural component characterized as “thread 1”, that is revisited through cycles, implies flexibility or freedom at the molecular level. The ion drifts give the conformational freedom of exploring that space of flexibility. As hypothesized, N=N ligands, uncoordinated during a redox state transition can leverage the dispersive fluidity of the degrees-of-freedom of the quasi-free strand of $[R_{\text{coordinated}} \sim (N=N\text{-Ph})_{\text{free}}]$. For us, it is superb and interesting to see that heavy group-15 phosphole ligand, a Mes*-like “protecting group”, gold(I) ions, and a low coordinate π -accepting redox-active group 15 ligands or units can be mentioned in this section (see i) and j), Fig. 3.1.1). These groups, compounds, and chemistry are related in many characteristic aspects to the chemistry we have worked with and shown throughout this thesis. From a “neuromorphic” perspective, these devices are interesting for simulating dynamic processes in scalable devices. A similar approach computes response outcomes that cycle through learning objectives or cost functions (e.g., how does the memristor evolve its memory functions over time given slight peripheral kinks?) that are uniquely coupled to a set of material responses over the time of the experiments. This approach has been hypothesized to be fruitful in designing neural networks and machine learning models, where few-cycle algorithm optimizations have been hypothesized as potential realizations from analog systems. Successful approaches require much information to be processed, corrected, and accessed simultaneously. Thus, access to previously achieved states via storage modes from the material seems paramount (see Section 2.7 for a potential contribution from this thesis in this area). This approach contrasts the traditional “Von Neumann architecture”, which relies on sequential processing and memory access (i.e., the processor and memory are physically separate). In neuromorphic applications, as in biological organisms, utilization of pnictogens such as N and P is important because these provide structural forms or variation and, thus, optical and electrochemical variety. For example, **(i)** via discrete and distinguished electronic-chemical accessible states, **(ii)** available oxidation states with **(iii)** varying waveform responses (behavior or flow) and lifetimes, **(iv)** chemical or electrochemical reversibility (e.g., electrochemical), **(vi)** and potentially selective light component mode

coupling which allows reading information from a memristor with optical-electronic means without disrupting the memory effect, permitting the creation of modules and stacks, for example. The fluidic sophistication of biological cycles is exhibited, for example, by H₂O diffusion through tightly compartmentalized and flexible barriers (e.g., water solution or water solute-cell membrane interfaces), which are used to leverage complex and metastable or stable, intermediate, or temporary states (see HB and H₂O cluster relations to our work in Ch. 5). In order to mimic the reactivity, flexibility, and modularity of intelligent systems in future neuromorphic devices, the use of solid-state electronic materials with a degree of unsaturation and low coordination, such as semimetallic or semiconducting elements, will be necessary. This implies a potential role for heavy main group elements or heavy p-block elements in the chemistry of these systems. The compartmentalized solute-solvent (quasi-solid, liquid) environment of an organism is less compatible with modern solid-state electronics. Albeit, electrolyte-containing solid or liquid objects, are also studied in this area as we explored in the previous chapter for electropolymerization. In this way, low coordinate heavy element-based organic materials may play a unique role in the future of neuromorphic processes.

Although current application paradigms for organic materials are inherently based on “robust chemical stability” (which fallaciously evaluates to high heat and acid processing under non-inert conditions) toward low-cost applications, organic materials display excellent performance parameters based on principles. They are tremendously tunable, meaning each organic material and application object element necessitates its set of preparation routes, processing rules, methods, and precise operational ranges.

The type of concepts reflected in the materials studied in this thesis should bring new perspectives to the fundamental and applied device physics, materials science/chemistry, and process engineering domains in various directions. *a)* The development of synthetic methods due to their synthetic complexity. *b)* Soft, dry, inert process development due to atmospheric sensitivity. *c)* Material performance due to their novel aspects. Information from molecular motifs can also be extrapolated or projected toward the advancement of other material platforms using stoichiometries.¹²¹

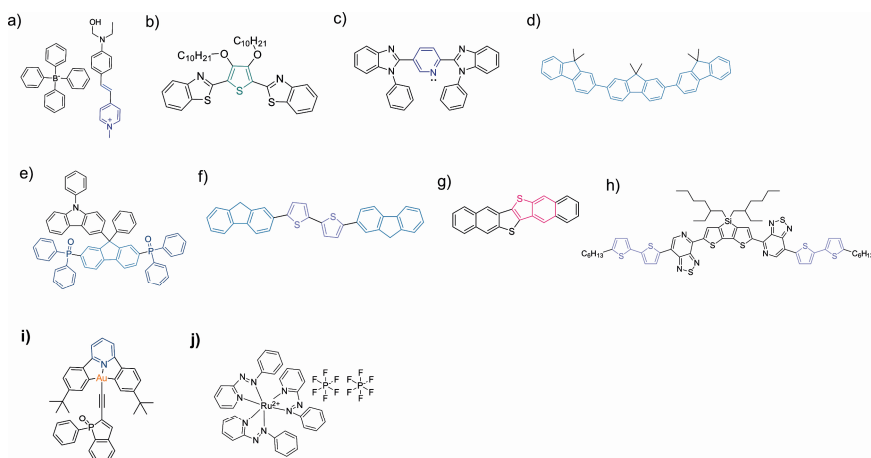


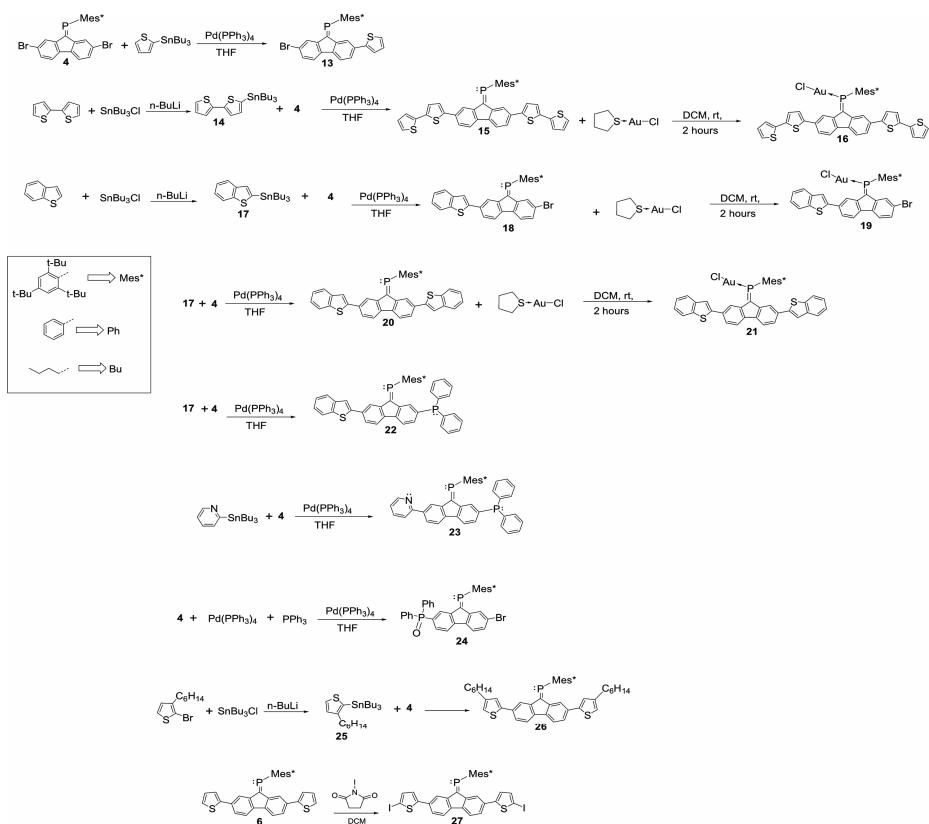
Fig. 3.1.1. The following literature research study comprised small-molecule materials with specific moieties as active materials in areas such as NLO, photon absorption/emission or charge extraction, or transport processes in OLEDs, OFETs, photovoltaics, and more. For interested readers, copy/paste the CAS # on SciFinder, Reaxys, or Google; **a)** 159721-38-7; two-photon absorption; **b)** 129922-11-8; second-order hyperpolarizability; **c)** 129922-12-9; second-order hyperpolarizability; **d)** 569343-08-4; hole-transport, dopant, high energy OLEDs; **e)** 1122104-12-4; bipolar host, blue OLEDs; **f)** 369599-41-7; p-type channel semiconductor in OFETs; **g)** 935280-42-5; semiconductor in organic thin film OTFT/OFET; **h)** 1351374-94-1; ED in OPVs; **i)** 1923771-98-5; three-state memory state; **j)** 871508-68-8; organic memristor.

3.2. Synthesis of materials. Stille coupling. Unique fluorene-substituted molecules via P=C induced asymmetric side accessibility.

It is vital to prioritize safety. Due to high toxicity, using tin, phosphorus, and arsenic compounds must always be preceded by a risk assessment before the experiment. We now describe the synthesis of these materials, which we studied around the creation of extended π -conjugated frameworks through functionalization of the parent building block **4**.

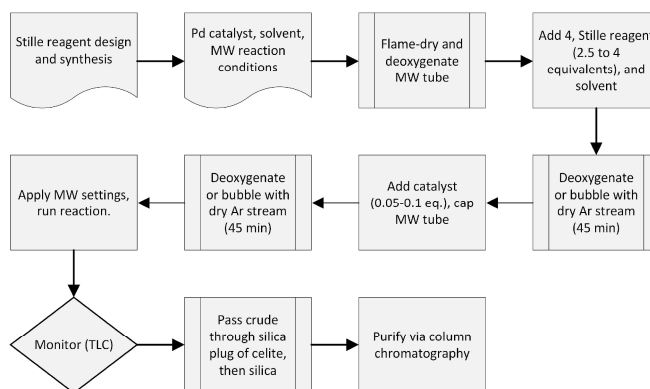
3.2.1. Synthetic procedures and schemes. Spectroscopic findings.

Briefly, the Stille reagents were prepared via selective lithiation of bithiophene or benzothiophene with 1 mol eq. of *n*-BuLi at low T, followed by adding the Bu_3ClSn reagents (see **14** and **17** below) (See Scheme 3.2.1.1). The synthesis of the substituted compounds was based on the procedures developed in Chapter 2 for thiophene and previous work in our group.



Scheme 3.2.1.1. Chapter 3 compounds incorporating low coordinate P=C. Synthesis of materials **13** to **27**. Selected reaction conditions were placed under and over the reaction arrows. Mes*: 2,4,6-tri-*tert*-butyl-benzene.

Nevertheless, the yields are usually acceptable since they were quantitative enough to use standard characterization methods. The reproducibility and explainability of all observations, the systems' complexity, and the Stille procedure's simplicity should be considered for future yield improvement process/method development, which could benefit from the tailoring of the existing procedure (Scheme 3.2.1.2). The products' stability was high, meaning that formation and not stability (except for ketone formation, in Suzuki conditions) is the only limitation for large-scale synthesis processes.



Scheme 3.2.1.2. Main process steps used during the preparation of the presented materials.

We have demonstrated the selective synthesis of asymmetric products as a proof of concept. We prepared the monobromo-monothieryl derivative **13** using a slight excess (~ 1.3 eq.) of the thieryl Stille reagent. Although challenging, a higher stoichiometric excess of the prepared Stille reagents yielded products **15** and **20**, the doubly substituted bithiophene and doubly substituted benzothiophene species; the main difficulty in the reaction was related to the presence of monosubstituted products, which could nevertheless be separated by liquid chromatography.

The compounds exhibited ^{31}P NMR resonances at $^{31}\text{P}\{^1\text{H}\}$ NMR (162 MHz, THF- d_8 , $\delta = 263.9$, **15**); $^{31}\text{P}\{^1\text{H}\}$ NMR (162 MHz, CDCl_3 , $\delta = 268.5$, **20**). Crystal structures were obtained under slightly varied conditions, e.g., from layered acetonitrile/DCM solutions of **15** in a tightened flask filled with argon; from pentane/DCM mixtures (90:10 – 99:1 gradients) of **20**.

After several trials, the monobromo-benzothiophene species **18** was obtained persistently as the primary product in every reaction $^{31}\text{P}\{^1\text{H}\}$ NMR (162 MHz, CDCl_3 , $\delta = 269.6$, **18**), despite the use of benzothiophene in excess. Increased steric hindrance of benzothiophene relative to thiophene, concerning the Mes* protecting group in the palladium intermediate of the Stille coupling reaction mechanism, may lead to pronounced monosubstitution.

After characterizing the reaction side products and impurities, product **22** was obtained reproducibly. The formation of the product was confirmed by single-crystal x-ray diffraction, which we describe in the next section. It is an exciting species, containing an oxidation-stable diphenyl-phosphine substituent buried under the Mes*, with benzothiophene as the opposite substituent.

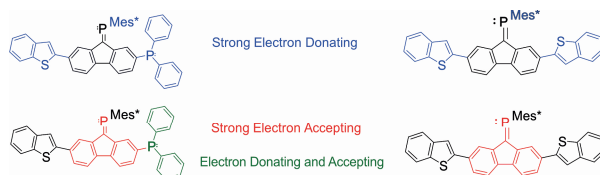


Fig. 3.2.1.1. Hypothesized electron donating and accepting ability of selected compounds, left (**22**), right (**20**); phosphine and benzothiophene can act as EDG, phosphine, and P=C can both act as EWG. Benzothiophene groups are ED, whereas P=C offers the counteracting effect.

One can think of species **22** as a highly mixed, asymmetric, donor-accepting scaffold, with electron-donating contributions arising from benzothiophene, Mes*, and fluorene core, and electron-accepting properties from the phosphalkene fulvenoid system and the phosphine ligand (electrostatic stabilization), which under accepting environments transform the fluorene core, also into an overall accepting unit through overall delocalization; compound **20** exhibits a more traditional donor-acceptor distribution with separated electron density contributions, as shown pictorially in Fig. 3.2.1.1, right.

The reactivity of **4** was probed with a commercially available pyridine Stille reagent. Interestingly, following the standard reaction monitoring through ^{31}P NMR, **23** was formed; this compound is a novel asymmetric, mixed phosphine pyridine fluorene phosphalkene. Product **23** was confirmed by NMR and mass spectroscopy. We gained information about the nature of the phosphine exchange on the previously obtained products; **4** was reacted with excess triphenylphosphine and Pd(0) catalyst without a Stille reagent. Remarkably, the phosphine oxide species **24** was obtained, with the phosphine oxide substituent opposite from the Mes* protecting group. The fact that the phosphine oxide was positioned opposite the Mes* confirmed that the Mes* provided phosphine products **22** and **23** steric protection against oxidation, which is interesting in terms of tailored ligand design. Additionally, the asymmetric nature of product **22** with two phosphorus centers is a motivating factor in the design of complex bimetallic compounds.

The phosphine oxide **24** without a stannylated Stille reagent proves the reaction occurs through a non-Stille mechanistic pathway. Given that the discovery of phosphine-substituted products **22**, **23** occurs with and **24** without stannylated agents, while non-oxidized phosphine substituents in **22** and **23** were found buried under Mes*, we could safely conclude that the reactivity of phosphine substituents **22** and **23** towards oxidation is attenuated by the Mes* role as a protecting group since **24** was found to be oxidized. Thiophene modifications towards hexyl-substituted materials yielded **26** $^{31}\text{P}\{^1\text{H}\}$ NMR (162 MHz, CDCl_3 , $\delta = 268.2$) as a difficult-to-manage pink solid glue-like material. Proof-of-principle functionalization extension of an extended π -conjugated framework in the presence of P=C was successful after iodination of

6, yielding product **27** in a roughly 50 % yield, after stirring at room temperature in DCM for 72 hours, $^{31}\text{P}\{^1\text{H}\}$ NMR (162 MHz, CDCl_3 , $\delta = 270.02$).

A raw literature review was done using several databases based on exact, similarity, and substructure searches of parent 9H-fluorene and 9-fluorenone. Despite the widespread use of fluorene derivatives, there are no previous examples of fluorene molecules with the combinations: phosphine oxide-bromo, pyridine-phosphine, benzothiophene-phosphine, or 2-bromo-7-thiophene groups. A general search for “fluorene” yields 44 938, 54 796, and 146 000 results on Reaxys, SciFinder, and Google Scholar, respectively. Although our primary goal is to understand and exploit the role of $\text{P}=\text{C}$ functionality, using $\text{E}=\text{C}$ species as intermediates is also intriguing. This approach may help to access more complex or stable asymmetric fluorene compounds, followed by reductive or other approaches. In some cases, incompatibility makes the sequential introduction of specific functional groups a challenging task synthetically (e.g., only isomers of the trivial 2-bromo-7-thiophene-9H-fluorene, $\text{C}_{17}\text{H}_{11}\text{BrS}$ have been reported in the literature). Before describing the gold(I) materials obtained in the laboratory and studied in this chapter, we present motivations and arguments for their use in small molecule π -conjugated applications based on selected and relevant literature reports.

3.2.2. Utilization of gold atoms in molecular Au(I) complexes. Synthesis of **16**, **19**, **21**.

We are interested in molecular and organic electronics as applications for our synthesis efforts.

It is crucial to understand the significant differences in the molecular contact to gold atom interaction in the two schemes, and thus we further motivate the utilization of gold ions to the materials or physicist community. We assume an organic semiconductor-gold electrode contact transistor and gold-molecule-gold interconnect or similar junction in the molecular electronics case.

In both cases, gold atoms are used as metallic interconnects or electrodes. Metallic Au and Au(I) display a high affinity for “soft” elements, such as heavier phosphorus and sulfur. Naturally, these are not equivalent to Au(0) (or Au(111)) metallic surfaces. However, the arguments about gold-phosphorus interactions are based on the general relationship between the Au-P atomic interaction in its zero metallic and + 1 oxidation state. For example, our group has studied acetylenic phosphalkene and gold nanoparticles, confirming $\text{P}=\text{C}$ -Au(0) interactions.²⁶ The interaction between a ligand with a cationic gold and that with a zero-valent neutral gold complex has essential differences. Thus far, the distinctions we found in the literature did not conclusively indicate the nature of the differences in bonding between L ligands and Au(I) or Au(0). However, the interaction between a phosphorus L ligand and Au(0) is found to be attractive and occurs through dispersion interactions with little

charge transfer. A P=C may be softer than a P-C phosphine L ligand-type system. The concomitant presence of Mes* protecting groups with dispersive interactions may be beneficial by diluting the induced dipole moment upon gold complexation and compactifying towards sub-nanometer architectures with high heat dissipation. We postulate the argument of a beneficial interaction that arises from an averaged effect over the overall change in degrees of freedom of the small molecule/metal interface. Contributions to the charge transport can arise from hopping through the π -scaffold and directly via P-Au interactions with increased covalent character.

Additionally, so-called ‘intraband’ mixtures of polaron and other quasiparticles, driven by the electron potential differential, can also lead to transfer from localized or delocalized modes. Lastly, less explored forms of transport (electron or heat transport) driven through VdW interactions via the localizability of protecting groups are of interest. In this work, we justified using expensive gold as the transition metal of choice. We describe the reactivity of these compounds with Au(I) ions. As before, we used the “well-behaved” chloro(tetrahydrothiophene) gold(I) complex (i.e., AuCl[tht]), which reacts smoothly with the lone pair of the phosphorus on P=C moieties via a displacement reaction.

Thus, reacting bis(benzothiophene) compound **15**, monobenzothiophenyl **18**, and bis(bithiophene) **20** with stoichiometric amounts of AuCl[tht] in solutions of DCM at room temperature for several hours (2-4 hours) yielded quantitative amounts of the desired complexes **16**, **19** and **21**, respectively (Scheme 3.2.1.1). NMR, HRMS, and single-crystal X-ray analysis characterized the complexes. The reactions were concomitant with intense optical changes in absorption. This increase in absorptivity is due to the increased charge transfer character of the interaction, manifested via frontier orbital electron densities encompassing the whole structure. Thus, a decreased HOMO-LUMO and optical gap were observed upon gold complexation.

The observed densities strongly suggested that the interaction with the metal opened the π -electron transmission pathway over the entire molecular motif, including resonant localized states over structural fragments separated in space, validating the picture we initially formed in Chapter 2 (see Section 3.5). We observed a shift of the ^{31}P NMR signal to lower chemical shifts by ~ 70 -80 ppm, indicative of the interaction between the Au(I) and the phosphorus atom of the phosphalkene (see Section 3.3). This significant shift implies a substantial change in the nuclear and electronic environment surrounding the phosphorus atom.

3.3. NMR Spectroscopy features.

The ^{31}P NMR of the synthesized species displayed deshielded chemical shifts characteristic of “normally polarized phosphalkenes” under an electronic

environment with excess electron density or negative charge, shifted towards the carbon atom, at hand with expected electronegativity trends. Below, a summary of the relevant phosphalkene ^{31}P NMR parameters for selected compounds is presented, sorted in descending order regarding their resonance shift number.

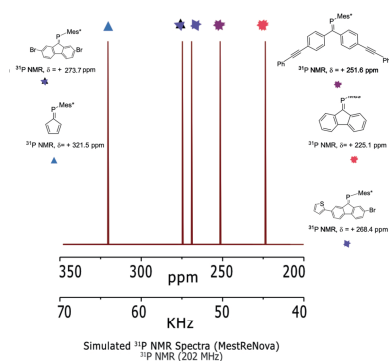
We now focus on examining the resonance position of selected and relevant compounds (Table 3.3.1), providing a qualitative interpretation where possible. The range of the solution-state phosphorus NMR shifts (161 MHz; vs. 85 % H_3PO_4) does not vary widely for gold complexes, indicating structurally similar electronic and atomic consequences following the complexation with gold(I) chloride fragments. Overall, the spread of the resonances of the unsubstituted systems is ~ 16.8 ppm, while that of the gold complexes is ~ 2.9 ppm (vs. ~ 4.7 ppm of the corresponding precursors without gold).

Compound #	^{31}P NMR* (ppm)	Substituents** (left - right; Mes* right)
4	273.7	Br - Br
27	270.0	Th(I) - Th(I)
18	269.6	BzTh - Br
13	268.4	Th - Br
26	268.2	Th(C_6H_{14}) - Th(C_6H_{14})
20	268.4	BzTh - BzTh
15	265.7	biTh - biTh
6	264.9	Th - Th
23	263.6	Pyr - PPh ₂
24	256.9	OPPh ₂ - Br
Au Complex #		
19	182.5	AuCl - (BzTh - Br)
21	181.4	AuCl - (BzTh - BzTh)
8	180.0	AuCl - (Th - Th)
16	179.6	AuCl - (biTh - biTh)

Table 3.3.1. ^{31}P NMR chemical shifts of selected synthesized species; * Solvent: CDCl_3 ; ** Substituents: Br (bromo), BzTh (benzothiophene), Th (thiophene), biTh (bithiophene), Pyr (pyridine), PPh₂ (diphenylphosphine), OPPh₂ (diphenylphosphine oxide), Th(C_6H_{14}) (3-hexyl-thiophene), Th(I) (5-iodo-thiophene).

A more extensive shift range of 16.8 ppm is evident among the parent class of compounds due to the more significant differences in the substituents. Since the upper (4) and lower-end compounds (24), with dibromo and phosphine oxide and bromo substituents, both provide no significant extension of π -conjugation and both comprise strong electronegative-containing-substituents groups (e.g., Br $\chi = 2.96$), a mixture of effects contributed to the observed phosphalkene nuclear phosphorus magnetic environments. Previous work in our group led to fluorenylidene and diphenylmethylene phosphalkene compounds;¹⁵ following their findings, the ^{31}P NMR chemical shifts exhibited no major, identifiable trends in the variation of their ^{31}P NMR shifts regarding substituents. We think that the bunching effect towards $\sim +180$ ppm (in some sense, reflecting the behavior from the ligands at $\sim +268$ ppm) for gold complexes relates to the more extensive distribution of the electronic effects within each complex and not by a localization effect by the AuCl extension exclusively, and which was supported in the previous chapter by showing the increased J constants of the complex 8.

Interestingly, the unsubstituted fluorene parent compound exhibits a comparatively shielded ^{31}P NMR resonance ($\delta = +225.1$ ppm),¹²² whereas the diphenyl-cyclopentadiene fulvenoid system resonates at $\delta = +321.5$ ppm (See Scheme. 3.3.1 below). Aromaticity steers the diene carbocycle towards a 6π cyclopentadienyl anionic mode, which results in an extra-positive P atom, explaining the deshielded signal. This behavior represents a natural instance of the multipolar or multiredox accessibility of heavy pnictogen atoms, which leads to unusual bonding situations. The resonance of the diphenyl-methylene phosphalkene system ($\delta = +251.6$ ppm) arises from a $\text{P}=\text{C}$ species in a highly disrupted π -structure through the deviation of phenyl rings from the plane; even so, the resonance occurs at a characteristic $\text{P}=\text{C}$ region. In the Scheme below, we exemplify this variability in the chemical shift resonance number, encompassing several types of families, which we project toward the broader applications arena.



Scheme 3.3.1. Schematic representation of the $\text{P}=\text{C}$ ^{31}P NMR resonances of selected fluorenylidene and fulvenoid systems with precise resonance frequencies. Each compound possesses several distinctive features. However, due to structural similarities, they show correspondences in their ^{31}P , ^{13}C , and ^1H properties. From left to right/clockwise: deshielded ^{31}P resonance (cyclopentadienyl- derivative) – quadrupolar atom dispersive relaxation through bromo atoms (**4**) – asymmetrically differentiated ^{31}P relaxation rates (**13**) – differentiated $\{^{13}\text{C}, \text{X}\}$ J couplings via acetylene substituents – parent species (bare fluorenylidene phosphalkene). We hypothesize that the tailored use of discrete mixtures in confined environments can generate stimulating effects inaccessible in single molecule-based applied architectures. These effects can be enhanced via diffusion-dispersion-relaxation rate differences and can optimize the system responses after a series of pulses.

Based on acceptable region assignments of ^{31}P NMR spectra of **13** and **24** (Fig. 3.3.1), we can see that the chemical shift of the phosphorus nuclei in a phosphalkene environment varies with the nature of the substituent as in a) below, which shows a spectrum from a complex solution containing the two maximally shifted ^{31}P NMR phosphalkene resonances (i.e., **4** vs. **24**), with minor contributions of two bromo-substituted isomers concerning the $\text{P}=\text{C}$. Moreover, the observed resonances can differ to a significant extent in the

relative position of the substituents, as evidenced in b), which shows tentatively assigned isomer signals of **13**. We put forward that the two shielded signals are well-resolved by the enforced structural asymmetry of the P=C center and subsequent shielding effect by Mes*, which provides the magnetic environment around the ^{31}P nuclei a differentiated response, even though their energy at room temperature is neither significant nor negligible. This effect is compared to the more pronounced chemical shift effect observed for the minor isomer species with a constrained sulfur atom under the Mes*, regarding its rotational isomer, which leads to two separate signals.

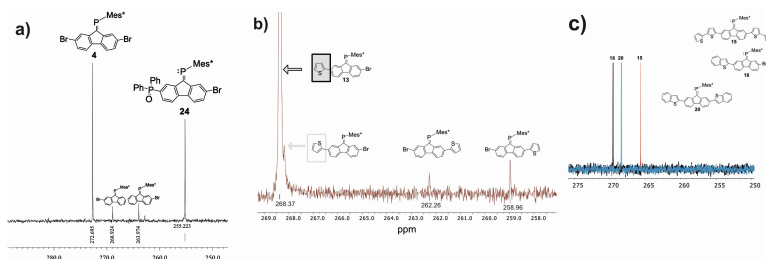


Fig. 3.3.1. High frequency, deshielded ^{31}P NMR regions of a) compound **24** (assignments based on chemical intuition and known NMR shifts) and b) compound **13** (assignments based on chemical intuition and reaction completion), c) compounds **15**, **18**, and **20** (normalized overlay).

The larger or inflexible substituent, such as bithiophene or benzothiophene, did not provide a resolved environment due to torsional/rotational collisions with Mes* during rotations (i.e., relative to our assignments in a) and b), which indirectly validates our assignments). We further substantiated our previous assignments in a) and b) by demonstrating a lack of rotational isomer resolution in the same ^{31}P setting via other experiments. Therefore, we compared the case of the larger substituents **15**, **20**, and **18**, which were separated, normalized and processed together (MestReNova 14.2.3; apodization → exponential: 2.00 Hz, auto-phase, and auto-baseline corrections → defaults), resulting in the overlay NMR spectrum shown in Fig. 3.3.1 c). No secondary isomeric products are visible, as predicted. Preliminary DFT calculations suggest that the direction/position of the substituents has a negligible effect on the total energy of the studied systems (although this may not be reflected in the observed X-ray structures and positional disorder, which adds a layer of complexity to the issue). However, a significant effect on the molecular dipole moments is observed, as expected in limited cases such as **24**, **18**, and **13**.

The P=C group motifs are essential because they allow the phosphorus atoms to direct the interactivity. In most cases, the molecular dipole moment is not parallel to the P=C bond, attesting to electronic asymmetry and potential anisotropy. However, the phosphalkene is close to the nuclear and electronic center of mass of the compound, providing a natural center of inertia for

rotational motion. The principal moments of inertia for compound **13** are 3976.446, 9721.897, and 11225.298 for S facing Mes*, and 4246.995, 9654.570, and 11425.604 for S opposite to Mes*. There are slight but non-negligible differences in the principal moments observed at lower temperatures or in concentrated mixtures under a bias. These differences can be used to construct complex state spaces or interactions based on the propagating changes in the evolving process (e.g., via NMR).

3.4. Single-crystal X-ray diffraction (XRD) study.

Now we will focus on x-ray crystallography results with a slight focus on relevant details from our published materials. As in Chapter 2, these phosphalkenes are kinetically stable in solution for several days and robustly stable in the solid state, which helped our crystallization process efforts. Our analysis will be divided into three parts, each consisting of a brief analysis of the i) basic molecular structures (Fig. 3.4.1), ii) interesting packing features of the bare molecules and gold complexes (Fig. 3.4.2), iii) intermolecular analysis for compound **15** (Fig. 3.4.3). The crystal structures of the bare small molecules and gold complexes are shown in Fig. 3.4.1, accompanied by the relevant details in the Fig. caption.

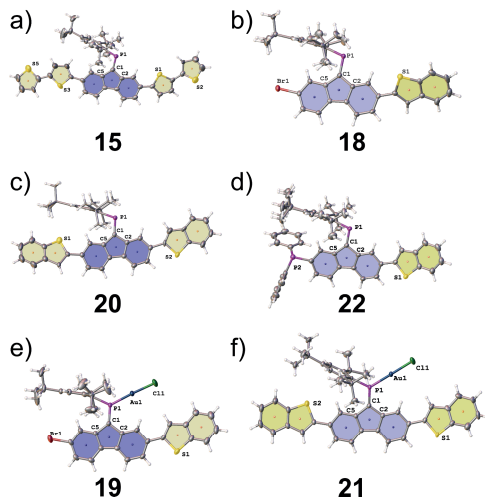


Fig. 3.4.1. Crystal structures of compounds a) **15**, b) **18**, c) **20**, d) **22**, e) **19**, f) **21**, as ORTEP representations of the solid-state structure, featured as ellipsoids (probability level 50 %).

In Fig. 3.4.1, ORTEP representations of the crystallized compounds illustrate their structures in the solid state. All P=C group motifs exhibited BL distances between the expected range (1.675-1685 Å). Compound **15** exhibited

increased disorder or solid-state dynamical phenomena on the external rings, illustrating the increased rotational freedom provided by bithiophene substituents compared to the annulated benzothiophene groups. Via diffractometry, gold-containing compounds **19** and **21** naturally exhibited the most significant densities (g/cm^3) at 1.685 and 1.608, compared to density values of ~ 1.2 for the non-complexed materials.

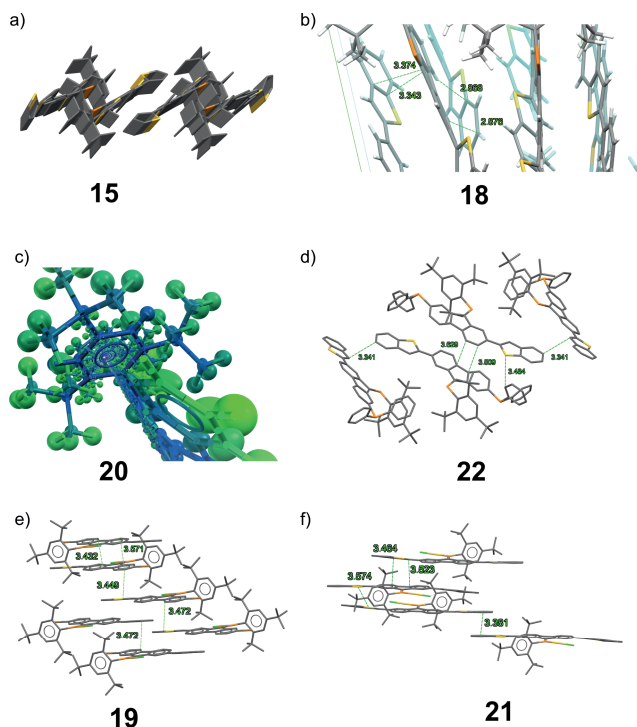


Fig. 3.4.2. Selected details from crystal structure analysis. a) Compound **15**'s miscellaneous motif. b) Close π -stacking interactions compound **18**. A mixture of alternated π -stacked-perpendicular- π interactions (quasi-slip-stacked and quasi-T-shaped) was observed (quasi prefix indicates angular twists from the ideal parallel-offset or perpendicular conformations). The quasi-T-shaped interactions between heterofulvenoid and benzothiophene exhibited shorter contact distances (2.87 and 2.88 Å) than the quasi-slip-stacked ones (3.37 and 3.34 Å). c) Close-view of bis(benzothiophene)-phosphaalkene **20** down the Mes* protecting groups, opening a transmission channel in the solid-state, which is alleviated by the presence of dispersion or disorder on the isochoric (i.e., volume-preserving process), and sterically encumbering *tert*-butyl groups in the surrounding, as opposed to unprotected benzene or similar stack. d) Close π -stacking interactions of phosphine-benzothiophene-phosphaalkene **22**. A mixture of quasi-slip-stacked and quasi-T-shaped contacts became evident, in addition to a secondary interaction of similar nature between the phosphine phenyl ring and benzothiophene sulfur; e) and f) gold complexes **19** and **21** exhibit intermolecular interactions of potentially increased strength given by the shorter contact distances and increased extent of planarization of the characterizing slip-stacked interactions.

Despite the significant distance (~ 19 Å, Fig. 3.4.2, c)), as conjugative and noncovalent interaction paths advanced in space, Mes* benzene rings (compound **20**) developed their transmissive channel, which is not only attractive with regards to particle transport in various areas but also relevant in accentuating the geometry of the solid-state material system. This instance type is potentially relevant in future applications, given that the surrounding *tert*-butyl groups are sterically encumbering and inclined to exhibit disorder or solid-state dynamical phenomena, which may localize the benzene-ring-superimposed interactions. The bis(benzothiophene)-phosphaalkene gold complex **21** also displayed perpendicular T-shaped CH- π stack interaction involving Mes* benzene rings and benzothiophene proton units, which extended along the crystallographic *b* axis. This interaction was characterized by inter-ring plane deviations of less than 15° between the two rings and short contact distances of ~ 2.7 Å. These two cases provided preliminary evidence for part of our thesis discussion on the utility of the Mes* groups, not only in protecting but also in imposing the creation of orderly domains due to the presence of unsaturated carbon units in the form of benzene rings.

Compound **15** (Fig 3.4.3) crystallized with four independent molecules in the unit cell. In comparison to the benzothiophenes, a decrease in backbone coplanarity was observed, which we had anticipated due to the non-fused backbone, which resulted in or allowed for more significant rotation along the thiophene-thiophene axes. A partial intermolecular analysis revealed the presence of strong VdW interactions between a Mes*-CH₃ methyl group and two sulfur atoms, one of which revealed two proton-sulfur distances ranging from 2.61-2.68 Å, and sulfur methyl carbon distances of 3.08 Å (Fig. 3.4.3 c), VdW radii C + S = 3.50 Å). Nevertheless, these are “atypical” interactions, which can become relevant due to the threefold proton involvement. There exist non-consecutive sets of π -stacking features (quasi-slip-stacked) with distances of ~ 3.50 Å, which are followed by perpendicular- π intermolecular interactions (quasi-T-shaped; C- $\pi \cdots$ C- π , directed from C instead of H) of ~ 3.58 and 3.52 Å. Slip-stacked interactions arise in some sense from steric minimization¹²³ (Fig. 3.4.3 a), b), below). These materials are a valuable addition to the study of NCIs, in contrast to simple polycyclic aromatic hydrocarbon compounds, and complement those with typical bulky or functional groups.

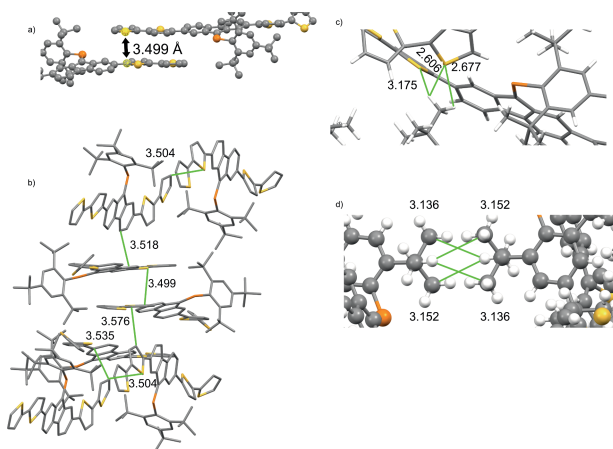


Fig. 3.4.3. Selected intermolecular interaction analysis for bis(bithiophene)-fluorenylidene-phosphaalkene **15**; a) π -stacking feature (quasi-slip-stacked). b) Extended π -stacking feature, exhibiting alternated π -stacked - perpendicular- π interactions (quasi-slip-stacked, quasi-T-shaped). c) $S \cdots (CH_3)$ intermolecular interactions (light-green-dotted line) from two different molecules to the methyl-hydrogen atoms of a third one; these interactions are of the (dipole to dipole + dipole to induced-dipole) type of VdW interaction. d) Attractive London dispersion intermolecular forces via CH_3 - CH_3 interactions.

Angular deviations unveiled the competition between steric minimization and packing forces from idealized geometries typically observed in simpler molecules, such as benzene and other stacks. Additionally, the presence of attractive or repulsive “dispersive force-based” phenomena such as molecular disorder (or solid-state dynamics) or more interactions such as London dispersion between CH_3 groups (Fig. 3.4.3 d)). Solid-state studies of compounds containing *tert*-butyl substituents have shown that the three-site interchange dynamics occurred relatively freely in the solid state, effectively offering a volume-conserving (“isochoric”) systematic process.¹²⁴ It could thus be interesting to quantify the disorder of *tert*-butyl groups based on $Mes^*-E=C-R$, R substituents. Disorder in crystalline phases may be a natural characteristic of functional materials. In crystallography, the presence of the disorder is neither trivial nor less attractive, and this is, from our stance, a future avenue of productive potential, particularly in Mes^* , methyl-containing, or other *tert*-butyl-containing protecting groups.¹²⁵

3.5. Computational chemistry (DFT) study.

This section summarizes the ground state characteristics of six different compounds via DFT. The frontier orbital densities of selected compounds are shown in an organized manner in Scheme 3.5.1 below. Compounds **15** and **16** have a unique LUMO perspective we have not seen previously, where, due to

the extended π -conjugation given by the bithiophene substituents via a second thiophene ring, the LUMO localizes on the acceptor orbitals under the Mes*, whereas the typical fulvene P=C π^* density shifts to the LUMO+1 orbital. The LUMO to LUMO+1 energy differences for **6**, **15**, and **16** were 23.4, 25.7, and 30.8 kcal/mol, respectively, which suggests the stabilization is significant for **15** and **16**.

Compounds **20** and **21** demonstrate the extraordinary conjugation abilities of benzothiophene ligands, expressed by their well-distributed orbital density delocalization across the backbone. Gold (bis)benzothiophene **21** is also distinctly characterized by Mes* density in the LUMO+2. Compounds **20** and **21** also exemplify the subtle differences in expressing π -delocalization as seen by the larger density delocalization (e.g., compare HOMO-1 and LUMO+1 vs. those of **15** and **16**) while suggesting less π -conjugation as observed by XRD group packing intermolecular distances (see above), and UV-Vis-NIR lowest energy absorption maxima (λ_{onsets} **15**, **16**, **18**, **19**, **20**, **21** = 494, 587, 486, 518, 486, 533 nm, respectively).

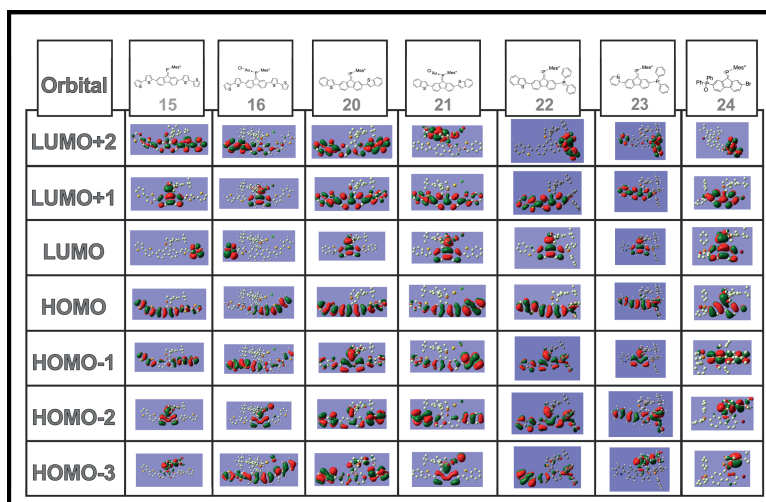
For compound **22**, the LUMO+2 is localized on the diphenylphosphine functional group's π^* orbitals, showing the dual donor-acceptor capabilities of phosphine, typically labeled as a donor. In contrast, the HOMO-3 is localized over the thiophene and phosphine groups with no contribution from the P=C lone pair of electrons, as we had previously observed. Thus, the P=C phosphalkene lone pair was further stabilized by the presence of the P-C phosphine lone pair of electrons. The exotic pyridine phosphine phosphalkene-containing compound **23** lived to its expectations as seen by an interesting *in silico* electronic structure, with a LUMO+2 localized on the thiophene and the phosphine functional group's π^* orbitals, a HOMO-2 of π symmetry over the phosphine fluorene pyridine backbone. The P=C phosphorus electron lone pair density is seen in the HOMO-3 orbital.

In contrast, the pyridine lone pair density is found in the HOMO-5 orbital (HOMO to HOMO-5 ΔE = 29.9 kcal/mol \sim 1.30 eV), which typically "commands" the electronic structure due to its reactive and coordinating lone pair, relationally, relative to the phosphalkene lone pair of electrons. This observation indirectly proves that As=C and P=C group motifs become the "directors", in some sense, of the electronic structure of these compounds. Lastly, the phosphine oxide bromo phosphalkene **24** possesses HOMO (π -symmetry) and HOMO-2 orbitals localized on the P=C bond and P=C lone pair of electrons, respectively, suggesting it is a more reactive species, interestingly.

Compound **23** has a dipole moment of 1.84 D that sits on the fulvenoid carbon buried under the Mes* and is directed away from the central plane towards a phosphine phenyl group. A HOMO-LUMO energy gap of 3.18 eV was calculated. Compound **22** has the lower electronegative sulfur atom (i.e., benzothiophene) compared to the nitrogen of the pyridine substituent. However, it exhibits a more significant dipole moment of 2.82 D. The dipole moment originates similarly, pointing quasi-perpendicularly towards a phosphine

phenyl substituent. A HOMO-LUMO gap of 3.02 eV was found for **22**. These findings are consistent with the increased bipolar character of pyridine substituents, which can act as π -acceptors. The bis(benzothiophene) compound **20** possesses a dipole moment of 2.04 D; a HOMO-LUMO energy gap of 2.99 eV was found.

In comparison, the bis(benzothiophene)-gold complex **21** exhibits a huge dipole moment of 10.66 D, clearly pointing at the significant effect caused by the doubly accepting nature of the P=C and $[\text{Au}]^+$ fragments, in addition to the high electronegativity of the $[\text{Cl}]^-$ ligand ($\text{Cl } \chi = 3.16$). As previously predicted for compound **8** (i.e., thiophene P=C gold complex) in Chapter 2, a decreased HOMO-LUMO energy gap of 2.52 eV was found for compound **21**. Surprisingly, compound **15** exhibited a HOMO-LUMO energy gap of 1.6 eV. The experimentally found electronic spectra optical onset energy (wavelength) of 1.9 eV (~ 633 nm) was the lowest (highest) among the unsubstituted compounds, as presented in detail in the SI of our article, which indicates the different effects provided by the two other thiophene rings, in comparison to annulated benzothiophene, both invigorating cases. Phosphine oxide bromo-substituted product **24** exhibits a dipole moment of 4.66 D and a HOMO-LUMO energy gap of 3.41 eV, which is a crucial example of a compound with a high HOMO-LUMO gap coupled to a potentially high reactivity based on the location of HOMO orbital density on the P=C group motifs, and the higher HOMO-2 orbital energy of the P=C electron lone pair.



Scheme 3.5.1. Frontier molecular orbital densities of **15**, **16**, **20**, **21**, **22**, **23**, **24**; LUMO+2 to HOMO-3. Details are provided in the main text. For **15**, **16**, **20**, **21** (PBE0/6-311G**) and using the same core potential approach and basis sets for gold as described in Ch. 2. For compounds **22** and **23**, PBE0 was not successful, and optimizations were acquired with (B3LYP/6-311G**).

3.6. Summary, conclusions, and outlook.

We reported a large set of new P=C compounds, expanding the family of fluorenylidene-phosphaalkene materials and presenting new functional groups in the 2,7-substituent positions. The compounds exemplified and accentuated some of the exotic characteristics arising from the P=C group motif introduction, for example, by providing synthetic access to unprecedented fluorene-substituted moieties with phosphine and pyridine, while each material also being illustratively represented by an exciting set of distinctive features, as shown by DFT as well as XRD and UV-Vis-NIR studies. Future work should establish dedicated synthetic routes for **22**, **23**, and **24** and further characterize them by electrochemistry. These exciting materials presented significantly decreased HOMO-LUMO and optical gaps based on experimental observations and *in silico* theoretical calculations using DFT and TD-DFT. Perturbation with AuCl substituents enhanced their acceptor properties, which makes these systems relevant and with potential for use in organic electronics.

Ch. 4. Functionalization, reactivity, and interaction of Arsaalkenes, Disilenes, Phosphines, Phosphaalkenes, Siliconoids.

4.1. Introduction and scientific motivations.

The following corresponds to unpublished work from an unfinished project, which we present in this chapter as a manuscript in preparation, discussing scientific, logical, and philosophical aspects of the work, with a presentation of the experimental results corresponding to NMR and DFT characterization only. This section will summarize our introduction and motivation for this project, from general and group 14 perspectives, without dwelling on too many details, concepts, or ideas we have familiarized ourselves with from previous chapters. We will introduce our attempts at incorporating two unsaturated heavy p-block motifs from two crucial groups of the periodic table (14, 15) onto organic frameworks. The presented organic materials contain the following groups simultaneously: disilene-phosphaalkene, disilene-arsaalkene, and phosphaalkene-siliconoid (unsaturated Si_6), which are unprecedented. The preparation or isolation of these compounds serves to trace relations to a wide area of topics. **(1)** The ubiquitous olefins ($\text{C}=\text{C}$) present in biological and artificial networks. **(2)** The small-atom-limit representations of inorganic semiconductors, especially unsaturated segments, either in (or on) the surface or the bulk. **(3)** Connection to important concepts on π -conjugation and aromaticity in their acyclic state and heavy benzene Si_6 unsaturated siliconoid clusters homologs in their cyclic state (e.g., dismutational aromaticity, π -delocalization, through-space π -interaction effects).¹²⁶

Disilenes are reactive under atmospheric conditions in most cases. Several examples of tricoordinate-phosphorus-substituted disilenes and phosphasilenes,¹²⁷ have been shown.¹²⁸ It has been challenging to synthesize disilenes in extended π -frameworks, with only a few examples reported in the literature. To the best of our knowledge, no space-separated phosphaalkene-disilene, arsaalkene-disilene, phosphine-disilene, and phosphaalkene-siliconoid (unsaturated) have been studied to date.¹²⁹ The reactivity of phosphaalkenes varies. At the same time, while some species are highly reactive based on phenomenological observations if “structural frustration” (Ch. 5), low steric protection, or kinetic lability (Ch. 6) is present, some others tend to be more stable in comparison to disilenes and arsaalkenes. Arsaalkenes are difficult to

synthesize and harder to handle. Nevertheless, illustrative examples exist as small molecule units and as we described into polymers. As basic semiconductor units in their inorganic form, we should understand the relation between simultaneous incorporation of unsaturated arsenic or phosphorus, and unsaturated silicon, into organic frameworks.

The multiple heavy bonds and heavy atoms are polarizable and prone to exhibiting distinct types of NCIs. These group motifs also lead to compounds with more elaborate properties than lighter alkene homologs, for example, based on their larger size and potentially realizable electron configurations (e.g., multiple redox states or valence potential, hence, resulting metastable intermediate states or resulting products), along with the NMR spin-active (^{31}P , ^{29}Si).

Further enhancement of electronic and photonic properties can be expected when the concomitant incorporation of two or more such motifs is achieved. Incorporating two atypical group motifs into extended π -conjugated frameworks can generate species with “multiple equilibrium centers”, each respecting mutually exclusive sets of conditions, which may still be used reversibly to establish an interactive (or interaction) image. These mutual or simultaneous types of potentially interfering effects that may negate the establishment of interaction and thus defy some ontological or logical order representation can simultaneously provide access to equilibrium states based on their degree of competitiveness, coupling constant potential, periods, energies, size, and more. These effects can generate reversible access to molecular functionality and modularity.

This functionalization is hard to acquire in small or bare disilenes, siliconoids, phosphalkenes, or arsaalkenes, whose primary reactivity paths under constrained conditions tend to be irreversible (such as rearrangement, cyclization, metallization, or polymerization processes). Interestingly, disilene-silylene, phosphalkene-diphosphetane dynamic equilibria, and others have been reported.¹³⁰

It has been suggested that disilene substituents with bulky pendant groups have favored the dissociation of disilene towards the silylene singlet state, whereas electropositive atoms and π -accepting groups (e.g., P, As; $\text{P}=\text{C}$, $\text{As}=\text{C}$) favored the triplet disilene ($\text{Si}=\text{Si}$) states.¹²⁹ This observation could mean that fluorenylidene phosphalkenes (or fluorenylidene arsaalkenes) with disilene substituents can contain competing functionalities. For example, $\text{P}=\text{C}$ or $\text{As}=\text{C}$ may be stabilizing towards the dissociation of disilenes (to silylenes, for example) by presenting encumbering Mes^* protecting groups in the interactive (or interaction) subspace. However, $\text{P}=\text{C}$ or $\text{As}=\text{C}$ could function as “contextually stabilizing”, for example, by being more electropositive relative to C, C itself acting as a decoupled or indirect factor, since we are considering the electropositivity of either P or As, or $\text{P}=\text{C}$ or $\text{As}=\text{C}$, regarding the occurrence of an effect on the equilibrium of Si in triplet states, or $\text{Si}=\text{Si}$ group motif. Nonetheless, C mediates the covalency of the interactions between

these two independent groups and affects their effective electronegativities via π -framework and σ -framework effects. $\text{P}=\text{C}$ or $\text{As}=\text{C}$ could, in some sense, also stabilize the $\text{Si}=\text{Si}$ state through their π -accepting nature.

Furthermore, while nuclear characteristics are individual, ^{31}P and ^{29}Si atoms cherish magnetically active and abundant $\frac{1}{2}$ nuclear spins (100 and 4.5 %), which can be tuned in parallel. Magnetic energy, stabilization, and interactions can be cherished from tailored utilization of nuclear-nuclear or nuclear-electron interactions of $\text{Si}=\text{Si}$ and $\text{P}=\text{C}$ groups based on resonance frequency profile, selection rules, structural symmetries, and conformational factors, which may be imparted extrinsically.¹³¹ Rotationally free iso-propyl and tert-butyl groups tend to generate solid-state dynamical phenomena, and this should not be categorized as a general disadvantage. It has become clear that increased complexity and functionality can be acquired through the application of correlated disorder¹²⁵ to design functional materials programmatically. These two groups are a source of rotations, which do not increase the volume of the molecular ensemble (i.e., “isochoric” transformations), potentially useful in terms of information or heat dissipation and dispersion.

Towards a meaningful goal, the presence of rotational groups and unsaturated heavy p-block elements is of interest in designing advanced molecular systems in which different functional groups or group motifs can act as group generators, modular forms, interactors, or operators at the few-atom level.¹²⁴ Due to the asymmetric character of many $\text{P}=\text{C}$ (and $\text{As}=\text{C}$), $\text{Si}=\text{Si}$ (and Si_6 siliconoids) group motifs and the intrinsic anisotropic character of their atomic constituents, solution-based or solid-state deposition methods could be designed to pattern orderly domains or segments relative to multi-tube containers, semiconductor or metallic substrate elements, respectively. The magnetically driven resonances from complex environments can be a natural source of selective or stochastic statistical features in optoelectronics or other areas such as fast-pulse quantum NMR processing and other computational paradigms, given the locally complex subspaces of each microenvironment (i.e., isomer types, aggregated neighborhoods, or basins).

Below, we describe these as configurationally locked states or basins. With advanced microelectronics and encapsulation techniques via metal, inorganic, and hybrid materials, organic materials' room for action will expand.¹³² Finally, the low-coordinated silicon, phosphorus, and arsenic organic chemistry of conjugated materials provide an interesting basis to hypothesize about emergent forms in carbon-silicon-(phosphorus) or carbon-silicon-(arsenic) rich and oxygen-(water) deprived or compartmentalized atmospheres. This knowledge can be used in the future, given the fast-paced development.¹³³

Disilenes ($\text{Si}=\text{Si}$), phosphalkenes ($\text{P}=\text{C}$), alkene ($\text{C}=\text{C}$), and arsaalkene ($\text{As}=\text{C}$) moieties can be presented as members of two sets, in which they share equivalences or distinctive features in the form of overlapping effects or properties and contrasting characteristics, for example, on aspects related to bonding isoelectronics, reactivity, stability, and more. In contrast to most alkenes,

the heavy silicon double bonds in disilenes characteristically acquire a geometrical trans-bent conformation to maximize attractive interactions. This attribute resembles the structural differences of arsenic and phosphorus atoms in $\text{As}=\text{C}$ or $\text{P}=\text{C}$, compared to carbon or nitrogen atoms in $\text{C}=\text{C}$, $\text{C}=\text{N}$, or their representative rings. For example, the different planes of the protecting group from $\text{As}=\text{C}$ or $\text{P}=\text{C}$, compared to imines. Like singlet-triplet carbenes, silicon-silicon double bonds may repulsively be driven towards forming separated units with a lone pair of electrons in their frontier orbitals. Singlet states in the form of silylenes (Si in +2 oxidation states; see **32-b**, the primary product from 1:1 arsaalkene disilenide reactions, tentatively categorized as silylenes¹³⁴) can coexist in dynamic equilibria with disilene constituents in fluid solutions.¹²⁹ This transformation occurs in how $\text{P}=\text{C}$ or $\text{As}=\text{C}$ groups contrast with singlet-like phosphinidene and arsinidene moieties. These representations contribute distinctly or simultaneously (when present in an equilibrium) to the detected results following NMR experiments due to their inequivalence on structural, energetic, or electronic factors (see Scheme 4.1.1. d)). The differences in reactivity observed for products between phosphalkene:disilenide, arsaalkene:disilenide (1:1 vs. 1:2 molar ratios), and phosphalkene:siliconoid become particularly relevant in our case, as we will see in the following section. These differences can lead to irreversible transformations to a specific product, as opposed to isostructural reactions occurring at different molar ratios. Furthermore, homologous or lighter phosphalkene:disilenide systems often react equivalently regardless of the molar ratio. In the case of phosphalkene:siliconoid, however, the formation of highly reactive species is avoided through a dynamic equilibrium, as demonstrated by NMR spectroscopy.

In addition to intrinsic structural (i.e., nuclear and electronic) factors that lead to non-isomorphic state and descriptor state representations with some structurally homomorphic representation (e.g., pnictidene types; arsinidene, arsaalkene), the presence of temporary states (e.g., “configurationally locked basins” ~ isomers ~ conformers, and more), which are not representative of a global minimum or even a local minimum among a basin comprising one or more energy minima (e.g., over some arbitrary cycle such as a timeframe), may arise during the preparation of materials. For example, during formation processes involving (I) typically “fast” reactions (e.g., lithium halogen elimination, due to the kinetic and thermodynamic factors given by size and energy of formation), (I) in the presence of frustrated, (I) steric, (I) reactive sites. Also, these occurrences, as observations corresponding to finite states, are driven during an NMR experiment. These properties or states in the solution may be temporary. They may not be visible in a crystalline material in the solid state, a single representation of the locally found structural minima as a lattice, grown a priori within a slowly diffusing crystallization environment. However, it is crucial to study these occurrences in solution so that sophisticated methods and processes allow for their realization in the solid-state,

following distinctive preparative routes or settings, allowing access to this wide “structural variety” in the solid state.

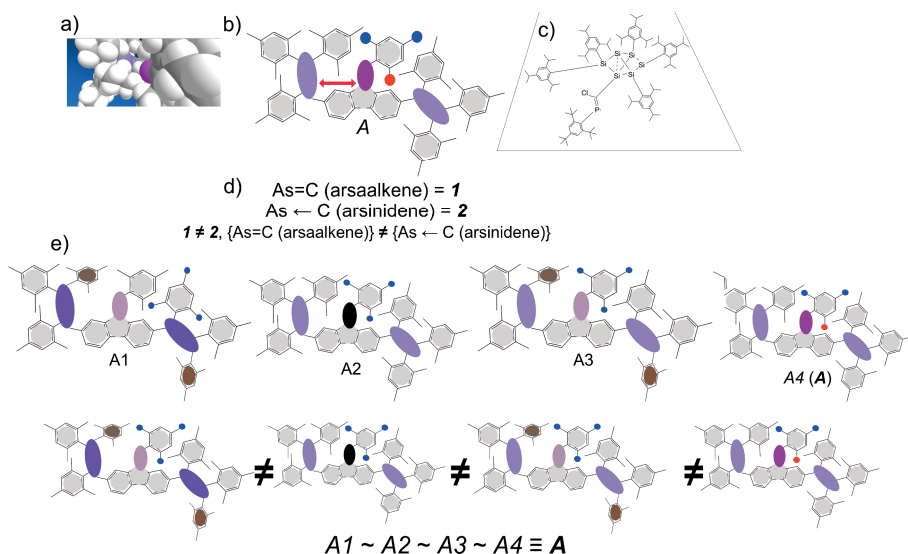
It is critical to describe fundamentally complex interactions in solution, as exemplified by the compounds we present here. They must begin at a basic characterization level (e.g., NMR, DFT), as is typical in complex macromolecules or networks, where standard characterization using many techniques may not be initially possible due to some factors, such as the sensitivity of materials or availability of conforming processes.

Due to (i) crowding, (ii) repulsion, (iii) inherent dynamics, the type of systems studied here can be driven to “configurationally locked” (i) conformations, (ii) states, (iii) basins, in their solid and solution states (see Scheme 4.1.1 e), f)). After some transformation, the structural label descriptor may be in equivalence with a plurality of non-isomorphic structural label descriptor representations (i.e., the chemical structure symbolic state representations in e)), even though these descriptor states (the letter representations in e), i.e., {A1, A2...}) can faithfully be described by the single descriptor (i.e., A, in e)), simply according to Brownian motion or stochastic variation over time or depending of the applied bias, which transforms one symbolic state representation to another over time, and therefore, also their structural label descriptors (state representations).

The observation of NMR signatures corresponding to isomers, rotamers, and resonance during reversible equilibria studies are examples of this notion. Recently, a quantum computing solution instance of a reaction mechanism of a quantum chemistry problem was solved by a superconductor-qubit-based quantum computer (diazene isomerization mechanistic abstractions and energies).¹³⁵ This example is highly relevant, concerning our comment also, because the problems presented here may be cherished as quantum state correlations in a more general setting. We also found an interesting perspective on solid-state structural representations versus descriptor variations; the article’s perspectives established relations between materials and AI, such as the necessity of explaining complex material families whose reactivities differ from those observed through a typical organic chemistry lens.¹³⁶ The authors suggested that some adaptation of classical macroscopic definitions and language was deemed necessary, which fully supports our premises and the type of language used during the thesis, despite its lexical differences with more specialized chemistry fields, which are accustomed to utilizing instances of some language or overgeneralize preconceptions.

Some examples of these notions, relevant here, correspond to (i) locking or locked configurations that occur due to kinetics during synthesis formation or evolution, an effect which is intensified here by the thermodynamic nature of LiBr or LiCl formation (elimination). At the “fast” velocity of the reaction and “slow” velocity of motion variation at slightly lower temperatures (lowest T: 173 K), product formation may occur for vastly different symbolic state descriptor representations, which can be proven to be equivalent under some

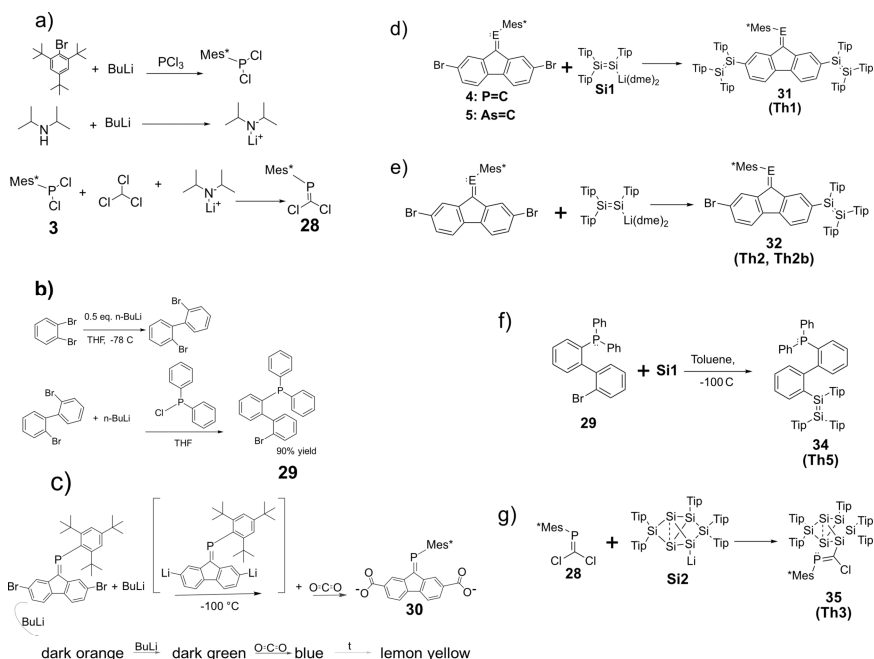
premises, from the mere fact that all byproduct representations correspond to LiBr or LiCl in other cases. This notion is not equivalent to catenates or similar supramolecular structures, which must lose their topology via covalent bonding breakage between sets of transformation-inducing conditions). (ii) Structural conformation driving towards some NMR resonance feature, such as magnetization inequivalence or resonance signal bunching (e.g., while samples spin during NMR). (iii) Reversible equilibrium phenomena characterized as equilibrium forms from many condition observations, such as transient or reversible and broad or enveloped signals. (iv) “Quantum noise” due to coherence or coupling/decoupling along some structural trajectory (e.g., non-diagonal or diagonal t_1 or t_2 noise in 2D-NMR, which is not noise under certain conditions, such as the presence of structural rearrangements, magnetic effects, or dynamic phenomena, as we observe below). (v) Signal dispersion (e.g., separation or broadening). These transformations lead to spectroscopic signatures whose characteristic spectra do not conform to processing techniques, leading to obfuscated or complex spectra (e.g., low intensity, broad signals, and more), which may be easily dismissed or ignored while ignoring all the functionality and wide variety of expression some molecular systems may incorporate. A system must possess some minimum number of salient features to be typified or utilized in some computational fashion. Otherwise, it would be a random generator. For example, a salient feature of π -conjugated acyclic disilenes is the characteristic resonance frequency “quasi-bunching” of ^{29}Si NMR signals at + 70 to 75 ppm for one silicon and + 50 to 55 ppm for the other, with various species presenting characteristic shifts in this narrow region. In our cases below, we will see ^{31}P NMR signal bunching effects towards + 254 ppm, intensified in THF, presented after different phosphaal-kene-disilene experiments from bromo-substituted and (bis)disilene-substituted cases. In most cases where complex applications are envisioned (micro-electronics and nanoelectronics), the understanding and elucidation of these observations are necessary. They should not be confused (or rejected) with the presence of “anomalous”, “noise”, or “impurity” signals, where appropriate (i.e., when they correspond to some form or type, in correspondence with the flow of the experiment, or with some first-principles characterization of their features, and not a trivial or extremely non-trivial/random spectroscopic response). Therefore, even though some of the signatures and NMR resonances we observed and described below may not conform to the degree of typicality expressed by the NMR spectra of simpler molecules, in the cases we present below, the absence of tidiness does not represent “dirtiness” or “impurity”. Therefore, we believe it is imperative to report these results, given the high complexity and exciting nature of the presented families of molecules and their spectral responses, our efforts, coupled with our motivations and interests, which were elementarily or succinctly explained above. (Scheme 4.2.1 below).



Scheme 4.1.1. a) Van der Waals sphere representation of the phosphorus-silicon-carbon-hydrogen; compound b) highlighted using double-headed red arrow. b) Scheme Tip-Mes*-fluorenylidene core. Light purple ellipsoids correspond to Si=Si, and the dark to P=C (or As=C). Mes* *tert*-butyl depicted as blue circles. c) Chemical structure representation of siliconoid-phosphaalkene highlighting the complexity of these compounds (difficult to draw with standard organic chemistry representation methods due to the high number of protecting groups). d) A comparison of elemental relations between "normally polarized arsaalkenes" & arsinidene singlet-like compounds shows inequivalence in structural label descriptors (i.e., **1** and **2**) and chemical structure-based symbolic state representations (i.e., bonding chemical formula). The above analogy applies to silylene vs. disilene, which, despite their similarities, exhibit fundamental differences in their chemistry and spectral properties. We must treat them differently and consider their unique characteristics when analyzing their behavior. e) However, in complex molecular structures, such as those with magnetically active unsaturated heteroatoms and large rotational groups, some symbolic state physical representations may become configurationally locked during compound formation, following a bias, or NMR experiments. While these symbolic state representations are not isomorphic, they can be expressed as equivalent structural label descriptors (e.g., **A**) due to the reversible nature of the interactions and the finite temperature. However, certain initial state representations (e.g., **A4**) may be privileged due to their energy, generating familiar symbolic or descriptor state representations. It is important to note that these equivalent descriptors do not necessarily indicate structural (electronic or nuclear) equivalence, especially when considering configurationally locked species, isomers, and conformers. The sequences or cycles that transform, for example, **A4** to **A1**, provide a rich source of computability, probability, and statistical properties that can be valuable in fields such as optoelectronics, classical/quantum machine learning, neuromorphic computation, and quantum information processing. These **configurationally locked basins** differ dramatically from similar concepts in typical organic chemistry (conformers, catenates, isomers) due to the higher steric constraints and low-coordinated π -conjugated environments with heavy NMR active main group elements. These basins have finite and workable spaces (or microlocal environments), resulting in dynamic (yet, discrete in a sense) frequencies/chemical shifts and other magnetic, optical, electronic, and structural properties of high interest.

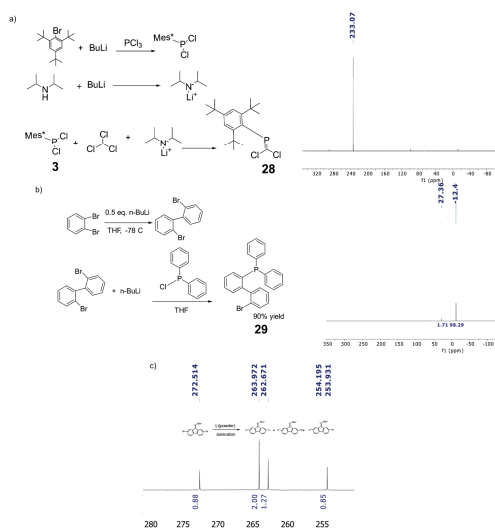
4.2. Synthesis and NMR characterization. Salient features of phosphalkene, arsaalkene, disilene, materials (steric hindrance, magnetic/structural inequivalences, π -conjugation effects) with potential applications. Comparison with phosphine-disilene compound with limited features. Evidence of dynamic equilibrium between phosphalkene/phosphindole-siliconoid species.

Synthesis of the presented compounds involves mixing the reactants and reagents in a solvent medium, lithium halogen elimination, and subsequent product formation. All reactions and products must be performed and kept in anhydrous and deoxygenated conditions. The concentration of the samples and extraction into nonpolar solvents, followed by concentration, led to dark materials in visibly microcrystalline states, which we could not crystallize as large crystals for XRD. Despite their high reactivity, the compounds were highly stable under anhydrous and deoxygenated conditions (kept in glove-box; 1 ppm H₂O, 1 ppm O₂). During our study, we checked sealed NMR mixtures or redissolved product solutions over 2-3 weeks, with no observable changes in major spectral features, aside from brief observations corresponding to statistical ensembles or dynamical responses due to slight changes in the environment over time or slight changes in measurement conditions. However, we confirmed successful reactions involving disilenides with fluorenylidene-phosphalkenes, fluorenylidene-arsaalkene (tentatively accompanied by a different reactivity path in the 1:1 molar case), siliconoid-phosphalkene/phosphindole equilibrium formation or simply the formation of both products, and disilene-phosphine preparation, as confirmed by multinuclear NMR spectroscopy. The resulting reaction products and mixtures show intriguing and reproducible NMR signatures, exhibiting atypical and consistent phenomena in a wide range of experiments. These phenomena result from dynamic and magnetic effects as nuclear-electronic transformations occur, leading to non-trivial phenomena such as magnetic inequivalence, conformers as configurationally locked basins, potential equilibrium formation, and resonance bunching limits in the product spectra. These effects were observed in both concentrated and dilute mixtures.



Scheme 4.2.1. Reaction conditions, structural formulas, and label descriptors (parenthesis labels agree with the theoretical model names) of studied compounds. a) Synthesis of dichloromethylene-phosphaalkene **28**. b) Synthesis of bromo-substituted phosphine **29**. c) Formation of lithiated phosphaaalkene, followed by carboxylic acid (**30**) transformation (color changes describe transformation sequence as reagents were added). d) Low temperature; various solvents (benzene, THF, toluene). Dibromo-phosphaalkene **4** or dibromo-arsaalkene **5** reacted with disilenide **Si1** in a 1:2 ratio, leading to **31** (P=C) or **33** (As=C). As an inclusion, NMR results for unknown compound **32-b** from the 1:1 reaction between arsaalkene and disilenide will be briefly shown below (unknown structure). e) Reactions between **4** and **Si1** in a 1:1 ratio led to **32** (P=C). f) Reaction between phosphine (**29**) and **Si1** led to **34**. g) Reactions between **28** and **Si2**, with the formation of **35**.

Disilenide (**Si1**) and anionic siliconoid (**Si2**) were prepared as reported previously. The ^{29}Si NMR signals of **Si1** occurred at + 101 and + 95 ppm (benzene-*d*₆). Compounds **28** and **29** were synthesized following a modified literature procedure.¹³⁷

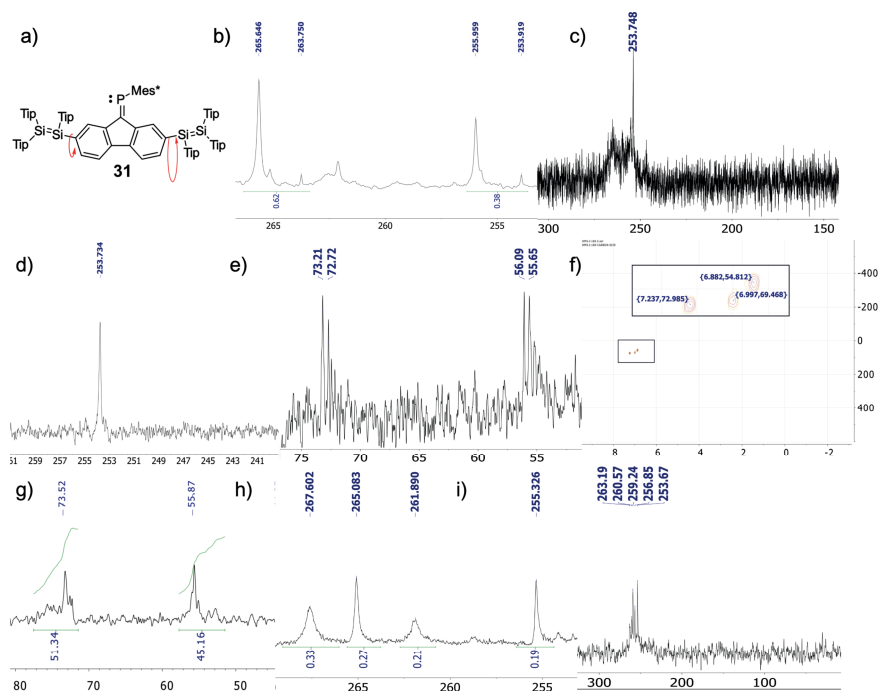


Scheme 4.2.2. Synthesis of a) **28**, b) **29**. c) Varied approach towards compound **30**. Dilithiated phosphaaalkenes achieved, despite slight impurities in the phosphine and phosphine oxide region, the process is promising towards synthesizing peripherally-lithiated phosphaaalkene motifs—reaction conditions: glove box, activated lithium powder, sonication.

Compound **31** was prepared by reacting **4** and **Si1** in a 1:2 ratio. For example, to a THF or toluene solution of **Si1** (2 eq.) at -80 °C, 1 eq. of **4** was added, yielding a dark green mixture. NMR spectra of **31** are shown below. Assignments were supported by 2D HMBC and traced relations across sequences of experiments. The spectra were complex and crowded; nevertheless, the reactions yielded P=C, and Si=Si signals only, agreeing with the formation of **31**. DFT models (see below) displayed regions of high electron density via through-space interactions, which becomes interesting from the perspective of π -delocalization/ π -delocalization/sterically-encumbering environment effects. The presence of transient or equilibria-derived species such as rotamers, isomers, and conformational networks can be abstracted from broad signals. Though they possess different “microlocal environments” during some period, these are representative of the same type of functional group based on chemical shifts (“structural label” or “descriptor” as stipulated before).

The presence of non-trivial effects in ²⁹Si and ³¹P NMR spectroscopy was evident. Magnetic and dynamic effects can lead to signal number and strength inequivalences due to the relative enhancement of some other signals. We validated this by the 1:1 correspondence between the two major P=C ³¹P NMR resonances in C₆D₆ compared to the corresponding 2 ppm deshielded neighboring “satellites” in each case (see Scheme 4.2.3. b). While intensity ratio and chemical shift separation confirmed that each feature was related to each of the more prominent neighboring peaks on the left, they were not typical satellites. In THF, the “doublet-like” or two set of signals was again observed

as a broad envelope (Fig. 4.2.3 c)), accompanied by an inner sharp and unique signal corresponding to the expected product behavior (more details after the figure); in other cases such as in i) (taken two weeks after NMR sample preparation; more details below)), the same underlying two-peak-set was observed but this time many inner sharp peaks were present, which shows that the “configurationally locked species” becomes available and can persist in the experimental energies, which is typically seen as an impossibility in “typical” organic molecules. As we have demonstrated, these phenomena, consistent with our arguments about non-trivialities and configurationally locked basins, become relevant in different environments and settings. A second experiment was performed on the well-dissolved sample shown in c) a few hours later and after thoroughly shaking the solution. This procedure resulted in a single signal in the spectrum shown in d), confirming the functional presence of the structural motifs (see Scheme 4.2.3 d) and caption). The observation in c) cannot be attributed to macroscopic inhomogeneities caused by undissolved material since it was well dissolved. Further supporting the exclusion of trivial errors, the “doublet-like” two-peak maximum envelope feature observed in c) is like that observed for the more prominent two peaks in benzene in b).



Scheme 4.2.3. a) Reaction conditions and formulas, **31**. b) ^{31}P NMR exhibited two major signals. Only P=C signals were evidenced. Two “satellite” peaks in equivalence to the two signals indicated magnetic inequivalence, which generated two phosphorus resonances. c) ^{31}P NMR of **31** (THF- d_8). Redox processes and higher solubility yielded species that aggregate in orderly segments or domains over time. Thereby, the simultaneous presence of a strong signal (+ 253.75 ppm) over broader envelopes (with two clear maxima). d) NMR measurement after mixing the same sample thoroughly, yielded one strong signal at + 253.73 ppm, supporting our arguments and suggesting that orderly (orderly by their two-maxima peak exhibition, for example) domains here, matched to the broad envelopes. A homologous behavior was observed for a Si_6H_6 aromatic heavy benzene analog in THF solvent.¹³⁸ e) ^{29}Si NMR of **31** in benzene- d_6 . Four major disilene signals representative of **31** can be observed. f) 2D ^1H ^{29}Si HMBC spectrum of **31** in toluene. ^1H ^{29}Si NMR ((300, 60) MHz, Tol) δ = (+ 6.88, + 54.81), (+ 7.00, + 69.47), (+ 7.24, + 72.985). The experiments confirmed major product formation based on silicon signals at + 72 ppm + 55 ppm, with no redox products. The signals at + 72 ppm showed two proton correlations compared to the single-correlated signal at + 55 ppm, which can be caused by the higher correlation of one silicon versus the other from a chemical environment perspective (e.g., E/Z isomerism, conformationally locked, increased π -conjugation, and more). g) ^{29}Si NMR spectrum confirmed major product formation in toluene. h) ^{31}P NMR **31** in toluene. Four P=C signals become evident, showing the configurationally locked basin view is achievable within experimental ranges (see main text). i) ^{31}P NMR experiment (THF) carried out from a different batch two weeks after the NMR sample was prepared confirmed only P=C signals were present.

In Scheme 4.2.3 h) and i), we present two different experiments which help us validate some of our premises (more details in the Scheme’s caption), such

as the presence of configurationally locked basins as potential conformers as seen in the toluene experiment in h) and the "bunching limit" at $\sim +254$ ppm in the THF experiment shown in i). In h), we show an experiment in toluene several hours after preparation, which showed 4 signals attributed to phosphalkene-containing structures, consisting of two pairs of "homologous" structures based on the similar shapes of the two sets present. Two of the signals appeared broader than the other two, and there was a variation in their concentration ratio. This observation suggests that the sample may contain two homologous structures or similar isomers. The ratio of each of the two signals is approximately 1.5 in both cases, indicating the possibility of a non-trivial magnetic inequivalence effect, which was observed for equivalent structures (in some sense confirmed by ^{29}Si NMR integrals and the number of signals). Therefore, it is possible that the 4 signals do not necessarily represent four different structures but rather two sets of similar or homologous structures in different ratios, which is very intriguing. The experiments in h) and i) (relative to b) and c), respectively) highlight the possibility of obtaining configurationally locked basins within the experimental range of available energies. The "bunching limit" at $+254$ ppm in toluene instead of THF suggests a structural population resonating at the limited frequency. In i) above, an experiment was characterized by five underlying sharp resonances from $+263$ to $+254$ ppm (over a broad envelope), showing the bunching effect towards $+254$ ppm and the presence of many configurationally locked isomers, in contrast to the experiment in c), as we argued above.

For typical organic compounds, and even for homologous compounds that simultaneously carry only one set of heavy p-block elements or groups (e.g., either 1 P=C or 1 Si=Si and 1 or 3 protecting groups, respectively, as opposed to 2 Si=Si and 1 P=C and **7 protecting groups per molecule** as in **31**), we fail to recognize or appreciate the simultaneous presence of structurally locked isomers (i.e., "configurationally locked basins") due to **(I)** their lower steric constraints, **(II)** narrower energy ranges for "equivalent structures", and **(III)** free rotational barriers, coupled with **(IV)** the absence of simultaneously present characteristic nuclei (^{31}P and ^{29}Si) in "unusual bonding" situations (and constrained environments).

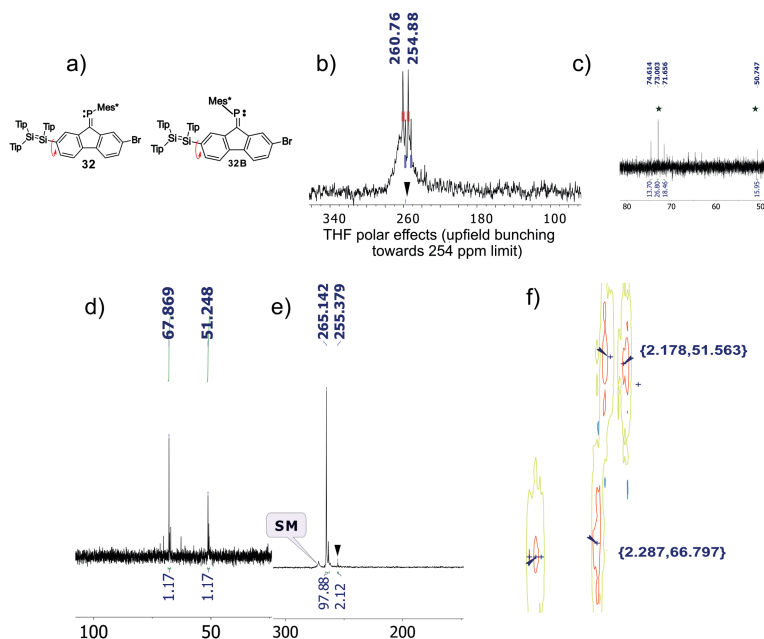
Without going into details, as we discuss and argue, we can think of the broad "envelope signal" of **31** as a "structural base" or "stack" from which one operates and "acquires" available "configurationally locked basins" as resonances or changes in the number of signals or intensity ratios, by changing environmental variables and parameters (e.g., spinning, temperature, additives, NMR pulse shape and intensity, secondary fields, and more). The "bunching limit" at $+254$ ppm for **31** provides the necessary boundaries or typicality for structurally allowable phosphalkene-disilene (in this case) configurations to be of computational value. Other features, such as **(1)** "inner resonances" (i.e., sharp peaks within the broad envelope or base) or **(2)** peaks within the range of allowable frequencies "for phosphalkene-disilene

environments" (or based on our problem), (3) ^1H - ^{29}Si 2D NMR correlations, (4) non-trivial magnetic/structural inequivalences based on peak intensity ratios, are consequences of the construction of these structural motifs, that live for a time or under a set of boundaries/limits within a "configurationally locked basin", some of which become accessible within the experimental ranges.

Compared to "typical" organic molecules, these atypical and bulky systems offer higher steric constraints (higher resistance to noise while maintaining controlled and accessible rotational barriers via ^1H NMR (and ^{31}P and ^{29}Si spectroscopy). The range of workability for configurationally locked basins allows them to encode and store information while establishing complex relationships between different basins based on environmental constraints, the compounds themselves, variables and conditions, including NMR pulses.

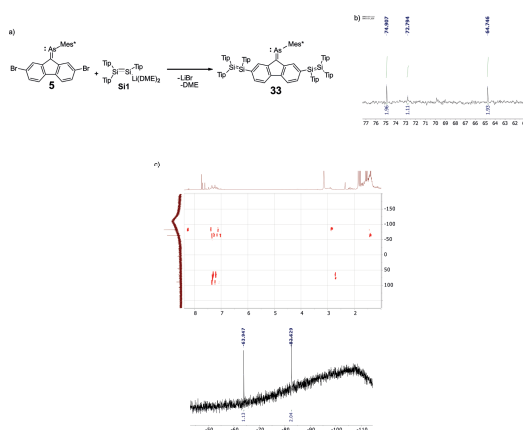
When we approach these systems from a fluidic and functional standpoint, we must let go of preconceived notions ("purity" or "single resonances") and instead focus on understanding the underlying principles that govern the observed phenomena. By doing so, we can better understand the inherent complexity and potential of these systems and effectively apply this knowledge to engineering and real-world applications.

We will now describe the reactions between **4** and **Si1** in a 1:1 stoichiometric ratio (Scheme 4.2.4), which were performed at room temperature inside a glovebox (< 1 ppm O_2 and H_2O). Product **32** was initially obtained with an intermediate yield of $\sim 80\%$ in THF due to increased redox processes or the higher temperature in the glovebox (see Scheme 4.2.4, b) and c)). We confirmed two phenomena reproducibly concerning the previous 1:2 molar experiments. (1) The THF solvent induced coalescence of the ^{31}P NMR signals. (2) The "bunching" or clustering of the resonance signals towards $+254$ ppm, which acts as a limit. Both phenomena suggested some ensemble or statistical equivalent effect for homomorphic or partially equivalent representations containing disilene-fluorene-phosphaalkene structures, which is enhanced in THF. After confirmation by toluene experiments, we can see the presence of two apparent isomers or non-equivalent forms in THF experiments, which we labeled, **32** as the major and **32B** as the minor (see two red squares, two thin blue strips in b)). We found out there is not a large energetic compromise between the DFT final energies of the two isomers in their optimized structure; however, one must consider that the formation may give a different picture. The main signal differed by > 5 ppm relative to the analogous signal observed for **31** in THF, confirming the novel nature of product **32**. The two major ^{29}Si NMR resonances at $+64.71$ and $+73.01$ ppm further confirmed this assignment. They were also accompanied by minor signals at $+74.62$ and $+71.66$ ppm, supporting the configurationally locked basin or isomeric picture.¹³⁹ Based on the 2D ^1H ^{29}Si correlation experiments, **31** has a more substantial π -conjugated/ π -delocalized backbone than **32**, given it correlated to fluorene, whereas the correlations here for **32** were to Tip proton groups.



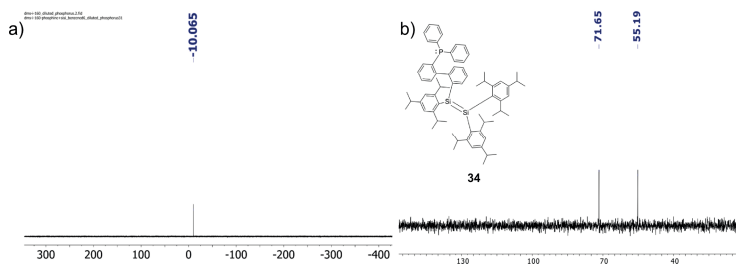
Scheme 4.2.4. a) Formulas of **32** (and **32B**). b) ^{31}P NMR experiment with 1:1 (phosphaalkene:disilene) molar ratio showed two sets of equivalent doublet-like signals. The minor set of resonances was more extensive and farther away from the more intense set (~ 3.1 ppm to the right in each case vs. ~ 2 ppm above). In the absence of coupling (no 100 % active nuclei) or two sets of signals of groups of phosphorus atoms per molecule (see e), for example, which shows only one primary resonance), we attribute this observation to a non-trivial effect related to the configurationally locked basin views. The broad peak envelope in the background indicates the presence of additional derivatives (which can be “operated” or “lifted” via environmental variable or NMR pulse changes). c) In the THF ^{29}Si NMR experiment, we observed four significant signals corresponding to **32** (and **32B**). One of the signals at + 73 ppm was more intense, providing further evidence for magnetic/structural causing integer peak ratios to be non-integer. d) Tol exp. confirmed greater success of reaction in the non-polar medium, characterized by two signals corresponding to **32** (major). Note their 1:2 intensity ratio due to magnetic and structural effects caused by the asymmetry induced by Mes* and P=C and the bulky environment, confirming our arguments above. e) ^{31}P NMR (Tol) showed a primary signal (+ 265.1 ppm), accompanied by a small isomeric signal (**32B**) as well as by a third signal (see inset) at + 255.4 ppm, close to the “bunching limit we have argued. f) 2D ^1H ^{29}Si HMBC spectroscopy confirmed the correlations between the two silicon atoms of **32** and proton atoms in the periphery. The proton signal correlation regions (+ 2.50 and + 2.25 ppm) provided convincing evidence for the structural assignments of **32** and **31**. Notably, the absence of the doubly substituted disilene-fluorenylidene-phosphaalkene core in **32** led to silicon-proton correlations with peripheral Tip protons rather than aromatic fluorene protons as in **31**, demonstrating the increased π -conjugation of **31**. In some scenarios where we might have been wrong, we would have expected to see either the same correlations in both experiments if the signals were associated with the aromatic protons on Tip in the first measurement above or a mixture of resonances in the former or the latter, neither of which was shown in the results.

We will briefly describe the 1:2 ratio experiments between dibromoarsaalkene **5** and **Si1** (Scheme 4.2.5), resulting in **33**. The experiment was performed in toluene at a low temperature, yielding a dark green solution as the reaction progressed and a dark solid after concentration. The ^{29}Si NMR produced three unique major peaks at + 74.91 ppm and + 64.75 ppm and another resonance at + 72.79 ppm. We believe that the results confirm our premises that **33** is the primary product since the major resonances occurred in the disilene region and were present as non-integer factors relative to the four expected resonances and integral integer ratios. These observations were previously attributed to non-trivial effects, structural (or magnetic) effects (or inequivalences), an idea we further strengthened in our experiments using heavier As=C instead of P=C group motifs. No significant redox product formation was observed.



Scheme 4.2.5. a) Structural formula, formation of **33**. b) ^{29}Si NMR spectrum of **33**. Major products appeared at + 74.91 and + 64.75 ppm. c) 2D ^{29}Si ^1H correlation spectroscopy of the reaction between disilene and arsaalkene **5** in a 1:1 ratio. Unknown product **32-b**, not to be confused with **32B** above, was formed as the primary product. Based on the shielded peaks (see lower spectrum), we hypothesize that two silylenes were formed in solution over time, relative to the 1:2 experiment above. The minor products (high-frequency and deshielded peaks) matched the signals for the redox byproduct and the expected disilene product in lesser amounts. One of the major reaction products is coupled to a deshielded proton corresponding to the fluorene distinguished by Mes^* asymmetry, whereas the other one is not, supporting our assignments for two silylenes in solution.

We will now describe the reactions between phosphine **29** and disilene **Si1** (Scheme 4.2.6), performed in toluene at -100°C , yielding a dark yellow-green product (compound **34**). The reaction proceeded smoothly, with a single ^{31}P NMR resonance at -10.07 ppm corresponding to the phosphine, and ^{29}Si NMR signals found at + 71.65 and + 55.19 ppm for the disilene. In contrast, the starting material **29** displayed a single ^{31}P NMR resonance at -13.02 ppm in the same experimental conditions.



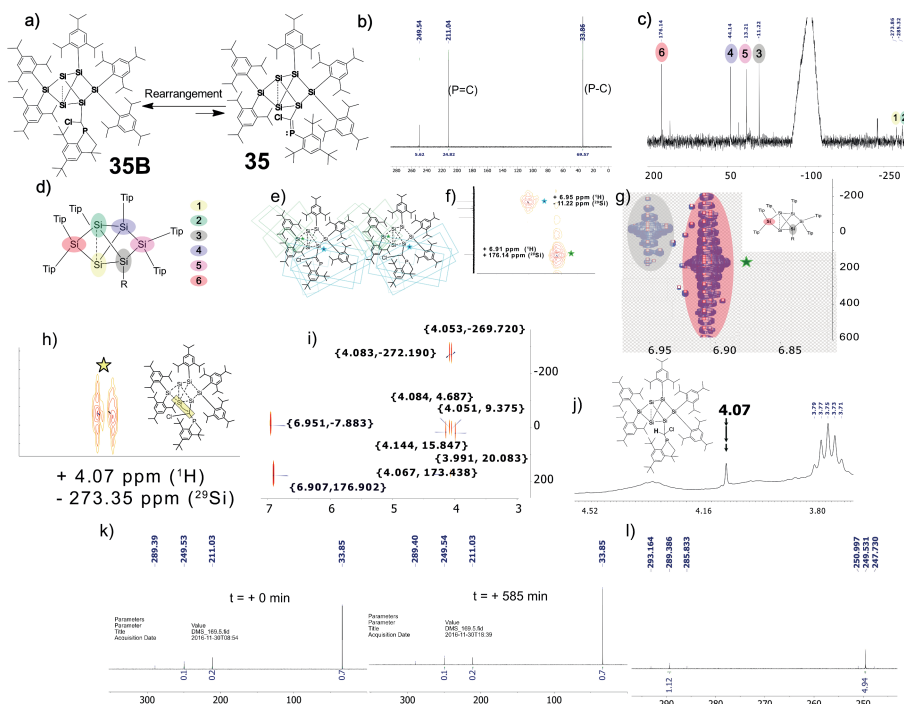
Scheme 4.2.6. a) ^{31}P NMR spectrum of **34**. b) ^{29}Si NMR spectrum of **34**. Primary product formation can be confirmed based on the spectra.

From the NMR spectra obtained for **34**, the much higher complexity of the previous reactions between disilenides and fluorenylidene $\text{P}=\text{C}$ and $\text{As}=\text{C}$ compounds was evident. Compound **34** is fascinating, given the spatially separated phosphine-disilene motifs, in the same system. The absence of π -conjugation may be responsible for the yellow color ascribed to the compound. TD-DFT results confirmed that the main electronic transition for **34** (**Th5**) occurs at ~ 457 nm, whereas for the previously studied compounds it occurs in the 750-800 nm range. There are several factors that influence the simplicity of the spectrum with respect to the previous observations. These factors include the absence of π -conjugation and rotation along single bonds, as well as the absence of some of the bulky groups (1 Mes* and 3 additional tip protecting groups for 1:2 molar ratio $\text{P}=\text{C}/\text{Si}=\text{Si}$ reactions). This absence confirms or validates our previous assignments and identifying of the salient features for the fluorenylidene compounds with two different ($\text{Si}=\text{Si}$ and $\text{P}=\text{C}$ or $\text{As}=\text{C}$) group motifs and no heavy Mes* substituents, plus extended conjugation thanks to the fluorene and $\text{E}=\text{C}$, as relevant and of potential value.

Finally, we will describe the results of reactions between methylene-chloride-phosphaalkene **28** and anionic siliconoid **Si2**, which are aimed at preparing an unprecedented, unsaturated siliconoid-phosphaalkene product (see Scheme 4.2.7 below). The phosphaalkene starting material **28** displayed a ^{31}P NMR chemical shift resonance at + 232.86 ppm in benzene-*d*₆, while **Si2** (anionic siliconoid starting material) presented six ^{29}Si NMR signals at + 160 (Tip₂-Si), + 28 (Tip-Si), + 13 (Tip₂-Si), - 67 (Si-Li), - 237 (Si), and - 238 (Si) ppm. We performed experiments under Schlenk conditions and glove box as before. The mixtures immediately turned dark orange. The main ^{29}Si NMR resonances occurred at + 176 (s), +44 (s), +13 (s), -11 (s), -274 (br), and - 285 (br) ppm, which confirmed the formation of a new siliconoid species. The main ^{31}P NMR signals appeared as sharp singlets at + 249.5 ($\text{P}=\text{C}'$ derivative or $\text{P}-\text{Si}$ product), + 211.0 ($\text{P}=\text{C}$), and + 33.9 ($\text{P}-\text{C}$) ppm. Based on our analysis, $\text{P}=\text{C}$ product formation occurred, which reacted toward the main product (+ 33.9 ppm) by establishing a CH-activated phosphindole isomer situation in a dynamic equilibrium (see below). The experimental data for product [**35**, **35B**] are shown in Scheme 4.2.7.

Before defending the existence of a dynamic equilibrium, we would like to develop the arguments that led us there. Several salient features suggested the possibility of a dynamic equilibrium phenomenon between the desired product and the available CH-activated phosphindole isomer. While the data obtained could be compatible with the formation of two major products, including a decomposition product of the initially formed P=C species at + 33 ppm, we have evidence that strongly supports the formation of dynamic equilibrium phenomena instead. This evidence includes (i) the presence of six siliconoid signals in the ^{29}Si NMR spectrum (as opposed to 12 relevant signals in the spectra), (ii) the expected correlation of a methylene proton with four silicon atoms of the siliconoid (all except Si 4 and Si 2) as seen in i), (iii) broadened and shielded signals for the *nudo* silicon atoms and (iv) dynamic signals that vary significantly in the chemical shift for two relevant silicon atoms (Si 3 and Si 6, in addition to the broadened Si 1 and Si 2) in the large structural rearrangement process. Very importantly, (v) a control experiment performed 10 hours after the initial measurement showed no decomposition of the P=C signal, indicating a constant ratio between the two species, as expected in a dynamic equilibrium. (vi) Satellite features in the ^{31}P NMR spectrum of two minor species associated with byproducts, in contrast to the two larger peaks, which possessed many ^{29}Si satellites in the form of a multiplet, which we associate with the structural rearrangements and occurrences during the transformation process during the dynamic equilibrium.

This type of ring closure is typically observed in processes where terminal phosphinidene compounds are thought to have formed as intermediates.^{140,141} However, in this specific case, such an intermediate could only be explained by very unusual [P - C - Si] bonding situations. Alternatively, the formation of product **35B** could be avoided by the existence of an equilibrium or reversible exchange between P=C and phosphindole species (i.e., [**35**, **35B**]) rather than driving the formation of product **35B** in an irreversible process. Although tentative, this possibility would imply the initial absence of a P=C species and could be energetically favorable by avoiding the formation of unreactive intermediates. The observed equilibrium or reaction process-derived product does not break the covalent structure of the siliconoid cluster, as the six siliconoid signals initially obtained by ^{29}Si NMR persisted over time. Some slight shift variations were observed, as shown in Scheme 4.2.7. f), g), h), and i), relative to the early experiments. These variations are a manifestation of the dynamic process based on the chemical shift dispersion of a few crucial silicon atoms, such as Si 3 and Si 6, which showed changes of $\pm 5\text{-}10$ ppm according to the data, while other relevant silicon atoms remained constant with variations of only ± 2 ppm.



Scheme 4.2.7. a) The reaction formula and the product **[35, 35B]** are shown. b) ^{31}P NMR spectrum of **[35, 35B]** is shown. c) Schematic representation of siliconoid atoms is shown with numbers and colored ellipsoids. It is assumed that no change in silicon covalent bonding occurred during the equilibrium. d) ^{29}Si NMR spectrum of **[35, 35B]** is shown. e) A schematic of the long-range correlations of Si 6 and Si 3 in **[35, 35B]** is shown. f) A 2D ^{29}Si ^1H HMBC shows correlations between aromatic Tip-H groups and corresponding silicon atoms (Si 3 and Si 6). g) 2D ^{29}Si ^1H HMBC correlations are shown as disks (rings) with areas proportional to the contoured values to better illustrate the extensive pattern signaling the existence of dynamical events associated with structural variations of Si 6. h) 2D ^{29}Si ^1H HMBC shows critical correlation signals from highly shielded Si 1 to the **35B** methylene proton signal of the equilibrium product. i) 2D ^{29}Si ^1H HMBC nicely shows equilibrium traces based on chemical shift dispersion indicating structural changes of silicon atoms, including Si 3, during the equilibrium exchange from **35** to **35B**. j) ^1H NMR of **[35, 35B]** illustrates the equilibrium exchange process by showing the methylene proton singlet signal at + 4.07 ppm. k) ^{31}P NMR spectra of the sample **[35, 35B]** taken at different times (10 hours apart) showed a constant signal ratio, supporting the idea of a dynamic equilibrium as opposed to an irreversible reaction that should decompose the phosphalkene. l) The ^{31}P NMR spectrum of **[35, 35B]** shows two distinct and highly deshielded sets of signals for which detectable silicon satellites are observed. These signals correspond to by-products, while the two primary signals (not shown) have a high number of silicon satellites but are not well-resolved due to a poor signal-to-noise ratio.

The sharpness of four of the six silicon resonances is attributed to the high solubility of the siliconoid clusters, whereas the two *nudo* vertex signals

exhibited significantly broadened resonances due to the nature of the fluctuation processes in solution.

Structural flexibility and respective rearrangements broaden the two resonances at the lowest chemical shifts (i.e., Si 1, Si 2 *nudo* vertices and associated NMR peaks), stabilizing the rearrangement processes during equilibrium. The six siliconoid signals are consistent with previous NMR chemical shifts based on functionalized siliconoids. In the ^{13}C NMR spectrum, a high-intensity doublet was detected at + 168.13 ppm (d, $J = 57.3$ Hz), the characteristic ^{13}C NMR region of P=C carbon resonances. A low-intensity doublet was found adjacent to this signal at $\sim + 167.4$ ppm (d, $J = 34.36$ Hz), indicating the presence of equilibrium phenomena or statistical isomers. Detectable silicon satellites were observed for the ^{29}Si NMR signals at + 289 ppm (1 % yield) and + 249 ppm (5 % yield) with calculated coupling constants of 450 Hz and 200 Hz, respectively (see Scheme 4.2.7 1) above). Several satellites were observed in a multiplet pattern for the two primary signals at + 211 ppm (30% yield) and + 33 ppm (63 % yield). However, the coupling constants from 2 to ~ 12 Hz before the noise cutoff still need to be resolved, a finding which nevertheless still supports the premises of equilibrium and corresponding structural rearrangements.

It is well-known that ^{31}P NMR signals can be influenced by variations in the environment surrounding phosphorus nuclei from solution or solid samples. Thus, the ^{31}P NMR resonance assignment at + 33.9 ppm for the CH-activated phosphindole equilibrium isomer is sound and in excellent agreement with the spectral evidence obtained and relates well to other similar types of compounds, such as the simpler phosphindoles.¹⁴⁰ Equilibria, reversibility, rearrangement, and irreversibility phenomena are intrinsically linked to the functionality of silicon networks, with similar events reported for siliconoids, disilenes, and phosphaaalkenes. The available information strongly suggests the formation of equilibrium products, with dynamical features associated with reversible and salient feature changes observed with high typicality, representing a potentially relevant development in the field. For example, in the most recent instance with methylene P=C and unsaturated siliconoids, observations of proton, heteronuclear, correlated NMR signatures (and correlated disk/ring behavior) were intricately linked to the demonstration of modulated behavior via structural rearrangements and signal dispersion (coupled to signal or structural stability) in the ^{29}Si NMR spectrum and signal diversity in the ^{31}P NMR spectrum. These materials may represent the first examples of two challenging and sophisticated families of organic materials that simultaneously include variations of the Si=Si, Si₆, and P=C, As=C group motifs: (1) disilene and phosphaaalkene or arsaalkene mutual incorporation into extended π -conjugated frameworks. (2) Unsaturated siliconoid and phosphaaalkene mutual incorporation into conjugated frameworks.

4.3. Computational characterization of phosphalkene-disilene-containing material, phosphalkene-siliconoid, phosphine-disilene. Analysis of orbital densities and energies, optical gaps, and π -delocalization using DFT and TD-DFT.

The characterization of the resulting materials was complemented by computational methods (DFT and TD-DFT), which helped us understand these fascinating compounds. DFT methods helped characterizing the structural, electronic, and basic optoelectronic properties of the systems, which exhibited interesting orbital densities characterized by exciting geometries and orbital densities due to the presence of heavier elements bonded in sterically encumbered π -networks. Significantly reduced HOMO-LUMO and frontier energy and optical gaps are observed computationally. We will discuss the main computational results.

Ground-state geometries were obtained and confirmed after optimization and frequency calculations using the B3LYP-D3 functional with the 6-311G** basis set. In some cases, we made use of the long-range interaction-optimized CAM-B3LYP. B3LYP tends to underestimate the optical and HOMO-LUMO gaps of organic compounds that possess long-range charge transfer interactions, so CAM-B3LYP has been designed for excited state calculations of such systems.¹⁴² In the past, CAM-B3LYP overestimated these gaps versus B3LYP and experimental data from CV and UV-Vis-NIR. Oppositely, B3LYP has offered the best descriptions in those cases, and our results are obtained using this functional as the model chemistry.

Calculations in benzene solutions for selected systems did not change geometric or other properties (e.g., calculated IR and UV/Vis spectra). Nevertheless, more significant dipole moments and slightly smaller HOMO-LUMO gaps were found in the solution calculations. The calculations used full-atom representations of the Mes* and Tip protecting groups.

The first compound we studied was **31 (Th1)**, consisting of two disilenes substituted in place of the bromo units. The HOMO to LUMO energy gap was found to be 2.01 eV.

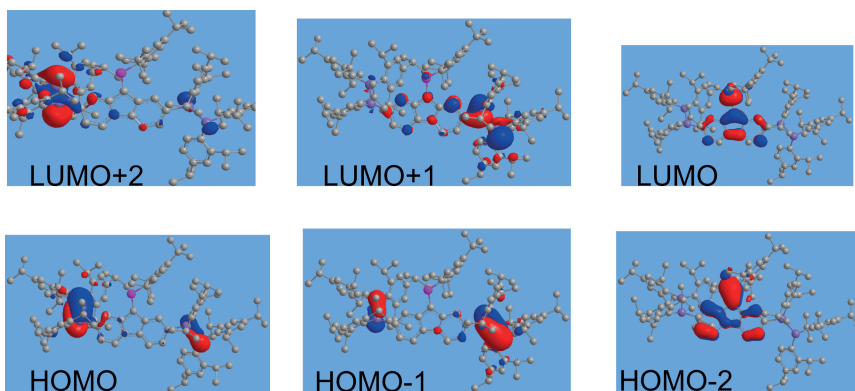


Fig. 4.3.1. Frontier orbital densities of **Th1**. The frontier orbital densities of HOMO to HOMO-2 orbitals lie remarkably close in energy, with a density distribution localized over each of the two disilene moieties in the form of π -orbitals (HOMO, HOMO-1). The HOMO-2 density corresponds to a combination of π orbitals over the fluorene and phosphalkene core. The LUMO density corresponds to π^* orbitals over the fulvenoid-phosphalkene core, with a small density contribution from *tert*-butyl groups. The larger size of the electron shells in silicon atoms and the *trans*-bent configuration of disilenes leads to nonplanar π -conjugation effects. Isosurface values = 0.03 a.u.

In Fig. 4.3.2, we observe the delocalization of the electron orbital density (LUMO+1, negative blue density) between the P=C phosphorus and a fluorene carbon, extending further towards the Si=Si disilene via a through-space (white star) and twisted (green star) orbital interaction, as shown in the blue density. This observation is a non-trivial and appealing finding, as the compound has no other through-space interactions involving both group motifs (P=C and Si=Si). The through-space interaction suggests a role of π -delocalization and π -conjugation between heavy p-block atoms through carbon bridges.

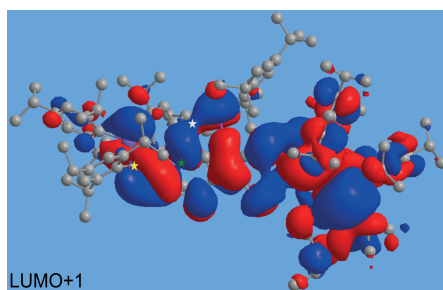


Fig. 4.3.2. **Th1** LUMO+1 density. The blue density communicates the phosphorus and the silicon via a through-space (see white star) and twisted (see green star) orbital interaction between the P=C phosphorus and two carbon intermediaries to the Si=Si disilene (see yellow star). In our view, this has relevance as there are no other “through-space” interactions in the compound involving both group motifs (P=C and Si=Si), which points to the role of increased π -delocalization, which is supported via through-space interactions. Isosurface value = 0.01 a.u.

The second set of systems we calculated (gas phase, B3LYP-D3//6-311G**) corresponds to the monobromo-disilene-phosphaalkenes, one with the disilene fragment buried under the Mes* protecting group (**Th2**) as well as the opposite isomer (**Th2b**). The HF energy difference between the two isomers is only $\Delta E = -0.68$ kcal/mol (-2.85 kJ/mol), larger for **Th2b**, which is thus slightly more stable. The dipole moment magnitude is larger for **Th2** (4.441 D) than for **Th2b** (1.201 D) and **Th1** (1.985 D). The HOMO-LUMO energy gaps for **Th2** and **Th2b** were found to be 2.10 eV and 2.03 eV, respectively. Both systems exhibit larger HOMO-1 to LUMO energy gaps at 3.47 eV for **Th2**, and 3.41 eV for **Th2b**, compared to **Th1** (2.21 eV). However, the differences between lower occupied orbitals become small in the three cases.

The third compound we calculated was the siliconoid **Th3**, corresponding to the experimentally assigned minor equilibrium product **35**. The HOMO-LUMO gap was 2.92 eV (with dispersion corrections). The ΔE between the ([HOMO]-[HOMO-1]), ([HOMO-2]-[HOMO-1]), ([HOMO-3]-[HOMO-2]), and more are 0.51 eV, 0.17 eV, 0.09 eV, 0.23, 0.03, and finally, 0.002 eV for ([HOMO-6]-[HOMO-5]). Thus, the energy difference between HOMO and HOMO-6 is ~ 1 eV, which is small and is consistent with the idea of equilibrium phenomena, since the total density of the lowest seven occupied orbitals encompasses the entire compound at high (i.e., relevant orbital, and thus electron densities) isosurface values, which is in some sense related to the potential structural variability accessible under the reaction conditions. The orbital densities are shown below in Fig. 4.3.3. The densities were also consistent with our idea of an equilibrium based on the unoccupied LUMO to LUMO+2 densities, all of which had contributions from external carbon atoms of *tert*-butyl groups, which should make the necessary (or involved) sites during the reactivity process available. Specifically, the presence of electron orbital density on *tert*-butyl groups, which is also delocalized along the entire molecule, indicates the potential for accessibility and reversibility of the equilibrium process. In contrast, an irreversible reaction would be expected to have a localized density at two different energy levels for different molecular fragments (or different orbitals, as typical). It is important to note that such orbital/energy delocalizability/degeneracy is very difficult to achieve in very confined or sterically constrained environments, which sheds light on the functional and modular (if an equilibrium is affirmatively established, the P=C-Si₆ compound is modular) role of group motifs.

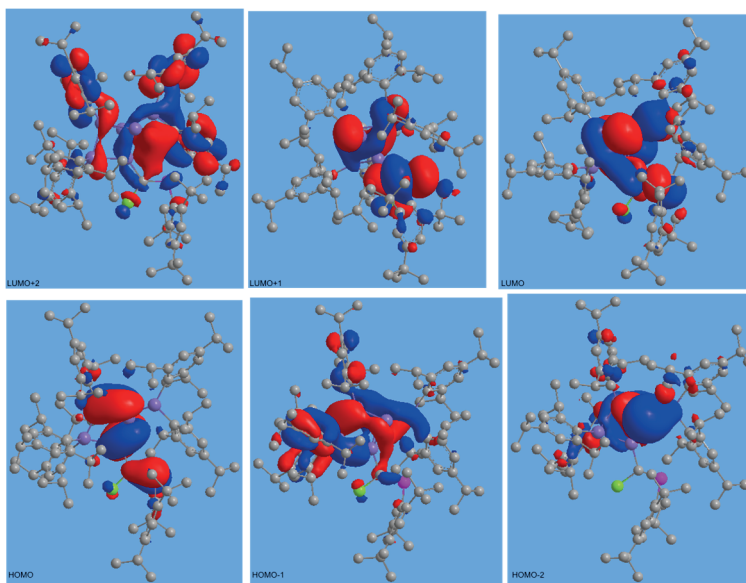


Fig. 4.3.3. Molecular orbitals of **Th3** (**35**). The density of LUMO+2 to LUMO orbitals is composed of π - π^* and σ - σ^* orbital contributions spanning the siliconoid atoms, the phosphaaalkene, and the chlorine moieties. A small contribution from σ^* orbitals on one of the outer carbon atoms of the *tert*-butyl group is observed, which still supports the phosphindole formation and possible equilibrium picture (or the two irreversible product formation, both; however, the occupied orbital/energy degeneracy supports our arguments. Remarkably, the HOMO orbitals contain three π orbitals, illustrating the 3D delocalization of the P=C and siliconoid clusters by π density. This observation indicates that the P=C is an integral part of the silicon cluster and not exogenously attached to it. Furthermore, the *tert*-butyl group contributions and the presence of π and σ orbitals in the occupied orbitals (HOMO and HOMO-1) and the slight energy differences between HOMO and HOMO-6 (structural flexibility) support our arguments for a CH-activated mechanism that transforms the P=C phosphaaalkene into a P-C phosphindole. Orbital density colors. Grey: carbon, light green: chlorine, pink: phosphorus, light purple: silicon. Isosurface values = 0.02.

We calculated the phosphine-disilene system **34** (**Th5**). The HOMO-LUMO gap was 3.10 eV. The frontier orbital densities are localized on the Si=Si, corroborating the fundamental differences between P=C-Si=Si and P-C motifs. The typicality of this system was experimentally confirmed by a smooth and straightforward set of NMR spectra compared to **Th1** and **Th2**. The fact that the phosphine moiety does not contribute to a frontier orbital is interesting, as it can be exploited in gold-semiconductor monolayer structures, where metal coordination through P lone pairs is likely to occur. The excited state properties and UV-Vis-NIR spectra were calculated using TD-DFT. Specifically, we calculated the doubly substituted disilene-fluorenylidene-phosphaaalkene **31** (**Th1**), the two monosubstituted isomers **32B** (**Th2**, disilene under Mes*) and **32** (**Th2b**), as well as the disilene-phosphine **34** (**Th5**).

Th1 shows the lowest energy onset in the TD-DFT calculations, with a band containing two transition maxima of different extinction coefficients. The asymmetry of the system may contribute to the non-trivial observations in the NMR section above, as we discussed. The observed differences in electronic spectrum and structure suggest that there may also be an effect on the NMR response of the materials that we have tentatively observed in previous studies, which could be further explored in future studies. Interestingly, **Th2b** possesses the largest extinction coefficient, and its lowest energy transition band is close to that of **Th1**, suggesting some effect of the asymmetry of the system while possessing a “freer” disilene system not under the Mes*, which can establish charge transfer event transitions or strong π -conjugation. Finally, the phosphine system is curious due to the absence of the lowest energy transition band, thus confirming our premises of extended π -conjugation and donor-acceptor character of the disilene-fluorene-phosphaalkene systems **31**, **32**, and **32B** (arsaalkene **33** and silylene **32-b** not calculated).

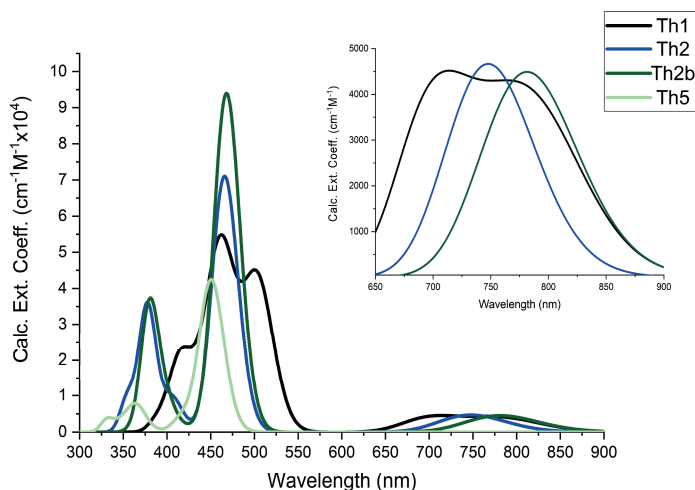


Fig. 4.3.4. Calculated UV-Vis-NIR spectra of **Th1**, **Th2**, **Th2b**, **Th5**. UV-Vis-NIR peak half-width at half-height (HWHH): 0.1 eV. Disilene systems have significantly smaller optical gaps based on their lowest energy transitions compared to phosphine **Th5**.

4.4. Summary and conclusions.

The compounds synthesized in this work exhibit a range of stimulating effects, as evidenced by NMR spectroscopy and DFT (TD-DFT) calculations. First, the compounds are stable, as observed by NMR experiments where decomposition was insignificant. These effects arise from a combination of factors such as ring torsion, locked asymmetry, branched alkyl substituents and respective

dispersion, rotation factors, and π -electronic effects, including through-space interactions and the simultaneous presence of magnetically active ^{29}Si and ^{31}P sources. The resulting nuclear-electron system response depends highly on the experimental conditions, including the NMR pulse or incoming stimulus shape and strength used, the temperature, and the degree of spinning (or mechanical input).

The salient features of the NMR spectroscopy experiments make these molecules promising for further study. For example, the "bunching" limit at + 254 ppm was prominent in THF and reproducible in various experiments with phosphalkene-disilene systems. Its presence was also observed in toluene experiments, for which it was the most shielded signal, proving that it was the limiting signal and not a random effect observed relative to THF. Reproducible two-peak broadened-enveloped ^{31}P NMR $\text{P}=\text{C}$ signals were obtained in THF for compound **31**. In contrast, the two-peak phosphorus responses in benzene were characterized by two small "satellite peaks" relative to the two more intense resonances, indicating the presence of rotamers or phenomena due to magnetic inequivalence. The non-integer ratios of 1/3 and 2/3 found for the ^{29}Si NMR $\text{Si}=\text{Si}$ resonances from two different environments in different experiments support the magnetic variation (inequivalence) argument. In the presence of two or four silicon atoms, these non-integer signal strength ratios were attributed to the presence of multiple active sites and configurationally locked basins in solution, which can cause magnetic effects and inequivalences, further enhanced by the Mes^* -induced asymmetry. UV-Vis-NIR data from TD-DFT calculations showed that **31** and **32B** have exciting features related to the lowest energy absorption bands for **31** and the extinction coefficient and strong π -conjugation for **32B**. The simultaneous presence of sharp, broad, and representative peaks within ample peak envelopes or small, shifted peaks within the same spectral region indicates the presence of rotameric isomers and dynamic effects. Correlation differences between **31** (**Th1**) and **32** (**Th2b**), as seen in the ^{29}Si - ^1H HMBC experiments, suggest more substantial π -electronic effects, such as π -delocalization, driving the correlations for **31** due to increased extending of the π -conjugation compared to the monosubstituted products **32** and **32B**.

Compared to typical organic molecular systems, the NMR responses of these compounds show greater flexibility and complexity while still exhibiting specific resonance regions and characteristic resonances (e.g., + 254 ppm for phosphalkene products in THF based on ^{31}P NMR). As mentioned above, we also observed configurationally locked species and magnetic/structural inequivalences caused by the simultaneous presence of multiple active sites and locked basins in solution, as evidenced by changes in spectral weight (e.g., 2/3 ratio signals for different silicon substituents based on ^{29}Si NMR or the maintenance of a two-peak broad-enveloped event while the development of sharper resonances by environmental variations became an occurrence in ^{31}P NMR spectroscopy). These observations suggest that it may be possible to

control the interactions between these compounds and structures in future applications.

The complexity of these systems is relevant to applications involving deterministic or stochastic processes because they have many degrees of freedom and microlocal environments that allow for a range of interactions. The molecules have many degrees of freedom while maintaining a space of interactions in each space or microlocal environment (which we denominate “configurationally locked basins”). For example, in separate groups of comparable experiments, the consistent reappearance of representative output responses was observed after the brief appearance of intermediate events. Thus, yield differences between systems **A** and **B** exhibit a feedback S_A and S_B , respectively, and include an initial byproduct (or “noise”) given by N_1 and N_2 for noise, where $N_1 \neq N_2$. Here, $(A \cdot N_1)O(S_A) \equiv S_A \sim (B \cdot N_2)O(S_B) \equiv S_B$ for responses, where O is an element linking some correspondence \sim in their responses. For example, by generating a pulse that targets a configurationally locked basin S_A , allowing S_A to undergo a change in NMR and environmental settings to S_B , coupling S_B to a vicinal population N_1 and N_2 , and then relaxing for some time and measuring S_A (or other parameters or variables) one can provide computability or generate sources such as signals or changes in resonance intensity or position or correlation strength that correspond to statistical attributes or parameter or variable values to improve model/algorithmic resilience or solve problems (e.g., optimization). Thus, the absence of increases in secondary products or side products (i.e., peak ratios and positions changed in restricted regions for $P=C$ and $Si=Si$ systems without incurring penalties such as the generation of irreversible products from decomposition processes) in separate groups of comparable experiments suggests that these results are not due to experimental artifacts but to relevant and accessible states.

In addition, the reaction between methylene chloride phosphalkene **28** and the anionic siliconoid **Si2** has led to a new and unprecedented siliconoid phosphalkene/phosphindole product [35, 35B]. The experimental data suggest a dynamic equilibrium between the desired phosphalkene and the CH-activated phosphindole isomer. Several results support this equilibrium, such as the presence of six siliconoid signals in the ^{29}Si NMR spectrum, the expected correlation of a methylene proton with four silicon atoms bound to the siliconoid structure, broadened and shielded events for the *nudo* silicon atoms, dynamic and active signals that varied considerably in the chemical shift for two relevant silicon atoms. Furthermore, the invariance between the phosphalkene/phosphindole ^{31}P NMR resonance ratio (while maintaining the six siliconoid silicon signals), which remained constant (as expected for a dynamic equilibrium situation) over several hours instead of decaying (as expected for an irreversible reaction and decomposition of the $P=C$ or siliconoid). The existence of equilibrium products with dynamic features or products associated with reversible and prominent structural changes observed with high typicality represents a potentially relevant development in the field.

Overall, studying the situation observed in this reaction can provide valuable insights into the functionality of silicon networks and related phenomena such as equilibria, reversibility, rearrangement, and irreversibility.

The DFT calculations revealed several unique themes. The locked asymmetry of the (P=C)-Mes* motif resulted in different dipole moment magnitudes and directions between the **Th1**, **Th2**, and **Th2b** systems, which are expected to interact differently with incident light and biasing stimuli. In addition, interesting molecular orbitals were characterized by non-planar, slightly twisted densities over slightly twisted single bonds and relevant "through-space" orbital delocalization, which can impart strong π -conjugation and π -delocalization to the organic framework, supporting our NMR and TD-DFT results (e.g., 2D ^{29}Si - ^1H HMBC and calculated UV-Vis-NIR spectra of **31** vs. **32/32B**), among others). The calculations also showed reduced HOMO-LUMO energy gaps and exciting optical properties for these compounds, confirming the fundamental differences between **Th1** (**31**), **Th2/Th2b** (**32**), such as small optical gaps and asymmetric effects as seen in TD-DFT spectroscopic resonance calculations, and the phosphine **Th5** (**34**), which has a higher HOMO-LUMO and wider optical gaps. The last and previous statements also support our ideas in general (i.e., π -conjugation, HOMO-LUMO & optical gaps, as well as P=C, As=C, Si=Si, and unsaturated siliconoid group motifs importance) by the indirect relation given by the simplicity of both the experimental NMR spectra of phosphine/disilene **34** and its computational properties, relative to other compounds.

These properties and features suggest potential use in future optoelectronic applications (and more) with molecular material systems. The complexity and contextual instructional perspective these materials provide are relevant in many areas, such as developing novel sources of statistical features or using them as sources of new programmable units linked to the interpretive frameworks within quantum/classical information science or algorithmic domains.

It is noteworthy that there are no reported experimental or theoretical studies of Si=Si or unsaturated siliconoid clusters that simultaneously present space-separated P=C or As=C bonded units within π -conjugated networks. This novelty is the aspect offered by these new families of compounds. This work represents an appropriate first step to stimulate and incentivize the development of molecular π -conjugated materials comprising two multiply bonded units of space-separated heavy p-block elements in low coordinated states from Groups 14 and 15 of the Periodic Table.

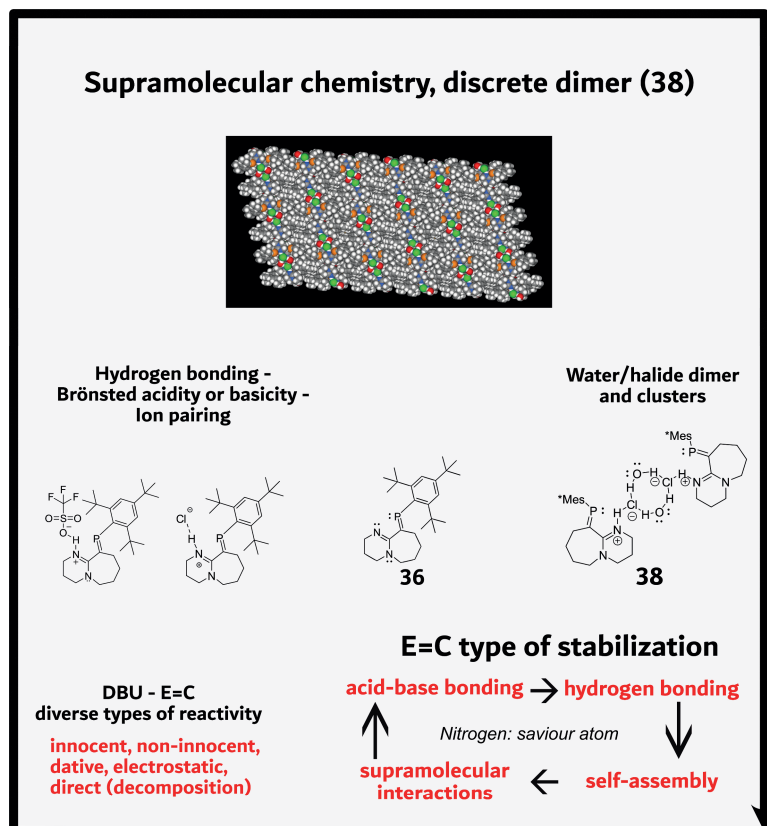
Ch. 5. Phosphaalkene-functionalized DBUs with hydrogen-bonded extensions: stabilization of E=C (P=C) via HB interactions.

We will introduce and study our work with phosphaalkene **36**, which counts with the support of a highly modular molecular backbone based on DBU, a commercially well-known organic base widely used in catalysis. A serendipitous finding initially resulted in the observation of compound **38**, characterized as a hydrogen-bonded, H₂O-containing P=C system by XRD. This compound appeared persistently as a single crystal, once spontaneously and twice reproducibly during its purposeful synthesis later in the project. The presence of intact P=C units implied that heavy group motif stabilization had taken priority over the typical P=C decomposition paths (i.e., hydrolysis, addition, oxidation, polymerization, and more). We studied the system retroactively and completed the synthesis and characterization of the neutral parent **36**, characterized structurally (i.e., XRD) and spectroscopically (i.e., FTIR, detailed NMR, and more; vide infra) in detail.¹⁴³ Different reactivity probing established a higher stability of **38** than **36**. We confirmed the selective formation of the hydrogen-bonded dimeric network in solution and the solid state, following the preparation of anhydrous HCl product **37** and after rigid control of the environmental conditions and experimental settings. Then, we evaluated the reactivity between **36** and TfOH and HPF₆ superacids, yielding products **39** and **40**, which kept intact P=C in the products, expanding our observations of hydrogen-bonded-derived stability of the P=C group motifs.

We will show that geometrically and strategically incorporating P=C onto the DBU core is a potentially accessible approach to the development of materials with E=C motifs of high reactivity. For these materials, primary E=C decomposition pathways may be non-preferential through hydrogen bonding interactions due to the presence of nitrogen savior atoms. Hydrogen bonding interaction of the reactive molecules through these savior units leads to E=C systems of remarkably high stability compared to precursors.

We will demonstrate that incorporating P=C into DBU is an attractive strategy for designing novel materials for small molecule activation, catalysis, transition metal synthesis, and supramolecular networks. A general,

preliminary scheme of the compounds and concepts we study in this chapter is shown below (Scheme 5.0.1).



Scheme. 5.0.1. Successful reactions with various reagents exemplified diversity in the types of reactivity **36** exhibits. The top figure nicely demonstrates the discrete dimeric nature of system **38**. We believe the type of stabilization presented here represents a “new” approach or conceptual construct for stabilizing highly reactive main group compounds through strategically located savior atoms in the periphery.

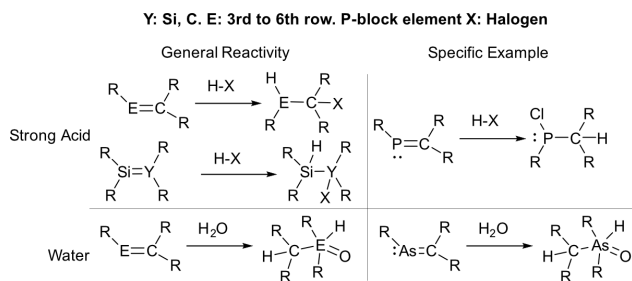
5.1. Introduction to relevant topics.

5.1.1. Literature review on reactivity of E=C bonds with small molecules highlights their irreversible reactivity (decomposition) as the norm.

Decades ago, the double-bond rule was broken by synthesizing low-valent or low-coordinated compounds that featured intact, neutral, unsaturated E=C fragments. The stability of these synthesized molecules was studied by testing

their reactivity with various small reactive molecules, including Brønsted and Lewis acids, bases, small gaseous molecules (such as CO₂, X₂, N₂O, and HF, where X represents a halogen), and archetypical molecules like H₂O and O₂. In addition to typical oxidation or reduction¹⁴⁴ and addition products with oxygen,¹⁴⁵ water, halogen-containing gases,¹⁴⁶ and strong acids, similar reaction paths have been observed with other reactive species (e.g., MeOH, R-OH, HX, and more).¹⁴⁷ Despite the kinetic and thermodynamic stabilization provided by i) sterically encumbering aryl/alkyl substituents, ii) introduction into rings or through other electronic effects, most of the E=C species are reactive and decompose if exposed to the atmosphere or these small molecules (Scheme 5.1.1.1). Of course, we found representative examples of atmospherically stable low-coordinate compounds in the literature and workup work where researchers obtained products after brine washes and extraction. These occurrences exemplify advances in the design of novel protecting groups, serendipity or brief manipulation in wet conditions, and strategies for stabilization. However, these are rare exceptions, and decomposition paths are preferential for energetic reasons.

On the other hand, if directly evaluated, the atmospherically stable species often do not possess the free energy or reaction modes to drive complex transformations such as catalysis or the activation of inert or reactive molecules. Thus, a critical need is to find molecules with diverse types or levels of stability to improve the design of systems with high reactivity, either with or without the persistence of heavy E=C units in different environments or settings. In this way, compounds with novel properties and behaviors, such as increased modularity or unique forms of stability, can be created, especially for the development of modular architectures in systems involving compounds with "atypical" or unusual bonding situations, which are typically considered either impossible or inadequate for applications due to their high reactivity.



Scheme 5.1.1.1. Typical reactivity of main group compounds with selected small molecules; for example, with strong acids or H₂O, addition or hydrolysis of the heavy double bond occurs. In the case of group-15-element species such as phosphaaalkenes, the halogen atom is added to the less electronegative carbon atom. With H₂O, hydrolysis of the main group unit leads to various products, such as pentacoordinate species. Other products, such as polymers or oxygen-containing heterocycles, occur.

5.1.2. Chemistry and applications of the DBU superbase.

DBU is a highly versatile compound that is used as a robust base in a variety of applications. Due to the high stability and high reactivity of the lone pair of electrons on the imine nitrogen atom, DBU has been used to execute proton abstraction processes in chemical transformations such as dehydrochlorination reactions. In other applications, DBU acts as an active catalyst (organic catalysis and renewable polymer chemistry).¹⁴⁸ DBU provided the two proton abstractions necessary for constructing P=C group motifs onto the DBU core, using a precise threefold molar concentration excess ratio. DBU is also a critical additive or component in ionic liquids synthesis.¹⁴⁹ Similar ionic liquid-like phenomena were observed in some cases below, in which dynamic products that exhibited changes in texture, viscosity, color, and spectroscopic responses were obtained. These changes were contingent on minor differences or experimental conditions (e.g., atmosphere, H₂O concentration, solvent), an area we did not explore in detail, but it is worth mentioning given its relevance, and we generated spectroscopic signatures representative of the phenomena. DBU is categorized as a superbase or “proton sponge”, the latter dual meaning as a pun due to its natural product nature as researchers previously extracted it from sponges (i.e., marine organisms).¹⁵⁰

5.1.3 Chemistry of strong acids and superacids. Water and water/halide clusters. Hydrogen bonding interactions.

The chemistry of strong acids and superacids is crucial to most biological and artificial processes. The study of the Brønsted acid & base theory paved the foundations of our current understanding of chemical reactivity. At an interface, the study of acid & base chemistry coincides with the study of hydrogen bonding. At the dynamic level, such as in solution mixtures, it is challenging to declare whether some observable is representative of a hydrogen-bonded adduct or the presence of hydrogen bonding. This challenge arises because hydrogen bonding is exhibited dynamically, as interchange or proton exchange, is accompanied by secondary, equally essential interactions, depending on the degree of electrostatic or electron orbital interaction and distance between the relevant adducts, which also depends on their medium.

In our case, we were attracted to hydrogen chloride (HCl) due to fate, which later became more of a realization since the chemistry of water/chloride interactions is related to the chemistry of water and HCl, which is crucial in areas ranging from astronomy to biology.¹⁵¹ The chemistry of water or water chloride clusters is crucial, and these small structures correspond to small-atom-limit or discrete representations of relevant natural processes in the universe.¹⁵² The chemistry of water/chloride networks embedded in hydrophobic environments provided by complex organic molecules is another recent area of research.^{153,154} For example, transporting solute chloride and solute water

through cell membranes or lipid-containing layers is critical in natural biological chloride channels and artificial membrane design for ion-based transport units or systems (sensors, batteries, advanced functional materials).¹⁵⁵

The chemistry of superacids is essential in various areas ranging from organic synthesis to industrial processes.¹⁵⁶ The reaction of **36** with triflic acid and hexafluorophosphoric acid were pleasant surprises, as mentioned (vide infra); these acids are orders of magnitude stronger than sulfuric acid and are known as superacids.

An essential aspect of the field examines the impact of factors such as the release or introduction of frustration or sterics and the presence of various functional groups on the reactivity of target adducts. This information can be used to explain variations in reactivity and the resulting reaction products. In all areas, the characterization of hydrogen-bonded adduct formation in solution has been done by spectroscopic techniques. The presence of hydrogen bonding is a general feature of the systems we studied. Several hydrogen bond categories have been described in the literature. Results have been discussed via distance and angular cutoff arguments, energy schemes, and general comparison, which complicate a compactified understanding of the hydrogen bond or bonding interactions (HB).¹⁵⁷ Sometimes, these discussions have been used for tailoring the definition or *relevance* of hydrogen bonds, which may direct biases in future studies. A good approach is based on a first principles-based, all-encompassing, and potentially accessible definition for the existence of hydrogen bonding interactions (i.e., hydrogen bonds) within a system. Any relation to hydrogen bonding discussions implies an equivalent representation, corresponding to affirmative responses: 1) on the existence of hydrogen bonding, 2) successful compactification of the resulting abstractions, from which then, and only then, a well-defined *relevance* principle for the specific systems under study can be constructed discernibly. All the systems we study here, except the palladium complex, exist within a continuum spectrum¹⁵⁸ where hydrogen bonding occurs. This interaction occurs between donor and acceptor sites, directly mediated by protons or hydrogen atoms.¹⁵⁹ The interactions with a substantial covalent character based on shared electron density through orbital interactions lie on one side of the spectrum.

In contrast, the protonated salts, ionic adducts, and contact pairs may be placed in some category opposite to the covalent type or one another based on some characteristic differences. Nevertheless, they all share equivalences, such as:

- Shared protons in the space between donors and acceptors are standard.
- The induction or generation of energy stability, or modulation, by an absolute or well-defined criterion (which implies that relevance or comparability exists).
- Hydrogen bond coordination number (≥ 2).

- The construction of larger structures.

These equivalences render them all as representative hydrogen bonds when appropriate (i.e., when there are well-defined equivalences and conditions between the different compared instances). Higher order or intermediate variants exist between the covalent and the ionic hydrogen bonds, fundamentally dependent on the environment and internal or external modulation.¹⁶⁰

In the case of the H₂O-containing dimer **38**, a sequential interaction approach consisting of electrostatic, charge transfer effects, and "transient covalence" is best suited to explain the types of HB interactions present in the system. First, an HCl molecule acts as a hydrogen bond donor (HB-donor) with a P=C-containing DBU-like base as a hydrogen bond acceptor (HB-acceptor). Then, interaction occurs between the $[(\mathbf{36}\text{-H})^+\cdots(\text{Cl})^-] \leftrightarrow [\mathbf{36}\cdots\text{H-Cl}]$ (i.e., **37**) and the water molecule with H₂O acting as the HB-donor (i.e., **38-monomer**). Then, the self-assembly of the well-defined dimer structure **38** occurs. Finally, further stabilization by other NCIs occurs, preceded by cluster or HB network occurrences (**38** or **38-derivatives**). It is crucial to recognize that in dynamic mixtures in solution, the degree and extent of HB varies subtly with minimal changes based on temperature, atmosphere (Ar vs. CO₂), solvent (i.e., aprotic, protic, polar, nonpolar), [H₂O] or [O₂] concentration, and more. Therefore, contributions exist in which a formally [HCl] molecule instead of the [Cl]⁻ generates an HB-acceptor interaction with an HB-donor H₂O molecule.¹⁶¹ Thus, we used the notion of "transient covalence" (supported by FTIR observations) to refer to H₂O-based or HCl-based neutral hydrogen bonds, for example.

5.2. Synthesis and characterization of DBU-phosphaalkene (**36**), hydrogen-bonded HCl adducts (**37**), and water-containing dimer (**38**).

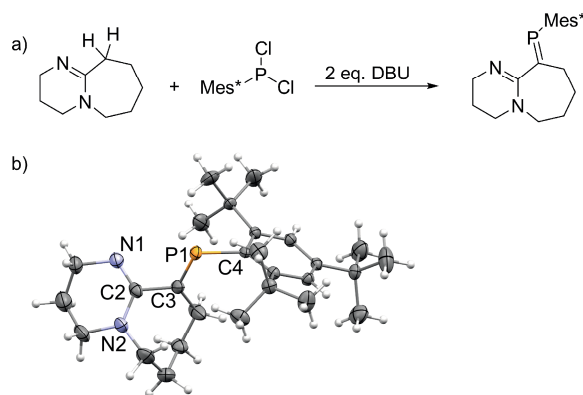
In this section, we will study the synthesis and characterization of the parent compound **36**, hydrogen chloride product **37**, and hydrogen-bonded species **38** from the reactions between the central parent system **36** with a solution of HCl under anhydrous and deoxygenated conditions, as well as with HCl and a stoichiometric amount of water under anhydrous and oxygen-free conditions also.

The characterization of the hydrogen-bonded supramolecular adduct **38** is presented, along with a plethora of evidence confirming HB's existence in solution. We provide evidence in the form of NMR and ATR-FTIR to prove the existence of the supramolecular dimeric hydrogen-bonded network **38** in solutions of CDCl₃, CD₂Cl₂, and toluene-*d*8. For NMR, our conclusions were based on representative chemical shift changes in various settings, DOSY-NMR spectroscopy. Whereas for IR spectroscopy, we determined our

discoveries on the symmetry and the discreteness of the response of the $\nu(\text{O-H})$ H_2O frequency relative to the water concentration. The preferential formation of a dimeric interaction can be explained by the increased cooperativity or self-complementarity, given by a system of increased symmetry, in the aprotic and low polarity solvent media where experiments were performed. High cooperativity towards dimer formation can be further explained by NCIs (dipole-dipole, induced-dipole-dipole, or “secondary hydrogen bonds”). The existence of secondary HB interactions was confirmed from solution and solid-state responses, corresponding to interactions with increased $[(\text{Mes}^*-\text{CH}_3)\cdots(\text{OH}_2)_2]$ character, for example.

5.2.1. Synthesis and high reactivity of DBU-PA (**36**) due to structural frustration (π -conjugation + bicyclic torsional strain + sterically-encumbering Mes^* substituents).

Researchers previously reported the preparation of compound **36** before. However, we provided the first XRD characterization of the compound. We obtained single crystals after several months of occasional trial and error due to the high reactivity of the compound (Scheme 5.2.1.1 b). The synthesis and relevant structural parameters for **36** are shown in Scheme 5.2.1.1.¹⁶²



Scheme 5.2.1.1. a) Synthesis of **36**. b) Single-crystal ORTEP representation of **36**; relevant BLs (Å): P1=C3: 1.676, N1=C2: 1.285, N2-C2: 1.370, C2-C3: 1.496. Short N (amine) - CH_3 (*tert*-butyl) ($\text{H}\cdots\text{N} = \sim 2.9$ Å) interactions were also evidenced.

In the original procedure and at the beginning of our project, three DBU eq. were added to Mes^*PCl_2 (-78 °C). We improved the protocol by exchanging reaction steps by the addition of a THF solution of Mes^*PCl_2 (1 eq.) to a solution of dry DBU at rt, which yielded the product immediately, with the advantage that immediate precipitation of $[\text{DBU}\cdots\text{HCl}]$ was visible. The ^{31}P NMR of **36** displayed a signal that ranged from + 251 (C_6D_6), + 254 (CDCl_3), and + 257 ppm (CD_2Cl_2) (e.g., Fig. 5.2.1.2). This signal varied in position and

line shape, depending on the environment (i.e., molarity, salt, impurities, solvent, H₂O, or O₂ presence). The P=C resonance was sensitive to the local environment during measurement, evidenced by broad resonances in most instances. The wider resonances occurred counterintuitively during experiments with the “cleanest” samples. In these experiments, solvents and impurities were evaporated and removed more rigorously. This observation points to increased HB in solutions with fewer disruptions. It has been hypothesized, and it is empirical knowledge, that HB-donor and HB-acceptor solutes exhibit decreased HB abilities in THF solutions relative to the same species in DCM or CHCl₃ solutions. A lower degree of association in THF mixtures due to moderate polarity, higher salt solubility in THF, and H₂O miscibility have been proposed as causes. Therefore, except for very polar solutes, increased solvent polarity or increased H₂O content (or high salt concentrations) “weaken” HB or the extent of its evidence in solutions. The low degree of association or aggregation in THF and increased salt concentration ([LiCl], [DBU⋯HCl]) in crude mixtures explains the standard signal response of the ³¹P NMR resonance of **36** in THF experiments immediately after initial product formation. We confirmed several of the features that render **36** a fascinating compound. For example, the absence of high-frequency signals in various samples suggested no appreciable bonding between the imine nitrogen to a proton.

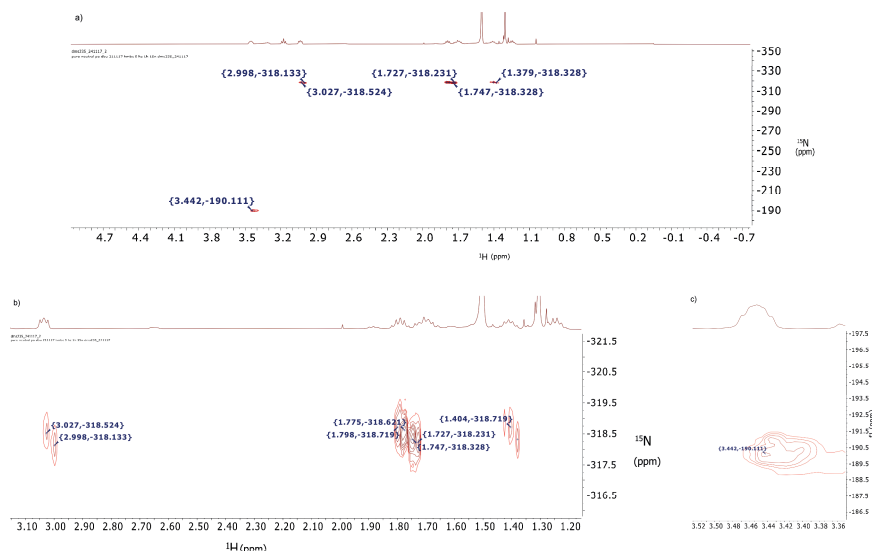


Fig. 5.2.1.1. a) ¹H ¹⁵N HMBC NMR spectrum (vs. CH₃NO₂) of **36**; despite the challenging nature of the non-enriched samples, clear signals were obtained for both nitrogen atoms at - 190 ppm and - 318 to - 319 ppm. No **36**-[H₂O] HB nor direct N-H bonding signals were evidenced. Based on HMBC principles, the signal should have been detected as either residual ¹J coupling noise or long-range coupling from the second nitrogen atom (we confirmed this in control experiments later using organic DBU-HCl). g) Relevant regions of the spectrum are shown in b) and c).

The slightly deshielded chemical shifts ($\delta = 1.61, 1.71$) of H_2O molecules in the solvent (in CDCl_3 : 1.56-1.57 ppm) indicated the H_2O molecules exhibited some HB (see Fig. 5.2.1.2 e)). This finding suggested the existence of HB between the residual H_2O molecules in the anhydrous and deoxygenated mixture. Experiments with (i) minimal amounts of H_2O (traces) under otherwise (ii) inert and (iii) nonpolar solvent medium conditions and hence (iv) no appropriate medium for hard oxygen anion-containing species to solubilize, and (v) no deshielded $[\text{N}-\text{H}]$ or $[\text{N}\cdots\text{H}]$ ^1H NMR signals, helped us confidently reject the $[\text{N}^+ - \text{H}\cdots[\text{H} - \text{O}]]$ formation (or similar species) hypothesis or argument, which was supported by a plethora of ^1H NMR experiments as well as above via 2D ^1H ^{15}N HMBC correlation NMR experiments.

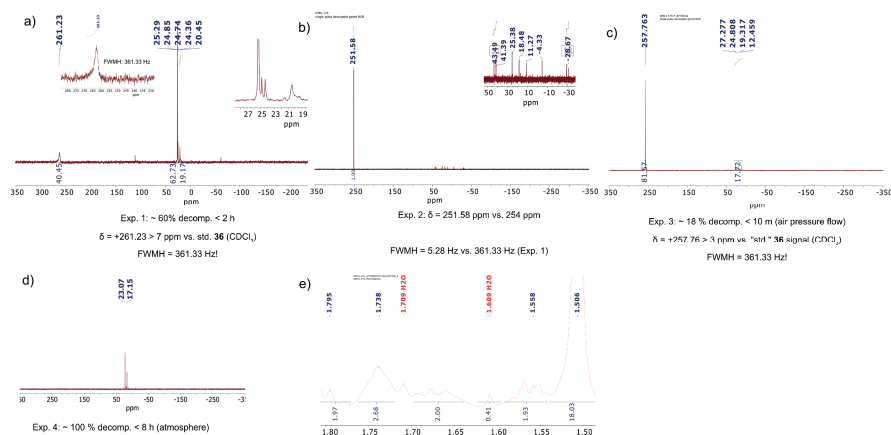


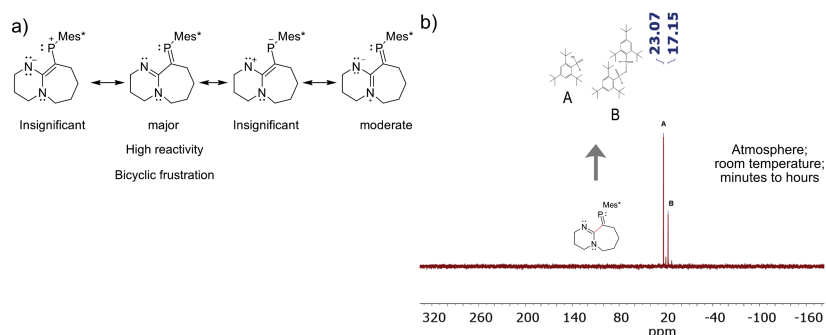
Fig. 5.2.1.2. a) ^{31}P NMR spectroscopy of **36** < 2 h of atmospheric exposure; > 70 % of the sample decomposed. Signal broadening with an FWHM of 361.33 Hz was observed. b) Recently synthesized **36** in THF (NMR: capillary tube, C_6D_6) exhibited a much sharper signal (FWHM = 5.28 Hz) using similar concentrations. c) About 18 % of **36** decomposed after ambient air bubbling for 10 min. d) Full decomposition after eight hours (overnight) of atmospheric exposure. e) ^1H NMR spectrum of **36** in an experiment (~ 0.0001 % or 1 ppm $[\text{H}_2\text{O}] \rightarrow$ based on manufacturer's analytical reported values for "anhydrous CDCl_3 " in a sealed container) under Ar after recrystallization. Two deshielded water signals were automatically assigned by MestReNova (version 14.3.1), which indicated the presence of HB prior to $\text{P}=\text{C}$ decomposition.

Thus, the substoichiometric amounts of H_2O and the slightly charged state of the resulting H_2O suggested some aggregation where deshielded signals representative of H_2O in hydrogen-bonded environments were present. Our study about **36** in the presence of minimal amounts of H_2O is relevant because the formation of $[\text{DBU}\cdots\text{H}_2\text{O}]$ is undesired in many applications that exploit the high basicity ($\text{pK}_b = 28$, CH_3CN) of DBU as a bare species. In contrast, **36** does not seem to provide a conducive environment for forming **36**- H_2O adducts through the imine nitrogen as expected or even through direct covalent

interaction while maintaining some relation based on the potential aggregation of H₂O molecules becoming hydrogen-bonded in the nonpolar medium.

However, as observed in the stability experiments in Fig. 5.2.1.2 a) to d), the exposition of **36** to atmospheric conditions led to rapid product decomposition in minutes to hours depending on the specific experimental conditions (see figure text insets and caption for conditions). We conclude that samples of **36** under oxygen-free conditions and substoichiometric or minimal H₂O concentrations took more time to react and decompose than ambient atmosphere-exposed or aerated samples, which decomposed readily. This observation suggested the dual role of H₂O/O₂, or the increased concentrations of either one through elevated exposure, to be relevant in the decomposition of **36**. In Fig. 5.2.1.2 above, the NMR spectroscopy of **36** samples was presented to reveal the differences of the ³¹P NMR resonances for various experiments. The experiments confirmed the dynamic nature of the resonant signal based on position and line shape, which also revealed the high reactivity of **36** under ambient atmospheric or similar conditions (i.e., aerated). Therefore, compound **36** is highly reactive under atmospheric conditions, as shown. The high reactivity of **36** was one of the complicating aspects of our studies since it was hard to purify, and the characterization of weak interactions in solution is extremely sensitive to the presence of O₂, H₂O traces, O-containing impurities, other impurities, and salts.

We rationalized that there is an increased frustration character of the small π -system of **36** due to the torsional strain imparted by the presence of a bicyclic structure, accompanied by a further sterically hindering Mes* component. These factors are responsible for the high atmospheric reactivity of the compound once communication with H₂O and O₂ is set. The compound decomposes quicker in moderately polar solvents such as THF or DMSO due to increased polarity and H₂O content (which implies O₂ content from the ambient atmosphere, although O₂ is nonpolar). NMR characterized two major decomposition products (Scheme 5.2.1.2).



Scheme 5.2.1.2. a) Potential resonance structure contributions to the electronic structure of **36**. Resonance structures are characterized by electron density towards the imine. The resonance structure on the left possesses a negatively charged nitrogen which is unlikely. In contrast, the other two resonances (positions on the right side) do not explain the results below (middle-right) and moderately contribute based on the absence of bicyclic torsional strain while explaining the results below based on low amine reactivity (right), respectively. Bicyclic torsional strain leads to **frustration** and hinders conjugative ability, e.g., single-bond lengthening (1.496 Å) based on XRD. Main atmospheric scavengers are poor HB-donor or HB-acceptor relative to their ability to decompose the E=C motifs, as proven in b). b) Structure representation and ³¹P NMR spectra of the hydrolysis/oxidation decomposition products of **36**.^{163,164}

5.2.2. DFT analysis of the neutral DBU-PA system (**36**) explains its high atmospheric sensitivity.

A comparison between the single crystal structure and the structure from the DFT-optimized model system for **36** (Fig. 5.2.2.1) showed excellent agreement in the theoretically obtained angles and bond length distances. The HOMO density is located on the π -orbitals of the N=C and P=C systems. The LUMO orbital is characterized by π^* density, with a high contribution from the P=C motif. Therefore, the high reactivity of **36** was well elucidated by its elementary electronic ground state structure, which showed an increased contribution of the P=C system to the occupied and unoccupied frontier orbital densities. This contribution contrasts with hydrogen-bonded systems, for which P=C groups are highly stabilized, as we will discover for the HCl adduct **37** below, for which the occupied density was localized on the chloride ions, after adduct formation.

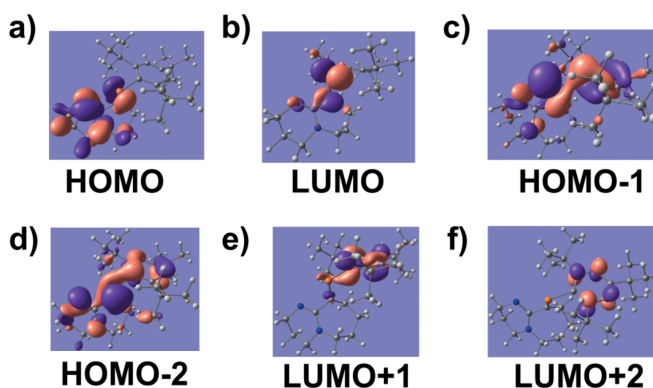
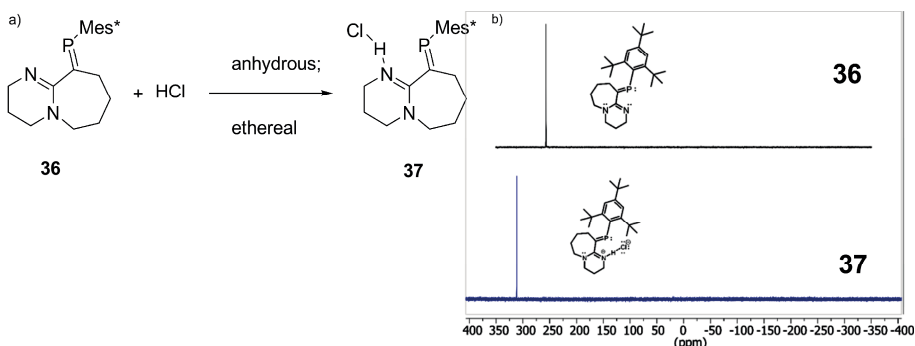


Fig. 5.2.2.1. a) to f) Frontier orbital densities of **36**. Isosurface values (0.02-0.06 A.U.) are plotted depending on the difficulty of the assignment.

5.2.3. Synthesis of **37** via the reaction between **36** and HCl in anhydrous and inert media.

The reaction between **36** and HCl was carried out in various solvents, such as ether, THF, CHCl_3 , and DCM, under strictly inert and dry conditions using Schlenk techniques and stoichiometric HCl from a 2M ethereal solution. Product **37** was obtained as a white solid in quantitative yield. Typically, diethyl ether solutions turned yellow after the dissolution of **36**, which turned white after adding HCl.

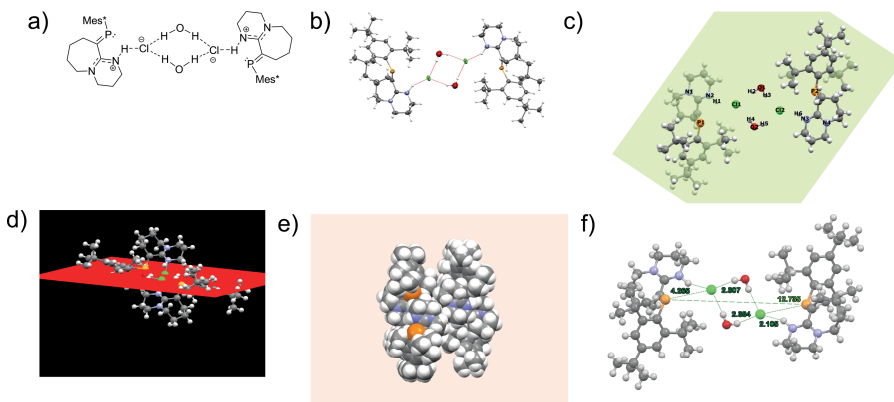


Scheme 5.2.3.1. a) Reaction formula and conditions for the synthesis of **37**; b) ^{31}P NMR reaction monitoring; synthesis of **37** under inert conditions.

For HB studies, extremely pure compounds (**37** and **38**) were obtained by washing and decanting with clean solvents such as MeCN, pentane, hexane, or Et_2O . A ^{31}P NMR resonance change characterized product formation from around + 254 ppm to + 310 ppm (Scheme 5.2.3.1). Despite numerous attempts, we could not obtain single crystal structures of **37**. However, when the compound was allowed to crystallize in open containers under standard

atmospheric conditions, the crystal structure of **38** was obtained reproducibly (see Scheme 5.2.4.1).

5.2.4. Formation and crystal structure of **38**. A water-based hydrogen-bonded dimeric network containing phosphalkenes.



Scheme 5.2.4.1. a) Molecular structure of **38**. b) ORTEP representation of **38** (ellipsoids; 50 % probability; white: H, grey: C, red: O, green: Cl, light blue: N, orange: P). c) Stick and ball of **38**; a plane of the network is shown; two separated phosphorus atoms (~ 1.3 nm; 12.73 Å) were found to be spanned by the plane, as better seen in d) with $[\text{N}-\text{H}\cdots\text{Cl}]$ hydrogen bonds between imine and chloride slightly above and below the plane. e) Space-filling superhydrophobic capsule around the central network. f) **38** with relevant crystallographic features; other potential secondary interactions, such as hydrogen bonds between $[\text{CH}_3]$ protons and $[\text{Cl}^-]$ or $[\text{H}_2\text{O}]$, are not shown. The D-A HB distance was $3.097(3)$ Å, whereas the DHA angle was 154° .

5.2.5. Confirmation of the HB nature of **37** and **38** and the existence of H_2O and $\text{H}_2\text{O}/\text{Cl}$ clusters. Unanimous dimeric nature of **38** confirmed by DOSY-NMR spectroscopy.

We will now characterize the hydrogen bonding interactions in adducts **37** and **38**. Below, we present relevant experimental observations for the characterization of solutions of the anhydrous $[\text{HCl}]$ product **37**. These were prepared in dry and deoxygenated conditions to avoid the formation of supramolecular compounds, such as **38** and derivatives. The formation of the desired HB anhydrous complex representative of **37** was successful. The single resonance in the deshielded region of the spectra shown in Fig. 5.2.5.1, the accurate integrability of the spectra, and the observed deshielded shifts in different experiments as concentration increased, confirmed our hypotheses.

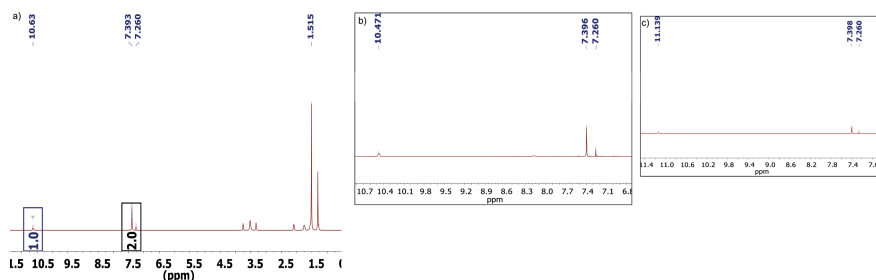


Fig. 5.2.5.1. a) ^1H NMR spectrum of **37** in CDCl_3 ; a signal at 10.63 ppm was obtained and assigned to $[\text{N}-\text{H}\cdots\text{Cl}]$ interactions. No H_2O was present (in $\text{CDCl}_3 \rightarrow$ Dissolved H_2O in solvent = ~ 1.56 ppm. Bulk H_2O or hydrogen-bonded H_2O clusters in solvent = \sim or > 4.19 ppm. See referenced work for bulk H_2O or hydrogen-bonded H_2O cluster type of assignment, which becomes relevant later in the Section).¹⁶⁵ b) Experiment in which the dynamic $[\text{N}\cdots\text{H}]$ signal was probed in an experiment with ~ 10 mg (0.6 mL CDCl_3), in which a signal at 10.47 and another one at ~ 8.17 ppm (broad) were detected vs. c) with ~ 12 mg (0.6 mL CDCl_3). The slightly higher concentration of **37** in c) led to a deshielded $[\text{N}-\text{H}\cdots\text{Cl}]$ signal at 11.14 ppm (from 10.47 ppm) without the presence of other species. The deshielding was attributed to the increased HB in c). The shielded signal might correspond to an equilibrium species (see below). In summary, we postulate that the anhydrous adduct exists in different HB environments. For example, such as $[(\text{N}-\text{H})^+ [\text{Cl}]^-] \leftrightarrow [\text{N}\cdots\text{H}-\text{Cl}] \leftrightarrow [(\text{N}-\text{H})^+\cdots(\text{Cl})^-]$, where the resonance on the left represents the proton transfer or protonated iminium species (not HB), the middle ones the more covalent type of hydrogen-bonded environment (e.g., between “HCl” and “imine”). In contrast, the resonance on the right represents the more ionic type of HB environment between the imine (iminium, formally) and the chlorine (chloride, formally) with a hydrogen atom (proton, formally) in between. Based on our understanding of hydrogen bonding, the resonance on the right should not be confused with an ion-paired system per se, although there may be similarities and even equivalences between the two concepts. A twisted $[\text{D}\cdots\text{H}-\text{A}]$ or $[(\text{D}-\text{H})^+\cdots(\text{A})^-]$ HB angle may be categorized as an ion-paired system by some researchers based on angular or spectroscopic criteria. For example, in some ion-paired cases, there may be no deshielding or shielding (as settings are changed) or even no coupling or resonance with respect to the acceptor sites due to pronounced structural stabilization in the ion-paired form present (see Fig. 5 in the referenced material, for example)¹⁶⁶. In contrast, others consider species such as $[(\text{D}-\text{H})^+\cdots(\text{A})^-]$ a strong hydrogen bond (i.e., an ionic hydrogen bond, for example), while the particular form is also indicated as a contact ion pair also (e.g., see the abstract of the referenced material)¹⁶⁷. In general, however, the exchange of signal positions with changing conditions (e.g., temperature, concentration) is a good indication of the presence of HB, regardless of whether it is presented in a covalent or ionic character. At the same time, in limited cases, the resolution of both equilibria and the free protonated form can be detected.¹⁶⁸ The broad signal at 8.17 ppm in b) can be assigned to the protonated site. Its disappearance as the representative concentration of the experiment increased, as seen in c), nicely confirmed the assignment of both the HB adduct or complex in c) and the presence of the protonated-only site in b).

We further validated the existence of HB adducts in **37** solutions after synthesis of the all-organic system $[\text{DBU}-\text{HCl}]$ (**42**), including by XRD (studied alone in Section 5.6 later). We confirmed the existence of HB in the solid state

and solution via ^1H NMR experiments. A primary high-frequency signal at 11.09 ppm was attributed to being representative of HB interactions. A second signal at 8.99 ppm was attributed to the ion-paired ionic type of HB ($[(\text{DBU}-\text{H})^+\cdots(\text{Cl})^-]$), whereas the signal at 8.71 ppm was assigned to free protonated states ($[(\text{N}-\text{H})^+ [\text{Cl}]^-]$) as seen in Fig. 5.2.5.2 a). A 1:1 molar mixture of **37** and **42** was prepared as a solution under anhydrous and deoxygenated conditions (Fig 5.2.5.2 b)). Remarkably, the shielded resonances at around + 8.71 and + 8.99 ppm disappeared in the experiment (i.e., in b) vs. a)). We assumed that these signals would resonate equivalently in both b) and a), which is reasonable given that CDCl_3 and CD_2Cl_2 are very similar solvents. We attributed the disappearance observation and maintenance of a deshielded signal at 11.09 ppm in b) as a strong confirmation that the deshielded signals (> 11 ppm) in a) represented HB, which is supported by the equivalent analogy in b) and c) in Fig 5.2.5.1 above. We justified the shielded signal disappearance by the higher concentrations of resulting solutions in both experiments after comparing compound signals to solvent peak signals between b) and c) above and a) and b) below. Moreover, we justified their disappearance in b) below based on the more extensive hydrogen bonding support by **37** due to the presence of nonpolar substituents, which are more conducive towards HB than ionic environments. The increased support increased the overall extent of HB by driving the equilibrium away from contact ion pairing or protonated products compared to reaction solutions of bare **42**, and therefore the disappearance of shielded signals ($\sim 8.70\text{--}9.0$ ppm). Consequently, given the single signal of anhydrous **37** in a) above and the traced relationships of the previous paragraph, we can firmly conclude that anhydrous **37** can be driven towards the exhibition of HB under controlled conditions.

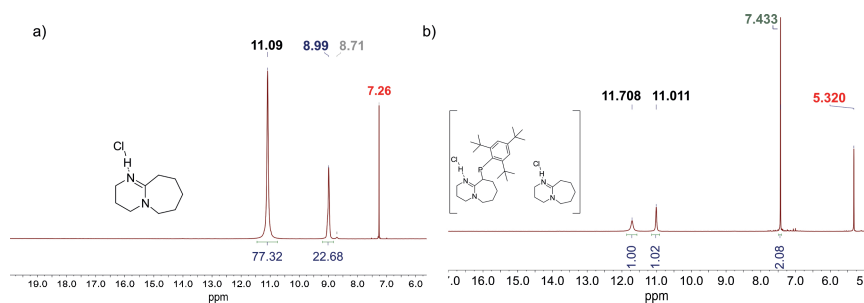


Fig. 5.2.5.2. a) High-frequency ^1H NMR region of **42**; chemical shifts are indicated by color. Black: HB **42** species. Blue: ion-paired HB species. Gray: free protonated or proton transfer species. Red: CDCl_3 . b) High-frequency ^1H NMR region of the product of a 1:1 equimolar reaction of **42** and **37**. Black: HB **37** and **42** species, respectively. Green: Mes^*Ar proton species. Red: CD_2Cl_2 . The disappearance of the blue and gray signals for **42** resulted from the equilibrium being driven towards HB via the “HB support” provided by **37** in the presence of less polar environments of Mes^* *tert*-butyl groups.

We characterized **38** as a discrete dimer in solution through its generation in controlled environments using aprotic and low permittivity (i.e., nonpolar) solvents under anhydrous and deoxygenated conditions (i.e., with one molar equivalent of deoxygenated H₂O vs. **37** using a Hamilton syringe). The equimolar approach stimulated the construction of HB and incorporation of NCIs while minimizing the contributions from competing paths, such as (a) the formation of equilibrium species (small NMR signals, operated via slight environmental changes) or (b) the generation of charged species (decomposition over time). The complexity of identifying hydrogen bonding interactions in solution makes our investigation of **38** as a hydrogen-bonded dimer particularly noteworthy, as it successfully exemplifies the presence of hydrogen bonding in both solid and fluid states using isomorphic structural descriptors (i.e., 1:1 correspondence between the solid state and solution-state representations). Compounds **37** and **38** exhibited interesting changes in texture (and viscosity, based on eye observation) depending on the evaporated solvent. Dramatic line-shape changes in ³¹P NMR were observed in analogy to those found for **36**. Reversible color changes were observed in highly purified solutions of compounds **36-38** upon dissolution and concentration. In addition, difficulties were occasionally encountered in recovering the compounds in solid form, which resulted in very viscous or pasty materials. We attributed the observation to the formation of ionic liquids or clusters depending on the concentration of dopants and solvent medium. The color changes are due to the formation of charge transfer complexes by hydrogen-bonded or contact ion-paired adducts with solvent or substoichiometric water transients. Several experimental observations suggested that the formation of [H₂O] clusters or [H₂O, Cl] clusters in discrete environments had transpired. For example, 1 or 2 integrable, discrete, extra deshielded H₂O signals (4.2-6.7 ppm) indicated the presence of “hydrogen-bonded bulk water” environments.¹⁶⁵ The additional deshielding occurrence was based on the standard “bulk water” microdroplet signal (~ 4.19 ppm in solvents we used) in solutions with slight H₂O excess (e.g., 50 to 100 excess molar equivalents, which is minimal compared to a microdroplet). The integration ratios and signal types suggested the formation of dimeric **38** and the formation of extended networks of **38**, or **38-derivatives** in some cases. That is, the presence of “secondary” or “primary” HB H₂O resonances characterized by deshielding of high-frequency bulk water ($\delta > 4.2$ ppm) or low-frequency water in solvent ($\delta > 1.6$ ppm, CDCl₃) representatives, was respectively evidenced, which is a rare finding. In NMR spectroscopy, hydrogen-bonded H₂O signals are characterized by deshielding relative to the base, reference, standard, or relevant signal under study. We demonstrated the presence of HB in general. The 1:2 [N-H \cdots Cl] to [Cl \cdots H-O]₂ integration ratios, narrow FWHM, and symmetry of the deshielded H₂O signal provided a moderately convincing argument supporting the formation of **38** as a discrete dimer.

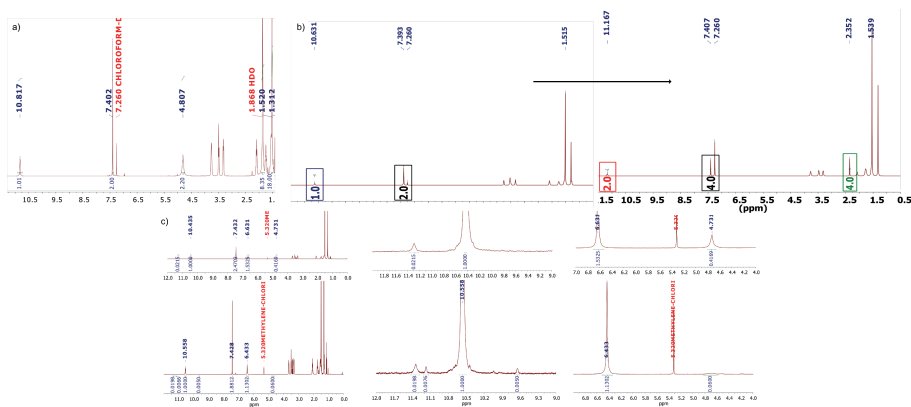


Fig. 5.2.5.3. a) ^1H NMR of **38** (i.e., **37** in THF + 50 H_2O eq. in THF via Hamilton syringe, followed by evaporation under vacuum and redissolution in CDCl_3). HB bulk H_2O cluster signal occurred at 4.81 ppm (2 H) vs. $[\text{N}\cdots\text{H}\cdots\text{Cl}]$ (1 H) and H_2O in solvent signal at 1.87 ppm (8 H), suggesting small H_2O cluster formation, an argument supported by the two types of $[\text{H}_2\text{O}]$ signals observed. b) ^1H NMR of **38** (**37** + 1 eq. of H_2O via Hamilton syringe). The $[\text{N}\cdots\text{H}\cdots\text{Cl}]$ signal deshielded from 10.63 to 11.17 ppm. Deshielding and integration of the H_2O in solvent signal to 2.35 ppm confirmed HB. The *symmetry* and *integration* strongly suggested the formation of **38** as a dimer; therefore, the bottom integrals were assumed to represent the dimer. c) CD_2Cl_2 exp. of **38** with 1 H_2O eq. (Upper spectrum). Deshielded signals (6.63, 4.73) were attributed to $[\text{Cl}\cdots\text{H}-\text{O}-\text{H}]$ and $[\text{Cl}\cdots(\text{H}-\text{OH})-\text{H}\cdots\text{OH}]$ external $[\text{H}_2\text{O}]$ protons and HB-bounded interactions. The second integration of ~ 0.42 yielded a low absolute value by ~ 0.5 eq. Relative to Mes^* aromatic protons (i.e., $\sim 1:2$ ratio), which suggested that non-monomeric free protons were present after doubling all integrals compared to experiment 72 hours after (Bottom spectrum), which indicated the presence of monomeric species. Tiny integrated signals denote equilibrium species such as supramolecular species (e.g., **38**-derivatives).

We had initial difficulties acquiring more robust evidence. We then changed our strategy and focused on the utilization of (i) very concentrated solutions, (ii) formation of **38** in open vials at low T (freezer), (iii) use of very hydrophobic solvents (benzene, toluene), despite low solubility. Relevant results supported the formation of **38** as a dimer in solution with reproducible observations in different media. For example, we confirmed the presence of high-frequency signals relative to bulk water in CDCl_3 , CD_2Cl_2 , and toluene- d_8 (Fig. 5.2.5.3 above and 5.2.5.4 below). In experiments with minimal amounts of water, hydrogen-bonded structures were formed with solvated water or water in solvent molecules, including **38** in the relevant (i.e., stoichiometric) cases shown above. This event resulted in deshielded chemical shifts in CDCl_3 greater than 1.56 ppm, indicative of the formation of hydrogen-bonded water clusters.

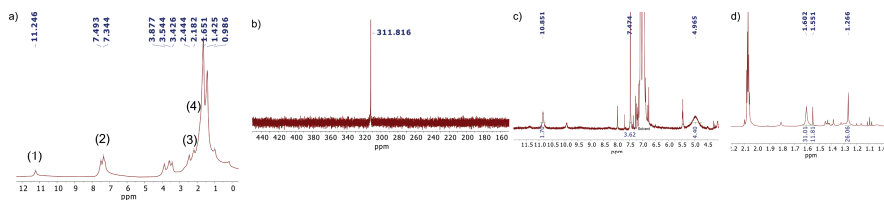
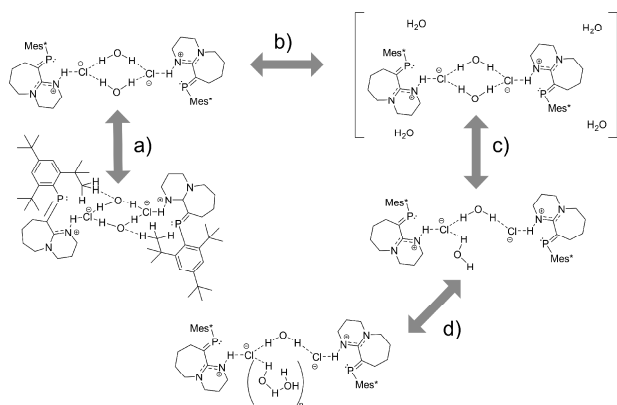


Fig. 5.2.5.4. a) Although tentative, we present an experiment with concentrated CDCl_3 ^1H NMR of **37** after several days in the freezer (i.e., slow formation of **38**). The highly concentrated sample had no solvent signals (7.26 ppm). (1) A strongly deshielded broad signal was formed at 11.25 ppm. (2) Two overlapping broad singlets with δ_{max} at 7.49, 7.34 ppm indicated two Mes* aromatic environments in contrast to the typical singlet signal observed at 7.40 ppm. (3) Two deshielded broad singlets at 2.44 and 2.18 ppm were tentatively assigned to hydrogen-bonded H_2O in solvent resonances, although integration was not possible due to the high baseline. (4) Deshielded *tert*-butyl δ_{max} broad multiplet signals occurred at 1.65 ppm, indicating an increase in secondary HB since in CDCl_3 , the δ_{max} signal is shielded to 1.52 ppm, which represents a significant deshielding (> 0.3 ppm). b) ^{31}P NMR of the previous sample, characterized by δ_{max} exchange from ~ 310 to ~ 312 ppm in CDCl_3 and broad signal. Some deshielding of the $\text{P}=\text{C}$ ^{31}P NMR was observed, which may represent increased HB degree or strength peripherally. However, as previously observed (e.g., see Fig. 1 b) in referenced work),¹⁶⁸ assigning or following peripheral HB via ^{31}P NMR spectroscopy is difficult. c) and d) Sample of **38** in toluene- d_8 , after titration with 10 M H_2O in THF (some excess). The signal at 4.97 ppm corresponds to H_2O cluster species, and its accurate 2:4:4 integration relative to $[\text{N}-\text{H}\cdots\text{Cl}]$ and *tert*-butyl signals strongly supported the formation of dimeric **38**. The low solubility of H_2O in toluene and supportive hydrophobic environment “embedded” the clusters, as seen in d) by the highly differentiated shielded ^1H NMR aliphatic Mes* region environment relative to those seen in chlorinated solvents. The two *tert*-butyl group signals had a reversed δ_{max} order relative to their standard expression, suggesting a vastly different structure was achieved in non-polar toluene- d_8 . This signal order exchange is congruent with the existence of hydrophobic effects and, in some sense, homologously to the solid-state XRD structure, given that the *ortho* signals in the solid-state solutions displayed a more significant extent of HB interactions, which in solution is equivalent to their deshielding relative to the *para* signals, as we observed. The remaining signals illustrated solvent excess (non-deuterated toluene and a small amount of THF solvent residual signals).

As reported in previous studies,¹⁶⁵ highly deshielded signals at higher frequencies were linked to high-frequency bulk water with a resonance greater than 4.19 ppm, which correspond to water clusters, potentially those in extended hydrogen-bonded networks or comprising more water molecules per site. The deshielding of water signals and accurate integrations were consistent across various solvents (CDCl_3 , CD_2Cl_2 , and toluene- d_8), supporting the hypothesis. The increasing water resonance frequency results from decreased electron density on the proton or decreased BL with the HB-acceptor site of the initial state, both aspects commonly associated with “stronger HB” or “increased degree of HB” in various cases. An increased degree of orbital mixing and, thus, smaller energy band gaps also increase the chemical shift in some cases;

this is the typical occurrence during HB situations (for example, charge-transfer complex observations mentioned above, where yellow solutions implied “smaller energy gaps”). Conclusive evidence related the deshielding of $[\text{CH}_3]_{\text{Mes}^*}$ and $[\text{CH}]_{\text{Mes}^*}$ signals to the presence of “weak HB” or increased HB character or HB degree. However, inverse chemical shift number changes occurred in more complicated cases where several factors played a simultaneous role. For example, for $[(\text{N-H})^+\cdots(\text{Cl})^-]$ and $[(\text{Cl})^-\cdots\text{H-O-H}]$ resonances, as rationalized in Fig. 5.2.5.3 c). Inverse chemical shift changes than expected were observed after experiments were measured later in more relaxed or complex conditions (i.e., modulated changes). In Scheme 5.2.5.1 below, we summarized our solution-state NMR spectroscopy observations via molecular structure representations of **38** equivalent systems and **38-derivatives**.

Potential representations of **38** in solution based on NMR results



Scheme. 5.2.5.1. The incorporation of secondary HB (“weak HB”) became evident based on the large deshielding of the relevant signals. In concentrated solutions and nonpolar solvents, deshielding of aromatic and *tert*-butyl protons was related to increased NCIs (e.g., $[\text{CH}_3]\cdots[\text{OH}_2]$ HB), as shown down from a). In some experiments, discrete amounts (i.e., two factors) of H_2O in excess suggested the presence of structurally bounded H_2O molecules in discrete microenvironments (see right from b)), such as HB clusters or extended supramolecular networks from H_2O molecules. Due to dynamics, the formation of divergent HB species was evidenced by the presence of non-integer integral ratios (or fractional signals) as seen by structure down from c). Lastly, the presence of signals representative of H_2O clusters or open networks in strongly HB environments was evidenced by high-frequency signals relative to bulk water signals. We postulate these occur in i) *n*-clustered-water-chains (zigzags), ii) *n*-clustered-water-containing graphs, as seen on the bottom structure, or in some homomorphic representation relative to these or the structures above.

Finally, we examined samples of **38** via DOSY-NMR spectroscopy (unpublished), which helped us confirm the existence of dimeric **38** in solution, as shown in Fig. 5.2.5.5. The DOSY spectra were generated from an

experiment of a sample with carefully titrated equimolar amounts of H₂O in an otherwise dry and anhydrous solution of **37** that was kept under inert conditions in sealed vials followed by dried NMR tubes (kept sealed under Ar) to minimize decomposition traces or HB disruption by solvent evaporation, or by O₂ and H₂O introduction. In summary, a Bayesian transform was applied over a sequence of experiments collected at various magnetic field strengths (G), which produced a 2D-NMR plot with diffusion coefficients over the vertical axis (f1) and ¹H NMR spectra on the horizontal axis (f2). Each set of contoured signals on the horizontal axis represents the ¹H NMR spectrum of each mixture component. The vertical axis corresponds to the representative diffusion coefficient values for each component. Only two horizontal components were observed in our experiments, indicating that only two compounds or species were present in the solution mixture. The most prominent component exhibited a diffusion coefficient of 6.72×10^{-10} cm²/s. The second component exhibited a higher diffusion coefficient value of 1.71×10^{-9} cm²/s. Similar diffusion coefficients have been observed for dimeric/monomeric equilibrium species using equivalent NMR techniques.¹⁶⁹ However, after accounting for CDCl₃'s dynamic viscosity and using Einstein's relation, we obtained a low diffusion coefficient (large particle) to high diffusion coefficient (small particle) hydrodynamic radius ratio of ~ 2.54 , which is in good agreement with a dimeric to monomeric ratio corresponding to the observations. Both components partially overlapped in their primary NMR spectral signals, which confirmed they had equivalent or similar structures.

The similarity of the ¹H NMR spectrum of the two components strongly indicated that these were illustrative of compound **38** in two different representative forms. The relative chemical shift magnitude contributions to the overall spectrum of each component varied slightly for some proton populations, such as the Mes* protons. This variation indicated differences between the two components as expected from monomer to dimer, despite their apparent homologous equivalence. Notably, both components shared the characteristically deshielded HB H₂O in solvent signal, centered at ~ 2.35 ppm (Fig 5.2.5.5, b)). The component with the lower diffusion coefficient (i.e., the component with larger MW or volume) exhibited two hydrogen-bonded H₂O resonances, whereas the opposite component was characterized by one feature at the same intensity and contour value, confirming our assignments. Additionally, both components overlapped in the high-frequency HB region centered at 11.19 ppm for the dimer and 11.18 ppm for the monomer. Resonance congruences confirmed their equivalence regarding the type of HB (i.e., between imine and chloride). Their chemical shift differences were minor, horizontally (which confirmed the accuracy of the DOSY-NMR transform process) and vertically (which confirmed the equivalence between the two components).

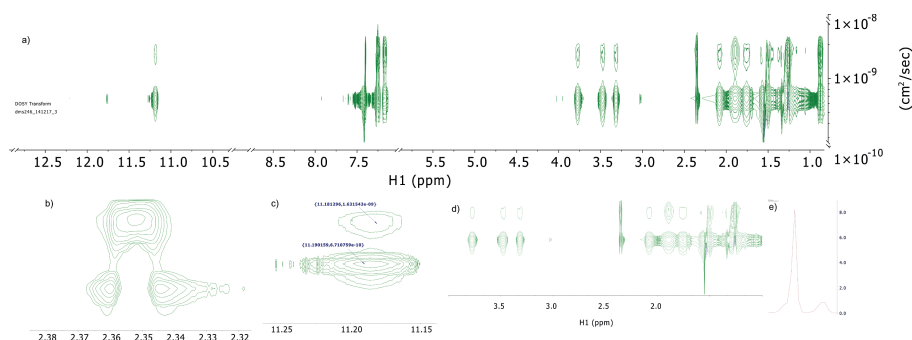


Fig. 5.2.5.5. (Unpublished). a) DOSY-NMR spectrum of **38**; aside from slight chemical shift differences, the acquired ^1H NMR spectrum in each case is comparable to the other for both components, corresponding to the expected monomer (upper spectrum) **38-monomer** and dimer (lower spectrum) **38** cases. b) Representative hydrogen-bonded deshielded H_2O signals at 2.35 ppm. Crucially, the component (lower spectrum) with the lower diffusion coefficient (i.e., the larger compound) contained two features (**38**) relative to the top, which strongly validated our postulates on the supramolecular (dimeric) nature of the bottom component. These two spectra correspond to two H_2O forms in solution, the lower one revealing the isomorphous structure of **38** in solution in connection to those previously found in the solid state via XRD. c) Similarities between the two components in the aromatic region were found. d) DBU CH_2 , HB H_2O , and Mes* *tert*-butyl regions exhibit slight differences, as expected from the symmetry differences between the two forms. e) Concentration ratio, with the dimer yielding $\sim 85\%$ of the mixture.

Their diffusion coefficients rest within reasonable boundaries compared to typical compounds in similar solvents.^{170,169} The remainder of this subsection contains our concluding remarks on the details of HB by NMR. The description of HB in liquid solutions has been challenging and is a challenge even for dedicated HB and NMR experts.¹⁶⁸ The low solubility of HB-donor-containing and HB-acceptor-containing species in aprotic solvents, the sensitivity of HB to noise, and the establishment of equilibria phenomena obfuscated and complicated the observation or assignment of the resonances that best characterized or represented the HB interactions. We and others argue that the presence of neutral and ionic hydrogen-bonded species (e.g., the latter, known as “strong hydrogen bonds”)¹⁷¹ may appear simultaneously in selected cases (e.g., **42**) being distinguishable in NMR spectroscopy. We evidenced equilibrium processes in several experiments, where the appearance and disappearance of minor signals occurred reversibly. The reversible or transient nature of the phenomena, coupled with different experiments using other nuclei or 2D-NMR, including DOSY-NMR, was thus only ascribable to the existence of structurally homomorphous structures in solution. The most relevant experiments were characterized by the existence of one species primarily, which, based on slight settings changes, exhibited reproducible and distinguishable spectrum changes only ascribable to HB species in solution as opposed to free protonated forms (which obviously would not change distinguishably or

present discrete relations with H₂O protons), which is a nice feature of **38**. In contrast, [DBU⋯HCl] (**42**) contained > 20 % of two secondary species, corresponding to hydrogen-bonded ion-paired and proton transfer or protonated species [DBU⋯H]⁺, as we tentatively attributed based on observations and referenced material. In most cases, it is essential to reiterate that the ion-paired complexes that possess a proton or hydrogen atom intermediary are still representative HB compounds. Strong HB has been linked to proton transfers, which inherently generate the charged species that characterize many HB ion-paired compounds. Similarly, it has been postulated that the higher the degree or extent of HB, the higher the chemical shift number, which we believe to be a reliable but not a generalizable criterion. About this last argument, we will study **39** and **40** below, which, based on XRD bond lengths and familiar principles delineated through the chapter, generate a more robust HB interaction in nonpolar solutions while exhibiting lower chemical shifts for the high-frequency signal, which is slightly puzzling. Moreover, in multicomponent systems where more than one HB is present (e.g., **38**), modulation of the interactions may lead to inverse changes of the chemical shift number (i.e., modular responses) relative to the empirically expected changes based on the increased or the decreased degree of HB within the studied system, following an action (settings change ~ change in concentration, for example).

5.2.6. Analysis of the elementary electronic structure of **37** and **38-monomer**. QTAIM analysis of **38**.

This subsection will briefly summarize our DFT-derived results on **37**, **38-monomer**, and a molecular graph representation of **38**, performed using Bader's analysis (QTAIM). Frontier orbital density analyses of **37** and **38-monomer** confirmed the compounds' increased stability compared to **36**. For **37** and **38-monomer**, the orbital density of the three highest occupied frontier orbitals (i.e., HOMO to HOMO-2) was located on the chloride ions, with additional contributions from the imine and amine moieties (esp. for **37**). In both cases, the LUMO orbital consisted of π^* density, with a moderate contribution from the P=C motifs for the **38-monomer**. Lastly, the HOMO-LUMO gaps were 3.06 eV (**37**) and 2.91 eV (**38-monomer**).

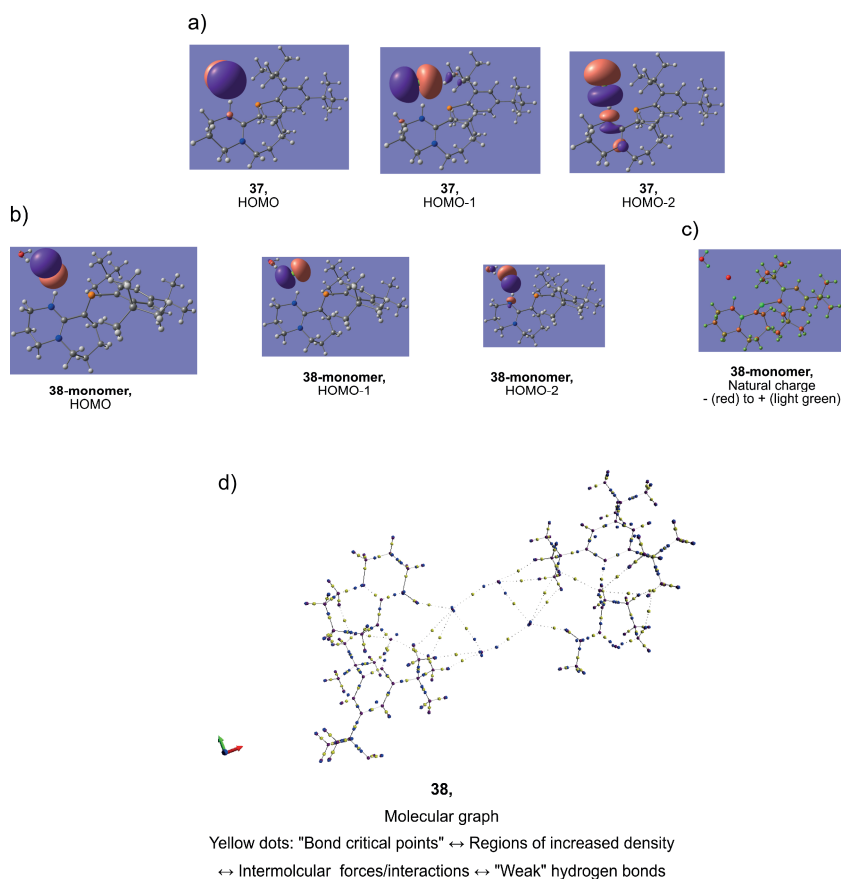


Fig. 5.2.6.1. a) HOMO to HOMO-2 frontier electron density of **37** using DFT. Calculations were performed in the gas phase at the B3LYP-d3/6-311+g(d,p) level. b) HOMO to HOMO-2 orbital density of **38-monomer**. c) Natural charges and d) Molecular graph of **38**. The analysis was performed from a DFT electronic density solution. Some caution should be exercised since it was impossible for us to fully optimize the structure of **38**. However, it is significant that the program predicted the ring structure of the central quadrilateral network, as well as HB interactions based on $\text{CH}_3 \cdots (\text{OH}_2)$ and $\text{CH}_3 \cdots (\text{Cl})^-$ interactions. Our original report predicted **38** to be the smallest water/chloride dimeric network containing two $[\text{H}_2\text{O}]$ HB-donor-only sites and two $[\text{Cl}]^-$ HB-acceptor-only sites, without considering secondary hydrogen bonding. However, now that we have a better understanding based on additional NMR, FTIR, and other data, and increased knowledge, we believe that "secondary" (or "weak") HB is critical to the expressed molecular structure, and *tert*-butyl protons also function as effective HB-donor. Therefore, the hydrogen-bonded quadrilateral network of **38** does not represent the smallest possible discrete water/chloride molecular network in a molecular system. However, it is difficult to imagine a "smaller" discrete HB network in solution or in the solid state.

5.2.7. FTIR/ATR spectroscopic and computational chemistry study of HB in solution mixtures of **37** and **38**.

Hydrogen bonding (HB) characterization via FTIR spectroscopy is often accomplished by observing a red-shifted vibrational stretching of the adduct signal relative to the free compound. Understanding new structural motifs involved in HB can lead to valuable connections, equivalencies, or relationships between different HB schemes and systems. In this study, we characterized the HB of species **38** by evaluating the expected $\nu_{[\text{O-H}]}$ stretching frequencies of hydrogen-bonded H_2O molecules as we varied the experimental environment. A visual and informal description reveals that the dipole change of non-bonded H_2O hydrogen atoms oscillates differently from the HB H_2O adduct, especially when the latter is part of a ring structure, as in species **38**. As a result, non-bonded H_2O interactions have higher vibrational frequencies.

The IR peak red-shift is not a universal rule characterizing hydrogen bonding; blue-shifted HBs also exist.¹⁷² The large amplitude, many-body-coupled vibrational features typical of large systems such as **36** and **38** can lead to complicated IR spectra.¹⁷³ The HCl absorption region is relevant (1900 to 2800 cm^{-1})¹⁷⁴ in finding hydrogen-bonded [HCl] equilibrium species due to “strong hydrogen bonding” or “covalent hydrogen bonding” situations. That is, as far as we are concerned, even when proton transfer or the formation of ionic hydrogen bonding has been assumed primarily (e.g., $[(\text{N-H})^+\cdots(\text{Cl})^-]$ interactions), we can also observe HB from formal HCl structures (see below) given the constant dynamics of molecular systems under mild conditions.¹⁷⁵ Even though we are deeply interested in $\text{P}=\text{C}$, assigning this band is impossible, given that most resonances correspond to coupled modes. From the analysis of theoretical DFT models, we found bending and stretching features with $\text{P}=\text{C}$ contributions (up to 10 % contribution for some bands), ranging from $\sim 700\text{--}1200\text{ cm}^{-1}$.

It is important to note that solid-state samples of **38** were confirmed to consist of the dimeric structure based on regular FTIR spectroscopy (see SI of published papers). We used FTIR-ATR spectroscopy from measurements of various liquid solutions of **38** in DCM with different relative differences of H_2O content to prove the formation or existence of **38** as a dimer. We postulated that the vibrational $\nu_{[\text{O-H}]}$ stretches of supramolecular-bounded H_2O exhibiting HB in hydrophobic environments would present distinctive features in comparison to amorphous, free, or bulk H_2O in aqueous and nonaqueous solutions or the absence of HB potentiating hosts (i.e., **36** + HCl, and slightly so, **36**, given the imine and amine HB-acceptor). More precisely, the discrete response of a two-coordinated HB-donor- H_2O -based dimeric complex in a symmetric environment (**38**) differs from that of a one-coordinated HB-donor- H_2O -based monomeric one. The latter being more asymmetric and potentially more anisotropic, we expected it to possess more significant complexity or peak broadening. We expected two discrete and closely separated $\nu_{[\text{O-H}]}$

stretch modes (symmetric, asymmetric) of the same intensity for a symmetric dimer like **38**. In our case, a central ring and a symmetrically cyclic structure had been observed in the solid state and NMR, as previously shown. We reasoned that the similarity and closeness of the signals would stem from the quadrilateral H₂O network's C₂-based symmetry, which is further enhanced via localization through the surrounding and embedding of hydrophobic-hydrophilic motifs. After an encapsulation-like process, the signals are decoupled from the surrounding reservoir events, which, we reasoned, gives rise to discrete features. Thus, we expected sharp features, contrary to the empirical assumption that hydrogen bonding (HB) leads to broad signals. On top of that, we rationalized that a weakly bound complex with sufficient structural lifetimes and a strict HB environment should lead to sharper spectroscopic responses, indicating increased order.

Thus, we performed four experiments (**I** to **IV**) with different H₂O/compound ratios to demonstrate the presence of a supramolecular hydrogen-bonded dimeric structure. Experiment **I** was performed with the neutral compound **36** under anhydrous conditions, while Experiment **II** was performed with the anhydrous HCl precursor compound **37**. Experiment **III**, designed to form non-dimeric structures (e.g., **38-monomer** or **38-derivatives**), was carried out with a threefold molar excess of H₂O in a dilute mixture containing 1/3 substoichiometric amounts of **37** in DCM. Experiment **IV** was designed to form dimeric structures (i.e., **38**) with equimolar quantities of compound **37** and H₂O in DCM. The spectra were obtained using the FT-ATR-IR technique, and the relevant spectral regions are shown in Fig. 5.2.7.1. Various computational chemistry methods validated the resulting experimental spectra and assignments. In Fig. 5.2.7.1 b) and c) below, we show the eight most relevant structures that formed our theoretical model. The structures were fully optimized and found to be minimum energy points, from which the IR spectrum was extracted in each instance (**A-G**). The SCRf technique with the standard PCM model was used for calculations in liquid solution.

The [O-H] stretches of **IV** occurred at 3489 and 3418 cm⁻¹, red-shifted relative to gaseous H₂O (3756, 3657 cm⁻¹), suggestive of hydrogen-bonded H₂O molecules. The symmetric environment, closeness, and discreteness confirmed our initial postulate about the two signals and the expected FTIR response of **38**. We confirmed the assignments by studying our computational models. For example, the FTIR of models **D** and **C**, relative to monomeric **H**, support our ideas and assignments. Model **F** was not included in the analysis due to the structurally divergent nature of the optimized structure, which had no relevant value to our problem. Interestingly, the same initial structure was successfully optimized in a DCM-solvent-solution calculation (model **E**) using the same level of theory. Model **E** provided essential clues, based on the IR spectrum, compared to monomeric model **G** using the ONIOM method (MP2: [N_{imine} + H] + [Cl] + [H + O + H]; PM6: (DBU) - [N_{imine}]).

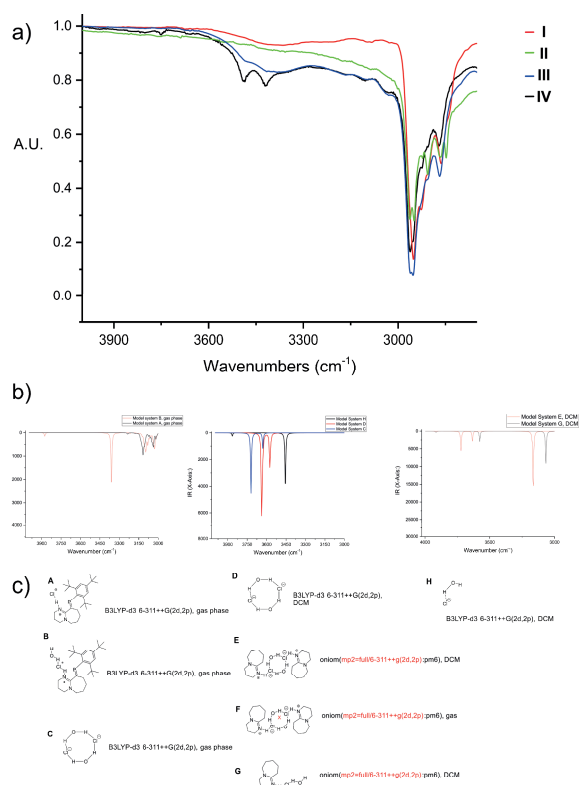


Fig. 5.2.7.1. a) FTIR-ATR spectroscopy of **36** (I), **37** (II) in anhydrous conditions, **37** (III) in a diluted DCM solution with a 1:3 excess H₂O concentration, and (IV) in a concentrated DCM solution with an equimolar amount of H₂O molecules. Thus, spectrum IV corresponds to **38**, nicely agreeing with our premises. No relevant vibrational stretches or features were visible for I and II in the [O-H] stretching regions > 3200 cm⁻¹. A featureless band representing indiscrete HB formation for III was evident at ~ 3450 cm⁻¹. Remarkably, the spectrum of IV demonstrated the discrete form of a dimeric species with two H₂O molecules in the same symmetrical environment, as evidenced by the sharpness and closeness of the two separated signals. b) Calculated IR spectra for A-G. See main text for details. c) Computational model structures with computational methods are shown in legends.

Our experiments also helped us confirm the presence of the hydrogen-bonded dimeric structure **38** in the ~ 2000 cm⁻¹ portion of the infrared spectrum. This region is typically associated with "strong hydrogen bonding"^{176,177} in embedded water molecules and is expected to exhibit characteristic HCl absorption signals indicative of an increased hydrogen-bonded [HCl] character based on previous knowledge,¹⁷⁵ and studies of HCl-hydrates and concentrated HCl solutions,¹⁷⁸ for example. We obtained well-resolved spectra using rigorous procedures, including careful preparation and removal of the solvent or blank and CO₂ (maxima: 2300 to 2400 cm⁻¹) and noise signals. Unlike III, experiment IV showed distinct dimeric signatures, such as two distinct peaks and a broad

spectral feature with many coupled modes (1958 cm^{-1} , presumably related to a coupled mode from the H_2O -based network), providing evidence of the hydrogen-bonded dimer species **38** (Fig. 5.2.7.2).

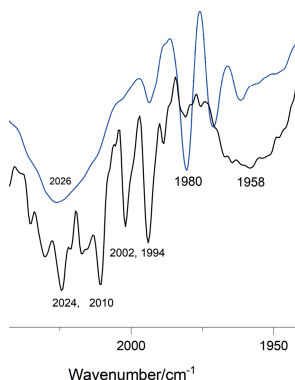
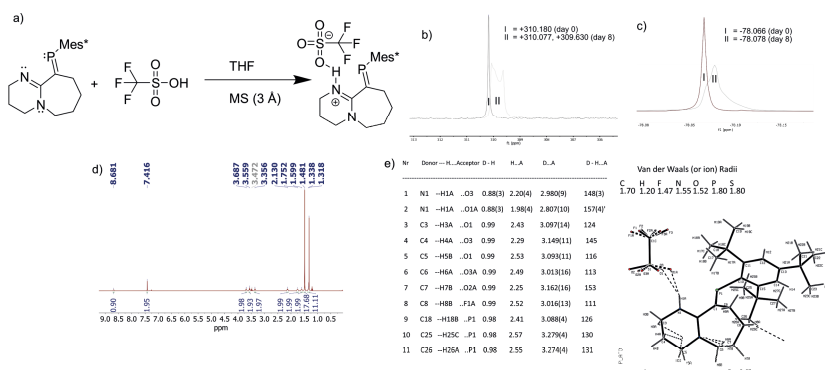


Fig. 5.2.7.2. FTIR spectroscopy of **III** (blue curve) **IV** (black curve) in the $1900\text{--}2100\text{ cm}^{-1}$ region. HB vibrational stretches can be seen for **IV** as well-resolved, discrete dimeric signals, one of which occurred at 2024 and 2010 cm^{-1} (and at 1994 and 2002 cm^{-1}). Oppositely, sample **III** presented an indiscrete, featureless band at 2026 cm^{-1} (and a single peak at $\sim 1994\text{ cm}^{-1}$). The two sets of equivalent signals in **III** and **IV** present additional evidence of the formation of dimeric product **38**. The red-shifted interaction for the first set of features in **IV** versus **III** (i.e., by $\sim 8\text{ cm}^{-1}$) can signify elongated ($\text{N}\cdots\text{H}$) bonds or interactions of increased $[\text{N}\cdots(\text{H}\text{--}\text{Cl})]$ character, with a more prominent covalent character between chloride and hydrogen. Lastly, and as mentioned in the main text, **IV** exhibited a highly-coupled feature at 1958 cm^{-1} , which we assigned to extended mode coupling involving the entire H_2O -based HB network. This argument is potentiated by the assignment and attribution given to the blue curve (**III**), which indicates an asymmetric and non-dimeric structure, and which can be ascribed to the formation of **38-monomer** (or **38-derivatives**), as we previously argued.

5.3. Reaction with superacids: Hydrogen bonding formation over $\text{P}=\text{C}$ decomposition after reacting with HOTf (**39**) and HPF_6 (**40**).

During our studies of **37** and **38**, we set out space for evaluating the reactivity of **36** with other acids. The reaction between **36** and trifluoromethanesulfonic acid (triflic acid: HOTf) was conducted at low temperature under anhydrous and deoxygenated conditions by adding 1 equivalent of triflic acid to a solution of **36** in THF in the presence of molecular sieves (MS: 3 \AA). We rationalized that using molecular sieves, as typical small molecule absorption agents (incl. as desiccants), could help trap H_2O . Due to their small pore size, other small molecule impurities (HF) could also be trapped before there was enough time or space to react with **36** via hydrolysis or other side reactions, increasing

our product yields. The reaction was immediately completed and characterized by a deshielded ^{31}P NMR resonance ranging from 301.3 ppm (C_6D_6) to 309-310 ppm (CDCl_3). A single crystal structure was obtained from the diffusion of *n*-hexane to a concentrated solution of **39** in DCM. A representative reaction formula scheme accompanied by relevant NMR and XRD data is shown in Scheme 5.3.1 below.



Scheme 5.3.1. a) Reaction between **36** and HOTf (from the shelf) to yield **39**; T = -50 $^\circ\text{C}$, anhydrous, deoxygenated conditions. b) and c) Representative ^{31}P and ^{19}F NMR spectra of **39** taken at different times (see inset text). d) ^1H NMR spectrum of **39**. e) Hydrogen bonding analysis using Platon. Table with relevant values and parameters. Table with relevant VdW Radii used in the analysis. Asymmetric unit view of the relevant HBs in **39**. In the stacking/packing view, the HBs were difficult to visualize; thus, we omitted them in the schematic visualization. In e), eight (1-8) hydrogen bonds are visible, with intramolecular (9-11) ones omitted for better visualization. Relevant angles ($^\circ$): N1-H1-O1a = 157(4), N1-H1-O3 = 148(3). BLs (\AA): N1-O1a = 2.807, N1-O3 = 2.980, C1-P1 = 1.689.

We confirmed the higher stability of **39** relative to **36**, confirming the type of stability we hypothesized and rendering this approach helpful in stabilizing E=C motifs relative to a parent system, in this case, a P=C. The reaction between the triflic acid may be expected to create an HB adduct through an oxygen atom directly bonded to the imine moiety and the hydrogen in between the two. This connectivity path was confirmed in the solid state via XRD. The most relevant HB naturally correspond to those between imine nitrogen and sulfonic oxygen atoms, shown in Scheme 5.3.1 e); secondary but relevant hydrogen bonds occurred between HB-acceptor oxygen and hydrogen atoms from HB-donor carbon atoms neighboring the nitrogen atoms on the DBU-CH₂ groups. Also, between HB-acceptor oxygen and hydrogen atoms on Mes*-*tert*-butyl CH₃ HB-donor groups.

Lastly, the reaction between **36** and HPF₆ from a 50 % aqueous solution was executed in THF under inert conditions at low T in the presence of molecular sieves (3 \AA), using HPF₆ (60 %). The reaction gave good yields after

adduct formation over decomposition of the P=C, the latter which implies structural break-down or oxidation of the DBU scaffold. DFT results advocated for this type of stability based on the absence of occupied P=C frontier orbital density for representative model systems **37** and **38-monomer**, as opposed to **36** models, which presented high π electron density contributions of the P=C bond in the HOMO and even HOMO-1 orbitals (see sections 5.2.2 and 5.2.6). More importantly, the energy difference between the HOMO and HOMO-4 (highest energy orbital with π -symmetry located on P=C bond) in model **37** was, for example, 1.21 eV (28.02 kcal/mol, 117.25 kJ/mol), which is significant and relevant in connection with our claims. We convincingly confirmed the increased stability of the obtained adducts following appropriate NMR stability studies, summarized in Fig. 5.4.1 below.

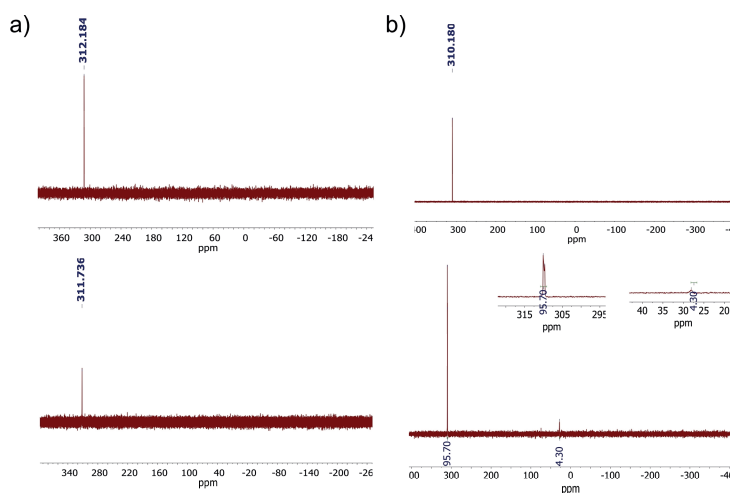
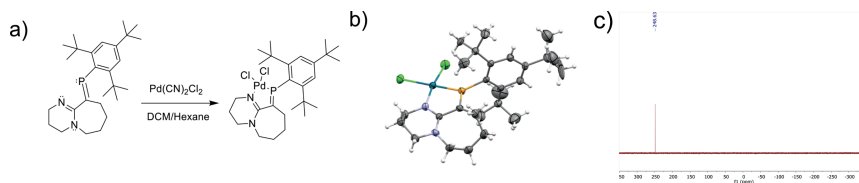


Fig. 5.4.1. a) Stability study of **37** (formation of **38** occurs); **day 0** (top) vs. **day 30** (bottom). NMR tube opened to the atmosphere and occasionally refilled during the 30 days. No other visible impurities. b) Stability study of **39**; **day 0** (top) vs. **day 7** (bottom). NMR tube opened to the atmosphere and refilled once during the seven days. Only ~ 4 % of impurities were detected.

5.5. Synthesis and characterization of Pd(II) complex (**41**) and organic DBU-HCl (**42**) species.

We probed **36** as a ligand for use in TM-based chemistry by use of the Pd(II) [PdCl₂(MeCN)₂] or [PdCl₂(PhCN)₂] precursors, which reacted stoichiometrically with **36** to yield **41**. A susceptible orange compound that decomposed readily under atmospheric conditions was obtained. Crystal structures were obtained from a layered hexane/DCM solution of **41** under argon. The handling and characterization of compound **41** were challenging due to the presence of isomeric/uncoordinated forms because of ligand exchange/scrambling

in the solution. The small ^{31}P NMR chemical shift change < 10 ppm after complexation validated this idea (Scheme 5.5.1).



Scheme 5.5.1. a) Synthesis of palladium (II) complex **41**. b) ORTEP representation of **41**; the P=C BL shortened to 1.648(7) Å. c) ^{31}P NMR spectrum of transition metal complex **41**; a single resonance at + 248.63 ppm was observed.

The square planar complex enforced a markedly increased planarity of the molecular scaffold, and as a result, the bicyclic torsion angle between imine and phosphalkene group motifs decreased to barely 12.4° , in comparison to the same angle for compounds **36**, **38**, **39**, and **40** (52 to 57°). The additional structural frustration of the system (on top of the bicyclic torsional strain) could also explain the high reactivity of **41** vs. **36** and the HB adducts. It was interesting to find the reduced atmospheric stability for a transition metal complex of **36** because it highlighted the stability of P=C given by HB and supramolecular chemistry interactions and, thus, the potential of our concept.

Lastly, we synthesized the organic [DBU-HCl] complex **42** by a stoichiometric reaction between DBU and HCl under anhydrous and deoxygenated conditions. The compound helped us compare the chemical shifts corresponding to [DBU-HCl], which was helpful by increasing the stringency and reliability of our analyses. Despite its generality, the crystal structure of **42** had not been reported in the literature previously (see Fig. 5.5.1). Compound **42** exhibited a longer DHA bond length distance of 3.156 Å in the solid state than those found for P=C-containing HB compounds **38** to **40**, in some sense confirming our notions of “HB support” provided by the hydrophobic and less polar Mes* and group motif P=C presence. On the other hand, the HB donor-acceptor (DHA) angle was closest to the ideal 180° value for **42** (176° ; see figures above and SI section of our article for more details on the other compounds).¹⁶²

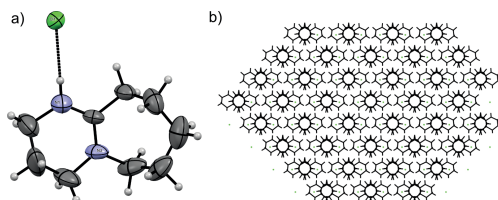
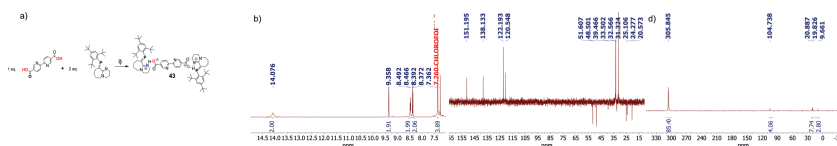


Fig. 5.5.1. a) ORTEP representation of **42**. Hydrogen BL: Cl-N (imine) = 3.156 Å. b) Solid-state packing view down the crystallographic “a” axis.

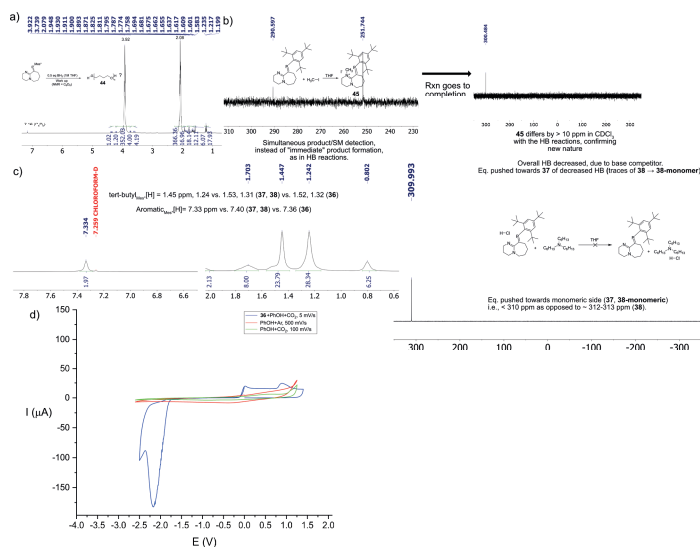
5.6. Miscellaneous: Unpublished work and future avenues.

We briefly describe other reactivity paths we evaluated, such as the reaction between **36** and a double HB-acceptor carboxylic acid derivative (Scheme 5.6.1). The reaction proceeded straightforwardly, and sole product formation was confirmed by multinuclear NMR spectroscopy.



Scheme 5.6.1. Synthesis of compound **43**. i) chloroform; RT; sonication, 30 seconds; stirring, 30 minutes. b) ^1H NMR spectrum of **43** (CDCl_3). The deshielded signal at 14.08 ppm was significantly deshielded. Carboxylic acids tend to create strong HB and resonate in this region. c) ^{13}C DEPT-135 NMR spectrum of **43**. The number of $[\text{CH}]_{\text{pyr}}$ aromatic signals was characteristic of a symmetric environment, with a 1:2 (acid to $\text{P}=\text{C}$) ratio, as shown by the larger signal at 122.19 ppm corresponding to $[\text{CH}]_{\text{Mes}}$ carbon nuclei and the low dispersion of the three pyridine signals (corresponding to six carbon atoms). By the good resolution of the spectrum, the monosubstituted case would have split distinctly, up to six signals. d) ^{31}P NMR spectrum of **43** confirmed major product formation as a single broad resonance centered at 305.85 ppm. In summary, compound **43** was characterized by a broad ^{31}P NMR resonance centered at + 305.85 ppm. The nature of the compound may be readily ascertained from symmetry grounds and the integration of signals on the spectra.

Reactions between **36** and BH_3 in ethereal solutions were performed; interestingly, we were surprised to find very viscous material after the reaction product workup. The NMR evidence suggested that polymerization of THF to some form of poly-THF had taken place (Scheme 5.6.2. a)).¹⁷⁹ Scheme 5.6.2, shows a brief schematization of the polymeric reaction product (**44**), of the reaction product (**45**) from reactions between **36** and electrophilic methyl-iodide (MeI), and of the equilibrium product from the reaction between **37** (traces of **38** assumed also) and trihexylamine as an HB disruptor (which also minimizes traces of **38** towards **38-monomer** or **37**) by competing towards complexation with HCl or by driving equilibria away from HB adducts. Finally, we present a small part of our project in the study of the reactivity of **36** under CO_2 atmosphere, which strongly suggests the electrocatalytic reduction of CO_2 (see scheme 5.6.2 d) and caption). The superposition of the experiments conducted under Ar and phenol under Ar/ CO_2 shows no increase in current, indicating that catalysis is not occurring, in contrast to the experiment with **36**/phenol under CO_2 , which shows dramatic increases in current (blue curve).



Scheme 5.6.2. (Unpublished). a) Reaction between **36** and BH₃, which led to tentatively assigned polymerization of THF (**44**), based on NMR of workup product after previous thorough evaporation of mixture, digestion into toluene, filtration, concentration, and redissolution in C₆D₆; observed chemical shifts are deshielded relative to THF, and the NMR presents typical features of polyether (poly-THF) polymers (see reference)¹⁷⁹. b) Reaction conditions synthesis of **45**, NMR reaction monitoring, and NMR after reaction completion. Interestingly, we can differentiate the nature of this adduct from the HB products by two salient features. We could trace the reaction product in simultaneity with the presence of starting material (**36**), whereas for HB equimolar reactions, we could not do so. Two, the new nature of the product is established by its 10 to 12 ppm chemical shift difference from the typical HB product **38** (~ 312 ppm, CDCl₃). c) Experiment of a 1:1 equimolar mixture of **37** (assumed to contain some H₂O traces, and thus some finite amount of **38**) and trihexylamine, as an HB disruptor. Interestingly, the ³¹P NMR equilibrium is pushed towards the lower 310 to 312 chemical shift limit (i.e., lower frequency limit) we postulated represented the **38-monomer** ↔ **38** equilibria, based on observations, and the shielding of various shifts relative to **36**, **37**, **38**, as shown in the text insets on the ¹H NMR figure. d) This crucial experiment suggests that the DBU-phosphaalkene ligand, compound **36**, is a potential electrocatalyst for CO₂ reduction in homogeneous solutions (with phenol as a proton source).

The catalyst product could not be identified in this study due to limitations and time constraints. Nevertheless, the reproducibility of the behavior over multiple experiments using CV is a promising indication of potential of **36** as an electrocatalyst. Further research is needed to identify the catalytic product using dedicated GC instrumentation. Notably, to our knowledge (limited to 2020 for this project), there are few to no other examples of pure organic and neutral molecules that can perform this type of transformation alone, making this project noteworthy for future funding and studies. The bidentate molecular structure in the pocket space between imine and P=C was identified as suitable for CO₂ interaction, coupled with the known reactivity of DBU and

DBU salts with CO₂. Future work should complete this potentially impactful project.

5.7. Conclusions.

The compounds **36-40** presented in this chapter contain hydrogen bonding and secondary forms of non-covalent interactions, including so-called "weak hydrogen bonds", which we have thoroughly characterized in liquid solutions and in the solid state. Compared to the numerous available phosphine (P-C) and imine (C=N) congeners, a unique P=C group motif in these compounds makes their study particularly attractive due to their functional and modular nature. The results we obtained revealed two intriguing relationships. First, as demonstrated in compounds **37-40**, hydrogen bonding significantly reduced the typical hydrolyzable and oxidizable behavior of the P=C group, as observed in highly reactive species **36**, as well as in other E=C-containing compounds in atmospheric or acidic environments (see the references). This reduction in reactivity offers the potential for the design of novel stabilization strategies for heavy E=C units. Second, the work exemplified the challenge in demonstrating isomorphic supramolecular representations from solid-state to liquid solutions, highlighting the potential of these compounds to shed new light on self-assembly and HB interactions. The peripheral imine group and its "savior" nitrogen atom played a critical role in these compounds, emphasizing the importance of HB interactions. Second, the challenge of detecting and demonstrating isomorphic supramolecular representations from solid-state to liquid solutions, which we successfully achieved, highlights the potential for these compounds to shed new light on self-assembly and HB interactions. The functional mechanism of self-assembly into a hydrogen-bonded H₂O-based network in the case of **38** is of interest for various applications. The way in which the physical properties and spectrum of the compound establish correspondences and relations following different actions (e.g., color/physical changes based on different sequences of solvent exchange operations or minimal concentration differentials, hydrogen-bonded and H₂O cluster formation based on precise environmental conditions and experimental settings and other factors as evidenced via XRD and NMR) is particularly striking and exemplifies the modular character P=C introduces into the molecular scaffold. The preferential dimeric formation of compound **38** via cooperativity or self-complementarity makes it a particularly relevant system to study for future applications. In conclusion, our results highlight the potential of hydrogen bonding interactions in stabilizing and self-assembling compounds containing P=C group motifs. Further studies on the functional and modular nature of these compounds may lead to new insights into their potential applications in various fields.

Ch. 6. Photophysical and electrochemical properties of an emissive Cu(I) complex with DBU and Phosphaalkene ligands.

6.1. Literature background. Introduction to low-coordinated P=C ligand-based copper(I) complexes.

The development of new photosensitizers or photocatalysts that can be used as light harvesters to convert solar energy into electricity or chemical fuels and photoactive compounds as elements for optoelectronic devices in organic electronic applications such as ultrafast switches and metal-containing components is of interest to various industries.^{180,181,182,183}

This section introduces the study of Cu(I) complexes focusing on those featuring P=C ligands. The coordination number (CN: 2 to 4) and structural diversity (e.g., mononuclear versus polynuclear Cu complexes) of copper(I) centers are at an interplay with the stereoelectronic factors that depend on the stabilizing counterion salt and the underlying ligands (e.g., bite angle, denticity, ligand charge).¹⁸⁴ The differences between Cu(I) and Cu(II) that favor various types of CN: 4 geometries based on electronics are fascinating and highly relevant to this chapter.

Fig. 6.1.1 below shows some previously reported copper(I) phosphaalkene complexes (**I-IV**). Compounds **I** (and **II**) and **IV** are copper(I) complexes with phosphaalkene (and bisphosphaalkene) bidentate (P, P) and phosphaalkene tridentate (P, N, P) ligands, respectively. Compound **III** presents an attractive binuclear complex as a centrosymmetric dimer with two tetrahedral Cu(I) sites in coordination with P atoms. The compound we study in this chapter (**46**) was characterized through HRMS, cyclic voltammetry, NMR, and various photophysical methods.

The generation of two isomeric computational models, **M1** and **M2** (Scheme 6.2.1), provided important clues that helped us thread through this chapter. According to our literature survey, **46** is the first example of an archetypal 1:2 Cu(I):phosphaalkene (i.e., two neutral bidentate ligands per one copper center).

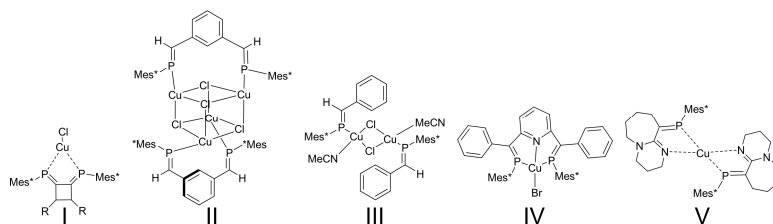


Fig. 6.1.1. Relevant examples of Cu(I) complexes possessing P=C ligands (**I–IV**) are shown, including the studied system, compound **46** (**V**). Details about the compounds are described in the main text.

Furthermore, no studies about the photoluminescent or electrochemical properties of copper(I) phosphalkene complexes have been presented to date, apart from a report on the absorption properties of copper(I) complexes of pyridine-bridged tridentate phosphalkene-oxazoline ligands, which resulted in compounds with robust absorptive features in the visible region of the spectrum.¹⁸⁵ In the next section, we will introduce compound **46** from the general standpoint of emissive Cu(I) complexes with neutral bis(diimine) ligands.

6.2. Copper(I) complexes with bis(diimine) ligands.

Characterization of **46** by photophysical, electrochemical, NMR, and DFT/TD-DFT.

The primary motivators for the synthesis and study of Cu(I) complex **46** are related to the potential of obtaining emissive P=C compounds with observable excited state lifetimes and rich electrochemical responses. Because of the presence of a tailored DBU-based P=C-containing backbone (compound **36**, from Chapter 5), we hypothesized that steric and electronic constraints could play an aggregated or modulated role in the exhibited properties of the resulting material when in concert with a transition metal. Steric, electronic, and degrees-of-freedom factors could derive from Cu(I) complexes with potentially unique features, some of which we now describe. **(1)** The presence of several *tert*-butyl groups could give rise to decreased non-radiative decay from increased steric hindrance and resulting structural rigidity, furthered by transition metal complex formation. **(2)** The steric restraining could drive an intensified response from photoexcitation. **(3)** The imine-phosphalkene bicyclic-derived torsional strain from DBU and consequent frustrated π -conjugated path in ligated or free ligand states could lead to the formation of degenerate ground forms that release frustration upon metal complexation or that produce more expressive responses after photoexcitation or electron removal (and vice versa). **(4)** The π -acceptor and unsaturated nature of N=C and P=C functional groups as ligands coupled by a saturated

framework complement could generate well-defined electronic and photonic interactions between ligands and metal centers.

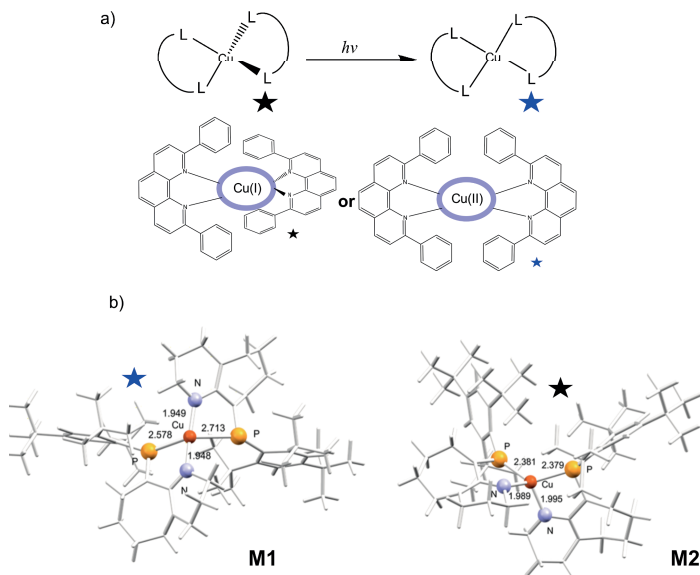
Copper(I) complexes with bis(diimine) aromatic ligands possess strong absorptivity and long emission lifetimes. These emission events and respective lifetimes are related to internal rearrangement processes. These different rearrangement processes are explained through mechanisms corresponding to events that generate states from charge transfer (CT). For example, electronically excited states can be described by their character as metal-to-ligand-charge-transfer ($^1\text{MLCT}$ or $^3\text{MLCT}$), ligand-to-ligand-charge-transfer (LLCT), mixed character, and more. The generated (or emitted) light by Cu(I) complexes can be characterized as arising from fluorescence, phosphorescence, thermally activated delayed fluorescence (TADF), and more.¹⁸⁶

Cu(I) complexes are characterized by fast structural switching behavior following photoexcitation. A relative flattening of the dihedral angle between ligands occurs as a distortion in the excited state (Scheme 6.2.1). Photoexcitation of d^{10} Cu(I) complexes corresponds with the generation of formal d^9 Cu(II) complexes from MLCT state formation prior to photon radiation or non-radiative relaxation. According to ligand field-based orbital theory and the “Jahn Teller distortion effect”, a d^9 Cu(II) state is driven from a tetrahedral geometry towards a flattened-distorted or more planar conformation. In the Cu(II) flattened-distorted state, donor solvent or counteranion ligands may occupy one or two additional coordination sites. The geometry of the d^{10} Cu(I) ground state structure is characterized as more perpendicular (in the idealized limit, ground state vs. excited state is associated with tetrahedral vs. square-planar geometries). According to point group symmetry rules, the tetrahedral geometry, in this case, is of higher symmetry and typically possesses a lower dipole moment.

The flattened distortion has been linked to excessive non-radiative decay in copper(I) ligands without steric protection. Increased non-radiative decay rates have led to lower emission intensities or quantum yields. The perpendicular (i.e., prior to flattening) structures have been detected by ultrafast spectroscopy as metastable states with intrinsic lifetimes, adding more complexity to the Jahn-Teller-derived arguments explaining the derived structural photoexcitation effects on the emission properties of Cu(I) complexes.

Flattening effects may reduce the kinetic stability of Cu(I) complexes in the ground states via increased ligand exchange or scrambling. A slight deviation from the tetrahedral structure and increased rigidity, such as via sterically encumbering constituents, can impose constraints against fast flattening distortions during photoexcited or decay processes, which may increase emission intensity or lifetimes. For example, in solid-state experiments, emission from copper complexes with 2,9-unsubstituted phenanthroline ligands was achieved by using increased rigidity.¹⁸⁷ According to relevant studies,¹⁸⁸ moreover, ultrafast internal conversion ($S_1 \rightarrow S_0$) from flattened-distorted to ground state structures (~ 2 ps), rather than intrinsic intersystem crossing rate

($S_1 \rightarrow T_1$) by comparison to bulkier ligands, causes the undetectable fluorescence of unsubstituted phenanthroline ligands.



Scheme 6.2.1. a) Schematized overview of lower non-radiative decay with Cu(I) bis(diimine) ligands with 2,9-substituents. Upon photon absorption, the more perpendicular conformation (black star) in a pseudo-tetrahedral geometry is driven towards a more planar conformation (blue star). The presence of phenyl substituents decreases the non-radiative decay rate, potentially due to increased steric clashing and slowing of the fast rearrangement process relative to the unsubstituted cases. b) Calculated structural models using DFT (BPE86/Def2TZV). **M1** and **M2** are both representatives of **46**. **M1** resembles the more planar structural form of the specific excited state product and vice versa.

Understanding the excited state kinetics and dynamics is a multidimensional problem, where overlapping manifolds with different energy-fold and time-fold boundaries and endpoints may generate differing excited state decay paths. Cu(I) photoemission dynamics may encompass various paths. In Fig. 6.2.1, a summarized diagram is shown, where the outer matrix processes in the top row correspond to absorption processes, followed by the relevant relaxation paths before emission, which have been specified for the types of compounds under study here.

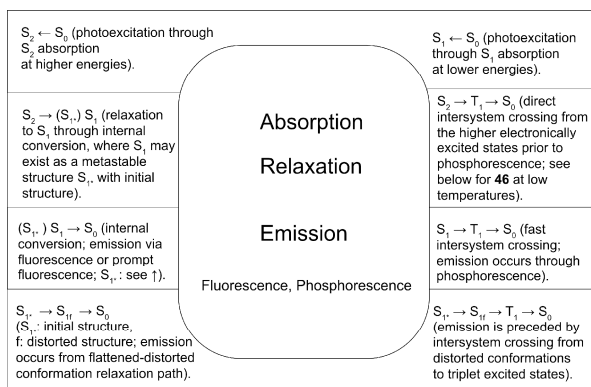


Fig. 6.2.1. Ignoring high electronic state processes or more complicated processes such as TADF, the following events follow the light excitation to light emission process of luminescent copper(I) complexes.

The processes that populate triplet phosphorescent states in Cu(I) complexes (IC + ISC \sim direct ISC \sim 1-100s ps)¹⁸⁹ typically occur at low energies ($\sim > 700$ nm) below the singlet events (e.g., ¹MLCT, ¹LLCT)¹⁹⁰. Fluorescence from various excited states (e.g., $S_n \sim < 450$ nm, and $S_n \sim 450$ -700 nm) ¹MLCT, ligand-containing initial donor transitions such as ¹(M+L)LCT and ¹LLCT, are concurrent events, even in the general occurrence of phosphorescence. Despite the presence of processes that populate triplet manifold states, competitive fluorescence processes, and low-energy fluorescence event occurrences complicate assignments.¹⁸⁶ Additional mechanisms based on TADF, where ISC from generated triplets or singlets is up-converted or down-converted based on small $\Delta E(S_1-T_1)$ gaps, may also offer relevant emission paths that explain our observations.¹⁹¹ Thus, interpretation and discussion of our photophysical results are founded on absorption and emission events as conditions varied and on calculating excited state decay time constants. For us, hindering the flattening distortion process by increasing the steric components of the ligands, given the large Mes* size and semi-rigid DBU backbone, seemed natural and intuitive. Given the ligands' asymmetrically mixed (i.e., P, N) nuclear and electronic character, increased ground-state distortion relative to ideal geometries is also expected. A lower rate of nonradiative decay due to increased rigidity and a small energy gap may couple with optimal emission or generate small $\Delta E(S_1-T_1)$ gaps coupled with efficient IC or ISC processes, yielding observable radiative processes. For example, it is expected that TADF may be potentiated in Cu(I) complexes with space-separated frontier orbital differences,¹⁹¹ with localized copper d-orbital HOMO densities and ligand π^* symmetry LUMO orbital densities.¹⁸⁶

Given the relevant background, we now explore our study of copper(I)-P=C chemistry by presenting our work with compound **46**. The synthesis of **46** was achieved by the introduction of [CuBF₄] \cdot 4MeCN or [CuPF₆] \cdot 4MeCN

in a ~ 1:1 (% vol) DCM/MeCN mixture used for increased solubility. Reaction onset occurred instantly and was characterized by a profound color change from light yellow to dark pink-to-red, suggestive of metal-ligand charge transfer (MLCT) state generation in the visible region of the electromagnetic spectrum. Complex **46** was obtained as a hygroscopic and sensitive solid, rapidly decomposing when exposed to atmospheric conditions. A deep green color was obtained as a reaction product in solution exposed to the atmosphere for one week, which implies the formation of copper(II) species. Thus, all the reported experiments were performed using standard air-free and anhydrous protocols. The structural nature of **46** was confirmed by HRMS (ESI), which identified the single fragment representative of **46** (found: $m/z = 915.56106$, corresponding to the $[\text{CuL}_2]^+$; calculated mass **46**: $m/z = 915.56182$). The generation and detection of ionized fragments confirmed the successful formation of the postulated structure and indicated that **46** is a stable complex in some kinetic and thermodynamic sense. A broad singlet appeared in ^{31}P NMR spectroscopy at $\sim +242$ ppm. This NMR signature initially supported the argument of having a single structure (see Fig. 6.2.2 a)); broadening and complicated ^1H and ^{13}C NMR spectra suggested the presence of secondary stable states, such as isomeric forms or dynamic processes in solution. The ^{31}P NMR resonance of **46** did not significantly vary between experiments using the different counterion salts ($[\text{BF}_4]^-$, $[\text{PF}_6]^-$). In CDCl_3 , the ^{31}P NMR resonance was shielded relative to the free ligand, $\delta = +241$ to $+243$ ppm (**46**) vs. $+254$ to $+257$ ppm (**36**). Signal broadening and small chemical shifts upon complexation may have been characteristic of weak bonding situations (i.e., labile), as observed for some ligands. A detailed assignment of the signals by NMR was complicated; however, the shape and number of NMR signals confirmed the formation of the desired complex. It is relevant to note that coordination with bulky ligands may inhibit ligand scrambling in some cases. So, our arguments about (i) a conformer/isomer species in solution may be emphasized, supported by our DFT/TD-DFT set and the photophysical measurements. Furthermore, assuming that **46**'s sensitivity (ii) was caused by additional structural frustration as explained for Pd(II) complex in the previous chapter and the fact (iii) that ESI detected the whole complex, which (iv) was also stable through cyclic voltammetry in situ formation experiments (vide infra), then our argument about the existence of an isomer is potentiated.¹⁹²

We studied the ground state and excited state properties of complex **46** using DFT and TD-DFT methods in the gas phase and solutions. During the optimization of the ground state geometries, two different local minima conformations were relevant. We labeled them **M1** and **M2**. The difference in energy between the two conformers was ~ 15 kJ/mol (higher for **M1**), which is small. The slight energy difference is explained by the shallow nature of the PES, as characteristic of systems possessing large protecting groups or many degrees of freedom. In the case of **46**, the structural effects from the previous paragraphs are further potentiated by the weaker bonding interactions between

the Cu-N or Cu-P units. The two structures (**M1**, **M2**) were characterized by their distorted arrangements in their optimized geometries, which deviated from the tetrahedral (perpendicular) or square-planar (flattened) geometries expected for idealized or typical structures in the ground or excited state, respectively. **M1** presented longer P-Cu BLs (2.58, 2.71 Å) than those from previous reports of P=C copper complexes (~ 2.30 Å); oppositely, **M2** exhibited shorter Cu-P BLs (2.38 Å), which are still longer than those from previous observations (2.30 Å). Complex **M1** exhibited widened $L_{1,2}$ -Cu (L_1 : P, L_2 : N) angles, whereas **M2** possessed reduced angles (113.1 and 124.1°). The plane-to-plane dihedral angle of **M1** was reduced (52.8°) relative to **M2** (79.8°), the latter sitting closer to the right-angle indicative of pseudo-tetrahedral geometry. The ground-state calculations demonstrated the likelihood of two isomeric forms in liquid solutions by energetic considerations and the proactively inductive type of structure of **M1**, which resembled the (meta)stable structures typically observed in the excited state. Correspondingly, **M2** resembled the ground state's tetrahedral Cu(I) situation, whereas **M1** resembled the photo-excited systems' flattened, distorted, excited-state Cu(II) structure. Phosphaalkene-copper bonds may be more labile than imine-copper ones, which, coupled with the larger BLs, the higher energy of **M1** relative to **M2**, and its more distorted configuration, suggest that **M1** "plays a role" as a particular type of representative structure in connection to the excited state structure precursor that is formed upon photoexcitation, which was an exciting success for the analysis.

The basic photophysical properties of **46** were elucidated by steady-state electronic absorption and emission spectroscopy in liquid solutions and frozen solvent matrices. Several types of experiments were performed based on counterion (i.e., [BF₄]⁻, [PF₆]⁻) or solvent medium (DCM vs. MeCN) choice. The resulting spectra did not vary at room temperature. Altogether, the slight variation in the results for different reaction products in terms of counterion implied the imposed constraints by the type of ligands and the several possible configurations in solution, rather than the counterion of choice and its potential binding, determined the observed properties of **46**. For example, absorption spectroscopy of **46** with the tetrafluoroborate counterion in DCM was obtained (see Fig. 6.2.2 b)). These results were compared to TD-DFT calculations of **M1** and **M2** in DCM.

Experimentally, the UV-Vis-NIR spectra consist of two major bands. The most substantial transition presented an absorbance maximum at 277 nm (13.160 M⁻¹cm⁻¹) and was assigned to combinations of ligand-centered (LLCT; $\pi \rightarrow \pi^*$) and metal-ligand charge transfer states (MLCT; $d \rightarrow \pi^*$), as it is well-known. The lower energy events were characterized by a broad event with inflection points in the visible region (380 nm). The broader event band assigned to the typical MLCT transitions extended well into the lower energy portion of the visible region ($\lambda_{\text{onset}} = \sim 600$ nm). The red-shifted nature and tailing of the low energy absorption bands have been related to isomerism in

solution and distorted structures in the solid state or solution.^{193,187} The TD-DFT results revealed dramatic differences in the oscillator strengths (f) of the two lowest transitions for **M1** and **M2**. More pronounced oscillator strengths were obtained for the lowest energy transition of **M1** at 515 nm (0.0753) compared to the band at 460 nm (0.0057). Conversely, **M2** exhibited a more robust $S_2 \leftarrow S_0$ transition at 458 nm (0.0585) than the $S_1 \leftarrow S_0$ event at 495 nm (0.0015). This finding is consistent with the expectation that the more flattened structure (in this case also **M1**) should contribute to the $S_1 \leftarrow S_0$ electronic transition or the red-shifted nature of the spectrum for excited states, in some sense corresponding to the emission spectrum. As mentioned above, **M1** has higher free and electronic energies (ΔG , ΔE) than **M2**. These observations agree with the general trends found by others and with the experimental observations and explanations in our case, which increase the analysis's confidence.

EDDM plots of **M1** and **M2**, in addition to differences in oscillator strength, showed that the lowest energy bands were associated with different MLCT transitions for both **M1** and **M2** (while the higher energy bands contained more ligand character). At the same time, **M2** surprisingly exhibited a lowest-energy transition band with mixed (LLCT + MLCT) character (~ 475 nm). Thus, we assigned the lowest-energy broad absorption and tailing events to different MLCT states and some ligand-based characteristic events, indicating the “non-innocent” nature of phosphalkene ligands. Since **M1** and **M2** are relevant energy minima structures, the results supported the premises of the existence of two isomeric forms in the solution.

Aside few exceptions, a general characteristic of P=C compounds is their non-emissive nature.¹⁹⁴ We rationalize that effective non-radiative quenching, coupled with low oscillator strengths for low energy events and poor emission rates, creates poor emission and fast decay through the particular electron lone pair of P=C group motifs and rotational *tert*-butyl-derived quenching effects. Consequently, we were intrigued by the luminescence of **46**, initially confirmed in the dark under UV light illumination. Motivated by the evolution of Cu(I)-bis(diimine) complexes from non-emission observations to robust emission observations and vast research output over time, we performed several studies on the photoluminescent properties of **46** to stimulate future research of **46** or homoleptic and bidentate phosphalkene-imine Cu(I) complexes.

The steady-state emission spectrum of **46** was taken at room temperature. An initial overview of the emission for various liquid samples of **46** led to emission spectra characterized by a single, broad, and featureless band centered at ~ 560 nm, in agreement with MLCT transitions. Interestingly, through excitation with a 470 nm wavelength (λ_{exc}), we reproducibly observed the event centered at ~ 560 nm, as well as another feature centered at ~ 765 nm, which was resolvable in various instances above (e.g., Fig. 6.2.2, c), d), and low-temperature experiments below (i.e., Fig 6.2.3. a) and Raman-free spectrum abstraction b)). The steady-state emission spectroscopy experiments

exhibited a concentration-dependent variation of the intensity. For example, a comparison of 0.1 mM and 1 mM revealed a dramatic decrease in the emission intensity (I_{Em}). Solvent-solute effects and structural insights were gained by solvatochromic observations from UV-Vis-NIR absorption spectroscopy of **46** solutions relative to solvents of varying polarity. We focused on measurements with methylcyclohexane (MeCy, relative permittivity = 2.2), dichloromethane (DCM, relative permittivity = 9.1), and acetonitrile (MeCN, relative permittivity = 37.5), respectively following a simple order of increased polarity (right-to-left) as shown in Fig. 6.2.2. e). For each solvent, the wavelengths of the three more significant event occurrences starting from the spectrum's lower-energy side were traced, and all were identified as points and extracted from the graphs (λ_1 -to- λ_3 ; top-to-bottom).

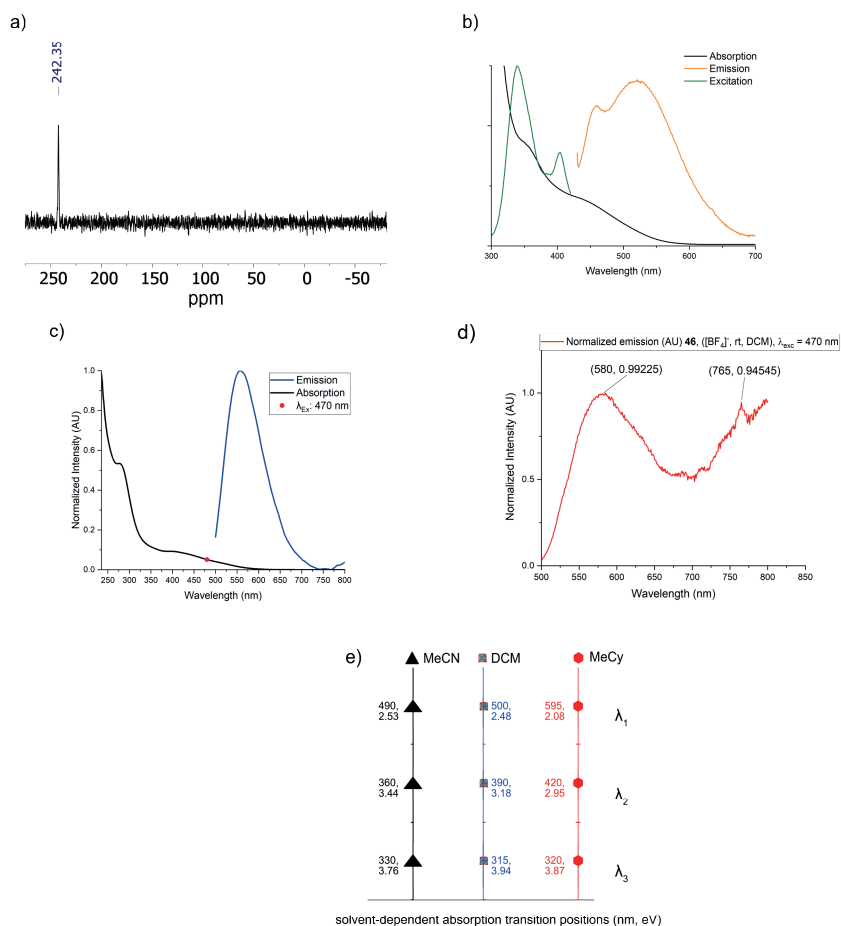


Fig. 6.2.2. a) ^{31}P NMR spectrum of **46**, which exhibited a broad resonance centered at 242 ppm (CDCl_3). b) UV-Vis-NIR absorption, excitation scan, and steady-state emission spectra overlay of **46** ($[\text{BF}_4]^-$, DCM). The excitation scan (green curve) coincided nicely with the two shoulders in the absorption spectrum (black curve). The broadening of the NMR resonance signal and the shoulders in the absorption spectrum indicated the presence of conformers or equilibrium in the solution. c) UV-Vis-NIR absorption (black curve) and steady-state emission (blue curve) at $\lambda_{\text{exc}} = 470$ nm; a second feature at 765 nm was slightly visible, which we briefly explore below. d) Emission spectrum of **46** ($[\text{BF}_4]^-$, rt, DCM). An emission wave at 580 nm was present, accompanied by a potential feature at 765 nm ($\lambda_{\text{exc}} = 470$ nm). e) Solvatochromic analysis based on UV-Vis-NIR absorption spectra of **46** in three solvents of different polarities. For each solvent, the three major event positions ($\lambda_1, \lambda_2, \lambda_3$) were estimated based on the midpoints of the largest slope positions after equivalent expansion or spectral blowing. For the two lowest energy transitions (λ_1, λ_2 ; top, middle), blue shifts occurred with increasing solvent polarity from MeCy \rightarrow DCM \rightarrow MeCN. MeCy: methylcyclohexane.

A red shift of the two lowest-energy sets of events was observed as solvent polarity decreased, which meant that the ground states were stabilized relative to the excited states as solvent polarity increased, corresponding to negative solvatochromic phenomena.¹⁹⁵ For the third set of events ($\lambda_3 = 330$ nm; MeCN), a red shift occurred for MeCN (bottom left). For λ_3 , the excited state was stabilized relative to the ground state, an argument which may relate to a flattened-distorted conformation with high activity from the P=C and N=C ligands, stabilized in the photoexcited state. The high energy “behavior inversion” change points at modular phenomena from **46**, in that we observed an absorption spectroscopy effect that cannot be explained by Cu(I) or ligands individually, which could be ascribed to the π -accepting nature of P=C ligands. This behavior agrees with low-temperature quasi-3D emission spectroscopy observations in the same excitation energy region (see Fig. 6.2.3. below), which suggested the concomitant activation of LLCT and other emission events, the latter of which pointed to the presence of stabilized excited state manifolds in the second temperature setting. That is, [inversion solvatochromic behavior absorption, λ_3] \sim [λ_{exc} , atypical observations emission at low temperature], where \sim establishes a correspondence or relation between the two events. From the solvatochromic explanations alone, one could say that various events, such as increased stacking, NCIs, or P=C charge accepting character, stabilized the excited state versus the ground state, which generated the relative red shift of λ_3 for MeCN relative to both DCM and MeCy. We observed the same signal events in a quasi-3D emission/extinction experiment at 77 K in a frozen MeCN matrix. Notably, this experiment was performed using the opposite counterion ($[\text{PF}_6^-]$) and solvent (MeCN), as seen in Fig. 6.2.3 a). The intense emission events centered at 434 nm at the equivalent excitation energy ($\lambda_{\text{exc}} = 342$ to 344 nm, corresponding to a slight 0.5 kcal/mol energy difference) were congruent or coincident with other events at 750 nm, as seen by the presence of a second island. This “dual emission” is hard to explain intuitively. The caption shows that these two events do not correspond to solvent or H₂O Raman signals, so both can be attributed to **46**. The lowest energy emission island may correspond to isomer or structural-based feature differences, intensified in the frozen and thus rigid acetonitrile matrix. Given the marked temperature, solvent, and counterion environments in which this event was observed at rt, relative to the low-temperature matrix experiments, we tentatively discard dimeric or excimer-based effects concerning the event. Thus, our predicated logical approach to this argument leaves us with the phosphalkene-imine ligand as one of the few remaining variables or parameters of direct *influence* on the observations, further related to them by the solvatochromic relation established above, directly related to the phosphalkene by the high π -acceptor character and unoccupied acceptor frontier density of P=C group motifs or high contributions to charge transfer accepting events in the visible region (π^* -based symmetry acceptor orbitals). The low-

energy emission feature could indicate increased radiative rates based on the intensities known to be potentiated at low T.

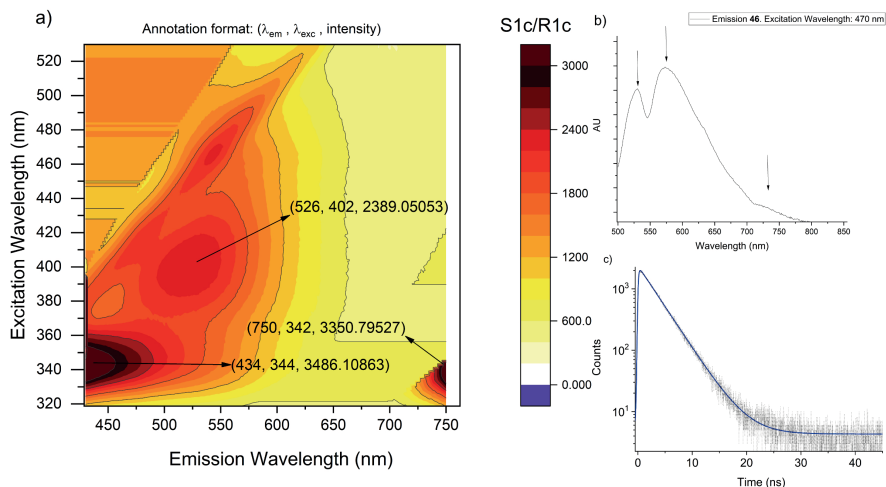


Fig. 6.2.3. a) 3D emission versus excitation map of **46** (0.4 mM, [PF₆]⁻, T= 77 K, MeCN), with signal assignments corresponding to LC and MLCT emission, and presumable Raman events from water and solvent emission, as seen on the mapped spectra. The LC + MLCT emission events are centered at ~ 434 nm, whereas the MLCT events are centered at ~ 526 nm, as the excitation scan energy was varied. The other events are located at ~ 750 nm and are slightly blue-shifted relative to the 765 nm observations at rt above and minimally red-shifted relative to the λ_{exc} at 344 nm (see below). We assume no artifacts caused the emission events at λ_{exc} of 343 nm. Thus, their intensification could relate to potentiated emission events at low T (relative to higher T experiments) or due to higher λ_{exc} energies (relative to both higher T experiments and the same experimental signals at higher λ_{exc} wavelengths or lower energies). b) Reconstructed emission spectrum of **46** after H₂O Raman emission subtraction. Three events were observed at 530 and 572 and a wavelength of approximately 750 nm. The third signal was not immediately discarded as noise or artifact, given that we observed it in room T experiments and higher excitation scan energies within the same set. Interestingly, it was not easy to find literature reports that exemplify this type of phenomenon, supporting the isomer/conformer picture (the ref. review shows instances of similar emission features, albeit independently or not in concurrence).¹⁹² c) Generated transient fit from time-resolved fluorescence spectroscopy of **46** (0.1 mM, [BF₄]⁻, DCM, rt, λ_{exc} = 470 nm). The blue curve displays the fit, underlined by the raw data (black, scattered-point data set).

Concentration-dependence quenching was observed in other Cu(I) compounds (e.g., substituted phenanthroline ligands)¹⁹⁶. Emission quenching has been related to ΔE effects related to ground-state and ³MLCT events as solvent effects upon flattening. However, we believe that the same set of relations, given by the different experimental observations of **46**, is new in some respects and further interesting due to the potentially vital role played by non-innocent P=C group motifs.

In Chapter 5, we studied the behavior of **36** and derived HB adducts. In various conditions, sudden or non-trivial changes were observed in liquid or saturated solutions. For example, the intensely yellow solutions of **36** indicated the formation of charge transfer complexes or viscous product solutions of HB H₂O-bounded HCl adducts. In the case of **46**, we expect to observe similar phenomena in differentiated settings such as low T, under light, or another bias (e.g., certain λ_{exc} -based occurrences or occurrence changes and respective ΔE). Hence, secondary event resonance or energy coincidences between **46** and solvent (e.g., coordination) or H₂O may be generated. For example, effects inducted by coincident solvent or water Raman emission energies or resonant confluences, or by population densities in congruence with precise structural forms as structurally derived occurrences overlap, may be hypothesized to influence the observed emission nature, intensities, resonance, or emission band positions, and lifetimes of **46** and emissive copper(I) complexes in general. The H₂O Raman signal occurred close to the critical emission event at 526 nm, as seen by the respective, smaller signal, centered at $\sim \lambda_{\text{exc}} = 410$ nm, $\sim \lambda_{\text{em}} = 475$ nm in Fig. 6.2.3. a), above) at a slightly higher excitation wavelength (i.e., slightly lower excitation energy). This observation implies that as the excitation wavelength was decreased in energy (i.e., increased in wavelength) and concomitant closeness in energy to the H₂O Raman resonance condition became present, a quenching of the low energy emission event and the major event became occurrences, either through resonant confluences as predicated or via rate competition. Further increasing of the λ_{exc} was congruent with the complete loss of emission detection from all **46** forms (i.e., major and minor isomeric forms, assuming two major species as seen based on in-silico and photophysical-based occurrences, further validated below via cyclic voltammetry), as expected for some photon energies lower than the arbitrary minimum energy requirement. The emission response by **46** (e.g., see Fig. 21 and 26 in the reference),¹⁹⁰ resembled others from Cu(I) complexes, for which singlet excited state emission bands linked to events between 520-580 nm, whereas, for some phenanthroline ligands, > 700 nm signals were assigned to other events. As seen in some of the referenced works, literature studies have suggested that frozen matrices potentiate the fluorescence or phosphorescence intensity of Cu(I) complexes by blocking the flattening distortion, which directly applies to our considerations. Interestingly, our data suggested that at lower excitation energies, some concerted processes differentiated the emission spectrum of **46**, depending on λ_{exc} , T, and the H₂O Raman signal.

The excited state dynamics of compound **46** were probed in DCM or MeCN solutions by time-resolved emission spectroscopy using a laser pulse. After a few experiments, a time constant ($\tau = 9$ ns) was observed for a 10^{-4} M solution of **46** in DCM. Increased concentrations typically led to decreased lifetimes, which could go at hand with the increased intensity quenching previously mentioned. It is relevant to note that studies with Cu(I)-bis(diimine)

compounds have taken years of research and generated hundreds of studies grounded by initial excited state lifetime observations limited to the picosecond regime. The first emission report of high relevance and at room temperature was limited to ~ 50 ns, which is within the same order of magnitude as our results for the first emissive example of this family of compounds, for P=C-containing ligands which are typically non-emissive or emission quenchers.¹⁹⁷ Thus, the obtained lifetime of 9 ns in DCM could be reflected in more optimal or longer lifetimes or more robust responses in optimized settings, while more generally and positively, an excited state lifetime of 9 ns could be ideal for specialized applications. Based on the results, small ΔE gaps, significant structural changes, and intermolecular or structural effects corresponding to the observation of an isomeric form were associated with interesting photophysical properties (e.g., temperature-dependent changes in emission, nanosecond regime lifetimes, and more) of **46**.

Electrochemical experiments via CV helped us understand the behavior of **46** under an electric potential bias. Within the 3.82 V EW of the study (-2.57 V to $+1.25$ V vs. Fc/Fc^+), the obtained data was characterized by various electrochemical events assigned to ligand-centered or metal-centered electron redox processes. A comparison of the electrochemical responses of the parent molecule **36** (free ligand) and copper(I) complex **46** is shown in Fig. 6.2.4 a).

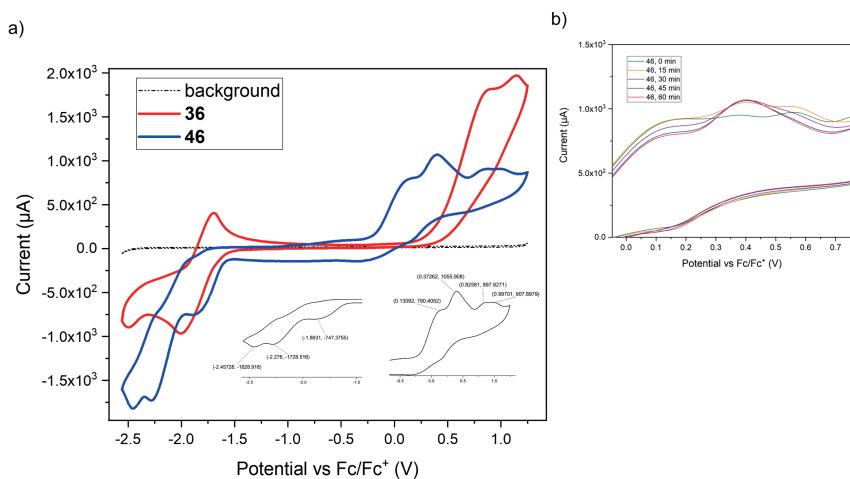


Fig. 6.2.4. Electrochemical study of complex **46** and free ligand **36**. a) cyclic voltammetry, full electrochemical window scan, **36**, **46**. b) In situ generation and formation of **46**, resulting cyclic voltammograms at separate times after initial formation (0 min). SR = 0.1 Vs^{-1} , DCM, rt.

For **36**, reversible one-electron reduction events peaked at -1.85 V. The reduction was assigned to one-electron processes with high contribution from the low-lying π^* P=C orbitals, which gained a negative charge, with

secondary contributions from the N=C or metal center. For **46**, in the anodic scan, three to four irreversible events were assigned to two one-electron oxidation processes (+ 0.13, + 0.37, + 0.88, and + 1.15 V) that generated increasingly more cationic species, whereas the latter corresponds to secondary events arising from previous oxidations (*vide infra*). Alternatively, the various signals of the first set of events at low oxidation potential could correspond to the presence of an isomer or conformer, as discussed in the chapter. Given our previous observations regarding the potential ligand lability and the presence of an isomeric form in solution, we were pleased to observe the rich electrochemical profile of **46**, characterized by stability and rich ambipolar behavior. The profile and features were congruent with **46** as a transition metal complex of high stability. The complex exhibited three electrochemical events in the cathodic cycle at - 1.86 V, - 2.29 V, and - 2.46 V, which were attributed to the ligands based on their contributions to the LUMO orbitals. These redox events were probed at scan rates up to 1 Vs⁻¹ and were shown to be chemically irreversible under experimental conditions. The redox couples in the anodic sweeps occurred at lower potentials than those of **36**, suggesting a role for metal introduction and metal-based or metal-ligand-based oxidation processes. We were curious whether the proximity and nature of the mildest oxidation events were related to the presence of a more complex mixture in the solution. Based on theoretical calculations, we assigned the first events in the anodic sweep to Cu^I/Cu^{II} and similar oxidation processes, with significant contributions from the Cu(I) metal and minor contributions from the antibonding metal-ligand orbitals of the resulting cationic species. It is known that these events can cause ligand dissociation; more likely, this event causes or is associated with structural rearrangement processes such as flattening distortion and increased solvent or salt accessibility to the coordinative metal sphere.

The nature of the mildest oxidation events of complex **46** during anodic sweeps was better understood by performing an *in situ* electrochemical formation experiment with a slight excess of free ligand and the corresponding Cu(I) salt. Fig. 6.2.4. b) shows three initial oxidation signals at the onset of formation of **46**, as indicated by the signal range from + 0.17 to + 0.57 V. The first signal appeared at + 0.17 V and decreased in intensity but persisted as the system evolved. After 15 minutes, the second signal peaked at about + 0.40 V. The third set of signals was observed at + 0.56 V and finally transformed or disappeared under the primary signal after 30 to 45 minutes. We propose the following events for the initial oxidation waves during the formation of **46** and its structural representations: **(I)** The rapid onset of the metal-ligand reaction characterized the presence of different structural representations. **(II)** Over time, destructuralization-structuralization and ligand scrambling-de-scrambling processes and isomeric or equilibrium changes followed. **(III)** The equilibration process was further characterized by the emergence of a major signal at + 0.40 V after 60 min. The three-step process suggests the presence

of an isomeric species. **(I)** The slow onset of partial structures was due to steric congestion and isomerization processes from structural changes. **(II)** Over time, the development of ligand scrambling processes resulted in variations in the relative positions and intensities of the oxidation events of **46** and its structural representations. **(III)** A dynamic equilibrium event where concentrations reached a steady state, with the prominence of a major signal, given the slight excess of ligand. The intermediate signal at about + 0.40 V in the 60 min voltammogram indicated the higher structural order or symmetry of the final product compared to the initial and intermediate voltammograms, which were more consistent with the expectation that isomers/conformers become experimental events under equilibration considerations. The last two oxidation events at $\sim + 0.9$ V were close to the oxidation potential of the free ligand (**36**: + 0.86 V, + 1.15 V), whereas these occurred at lower oxidation potentials for **46** (+ 0.82 V and + 0.99 V). We hypothesize that the confluence of the first event in both samples (+ 0.82 V and + 0.86 V) is due to ligand scrambling, which generated species of **46** with similar redox potentials and structures to **36**. The exact reason for the lower oxidation potential of the second set of signals of **46** is non-trivial to trace, but we postulate that the introduction of copper and the absence of coordination were relevant. The second set of signals had similar symmetry and charge magnitude, indicating that they likely originated from structurally ordered isomers or conformers in a flattened-distorted square-planar form attributed to copper(II). The presence of solvents or counterions may stabilize this coordination geometry. The last argument assumes that the latter events are generated by ligand-based processes with reducing support from counterion-bound or solvent-bound copper metal centers due to their oxidation occurring at lower potentials and the increasing cationic charge of the complex. The quasi-reversibility of the first set of oxidation waves and the greater irreversibility of the second events indicated ligand dissociation processes with only partial return or partial reassociation of the lost ligands.

6.3. Conclusions and outlook.

HRMS, CV, NMR, and photophysical methods confirmed the synthesis of complex **46**. Initial characterization of its luminescent properties revealed an exciting profile characterized by light emission, a rare occurrence for P=C compounds. The presence of high-density acceptor contributions from P=C ligands on **46** at higher energies was found via TD-DFT and changes in absorbance events in solvents of different polarities. For low-energy MLCT events, typical responses were found, indicating stabilized ground states relative to excited states as solvent polarity increased. Oppositely, for high-energy events characteristic of ligand-based and thus P=C states, blue-shifted responses were obtained relative to less polar solvents, indicating more stable

excited states. Emission experiments demonstrated a steady-state fluorescence response that varied only slightly at room temperature for different solvents or counterions and with little I_{Em} contribution from the phosphorescence or triplet-manifold-based events (> 700 nm). However, these manifolds were activated at low temperatures and coupled with the ligand-based emission events at higher excitation energies. The same events at higher excitation wavelengths (lower energies) were quenched for the low-energy triplet-manifold-based events (i.e., incl. phosphorescence) due to the coincident water Raman emission. In contrast, MLCT manifolds were not excited at lower excitation energies. Raman noise abstractions suggested that two **46** forms coexisted in solution. By linear comparison to lifetimes of emissive copper(I) bis(diimine) complexes during their initial development or discovery, excited state lifetimes of 9 ns may be classified as promising. Long emission lifetimes may correlate with decreased function output in some applications depending on the role or process.¹⁹⁰ Thus, the lifetime detection for a P=C compound and the introduction of a type of family of ligands for emissive copper(I) complexes with stimulating properties are positive feats from our work. Further lifetime improvements can be gained by accessing **46** in bulk amounts. The high intensity of the events in the frozen matrix experiments supported the potential of utilizing higher excitation energies in the future. Electrochemical experiments demonstrated that **46** is robust in dry and air-free conditions and possesses a rich electrochemical activity. Copper introduction to the ligand environment and the non-innocent nature of the P=C ligand concerning the metal center seemed to be vital components of the electrochemical functions. The decomposition of **46** generated a green byproduct which we assigned to a copper(II) species with inter-bridged copper-copper bonds based on a preliminary XRD solution (unpublished). Overall, one can project the compound for photoquencher or photoreduction studies coupled to some switching or structurally-based process in an application, given the ease by which it was oxidized electrochemically, the low onsets of the absorption events, and red-shifted and distinctive emission and electrochemical features at various excitation energies and scanning potentials, respectively.

Ch. 7. Summary and conclusions.

We can conclude that the introduction of heavy P=C (Ch. 2, 3, 4, 5, and 6) or As=C (Ch. 2 and 4), or Si=Si (Ch. 4) group motifs on fluorene or DBU backbones was a viable approach for the creation of π -conjugated or structurally-frustrated small molecules or polymers with increased functionality and demonstrated modularity (via memory-like, emergent effects, supramolecular differentiability in solution and solid states, salient spectroscopic feature observations for a variety of representations), relative to lighter species based on reported literature, and theoretical method comparisons of spectra and energy gaps. Electrochemical and spectroscopic studies of As=C polymers and P=C polymers with highly distinct and organized optical and electrochemical responses under light or applied potential stimuli suggested that the polymers benefited from the addition of nanostructure. Based on Ch 2, 3, 5, solid-state structure packing features were not explicitly hindered, either in the monomeric or polymeric forms, by the presence of sterically encumbering Mes* (1,3,5-tri-*tert*-butylbenzene), which demonstrated to be a source of functionality, for example via hydrophobic effects and “weak” hydrogen bonding. Quasiparticle and non-trivial spectral contributions were observed for both As=C and P=C polymers based on spectroelectrochemistry and Raman spectroscopy. For As=C polymers, observations suggested the mutual presence of redox polymer and conducting polymer states, which can interchange functions internally in the form of current transactions as potential is cycled, which were coupled to earlier instances characterized by highly atypical and expressive electrochemical responses, which from the considerations above were representative of increased interactivity instead of instability, as initially postulated. P=C polymers yielded simplified and resonant Raman responses that were enhanced from the non-emissive nature of P=C group motifs for the realization of intensified resonant Raman signatures, which, based on literature study comparisons, were reminiscent of nanostructured materials such as carbon nanotubes or other graphite forms, including graphene. The small molecules presented interesting structural motifs in the solid state, as well as interesting UV-Vis, electronic structures based on theoretical methods, or electrochemical responses, which lifted these compounds from the framework of fundamental studies to that of potential applicability in different areas such as extended π -conjugated materials of high functionality, modularity, and expressivity, or supramolecular materials, thanks to the presence of atypical

E=C group motifs. We can conclude that careful modification of variables or parameters such as solvent, counterion, temperature, ligand concentration, defect, or additive (e.g., discrete H₂O amounts) in solution, or discrete sequences of experimental settings, can be used to generate differential and expressive responses from P=C-containing DBU systems, reversibly realizing NCIs such as HB and supramolecular structures. Responses characterized by critical-point-like events, solvatochromic changes, supramolecular hydrogen bonding, light emission with distinguishing features on isomeric form expression or emission source or nature (i.e., singlet/triplet, high-energy/low-energy events) as excitation energies or temperature dependencies were probed, and electrochemically stable responses demarcated these compounds as intrinsically interesting and worth further studies under the same or increased levels of environmental rigor and relative freedom from reactive species while cherishing the representative settings and the optimal criteria suitable for their study.

Svensk sammanfattning

Det arbete som presenteras i denna avhandling syftar till att undersöka, utforma och utveckla organiska föreningar och system med hjälp av tunga p-blockelement. Vårt fokus låg på fosfor och arsenik från grupp 15. Vårt mål var att skapa material med ökad funktionalitet och unika egenskaper. Avhandlingen består av sju kapitel som beskriver våra forskningsresultat.

I kapitel 1 presenteras gruppmotiv av fosfaalken ($P=C$) och arsaalken ($As=C$) och deras införlivande i organiska ramverk. Vi presenterar också flera ekvivalenser eller relationer mellan oorganiska materialkombinationer (grafen, kisel, svart fosfor, svart arsenik med mera) och organiska material som innehåller lågt koordinerade tunga p-blockfragment (fosfaalkener, arsaalkener, disilener med mera).

Kapitel 2 fokuserar på våra studier av $P=C$ - och $As=C$ -motiv i små molekyler och polymera system baserade på thienylsubstituerade fluorener. Dessa optoelektroniska organiska material uppvisar stabil elektrokromism och modultärt beteende i sitt polymera tillstånd. Elektropolymerisering är en robust process som gör det möjligt för oss att förstå den naturliga potentialen hos polymera former utifrån olika kriterier. Traditionella kemiska polymeriseringsprocesser leder däremot till att material förlorar modularitet och komplexitet, vilket gör att gränsen för naturlig funktionalitet suddas ut. Utifrån grundläggande principer skapar vi ett ramverk som använder begreppen "optimala kriterier", "representativa inställningar" och "hystereseliknande kriterier" för att utvinna relevant information från polymerresponser. Vårt tillvägagångssätt ger en inblick i materialens beteende. Vi inför också krav för att kategorisera ett funktionellt material som ett "smart material" när de specifika villkoren är uppfyllda. Kraven omfattar modularitet, inre åtgärder, expressivitet, framväxande fenomen med mera. Genom att definiera dessa kriterier kan vi skapa "smarta material" och material som kan anpassa sig till sin omgivning och utföra specifika funktioner, vilket potentiellt kan ge oss innovativa lösningar på olika utmaningar i framtiden. Under vår karakterisering av polymerisering i elektrokemiska celler observerar vi signaturer av framväxande fenomen som strukturellt organiserad segmentering och minnesliknande fenomen som kännetecknas av diskreta och organiserade förändringar i ström när potentialen cyklas. Efter funktionalisering med guldjoner studerar vi också små molekyler och fosforpolymerer och finner att $P=C$ -gruppmotiven är mer reaktiva för $Au(I)$ -koordinering än $As=C$. Vårt arbete ger en detaljerad

karaktärisering av materialen, inklusive deras elektrokemiska och spektroskopiska egenskaper. Resultaten visar att $P=C$ - och $As=C$ -gruppmotiverna är mångsidiga och användbara vid utformning av "smarta material" och ger insikter i deras potentiella tillämpningar. I vårt arbete presenteras det första exemplet på en polymer som innehåller dubbelbindningar av arsenik och kol ($As=C$).

Kapitel 3 fokuserar på våra studier av nya små molekyler som innehåller $P=C$ -gruppmotiv. Vi utformar, syntetiserar och karakteriserar dessa material, vilket utökar den utmanande familjen av $P=C$ -innehållande fluorenbaserade π -konjugerade material. Genom NMR-, XRD- och UV-Vis-NIR-spektroskopianalyser visar vi att substituentskillnader och koordinering med $Au(I)$ modulerar egenskaperna hos dessa föreningar på ett betydande sätt, vilket framhäver mångsidigheten och potentialen hos $P=C$ -acceptorinnehållande material som byggstenar för avancerade funktionella material.

I kapitel 4 granskas våra opublicerade studier av föreningar som innehåller samtidiga kombinationer av atypiska grupp 14-fragment ($Si=Si$, Si_6 -omättade siliconoider) och 15-fragment ($P=C$, $As=C$). Studien skapar en sammanflödande väg för syntes och karakterisering av nya material som innehåller två atypiska gruppmotiv på en organisk molekyl, samt deras potentiella tillämpningar baserade på förekomsten av typiska och framträdande egenskaper. I framtiden kan denna typ av tillvägagångssätt användas för att utforma molekylära system i samband med en programmatisk process. I ett programmatiskt tillvägagångssätt utnyttjas föreningarnas komplexitet för framtida områden som ny systemdesign, organisk elektronik, molekylär elektronik eller kvantmaterial.

I kapitel 5 beskrivs våra studier av DBU-derivat som innehåller $P=C$ -motiv. Studien är inriktad på dessa föreningars och molekylers inblandning i icke-kovalenta interaktioner, särskilt av typen vätebindning (HB). Stabilitetsexperiment i lösnings-NMR utförs för att belysa HB:s och supramolekylär kemiens roll i stabiliseringen av $P=C$ -gruppmotiven bland uppsättningen produkter i förhållande till utgångsmaterialet. Spännande observationer är relaterade till plötsliga förändringar i fysiska eller spektroskopiska egenskaper hos material i förhållande till deras omedelbart föregående tillstånd eller baserat på en sekvens av operationer, vilket ger dem funktionell och modulär karaktär. Den mest inspirerande observationen gäller uppvisandet av ett vätebundet vattenätverk i en förening, vilket motsvarar den utmanande uppgiften att hitta exempel på komplexa supramolekylära material med likvärdiga vätebundna strukturer upp till isomorfism som kan genereras och observeras både i fast tillstånd och i lösningar. Våra resultat har betydelse för utformningen av supramolekylära material och syntesen av huvudgruppsderivat med specifika funktionella egenskaper.

Kapitel 6 avslutar avhandlingen med en omfattande studie av ett $Cu(I)$ -komplex med den homoleptiska och bidentata fosfaalken-liganden från föregående kapitel som en elektrokemiskt rik och emitterande förening med

intressanta fotofysikaliska egenskaper. Observationer görs för olika typer av emissionspopulationer. Det samtidiga uppträdandet av blandade händelser med ligandkaraktär vid högre energier åtföljer försvinnandet av de typiska metall till ligandöverföringshändelserna. Föreningen uppvisar en livlig elektrokemisk profil med ambipolära drag.

Sammanfattningsvis (kap. 7) ger införandet av tunga P=C-, As=C- eller Si=Si-gruppmotiv på fluor- eller DBU-rygggraden π -konjugerade eller strukturellt frustrerade små molekyler, salter, övergångsmetallkomplex och polymerer med förbättrad funktionalitet och påvisad modularitet. Packningsegenskaperna i fast tillstånd hindrades inte uttryckligen av närvaron av steriskt belastande Mes* (1,3,5-tri-tert-butylbensen). De små molekylerna uppvisade intressanta strukturella motiv i fast tillstånd, elektroniska UV-Vis-strukturer baserade på teoretiska metoder eller elektrokemiska processer. Kritiska punktlänkande händelser, modulära och framväxande fenomen, rika elektrokemiska och optiska egenskaper, hög uttrycksförmåga, solvatokroma förändringar, supramolekylära vätebindningar och ljusemission med distinkta egenskaper i fråga om emissionskälla eller natur kännetecknade reaktionerna och reaktionerna hos föreningarna. Dessa föreningar är i sig stimulerande och värda ytterligare forskningsstudier.

Acknowledgments

This dissertation is a tribute to my beloved Emilia. Her support has extended throughout the last few years of my Ph.D. as I selfishly pursued new avenues of knowledge and research. To my two children Mateo and Melissa (alphabetically), I will always love you and be by your side, and to my grandmother and mother, whose perseverance has shaped me. To Sophia, thank you. Despite the distance, thank you for being there when I needed you. I want to thank my family and my closest friends. Thank you all for always believing in me and my dreams. Erkki, Anne, and Cathrine thank you for being part of my family. Thank you for everything you have done to help us.

I thank my Ph.D. supervisor Andreas Orthaber for all the guidance and support during this Ph.D. journey, which is now successfully and officially completed. You have been supportive and dedicated from the beginning, spending enthusiastic and unimaginable (for most other supervisors) time guiding, supporting, and teaching me. We exchanged valuable information, generated new knowledge, and shared many experiences. We prepared several conferences and events in Uppsala, traveled and participated in meetings in Sweden and abroad, and were part of several groups and scientific teams during these years. All these experiences have helped me become a better researcher, investigator, and scientist.

I want to thank the scientific collaborators and co-authors of the articles who helped me achieve a large part of the work and results during my Ph.D. studies, some of which are part of and presented in this thesis. Andreas, Edgar, Sonja, Ming, Arvind, Josh, and Simon. Most of the results we all obtained were of exceptionally high quality. I express my gratitude and thank you for your work, input, output, and support.

I want to thank the people in the SMC (and physical chemistry and molecular biomimetics) unit(s) of the Department of Chemistry - Ångström, where we shared lab, office space, and scientific input/output during casual conversations, group meetings, time outside the office in activities, discussions with invited speakers, and more, including unit leader Sascha Ott. I am grateful for his scientific and general input at various points during my Ph.D. I would also like to thank the other group leaders in the unit, especially Henrik Ottosson,

Eszter Borbas, and Anders Thapper, for all the interactions, scientific discussions, and feedback during the Ph.D. years. I thank all the people involved in my Ph.D. in one way or another, from the analytical labs and Ph.D. courses (teachers). I also thank those whose work was invisible but helped me in other ways and contributed to my progress, e.g., suppliers, software, developers, hardware, services, programs, applications, models, algorithms, and more.

I thank all the group members, researchers, teachers, staff, and people I have met in the department and at Uppsala University. There are many people I have left out. It has been a long journey and many years since I met many of them. Nevertheless, I sincerely thank them if we have shared an optimistic, expressive, cohesive, or joyful time. I thank Anna, Mariia, Ashleigh, Keyhan, Giovanni, Michele, Max, Charlene, Brian, Starla, Jordann, Daniel, Martin, Palas, Lisa, Biswanath, Somnath, Ben, Hemlatha, Timofey, Marco, Sven, Jacinto, Luca, the administrative staff, and many others. Many of them and others supported me during my Ph.D. studies. I want to thank those who became my friends, Shameem, Nicolas, Juri, Juan David, Dulcie, and others.

I want to thank all the people I met in Sweden. Many of them became friends. They have been of significant help and support during all these Ph.D. years and others. We shared great times and had fun. Julian, Selvi, Mahir, Giovanni, Gianina, Felipe, Amanda, Andrea, Kristina, Louisa, Apostolos, Donovan, Samuel, Sara, Rami, Aliev, and many others.

I want to thank all my family members in Colombia, Spain, and the United States, including my aunts, uncles, cousins, my sisters in Colombia. I acknowledge my uncles and aunts and their respective others (uncles-in-law and aunts-in-law). Thank you for caring for me and being there when I needed you. Thank you for staying in touch. Despite these few times, I was not immediately available on the phone. There are too many to name, but I want to thank all my family. I hope to see you soon.

Finally, I would like to express my gratitude to all my friends in Colombia and the United States. I have had the good fortune to count on a few, albeit excellent, friends who have been faithful to me for many years and with whom I have shared many experiences, conversations, and moments: Juan D., Juan D., Juanjo, Santiago, Sebastian, Daniel, Cristian, Javier, Camilo, Joseph, Juanpa, Susana, Rachel, Sergei, Juanita, and a few others. I hope that we will continue to be friends and that we will share time again soon. I want to thank the Designer ("God" and universe image) and the free will and the freedom of identity and expression we have been given and have developed. We must fight and struggle for it. I believe, as many other scientists do, whether this is a simulation, material design, chaos, or otherwise, that there is One and All.

References

1. Morita, A. Semiconducting black phosphorus. *Appl. Phys. A* **39**, 227–242 (1986).
2. Chen, Y. *et al.* Black Arsenic: A Layered Semiconductor with Extreme In-Plane Anisotropy. *Advanced Materials* **30**, 1800754 (2018).
3. Powell, W. H. Treatment of variable valence in organic nomenclature (lambda convention) (Recommendations 1983). *Pure and Applied Chemistry* **56**, 769–778 (1984).
4. Recker, G. Bildung und Eigenschaften von Acylphosphinen. I. Monosubstitutionsreaktionen an substituierten Disilylphosphinen mit Pivaloylchlorid. *Zeitschrift für anorganische und allgemeine Chemie* **423**, 242–254 (1976).
5. Becker, G. & Gutekunst, G. Phenyl-[2,2-dimethyl-1-(trimethylsiloxy) propylidene]-arsane, an Arsane with an Isolated As=C Bond. *Angew. Chem. Int. Ed.* **16**, 463–464 (1977).
6. Mathey, F. Phospha-Organic Chemistry: Panorama and Perspectives. *Angew. Chem. Int. Ed.* **42**, 1578–1604 (2003).
7. Jutzi, P. New Element-Carbon (p-p) π Bonds. *Angew. Chem. Int. Ed.* **14**, 232–245 (1975).
8. Arduengo, A. J. *et al.* Carbene–Pnictinidene Adducts. *Inorganic Chemistry* **36**, 2151–2158 (1997).
9. Leclerc, M. Polyfluorenes: Twenty years of progress. *Journal of Polymer Science Part A: Polymer Chemistry* **39**, 2867–2873 (2001).
10. Imoto, H. & Naka, K. Recent progress on arsenic-containing functional polymers. *Polymer* **241**, 124464 (2022).
11. Vidal, F. & Jäkle, F. Functional Polymeric Materials Based on Main-Group Elements. *Angew. Chem. Int. Ed.* **58**, 5846–5870 (2019).
12. *Polyfluorenes*. vol. 212 (Springer, 2008).
13. Green, J. P. & Orthaber, A. Organophosphorus Polymers. in *Encyclopedia of Inorganic and Bioinorganic Chemistry* 1 (2019).

14. Parke, S. M., Boone, M. P. & Rivard, E. Marriage of heavy main group elements with π -conjugated materials for optoelectronic applications. *Chem. Commun.* **52** 9485–9505 (2016).
15. Svyaschenko, Y. V., Orthaber, A. & Ott, S. Tuning the Electronic Properties of Acetylenic Fluorenes by Phosphaalkene Incorporation. *Chem. Eur. J.* **22**, 4247–4255 (2016).
16. Shirakawa, H., Louis, E. J., MacDiarmid, A. G., Chiang, C. K. & Heeger, A. J. Synthesis of Electrically Conducting Organic Polymers: Halogen Derivatives of Polyacetylene, $(\text{CH})_x$. *J. Chem. Soc., Chem. Commun.* **16**, 578–580 (1977).
17. Heinze, J., Frontana-Uribe, B. A. & Ludwigs, S. Electrochemistry of Conducting Polymers—Persistent Models and New Concepts. *Chem. Rev.* **110**, 4724–4771 (2010).
18. Decken, A., Carmalt, C. J., Clyburne, J. A. C. & Cowley, A. H. Bonding of Phosphinidene or Arsenidene Fragments to a Fluorenylidene. Interrelationships between Phosphaalkenes or Arsaalkenes and Donor-Acceptor Complexes. *Inorg. Chem.* **36**, 3741–3744 (1997).
19. Swanston, J. Thiophene. *Ullmann's Encyclopedia of Industrial Chemistry* (2006)
20. Abbel, R., Schenning, A. P. H. J. & Meijer, E. w. Fluorene-based materials and their supramolecular properties. *J. Polym. Sci.* **47**, 4215–4233 (2009).
21. Back, O., Henry-Ellinger, M., Martin, C. D., Martin, D. & Bertrand, G. ^{31}P NMR Chemical Shifts of Carbene–Phosphinidene Adducts as an Indicator of the π -Accepting Properties of Carbenes. *Angew. Chem. Int. Ed.* **52**, 2939–2943 (2013).
22. Ma, J. *et al.* DDQ/tert-Butyl nitrite-catalyzed aerobic oxidation of diarylmethane sp^3 C–H bonds. *Tetrahedron* **71**, 6733–6739 (2015).
23. Rozhenko, A. B., Schoeller, W. W. & Povolotskii, M. I. Ab initio calculation of NMR shielding in phosphaalkenes $\text{X}=\text{P}=\text{CY}_2$. *Magn Reson Chem* **37**, 551–563 (1999).
24. Baiget, L. *et al.* New Halo Compounds of Si, P, As, and Sb Bearing a Bulky Substituted Fluorenyl Group. *Phosphorus Sulfur Silicon Relat Elem* **178**, 1949–1961 (2003).
25. Wei, X.-H. *et al.* Lewis Acid Enables Ketone Phosphorylation to Form a C–P Bond and a C–C Bond: Synthesis of 9-Phosphoryl Fluorene Derivatives. *Org. Lett.* **23**, 7100–7105 (2021).
26. Orthaber, A. *et al.* Cooperative Gold Nanoparticle Stabilization by Acetylenic Phosphaalkenes. *Angew. Chem. Int. Ed.* **54**, 10634–10638 (2015).
27. Aviram, Ari. Molecules for memory, logic, and amplification. *J. Am. Chem. Soc.* **110**, 5687–5692 (1988).

28. Damaceanu, M.-D. & Marin, L. Structure–property relationship in fluorene-based polymer films obtained by electropolymerization of 4,4'-(9-fluorenylidene)-di-aniline. *RSC Adv.* **5**, 97016–97026 (2015).
29. Roncali, J. Electrogenerated functional conjugated polymers as advanced electrode materials. *J. Mater. Chem.* **9**, 1875–1893 (1999).
30. Cosnier, S. & Karyakin, A. Electropolymerization: concepts, materials and applications. (2011).
31. Heeney, M. *et al.* Alkylidene Fluorene Liquid Crystalline Semiconducting Polymers for Organic Field Effect Transistor Devices. *Macromolecules* **37**, 5250–5256 (2004).
32. Gates, D., Tsang, C. & Yam, M. Polymerization of phosphalkenes. (2006).
33. Zhou, M. & Heinze, J. Electropolymerization of pyrrole and electrochemical study of polypyrrole: 1. Evidence for structural diversity of polypyrrole. *Electrochim. Acta* **44**, 1733–1748 (1999).
34. Onen, M. *et al.* Nanosecond protonic programmable resistors for analog deep learning. *Science* **377**, 539–543 (2022).
35. Grilli, J., Rogers, T. & Allesina, S. Modularity and stability in ecological communities. *Nat. Commun.* **7**, 12031 (2016).
36. *Transactions on Modularity and Composition I*. vol. 9800 (Springer International Publishing, 2016).
37. Johnson, S. *Emergence: The connected lives of ants, brains, cities, and software*. (Simon and Schuster, 2002).
38. Jansen, G. & Gollmar, P. *Reactive Systems Explained*. (O'Reilly Media, Incorporated, 2020).
39. Ott, E. Strange attractors and chaotic motions of dynamical systems. *Rev. Mod. Phys.* **53**, 655–671 (1981).
40. Wolfram, S. Statistical mechanics of cellular automata. *Rev. Mod. Phys.* **55**, 601–644 (1983).
41. Dueñas-Díez, M. & Pérez-Mercader, J. How Chemistry Computes: Language Recognition by Non-Biochemical Chemical Automata. From Finite Automata to Turing Machines. *iScience* **19**, 514–526 (2019).
42. Freeman, W. J. On the Problem of Anomalous Dispersion in Chaotic-Chaotic Phase Transitions of Neural Masses, and Its Significance for the Management of Perceptual Information in Brains. in *Synergetics of Cognition* (eds. Haken, H. & Stadler, M.) 126–143 (Springer, 1990).
43. Hillman, A. R. & Bruckenstein, S. Role film history and observational time-scale on redox switching kinetics of electroactive films. Part 1.—A new model for

permselective films with polymer relaxation processes. *J. Chem. Soc., Faraday Trans.* **89**, 339–348 (1993).

44. Feldberg, S. W. & Rubinstein, I. Unusual quasi-reversibility (UQR) or apparent non-kinetic hysteresis in cyclic voltammetry: An elaboration upon the implications of N-shaped free energy relationships as explanation. *J. Electroanal. Chem. Interfacial Electrochem.* **240**, 1–15 (1988).

45. Nishioka, Y. Polypyrrole soft actuators. *Electropolymerization, Intech, Rijeka* 159–186 (2011).

46. Inzelt, G. Simultaneous chronoamperometric and quartz crystal microbalance studies of redox transformations of polyaniline films. *Electrochim. Acta* **45**, 3865–3876 (2000).

47. Heinze, J. & Rasche, A. The memory effect in solution. *J Solid State Electrochem.* **10**, 148–156 (2006).

48. Grande, H. & Otero, T. F. Intrinsic Asymmetry, Hysteresis, and Conformational Relaxation during Redox Switching in Polypyrrole: A Coulovoltametric Study. *J. Phys. Chem. B* **102**, 7535–7540 (1998).

49. Villeret, B. & Nechtschein, M. Memory effects in conducting polymers. *Phys. Rev. Lett.* **63**, 1285–1287 (1989).

50. Aoki, K. Simulation of electrochemical slow relaxation at electrically conducting polymer-coated electrodes based on the concept of percolation. *Journal of Electroanalytical Chemistry* **373**, 67–73 (1994).

51. Otero, T. F. & Boyano, I. Comparative Study of Conducting Polymers by the ESCR Model. *J. Phys. Chem. B* **107**, 6730–6738 (2003).

52. Izhikevich, E. M. Neural excitability, spiking and bursting. *Int. J. Bifurcation Chaos* **10**, 1171–1266 (2000).

53. Dijkstra, E. W. Solution of a problem in concurrent programming control. *Commun. ACM* **8**, 569 (1965).

54. Lamport, L. Specifying Concurrent Program Modules. *ACM Trans. Program. Lang. Syst.* **5**, 190–222 (1983).

55. Reus, C. & Baumgartner, T. Stimuli-responsive chromism in organophosphorus chemistry. *Dalton Trans.* **45**, 1850–1855 (2016).

56. Scholz, R. W. *et al. Sustainable Phosphorus Management: A Global Transdisciplinary Roadmap.* (Springer Netherlands, 2014).

57. *Electrochromic Smart Materials: Fabrication and Applications.* (The Royal Society of Chemistry, 2019).

58. Alkan, S., Cutler, C. A. & Reynolds, J. R. High-Quality Electrochromic Polythiophenes via $\text{BF}_3 \cdot \text{Et}_2\text{O}$ Electropolymerization. *Advanced Functional Materials* **13**, 331–336 (2003).
59. Chang, I. F., Gilbert, B. L. & Sun, T. I. Electrochemichromic Systems for Display Applications. *Journal of The Electrochemical Society* **122**, 955–962 (1975).
60. Murto, P. *et al.* Highly Stable Indacenodithieno [3, 2-b] thiophene-Based Donor–Acceptor Copolymers for Hybrid Electrochromic and Energy Storage Applications. *Macromolecules* **53**, 11106–11119 (2020).
61. Heeger, A. J., Kivelson, S., Schrieffer, J. R. & Su, W.-P. Solitons in conducting polymers. *Rev. Mod. Phys.* **60**, 781–850 (1988).
62. Emin, D. Large (bi)Polarons for Novel Energy Conversion and Superconductivity. *Journal of Superconductivity and Novel Magnetism* **33**, 35–42 (2020).
63. Kim, Y. H., Foster, C. M. & Heeger, A. J. Polarons in high T_c superconductors: IRAV modes and electronic transitions to gap states as in conducting polymers. *Synthetic Metals* **29**, 603–608 (1989).
64. Zozoulenko, I. *et al.* Polarons, bipolarons, and absorption spectroscopy of PEDOT. *ACS Applied Polymer Materials* **1**, 83–94 (2018).
65. Demtröder, W. Laser Raman Spectroscopy. in *Laser Spectroscopy 2* 149–181 (Springer Berlin Heidelberg).
66. Barbosa, C. G., Bento, D. C., Péres, L. O., Louarn, G. & de Santana, H. Changes induced by electrochemical oxidation of poly(9,9-dioctylfluorene-alt-thiophene): towards a correlation between charge transport, molecular structure modifications and degradation. *Journal of materials science. Materials in electronics* **27**, 10259–10269 (2016).
67. Casado, J., Ponce Ortiz, R. & López Navarrete, J. T. Quinoidal oligothiophenes: new properties behind an unconventional electronic structure. *Chem. Soc. Rev.* **41**, 5672–5686 (2012).
68. Zeggari, S., Lapouge, C., Buntinx, G. & Poizat, O. Theoretical and experimental resonance Raman study of the fluorene radical cation. *Chemical Physics* **313**, 113–122 (2005).
69. Cerdeira, F. *et al.* Raman spectroscopy as a probe of molecular order, orientation, and stacking of fluorinated copper-phthalocyanine (F_{16}CuPc) thin films. *Journal of Raman Spectroscopy* **44**, 597–607 (2013).
70. Snively, C. M. & Koenig, J. L. IR and Raman Spectroscopies, Polymer Applications in *Encyclopedia of Spectroscopy and Spectrometry (Third Edition)* (eds. Lindon, J. C., Tranter, G. E. & Koppenaal, D. W.) 365–371 (Academic Press, 2017).

71. Brambilla, L. *et al.* Regio-Regular Oligo and Poly (3-hexyl thiophene): Precise Structural Markers from the Vibrational Spectra of Oligomer Single Crystals. *Macromolecules* **47**, 6730–6739 (2014).
72. Vidano, R. P., Fischbach, D. B., Willis, L. J. & Loehr, T. M. Observation of Raman band shifting with excitation wavelength for carbons and graphites. *Solid State Communications* **39**, 341–344 (1981).
73. Ferrari, A. C. *et al.* Raman Spectrum of Graphene and Graphene Layers. *Phys. Rev. Lett.* **97**, 187401 (2006).
74. Wang, Y., Feng, L. & Wang, S. Conjugated polymer nanoparticles for imaging, cell activity regulation, and therapy. *Advanced Functional Materials* **29**, 1806818 (2019).
75. Jorio, A. *et al.* Linewidth of the Raman features of individual single-wall carbon nanotubes. *Phys. Rev. B* **66**, 115411 (2002).
76. Tsoi, W. & Lidzey, D. Raman spectroscopy of fluorene oligomers in the α -, β - and γ -phases. *Journal of Physics: Condensed Matter* **20**, 125213 (2008).
77. Wagner, J. P. & Schreiner, P. R. London dispersion in molecular chemistry—reconsidering steric effects. *Angew. Chem. Int. Ed.* **54**, 12274–12296 (2015).
78. Maia, F. C. & Miranda, P. B. Molecular ordering of conjugated polymers at metallic interfaces probed by SFG vibrational spectroscopy. *The Journal of Physical Chemistry C* **119**, 7386–7399 (2015).
79. Tsoi, W. C. *et al.* The Nature of In-Plane Skeleton Raman Modes of P3HT and Their Correlation to the Degree of Molecular Order in P3HT:PCBM Blend Thin Films. *J. Am. Chem. Soc.* **133**, 9834–9843 (2011).
80. Ruiz Delgado, M. C., Hernández, V., López Navarrete, J. T., Tanaka, S. & Yamashita, Y. Combined Spectroscopic and Theoretical Study of Narrow Band Gap Heterocyclic Co-oligomers Containing Alternating Aromatic Donor and o-Quinoid Acceptor Units. *J. Phys. Chem. B* **108**, 2516–2526 (2004).
81. Campbell, I. & Fauchet, P. M. The effects of microcrystal size and shape on the one phonon Raman spectra of crystalline semiconductors. *Solid State Communications* **58**, 739–741 (1986).
82. Horovitz, B. Infrared activity of Peierls systems and application to polyacetylene. *Solid State Communications* **41**, 729–734 (1982).
83. Green, J. P. *et al.* An Air-Stable Semiconducting Polymer Containing Dithi-eno[3,2-b:2',3'-d]arsole. *Angew. Chem. Int. Ed.* **55**, 7148–51 (2016).
84. Allred, A. L. & Hensley Jr., A. L. Electronegativities of nitrogen, phosphorus, arsenic, antimony and bismuth. *Journal of Inorganic and Nuclear Chemistry* **17**, 43–54 (1961).

85. Newman, M. E. J. Modularity and community structure in networks. *Proceedings of the National Academy of Sciences* **103**, 8577–8582 (2006).
86. Milo, R. *et al.* Network Motifs: Simple Building Blocks of Complex Networks. *Science* **298**, 824–827 (2002).
87. Petty, M. C. *Molecular Electronics: From Principles to Practice*. (John Wiley & Sons, Incorporated, 2007).
88. Faza, O. N. & López, C. S. Computational Approaches to Homogeneous Gold Catalysis. in *Homogeneous Gold Catalysis* (ed. Slaughter, L. M.) 213–283 (Springer International Publishing, 2015).
89. Friebe, C., Hager, M. D., Winter, A. & Schubert, U. S. Metal-containing Polymers via Electropolymerization. *Advanced Materials* **24**, 332–345 (2012).
90. Wolf, M. O. Transition-Metal–Polythiophene Hybrid Materials. *Advanced Materials* **13**, 545–553 (2001).
91. Wang, S. M. *et al.* Synthesis of graphene on a polycrystalline Co film by radio-frequency plasma-enhanced chemical vapour deposition. *Journal of Physics D: Applied Physics* **43**, 455402 (2010).
92. Mei, J. & Bao, Z. Side Chain Engineering in Solution-Processable Conjugated Polymers. *Chem. Mater.* **26**, 604–615 (2014).
93. Hughes, G. & R. Bryce, M. Electron-transporting materials for organic electroluminescent and electrophosphorescent devices. *Journal of Materials Chemistry* **15**, 94–107 (2005).
94. Tang, H., Li, F. & Shinar, J. Bright high efficiency blue organic light-emitting diodes with Al₂O₃/Al cathodes. *Appl. Phys. Lett.* **71**, 2560–2562 (1997).
95. Hsu, F.-M., Chien, C.-H., Shih, P.-I. & Shu, C.-F. Phosphine-oxide-containing bipolar host material for blue electrophosphorescent devices. *Chemistry of Materials* **21**, 1017–1022 (2009).
96. Itoh, J. *et al.*, Platinum complex and luminescent element. (2013).
97. Li, Y., Liu, Y., Bu, W., Guo, J. & Wang, Y. A mixed pyridine–phenol boron complex as an organic electroluminescent material. *Chem. Commun.* 1551–1552 (2000).
98. Kulkarni, A. P., Tonzola, C. J., Babel, A. & Jenekhe, S. A. Electron Transport Materials for Organic Light-Emitting Diodes. *Chem. Mater.* **16**, 4556–4573 (2004).
99. Meng, H. *et al.* Oligofluorene–Thiophene Derivatives as High-Performance Semiconductors for Organic Thin Film Transistors. *Chemistry of Materials* vol. 15 1778–1787 (2003).
100. Bao, Z. & Locklin, J. Organic Field-Effect Transistors. (CRC Press, 2007).

101. Meng, H., Bao, Z., Lovinger, A. J., Wang, B.-C. & Majsce, A. M. High Field-Effect Mobility Oligofluorene Derivatives with High Environmental Stability. *J. Am. Chem. Soc.* **123**, 9214–9215 (2001).
102. Daskalakis, K. S., Maier, S. A., Murray, R. & Kéna-Cohen, S. Nonlinear interactions in an organic polariton condensate. *Nature Mater.* **13**, 271–278 (2014).
103. Bhawalkar, J. D., He, G. S. & Prasad, P. N. Nonlinear multiphoton processes in organic and polymeric materials. *Rep. Prog. Phys.* **59**, 1041–1070 (1996).
104. Kundi, V. & Thankachan, P. P. Packing of Large Two- and Three-Photon Activity Into Smallest Possible Unsymmetrical Fluorene Chromophores. *The Journal of Physical Chemistry A* vol. 120 2757–2770 (2016).
105. Plumhof, J. D., Stöferle, T., Mai, L., Scherf, U. & Mahrt, R. F. Room-temperature Bose–Einstein condensation of cavity exciton–polaritons in a polymer. *Nature Mater.* **13**, 247–252 (2014).
106. Zheng, Q., He, G. S., Lu, C. & Prasad, P. N. Synthesis, two- and three-photon absorption, and optical limiting properties of fluorene-containing ferrocene derivatives. *J. Mater. Chem.* **15**, 3488–3493 (2005).
107. Zhao, M. *et al.* Studies of third-order optical nonlinearities of model compounds containing benzothiazole, benzimidazole and benzoxazole units. *Chem. Mater.* **2**, 670–678 (1990).
108. Rasi, D. D. C. & Janssen, R. A. J. Advances in solution-processed multijunction organic solar cells. *Adv. Mater.* **31**, 1806499 (2019).
109. Kippelen, B. & Brédas, J.-L. Organic photovoltaics. *Energy Environ. Sci.* **2**, 251–261 (2009).
110. Sun, Y. *et al.* Solution-processed small-molecule solar cells with 6.7% efficiency. *Nature Mater.* **11**, 44–48 (2012).
111. Sun, R. *et al.* Single-Junction Organic Solar Cells with 19.17% Efficiency Enabled by Introducing One Asymmetric Guest Acceptor. *Adv. Mater.* **34**, 2110147 (2022).
112. Janata, J. & Josowicz, M. Conducting polymers in electronic chemical sensors. *Nature Mater.* **2**, 19–24 (2003).
113. Janata, J. *Principles of chemical sensors*. (Springer, 2009).
114. van De Burgt, Y., Melianas, A., Keene, S. T., Malliaras, G. & Salleo, A. Organic electronics for neuromorphic computing. *Nat. Electron.* **1**, 386–397 (2018).
115. Yuan, L., Liu, S., Chen, W., Fan, F. & Liu, G. Organic Memory and Memristors: From Mechanisms, Materials to Devices. *Advanced Electronic Materials* **7**, 2100432 (2021).

116. Yu, Y. *et al.* Small-Molecule-Based Organic Field-Effect Transistor for Non-volatile Memory and Artificial Synapse. *Advanced Functional Materials* **29**, 1904602 (2019).
117. Scott, J. C. & Bozano, L. D. Nonvolatile Memory Elements Based on Organic Materials. *Advanced Materials* **19**, 1452–1463 (2007).
118. Goswami, S., Goswami, S. & Venkatesan, T. An organic approach to low energy memory and brain inspired electronics. *Appl. Phys. Rev.* **7**, 021303 (2020).
119. Hong, E. Y.-H., Poon, C.-T. & Yam, V. W.-W. A Phosphole Oxide-Containing Organogold(III) Complex for Solution-Processable Resistive Memory Devices with Ternary Memory Performances. *J. Am. Chem. Soc.* **138**, 6368–6371 (2016).
120. Goswami, S. *et al.* Robust resistive memory devices using solution-processable metal-coordinated azo aromatics. *Nat. Mater.* **16**, 1216–1224 (2017).
121. Lovinger, A. J. & Rothberg, L. J. Electrically active organic and polymeric materials for thin-film-transistor technologies. *Journal of Materials Research* **11**, 1581–1592 (1996).
122. Märkl, G. & Raab, K. M. Phosphapentafulvene. *Tetrahedron Letters* **30**, 1077–1080 (1989).
123. Carter-Fenk, K. & M. Herbert, J. Reinterpreting π -stacking. *Phys. Chem. Chem. Phys.* **22**, 24870–24886 (2020).
124. Garcia-Garibay, M. A. Crystalline molecular machines: Encoding supramolecular dynamics into molecular structure. *PNAS* **102**, 10771–10776 (2005).
125. Keen, D. A. & Goodwin, A. L. The crystallography of correlated disorder. *Nature* **521**, 303–309 (2015).
126. Abersfelder, K., White, A. J. P., Rzepa, H. S. & Scheschkewitz, D. A Tricyclic Aromatic Isomer of Hexasilabenzene. *Science* **327**, 564–566 (2010).
127. Willmes, P. *et al.* From Disilene (Si=Si) to Phosphasilene (Si=P) and Phosphacumulene (P=C=N). *Angew. Chem. Int. Ed.* **53**, 2216–2220 (2014).
128. Fujimori, S. & Inoue, S. Low-Valent Silicon Compounds. in *Reference Module in Chemistry, Molecular Sciences and Chemical Engineering* (Elsevier, 2022).
129. Rammo, A. & Scheschkewitz, D. Functional Disilenes in Synthesis. *Chem. Eur. J.* **24**, 6866–6885 (2018).
130. D’Imperio, N., Arkhypchuk, A. I., Mai, J. & Ott, S. Triphenylphosphaalkenes in Chemical Equilibria. *European Journal of Inorganic Chemistry* **2019**, 1562–1566 (2019).
131. Heidrich-Meisner, F., Sergienko, I. A., Feiguin, A. E. & Dagotto, E. R. Universal emergence of the one-third plateau in the magnetization process of frustrated quantum spin chains. *Phys. Rev. B* **75**, 064413 (2007).

132. Gaita-Ariño, A., Luis, F., Hill, S. & Coronado, E. Molecular spins for quantum computation. *Nat. Chem.* **11**, 301–309 (2019).
133. Nassif, N. & Livage, J. From diatoms to silica-based biohybrids. *Chem. Soc. Rev.* **40**, 849–859 (2011).
134. Ottosson, H. & Steel, P. G. Silylenes, Silenes, and Disilenes: Novel Silicon-Based Reagents for Organic Synthesis? *Chem. Eur. J.* **12**, 1576–1585 (2006).
135. Google AI Quantum and Collaborators *et al.* Hartree-Fock on a superconducting qubit quantum computer. *Science* **369**, 1084–1089 (2020).
136. Kalinin, S. V., Ghosh, A., Vasudevan, R. & Ziatdinov, M. From atomically resolved imaging to generative and causal models. *Nat. Phys.* **18**, 1152–1160 (2022).
137. Goede, S. J. & Bickelhaupt, F. Synthesis and Reactions of P-Supermesityl-C-halophosphaalkenes. *Chemische Berichte* **124**, 2677–2684 (1991).
138. Abersfelder, K., White, A. J. P., Berger, R. J. F., Rzepa, H. S. & Scheschkewitz, D. A Stable Derivative of the Global Minimum on the Si₆H₆ Potential Energy Surface. *Angew. Chem. Int. Ed.* **50**, 7936–7939 (2011).
139. Weidenbruch, M., Willms, S., Saak, W. & Henkel, G. Hexaaryltetrasilabuta-1,3-diene: A Molecule with Conjugated Si=Si Double Bonds. *Angew. Chem. Int. Ed.* **36**, 2503–2504 (1997).
140. Champion, D. H. & Cowley, A. H. Reaction of a phosphaketene with diiron enneacarbonyl: Possible intermediacy of a terminal phosphinidene complex. *Polyhedron* **4**, 1791–1792 (1985).
141. Masuda, J. D. *et al.* A Lanthanide Phosphinidene Complex: Synthesis, Structure, and Phospha-Wittig Reactivity. *J. Am. Chem. Soc.* **130**, 2408–2409 (2008).
142. Yanai, T., Tew, D. P. & Handy, N. C. A new hybrid exchange–correlation functional using the Coulomb-attenuating method (CAM-B3LYP). *Chemical Physics Letters* **393**, 51–57 (2004).
143. Appel, R. & Krieger, L. Niederkoordinierte Phosphorverbindungen: LXIX. 1,8-Diaza-6-(2',4',6'-tri-*t*-butylphenylphosphanylidene)-bicyclo-[5.4.0]-undec-7-en, ein ungewöhnliches chelatisierendes phosphalken. *Journal of Organometallic Chemistry* **354**, 309–312 (1988).
144. Van der Knaap, T. A., Klebach, T. C., Lourens, R., Vos, M. & Bickelhaupt, F. Oxidation reactions of phosphalkenes. *J. Am. Chem. Soc.* **105**, 4026–4032 (1983).
145. Fink, M. J., De Young, D. J., West, R. & Michl, J. Chemical reactions of tetramesityldisilene. *J. Am. Chem. Soc.* **105**, 1070–1071 (1983).
146. West, R. Chemistry of the Silicon-Silicon Double Bond. *Angew. Chem. Int. Ed.* **26**, 1201–1211 (1987).

147. Klebach, T. C., Lourens, R. & Bickelhaupt, F. Synthesis of mesityldiphenyl-methylenephosphine: a stable compound with a localized phosphorus:carbon bond. *J. Am. Chem. Soc.* **100**, 4886–4888 (1978).
148. Coady, D. J., Fukushima, K., Horn, H. W., Rice, J. E. & Hedrick, J. L. Catalytic insights into acid/base conjugates: highly selective bifunctional catalysts for the ring-opening polymerization of lactide. *Chem. Commun.* **47**, 3105–3107 (2011).
149. Miran, M. S., Kinoshita, H., Yasuda, T., Susan, M. A. B. H. & Watanabe, M. Hydrogen bonds in protic ionic liquids and their correlation with physicochemical properties. *Chem. Commun.* **47**, 12676–12678 (2011).
150. Ishikawa, T. Superbases for organic synthesis: guanidines, amidines, phosphazenes and related organocatalysts. (John Wiley & Sons, 2009).
151. Seager, S., Bains, W. & Petkowski, J. Toward a list of molecules as potential biosignature gases for the search for life on exoplanets and applications to terrestrial biochemistry. *Astrobiology* **16**, 465–485 (2016).
152. Morrison, A. M., Flynn, S. D., Liang, T. & Doublerly, G. E. Infrared spectroscopy of $(\text{HCl})_m(\text{H}_2\text{O})_n$ clusters in helium nanodroplets: definitive assignments in the HCl stretch region. *J. Phys. Chem A* **114**, 8090–8098 (2010).
153. Curnow, O. J. & Crittenden, D. L. Structures and Spectra of Halide Hydrate Clusters in the Solid State: A Link between the Gas Phase and Solution State. *ChemPlusChem* **87**, e202100535 (2022).
154. Bisht, K. K., Kathalikkattil, A. C. & Suresh, E. Hydrogen-bonded one- and two-dimensional hybrid water-chloride motifs. *Crystal Growth & Design* **12**, 556–561 (2012).
155. Medhekar, N. V., Ramasubramaniam, A., Ruoff, R. S. & Shenoy, V. B. Hydrogen Bond Networks in Graphene Oxide Composite Paper: Structure and Mechanical Properties. *ACS Nano* **4**, 2300–2306 (2010).
156. Olah, G. A., Prakash, G. S., Sommer, J. & Molnar, A. Superacid chemistry. (2009).
157. Kroon, J. & Kanters, J. A. Non-linearity of hydrogen bonds in molecular crystals. *Nature* **248**, 667–669 (1974).
158. Thompson, W. H. & Hynes, J. T. Frequency Shifts in the Hydrogen-Bonded OH Stretch in Halide–Water Clusters. The Importance of Charge Transfer. *J. Am. Chem. Soc.* **122**, 6278–6286 (2000).
159. Gilli, G. & Gilli, P. The nature of the hydrogen bond: outline of a comprehensive hydrogen bond theory **23** (Oxford University Press, 2009).
160. Jeffrey, G. A. Hydrogen-Bonding: An update. *Crystallography Reviews* **9**, 135–176 (2003).

161. Delzeit, L., Rowland, B. & Devlin, J. P. Infrared spectra of hydrogen chloride complexed/ionized in amorphous hydrates and at ice surfaces in the 15–90 K range. *J. Phys. Chem* **97**, 10312–10318 (1993).
162. Morales Salazar, D., Gupta, A. K. & Orthaber, A. Reactivity studies of an imine-functionalised phosphalkene; unusual electrostatic and supramolecular stabilisation of a $\sigma^2\lambda^3$ -phosphorus motif via hydrogen bonding. *Dalton Trans.* (2018).
163. Quin, L. D., Yao, E.-Y. & Szewczyk, J. Special Properties Imparted to the 9-Phosphabicyclo[6.1.0]nonatriene system by a P-(2,4,6-tri-*t*-butylphenyl) substituent; ^{17}O NMR spectrum of a bicyclic phosphirane oxide. *Tetrahedron Letters* **28**, 1077–1080 (1987).
164. Esfandiari, K., Mai, J. & Ott, S. Unsymmetrical E-Alkenes from the Stereoselective Reductive Coupling of Two Aldehydes. *J. Am. Chem. Soc.* **139**, 2940–2943 (2017).
165. Oka, K. *et al.* Long-lived water clusters in hydrophobic solvents investigated by standard NMR techniques. *Sci Rep* **9**, 223 (2019).
166. Pregosin, P. S. NMR spectroscopy and ion pairing: Measuring and understanding how ions interact. *Pure Appl. Chem.* **81**, 615–633 (2009).
167. Sorgenfrei, N. *et al.* NMR Spectroscopic Characterization of Charge Assisted Strong Hydrogen Bonds in Brønsted Acid Catalysis. *J. Am. Chem. Soc.* **138**, 16345–16354 (2016).
168. Fleischmann, M., Drettwan, D., Sugiono, E., Rueping, M. & Gschwind, R. M. Brønsted Acid Catalysis: Hydrogen Bonding versus Ion Pairing in Imine Activation. *Angew. Chem. Int. Ed.* **50**, 6364–6369 (2011).
169. Alajarin, M., Pastor, A., Orenes, R.-A., Martínez-Viviente, E. & Pregosin, P. S. Pulsed Gradient Spin Echo (PGSE) Diffusion Measurements as a Tool for the Elucidation of a New Type of Hydrogen-Bonded Bicapsular Aggregate. *Chem. Eur. J.* **12**, 877–886 (2006).
170. Zanatta, M., Antunes, V. U., Tormena, C. F., Dupont, J. & Santos, F. P. dos. Dealing with supramolecular structure for ionic liquids: a DOSY NMR approach. *Phys. Chem. Chem. Phys.* **21**, 2567–2571 (2019).
171. Perrin, C. L. & Nielson, J. B. “Strong” Hydrogen Bonds In Chemistry And Biology. *Annu. Rev. Phys. Chem.* **48**, 511–544 (1997).
172. McDowell, S. A. C. & Buckingham, A. D. On the Correlation between Bond-Length Change and Vibrational Frequency Shift in Hydrogen-Bonded Complexes: A Computational Study of $\text{Y}\cdots\text{HCl}$ Dimers ($\text{Y} = \text{N}_2, \text{CO}, \text{BF}$). *J. Am. Chem. Soc.* **127**, 15515–15520 (2005).

173. Ghosh, S. & Wategaonkar, S. C–H···O Hydrogen Bond Anchored Water Bridge in 1,2,4,5-Tetracyanobenzene-Water Clusters. *J. Phys. Chem. A* **123**, 3851–3862 (2019).
174. Abou-Chahine, F. *et al.* Vibrationally resolved dynamics of the reaction of Cl atoms with 2,3-dimethylbut-2-ene in chlorinated solvents. *Chem. Sci.* **4**, 226–237 (2012).
175. Chalmers, J. M. Mid-Infrared Spectroscopy: Anomalies, Artifacts and Common Errors. in *Handbook of Vibrational Spectroscopy* (John Wiley & Sons, Ltd., 2006).
176. Furutani, Y., Shichida, Y. & Kandori, H. Structural Changes of Water Molecules during the Photoactivation Processes in Bovine Rhodopsin. *Biochemistry* **42**, 9619–9625 (2003).
177. Furutani, Y., Shibata, M. & Kandori, H. Strongly hydrogen-bonded water molecules in the Schiff base region of rhodopsins. *Photochem. Photobiol. Sci.* **4**, 661 (2005).
178. Agmon, N. Structure of Concentrated HCl Solutions. *J. Phys. Chem. A* **102**, 192–199 (1998).
179. Aouissi, A., Al-Deyab, S. S. & Al-Shahri, H. The Cationic Ring-Opening Polymerization of Tetrahydrofuran with 12-Tungstophosphoric Acid. *Molecules* **15**, 1398–1407 (2010).
180. Giereth, R. *et al.* Remarkably long-lived excited states of copper photosensitizers containing an extended π -system based on an anthracene moiety. *Sustainable Energy Fuels* **3**, 692–700 (2019).
181. Mara, M. W., Fransted, K. A. & Chen, L. X. Interplays of excited state structures and dynamics in copper(I) diimine complexes: Implications and perspectives. *Coord. Chem. Rev.* **282–283**, 2–18 (2015).
182. Sato, O. Optically Switchable Molecular Solids: Photoinduced Spin-Crossover, Photochromism, and Photoinduced Magnetization. *Acc. Chem. Res.* **36**, 692–700 (2003).
183. Takeda, H., Monma, Y., Sugiyama, H., Uekusa, H. & Ishitani, O. Development of Visible-Light Driven Cu(I) Complex Photosensitizers for Photocatalytic CO₂ Reduction. *Front Chem* **7**, 418 (2019).
184. Bergmann, L., Braun, C., Nieger, M. & Bräse, S. The coordination- and photochemistry of copper(I) complexes: variation of N[^]N ligands from imidazole to tetrazole. *Dalton Trans.* **47**, 608–621 (2018).
185. Serin, S. C., Pick, F. S., Dake, G. R. & Gates, D. P. Copper(I) Complexes of Pyridine-Bridged Phosphaalkene-Oxazoline Pincer Ligands. *Inorg. Chem.* **55**, 6670–6678 (2016).

186. Hamze, R. *et al.* Eliminating nonradiative decay in Cu(I) emitters: >99% quantum efficiency and microsecond lifetime. *Science* **363**, 601–606 (2019).
187. Cunningham, C. T., Moore, J. J., Cunningham, K. L. H., Fanwick, P. E. & McMillin, D. R. Structural and Photophysical Studies of Cu(NN)₂⁺ Systems in the Solid State. Emission at Last from Complexes with Simple 1,10-Phenanthroline Ligands. *Inorg. Chem.* **39**, 3638–3644 (2000).
188. Iwamura, M., Takeuchi, S. & Tahara, T. Ultrafast Excited-State Dynamics of Copper(I) Complexes. *Acc. Chem. Res.* **48**, 782–791 (2015).
189. Iwamura, M., Watanabe, H., Ishii, K., Takeuchi, S. & Tahara, T. Coherent Nuclear Dynamics in Ultrafast Photoinduced Structural Change of Bis(diimine)copper(I) Complex. *J. Am. Chem. Soc.* **133**, 7728–7736 (2011).
190. Leitzl, M. J. *et al.* Copper(I) Complexes for Thermally Activated Delayed Fluorescence: From Photophysical to Device Properties. *Top. Curr. Chem. (Z)* **374**, 25 (2016).
191. Duan, Y.-C. *et al.* Fluorescence, Phosphorescence, or Delayed Fluorescence?—A Theoretical Exploration on the Reason Why a Series of Similar Organic Molecules Exhibit Different Luminescence Types. *J. Phys. Chem. C* **122**, 23091–23101 (2018).
192. Scaltrito, D. V., Thompson, D. W., O’Callaghan, J. A. & Meyer, G. J. MLCT excited states of cuprous bis-phenanthroline coordination compounds. *Coord. Chem. Rev.* **208**, 243–266 (2000).
193. Bergmann, L. *et al.* Outstanding luminescence from neutral copper(I) complexes with pyridyl-tetrazolate and phosphine ligands. *Chem. Commun.* **49**, 6501–6503 (2013).
194. Sarkar, S., Protasiewicz, J. D. & Dunietz, B. D. Controlling the Emissive Activity in Heterocyclic Systems Bearing C=P Bonds. *J. Phys. Chem. Lett.* **9**, 3567–3572 (2018).
195. Reichardt, C. Solvatochromic Dyes as Solvent Polarity Indicators. *Chem. Rev.* **94**, 2319–2358 (1994).
196. Penfold, T. J. *et al.* Solvent-Induced Luminescence Quenching: Static and Time-Resolved X-Ray Absorption Spectroscopy of a Copper(I) Phenanthroline Complex. *J. Phys. Chem. A* **117**, 4591–4601 (2013).
197. Blaskie, M. W. & McMillin, D. R. Photostudies of copper(I) systems. 6. Room-temperature emission and quenching studies of bis(2,9-dimethyl-1,10-phenanthroline)copper(I). *Inorg. Chem.* **19**, 3519–3522 (1980).

Acta Universitatis Upsaliensis

*Digital Comprehensive Summaries of Uppsala Dissertations
from the Faculty of Science and Technology 2249*

Editor: The Dean of the Faculty of Science and Technology

A doctoral dissertation from the Faculty of Science and Technology, Uppsala University, is usually a summary of a number of papers. A few copies of the complete dissertation are kept at major Swedish research libraries, while the summary alone is distributed internationally through the series Digital Comprehensive Summaries of Uppsala Dissertations from the Faculty of Science and Technology. (Prior to January, 2005, the series was published under the title "Comprehensive Summaries of Uppsala Dissertations from the Faculty of Science and Technology".)

Distribution: publications.uu.se
urn:nbn:se:uu:diva-498018



ACTA
UNIVERSITATIS
UPSALIENSIS
UPPSALA
2023